UNIVERSITY OF BIRMINGHAM

MICROSTRUCTURE CHARACTERISATION AND CREEP MODELLING OF HP40 ALLOYS

by

MINSHI WANG

A thesis submitted to the University of Birmingham for the degree of

DOCTOR OF PHILOSOPHY

School of Metallurgy and Materials

University of Birmingham

May 2017

Preface

This research was carried out by Minshi Wang in School of Metallurgy and Materials, University of Birmingham (from September 2012 to September 2016), under the supervision of Dr YuLung Chiu and Prof Ian Jones.

The present work is original and no part of the work has been submitted for another degree at any other university. Wherever other researchers' work has been drawn or cited, it is acknowledged in the text and the references are listed.

Parts of the work has been published as follows:

1. M. Wang, Y. Chiu, I. Jones, N. Rowlands, J. Holland, Z. Zhang, and D. Flahaut, *Microstructural characterisation and microanalysis of creep resistant steels.* Journal of Physics: Conference Series, 2014. **522**(1): p. 012034.

Abstract

Steam reforming is responsible for 50 % of the world's hydrogen production. The efficiency of steam reforming depends strongly on the creep resistance of the material used for the reformer tubes. The currently most widely used reformer tube material is HP40 (25 Cr, 35Ni, 40 Fe and 0.4C) austenitic stainless steel. A further improvement in the creep resistance of HP40 is needed for efficiency improvement and for a cost reduction in steam reforming. In order to develop a next generation creep resistant alloy, three HP40-based alloys, namely Alloy A, B and C, with different chemical compositions and/or solidification rate were studied. Previous tests at 1000 ºC and 40 MPa have shown that the creep properties of Alloy C are slightly better than those of Alloy B, both being significantly better than Alloy A. Their microstructures have been analysed so as to understand their relative creep performance.

Two types of intergranular precipitate are observed in as-cast Alloy A (typical HP40 steel): primary Cr-carbide (M_7C_3) and primary Nb-carbide (MC), which formed a fragmented network after solidification. After creep, the primary Cr-carbides transformed from M_7C_3 to $M_{23}C_6$. The secondary precipitation of $M_{23}C_6$ and of finely sized NbN were also observed in the matrix. By comparing crept Alloy A and heat treated Alloy A, stress was shown to enhance the coarsening of precipitates by accelerating the solid state diffusion (distortion of the crystal symmetry and reduction of diffusion activation energy) and providing easier diffusion paths (increase of dislocation density).

Alloy B has a slightly different chemical composition from Alloy A: the additions of W and Nb suppressed the formation of carbides by reducing free carbon in the matrix. The combined effects of Ti and W led to a slower coarsening behaviour of the secondary $M_{23}C_6$ during creep of Alloy B than that of Alloy A. The precipitate evolution in Alloy B was analysed via studying the samples heat treated from 1 to 150 hours at 1000 ºC (service temperature). The area fractions of primary and secondary carbides, precipitate size and interspacing of secondary $M_{23}C_6$ in the heat treated samples were characterised quantitatively. The area fractions of primary Nb-carbide and secondary Cr-carbide

and the average size of secondary $M_{23}C_6$ increase continuously with the heat treatment time. The combination of M_7C_3 dissolution, $M_7C_3 \rightarrow M_{23}C_6$ transformation and $M_{23}C_6$ growth leads to a fluctuation in area fraction of the primary Cr-carbide within the first 20 hours of heat treatment, beyond with a continuous increase was observed.

Alloy C is in the same composition range as Alloy B, but was subjected to a higher solidification rate than Alloys A and B. A larger area fraction of primary Nb-carbide in as-cast Alloy C than in as-cast Alloy B was observed. Meanwhile, as-cast Alloy C contains less primary Cr-carbide. A higher coarsening rate of secondary $M_{23}C_6$ in the heat treated Alloy C (1~150 hours at 1000 ^{o}C) was observed. The transformation of primary Cr-carbide from M_7C_3 to $M_{23}C_6$ was analysed by EBSD and TEM and the results indicate that $M_{23}C_6$ nucleates at the interface between the matrix and the M_7C_3 and then grows into the primary M_7C_3.

The small intragranular $M_{23}C_6$ may have contributed significantly to the smaller creep rate, and thus a longer creep life for Alloy B and Alloy C as compared with Alloy A.

A microstructure-based climb-glide bypass creep model, which has a quantitative relationship to the microstructural features obtained from experiments, was described to predict the creep behaviour of HP40. However, only the simulated creep curve with precipitate volume fraction of 45 % fits well compared with experimental creep curve before tertiary creep stage. With a decrease of precipitate size, the creep life in the simulated creep curves increases, which can be explained by the larger back stress obtained from smaller precipitate size. The current model has its limitations and needs modifications including microstructural definition, precipitation evolution and grain boundary cavitation during the tertiary creep stage.

Suggestion on the next generation HP40 alloy has been made.

Acknowledgements

Firstly, I would like to express my deepest gratitude and appreciation to Dr YuLung Chiu and Prof Ian Jones, my academic supervisors, for their professional supervision, patient guidance and continuous encouragement throughout the entire project. Dr YuLung Chiu has provided enlightening suggestions and personal help since my undergraduate final year. Prof Ian Jones supervised my academic research with his wide scientific knowledge, cheered me up with his enthusiasm and spent lots of time correcting my thesis with his great patience.

I am also grateful to Dr Dominique Flahaut and Dr Zhu Zhang, my industrial supervisors, for their support of this PhD project and development of my thesis. I would like to thank Igor Novak from Doncasters Paralloy Ltd, for providing the materials and raw data on creep tests and for innovative discussions.

Many thanks is given to Dr Rengen Ding for his practical guidance and academic advice. I would like to thank Mr Paul Stanley and Mrs Theresa Morris of the Electron Microscope Centre for their support.

I am especially appreciative of the nice company provided by my colleagues in the EM group over these years: Xinxin Zhao, Ruiling Zeng, Yu Lu, Tina Su, Thiago Pereira, Rayan Ameen, Bo Pang, Jing Wu, Zhaoran Liu, Xinyu Lu, Daniel Higgins, Gareth Douglas, Jinsen Tian, Subash Rai, Shanshan Si and Ubaid Ur Rehman Ghori. It is a pleasant and wonderful experience to work with them.

Finally, I would like to thank my parents and girlfriend for their endless support, patience and love, which encourage me to be optimistic and enthusiastic in my study.

Table of contents

List of figures

List of tables

Chapter 1 Introduction

The use of non-renewable fossil fuels, which leads to a significant amount of carbon dioxide and volatile organic compound emissions, raises serious environmental concerns. There has therefore been an effort to diversify the energy supply. Hydrogen is considered the most attractive replacement for non-renewable fossil fuels since it can supply adequate energy without any carbon emission. Currently, steam reforming is responsible for 50 % of the world's hydrogen production because of its high energy efficiency and low cost. The key point for the further development of steam reforming is whether the materials used for reformer tubes can satisfy better the specific requirements of steam reforming, especially high creep resistance.

With continuous technological improvement throughout the last 70 years, a new family of austenitic stainless steels has been developed to fulfil the requirements of the steam reforming process. The currently dominant material used for steam reformer tubes is HP40, a centrifugally cast austenitic stainless steel containing (wt%) 25% Cr, 35% Ni, 40% Fe and 0.4% carbon, plus small amounts of other alloying elements.

A further improvement on the creep resistance of HP40 is needed for a corresponding improvement in efficiency and for a further reduction in the cost of the steam reforming process. The material creep properties are strongly dependent on the microstructure and can be improved by microstructural modification, such as altering the grain size and the intergranular/intragranular precipitation. The microstructure of HP40 can be refined by minor chemical modifications of the present alloy and by changing the solidification rate during centrifugal casting.

Doncasters Paralloy have supplied three HP40-based alloys, where chemical composition or solidification rate have been varied. Creep tests showed that Alloy B and C were significantly better than Alloy A, with Alloy C being slightly better than Alloy B. Their microstructures have been analysed so as to assess their relative creep performances.

An overview of the work is shown schematically in Figure 1.1 and the outline of this PhD thesis is as follows:

Chapter 2 presents the literature review and contains application overview of steam reforming, the requirements for materials in steam reformer tubes, the historical development of HP40, the effects of chemical composition and solidification rate on microstructure, the fundamentals of creep deformation, creep deformation mechanisms, strengthening mechanisms for creep resistance, the detailed creep behaviour of intragranular precipitation strengthened alloys and previous work on the creep behaviour of HP40.

Chapter 3 summarizes the materials and experimental procedure used in this study.

Chapter 4 characterises the microstructure of the as-cast Alloy A and after the creep test (crept Alloy A). The effect of stress on precipitation is also investigated by comparing crept Alloy A and heat treated Alloy A (HT-12).

Chapter 5 presents the microstructures of as-cast Alloy B and crept Alloy B and compares these with those of Alloy A to investigate the effect of *chemical composition*. The precipitation evolution in Alloy B during service is analyzed using samples heat treated from 1 to 150 hours at 1000 ^{o}C. Then the better creep properties of Alloy B are explained.

Chapter 6 describes the effect of *solidification rate* on microstructure by identifying the microstructural differences between Alloys B and C in as-cast, crept and heat treated conditions, respectively. The slight improvement of Alloy C creep resistance over Alloy B is hence explained.

Chapter 7 A microstructure-based climb-glide bypass creep model is described and applied to three alloys to predict the creep behaviour of HP40. Limitations and potential modifications are outlined.

Chapter 8 shows the main conclusions of this study and makes some suggestions for further work.

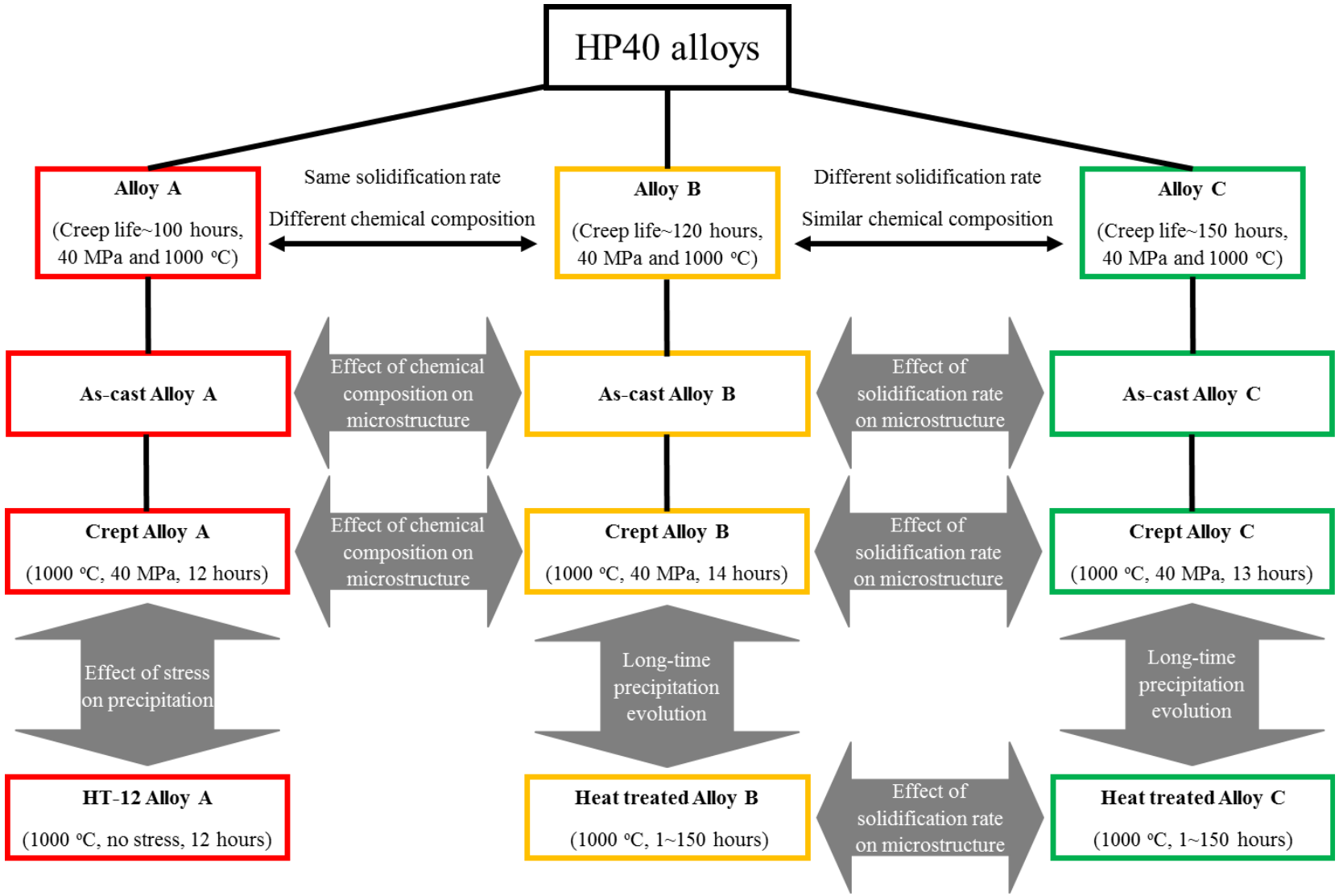

Figure 1.1 Scope of the work. Alloy B and C have similar chemical compositions, which is different from that of Alloy A. The solidification rates of Alloy A and Alloy B were controlled to be the same and lower than that of Alloy C.

Chapter 2 Literature review

2.1 Introduction

Hydrogen has been considered as the most attractive replacement of non-renewable fossil fuels. Steam reforming is currently responsible for 50 % of the world's hydrogen production, due to its high energy efficiency and low cost (Section 2.2.1). The key point for further development of steam reforming is whether the materials used for reformer tubes can satisfy better the specific requirements of steam reforming, especially high creep resistance (Section 2.2.2). With continuous technological improvement throughout the last 70 years, a new family of austenitic stainless steels has been developed to fulfil the requirements for the steam reforming process. The currently dominant material used for steam reformer tubes is HP40, a centrifugally cast austenitic stainless steel with a chemical compositions of 25% Cr, 35% Ni, 40% Fe and 0.4% carbon, plus small contents of other alloy elements (Section 2.3.1). However, the microstructure of HP40 is strongly dependent on the chemical composition of the material (Section 2.3.2) and the solidification rate during casting (Section 2.3.3). Since creep is the main deformation mechanism under the service conditions for steam reforming, its fundamentals are outlined (Section 2.4.1). For different stress and temperature ranges, the creep deformation mechanisms can be divided into diffusional creep and dislocation creep (Section 2.4.2). Meanwhile, the strengthening mechanisms for creep resistance need to be understood in order to achieve better creep properties (Section 2.4.3). The details of the creep mechanism in intragranular precipitation strengthened alloys are discussed (Section 2.4.4) since intragranular precipitates are the most effective way to improve creep properties. The creep behaviour of HP40 from references and as applied by Doncaster Paralloy Ltd. are summarized in Section 2.4.5.

2.2 High temperature resistance austenitic stainless steel in steam reforming

2.2.1 Application overview of steam reforming

The usage of non-renewable fossil fuels, which leads to a significant amount of carbon dioxide and volatile organic compound emissions, raises serious environmental concerns.

To deal with this issue, there has been an effort to diversify the energy supply, particularly for the transportation sector [1]. A range of replacements to fossil fuels exists, such as ethanol, biodiesel, gasoline, natural gas and hydrogen. Among the various options, hydrogen, which is an important chemical feedstock in the petrochemical industry, has become the most attractive alternative fuel since it can supply adequate energy without any carbon emission [1-3]. The potential demand of hydrogen is likely to increase sharply in the future due to breakthroughs in fuel cell technology since the late 1990s. However, the major disadvantage is that hydrogen is not a primary source and must be produced from fossil hydrocarbons or water. Therefore, the energy efficiency and cost of hydrogen production will be the dominant factors for controlling commercial exploitation.

Currently, the annual production of hydrogen is 55 million tons with consumption increasing by approximately 6 % per year [4]. The main methods of producing hydrogen are based on steam methane reforming [5-7], partial oxidation [8], coal gasification [9] or water electrolysis [10]. Table 1 lists a summary of the energy efficiencies and costs of hydrogen production via several methods. High efficiency and low cost (Table 2.1) make steam reforming the dominant hydrogen production method, now responsible for 50 % of the world's hydrogen production (Figure 2.1) [4]. However, the cost of hydrogen production via steam reforming remains higher than for fuel fossil production, indicating a need for improvement in efficiency and for reduction in cost. Meanwhile, the performance of the steam reforming process depends strongly on the properties of the material used for the structural components in the system. Therefore, the key point for further developments of steam reforming is whether the materials can satisfy better the specific requirements of steam reforming.

Table 2.1 List of hydrogen production technologies and costs [9]

Materials	Energy efficiency	Hydrogen selling price ($ / kg)
Steam methane reforming	83 %	0.75
Partial oxidation	70 – 80 %	0.98
Coal gasification	63 %	0.92
Water electrolysis	45 – 55 %	1.95

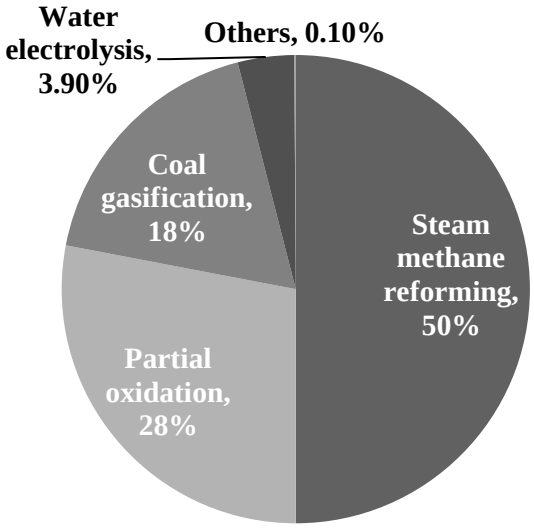

Figure 2.1 Technologies used globally in the production of hydrogen [4]

2.2.2 Requirements for materials in steam reformer tubes

Figure 2.2 illustrates a schematic layout of a steam reforming furnace. Depending on the amount of H_2 and/or CO required by a chemical or petrochemical process downstream other reforming technologies do exist. Basically, three types of SMR (steam methane reformers) technologies can be identified according to the heating burner system: side-fired, top-fired and bottom-fired furnace types. Usually, the first two technologies are used for large scale syngas consumption [11]. For instance, in the case of [12] the SMR furnace has 400 tubes disposed in eight rows of 50 catalytic tubes each with top-fired natural gas burners

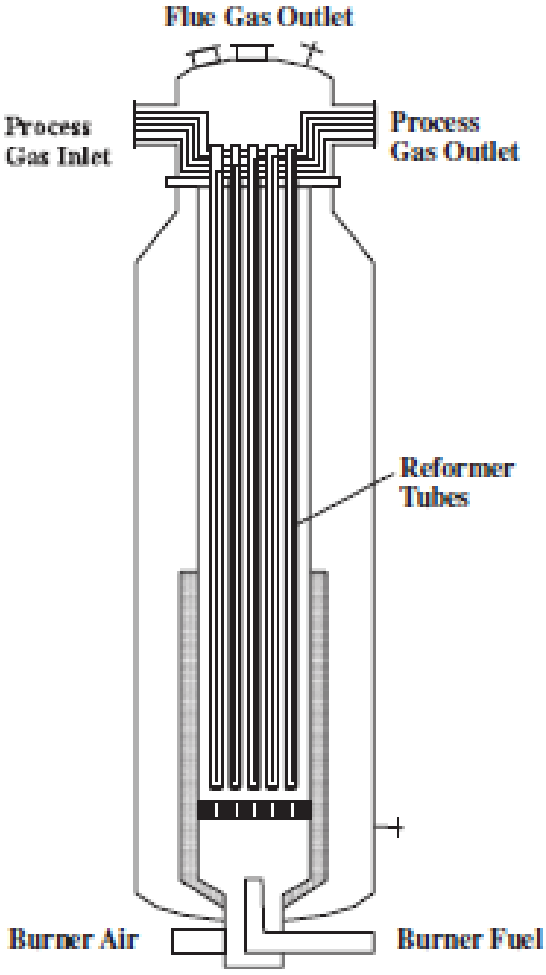

Figure 2.2 Schematic layout of steam reforming furnace [13]

The feed gas consisting of hydrocarbons (mainly natural gas), vapours and steam enters at the top end and flows down over the catalyst in individual tubes. The main steam methane reforming primary gas reaction is [14]

$$CH_4 + H_2O \rightarrow CO + 3H_2 \quad \Delta H = 251 \text{ MJ / kmol} \qquad (1)$$

The secondary reaction is [14]

$$CO + H_2O \rightarrow CO_2 + H_2 \quad \Delta H = -41.2 \text{MJ / kmol} \qquad (2)$$

Typical steam reforming reactions taking place over nickel catalysts (the most widely used catalysts for large scale industrial reformers are Al_2O_3-supported nickel [7, 9, 15]) are performed at high temperatures (750 ~ 1150 ^oC) and high pressure (5~40 MPa) due to the endothermic nature of the reaction breaking the strong C-H bond.

Based on these exacting service conditions involving high temperature and high pressure, creep becomes the main deformation mechanism and creep resistance is the major property required for the material for reformer tubes. Meanwhile, the large amount of hydrocarbons in the feed gas, combined with the relatively high temperature in the tubes, leads to a loss of material due to oxidation and/or carburisation. Since the heat generated from the burning of methane is transferred to the reformer tubes through radiation, the tube material needs to have a high thermal conductivity to reach the necessary reforming reaction temperature.

Beside the above physical requirements, for commercial hydrogen production, a competitive production cost is another main concern. Any unscheduled shutdowns due to component failure result in a serious reduction in profitability. Therefore, the average lifetime of reformer tubes is designed as approximately 100000 hours (11 years) [16], although reformer tubes still need to be taken offline every 2 ~ 3 years for catalyst replacement and system maintenance . The lifetime and thus cost of the reformer tubes are principally affected by the material's creep resistance.

For example, from the point of view of maintaining the wall thickness, a 5 % increase in creep strength will result in a 23 % improvement of reformer tubes' lifetime [17]. Alternatively, for the same designed lifetime, a 5 % increase of creep strength will lead to a 6.5 % reduction in wall thickness; every 1 % reduction in wall thickness can save 4~6 % of the metal cost [17]. One more advantage of a smaller wall thickness is to decrease the temperature gradient through the tube wall caused by catalyst exhaustion or start-up/shut-down of the system, leading in turn to a lower risk of another failure mechanism - thermal shock.

In summary, the materials used for steam reformer tubes must satisfy the following requirements, both physical and economic:

- High creep resistance
- Oxidation and carburisation resistance
- High thermal conductivity
- Lifetime expectancy of 100000 hours
- Competitive production cost

With continuous technological improvement throughout the whole 20th century, a new family of austenitic stainless steel has been developed to fulfil the above requirements for the steam reforming process. The most modern material used for steam reformer tubes is HP40, a centrifugally cast austenitic stainless steel with a chemical composition of 25 % Cr, 35 % Ni, 40 % Fe and 0.4 % carbon, plus small contents of other alloying elements.

2.3 HP40 austenitic stainless steel

2.3.1 Historical development of HP40

The choice of material for reformer tubes has become a key factor for the hydrogen production industry over the last 70 years. When the earliest commercial steam methane reformers were installed during World War II [18], steel, which is now still the most common material for industry due to its high strength and low cost, appeared to be the primary choice for reformer tubes.

However, as mentioned in 2.2, the high temperature gas feeding into reformer tubes contains a large proportion of hydrocarbons, mainly natural gas. Therefore, steel must have good oxidation and carburisation resistance requiring the addition of chromium, which can form a stable oxide layer on the surface. Figure 2.3 shows the importance of chromium in reducing oxidation. The oxidation at 1000 °C can be reduced to a very low value if 20 percent or more chromium is present. This content of chromium makes steel into stainless steel.

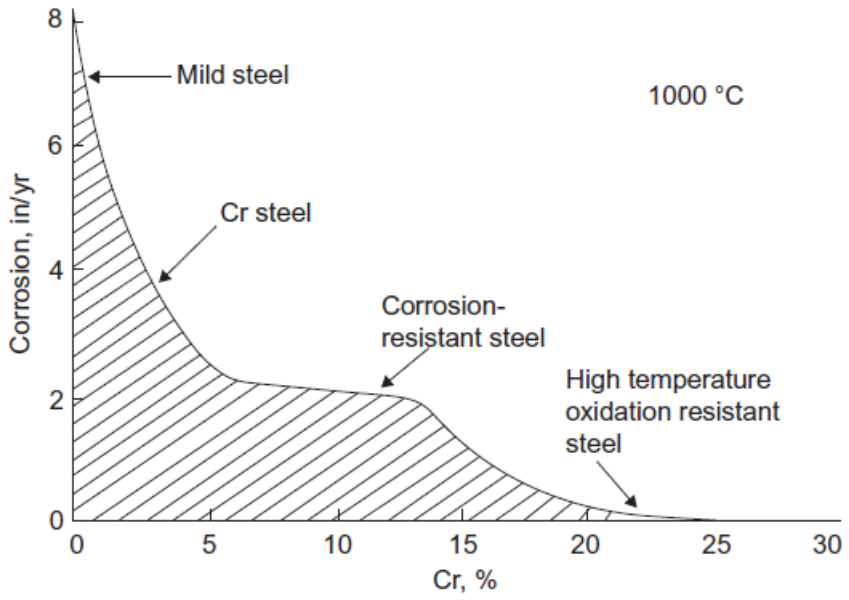

Figure 2.3 Effect of Cr addition on the corrosion rate of steel at 1000 °C [19]

Table 2.2 Mechanical properties of selected stainless steels at room temperature [20]

Stainless steel grades		Tensile strength / MPa	Yield strength / MPa
Austenitic stainless steel	201	760	380
	310	620	310
	347	655	275
Ferritic stainless steel	405	483	276
	430	517	310
	442	607	462
Martensitic stainless steel	410	1085	1005
	431	860	655
	440	760	450

Based on the structure of the matrix, stainless steel can be divided into three main types: austenitic, ferritic and martensitic. These are controlled by alloying and cooling rate. Table 2.2 lists the tensile strengths and yield strengths of several typical stainless steels at room temperature, indicating that the martensitic stainless steels are the strongest. However, when the temperature reaches 750 ~ 1150 ^{o}C for the steam reforming reaction, the strength of martensitic stainless steel decreases rapidly with increasing temperature while ferritic stainless steel shows the poorest mechanical properties over the whole temperature range (Figure 2.4). For austenitic stainless steel, the large additions of nickel, which acts as an austenite stabilizer, provide not only higher strengths than ferritic stainless steels but also a remarkable stability compared with martensitic stainless steels. Therefore, austenitic stainless steel turns out to be the most suitable material for reformer tubes due to its relatively high strength and outstanding stability at high temperatures.

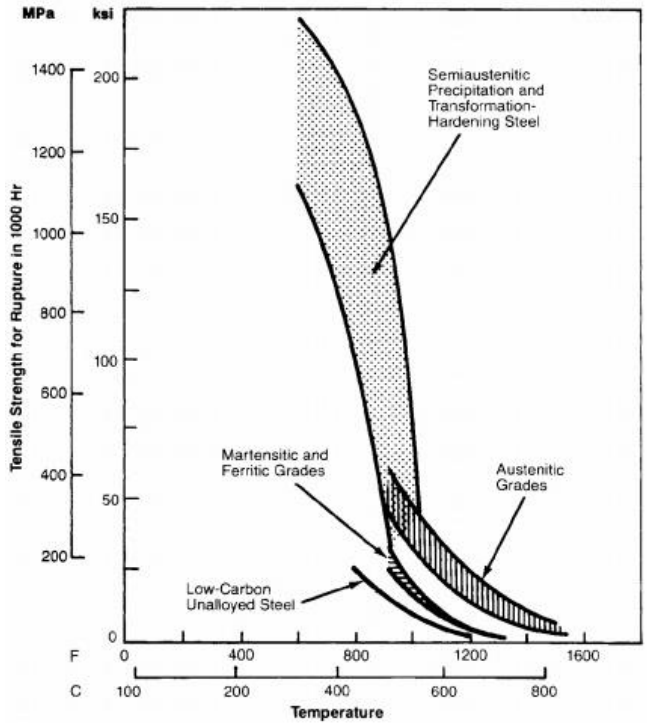

Figure 2.4 Tensile strength of various types of steels as a function of temperature [21]

Besides the steel type, the method of manufacture is the next most important influence on material properties. Wrought and cast, two mature steelmaking technologies, are potential choices for the production of steel used in steam reforming. The wrought product is more consistent in terms of structure, being free from defects such as porosity which are prone to be found on the surfaces of cast steels [22]. Meanwhile, the wrought tube is more ductile than the cast one due to its finer grains. Therefore, the first reformer tubes were made of Type 310 stainless steel, which contains 25 % Cr and 20 % Ni. However, with development of centrifugal casting, which can lead to a cost reduction, and the introduction of surface machining which can remove porosity, the original Type 310 stainless steel reformer tubes were replaced by HK40 tubes [18]. HK40 is a kind of austenitic stainless steel specially designed for centrifugal casting; it has a similar chemical concentration to Type 310, i.e. 25 % Cr and 20 % Ni. However, the carbon content is the main metallurgical difference between cast and wrought material of equivalent alloy content. Figure 2.5 illustrates the tensile rupture stress of Type 310 and HK40 at various temperatures, indicating that HK40 exhibits a strength twice that of the wrought 310. The higher strength of HK40 at elevated temperature makes it more capable of being heat-resistant. Other advantages of centrifugal casting are accurate wall thickness via control of the amount of molten metal, and a lower cost for production and fabrication than for wrought tubes. However, at the beginning, HK40 was not the only potential choice for reformer tubes: there was competition from other grades of centrifugally cast austenitic stainless steels, such as HU50 (18 % Cr-37 % Ni). HK40 finally won the competition due to its relatively higher strength at service temperature (Figure 2.5) and lower cost because of smaller Ni content. Around the 1950s, HK40 became the dominant material for reformer tubes and the base alloy for further development.

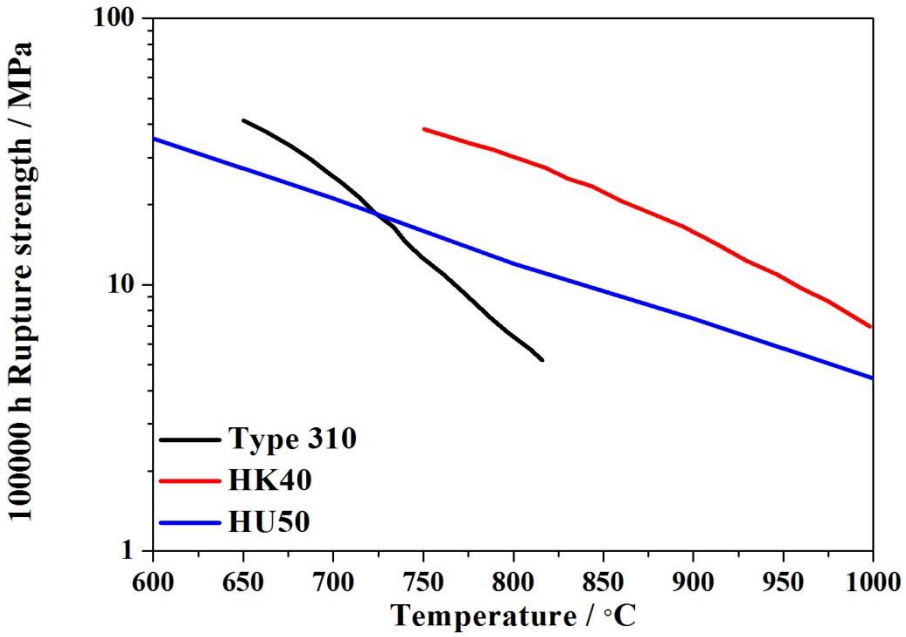

Figure 2.5 Rupture stresses for wrought Type 310, cast HK40 and cast HU50 at various temperatures [18, 23]

Since then, extensive work has been aimed at optimising the structure and high-temperature mechanical properties of HK40 based-alloys. In the 1970s, niobium was added to HK40 to improve its high-temperature properties, and this trend was followed by adding Ti and Zr. Hou and Honeycombe [24] compared the creep-rupture strengths of HK40, IN519 (24 % Cr-24 % Ni+1.6 % Nb) and IN519TZ (24 % Cr-24 % Ni+1.6 % Nb+Ti&Zr). From Figure 2.6, the addition of Nb provides a 20 % increase in strength via fragmenting the primary carbide network and delaying the coarsening of the secondary precipitates. However, the content of Nb is still maintained around 1 % for two reasons. Firstly, too much niobium will lead to the formation of unstable nickel-niobium silicide between 700 and 1000 °C, which is detrimental to the mechanical properties. The second reason is economic, due to the high price of niobium.

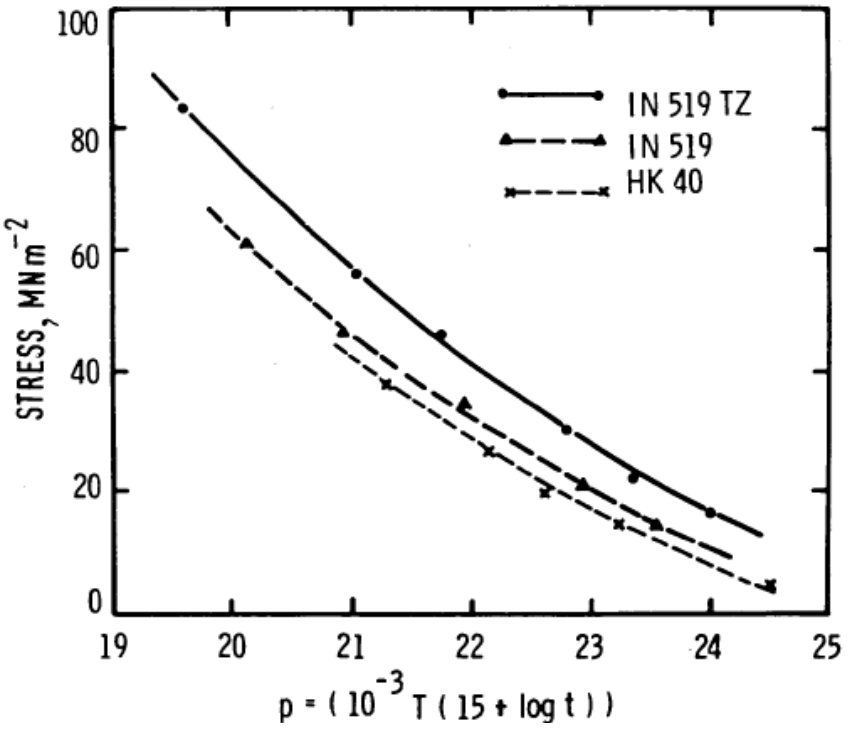

Figure 2.6 Rupture stresses for HK40, IN519 and IN519TZ [24]

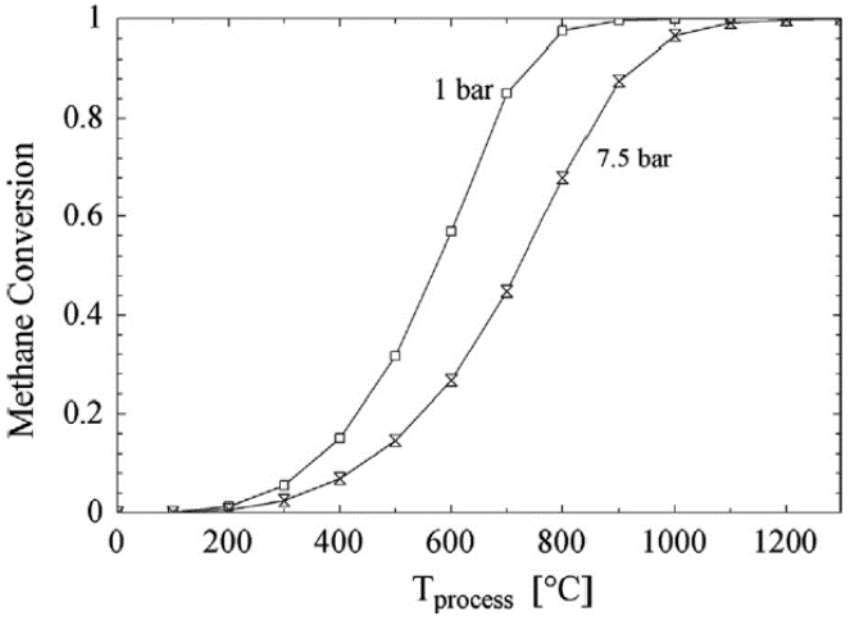

Figure 2.7 Conversion of methane in steam reforming as a function of temperature for different pressure levels [25]

Although it served without any failures for many years - especially with Nb addition - HK40 reached its limit around 1960s when higher service temperatures were required. From Figure 2.7, under elevated pressure, the conversion of methane in steam reforming will increase with temperature. Therefore, the tubes for new generation steam reforming furnaces are designed to operate at 1150 ºC or above to improve efficiency. At this temperature, HK40 is inadequate in terms of oxidation and carburization resistance. To solve this problem, a higher content of nickel is needed because the addition of nickel results in a significant reduction in the oxidation rate (Figure 2.8). Meanwhile, a higher nickel concentration will further stabilize the austenitic matrix. Based on these reasons, a new grade austenitic stainless steel, HP40, which contains 25 % Cr and 35 % Ni, was introduced into the steam reforming industry in the early 1960s.

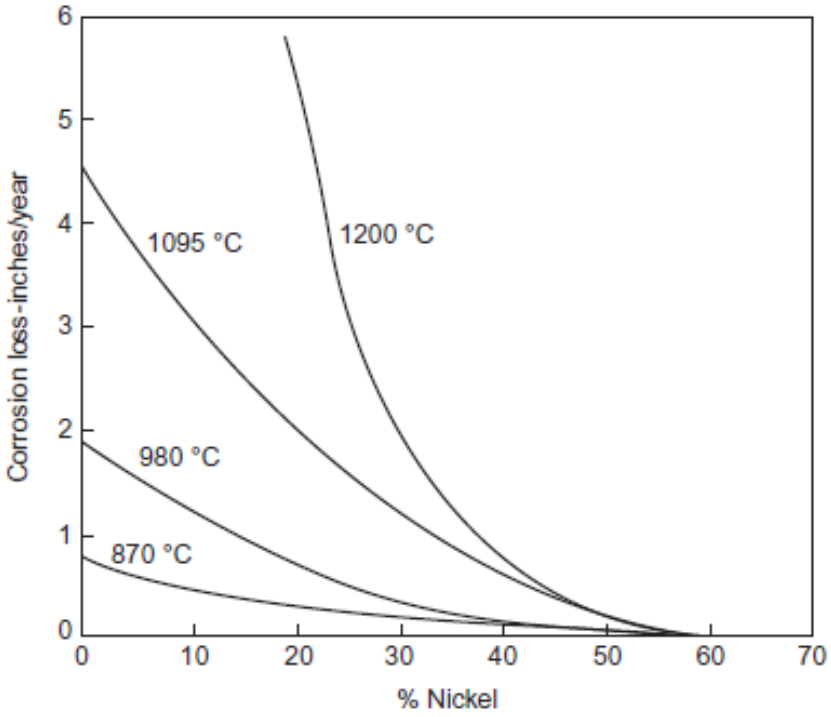

Figure 2.8 The effect of Ni addition on the oxidation of a Fe-11Cr alloy in air at various temperatures [19]

From Figure 2.9, the rupture strength of HP-40 is only slightly better than that of HK-40. To improve the high temperature properties, in the 1970s, niobium was also added to HP40 steels, leading to the formation of HP40-Nb. Based on the same reasons as for HK40, the Nb in HP40 is again limited to around 1 %. However, HP40-Nb does not appear to be as strong as expected, for example by extrapolation from IN519 steel. This led to the addition of other alloying elements to HP40-Nb, such as Ti, Zr, W and rare earth elements. With improvements in alloying procedures, a new micro-alloyed grade of HP40 was developed: HP40-Nb-Micro. HP40-Nb-Micro shows the highest creep strength among this steel group and has now become the dominant material for reformer tubes.

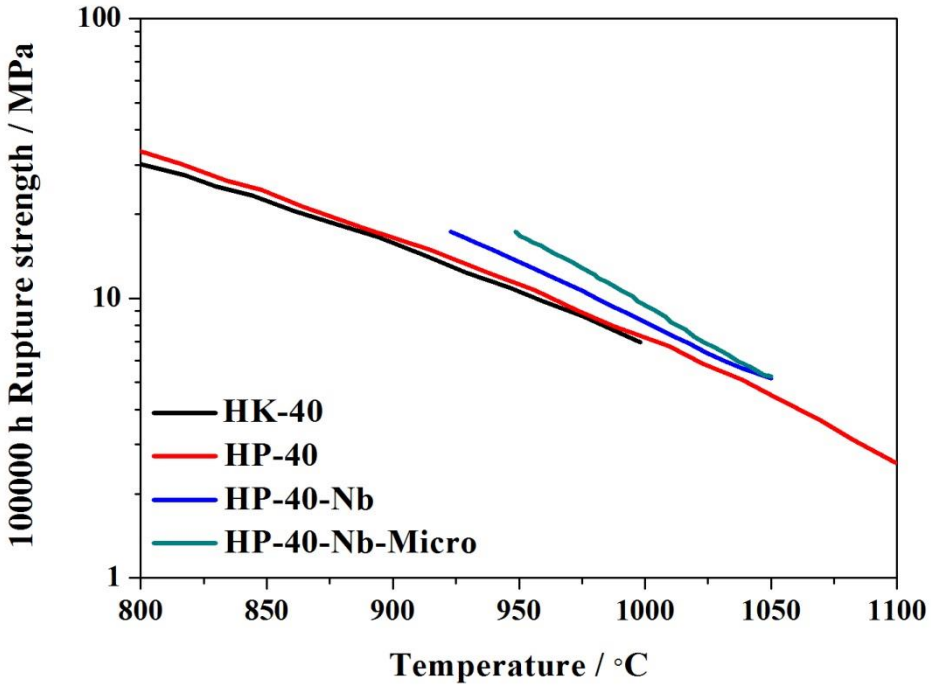

Figure 2.9 Rupture stresses for wrought HK40 and HP40 series steels at various temperatures [23]

With further requirements from the steam reforming process, the research to improve steam reformer tubes material has been progressing for 70 years and will no doubt keep moving forward (Figure 2.10). Therefore, the effect of chemical composition on the microstructure of HP40 needs to be understood at a fundamental level.

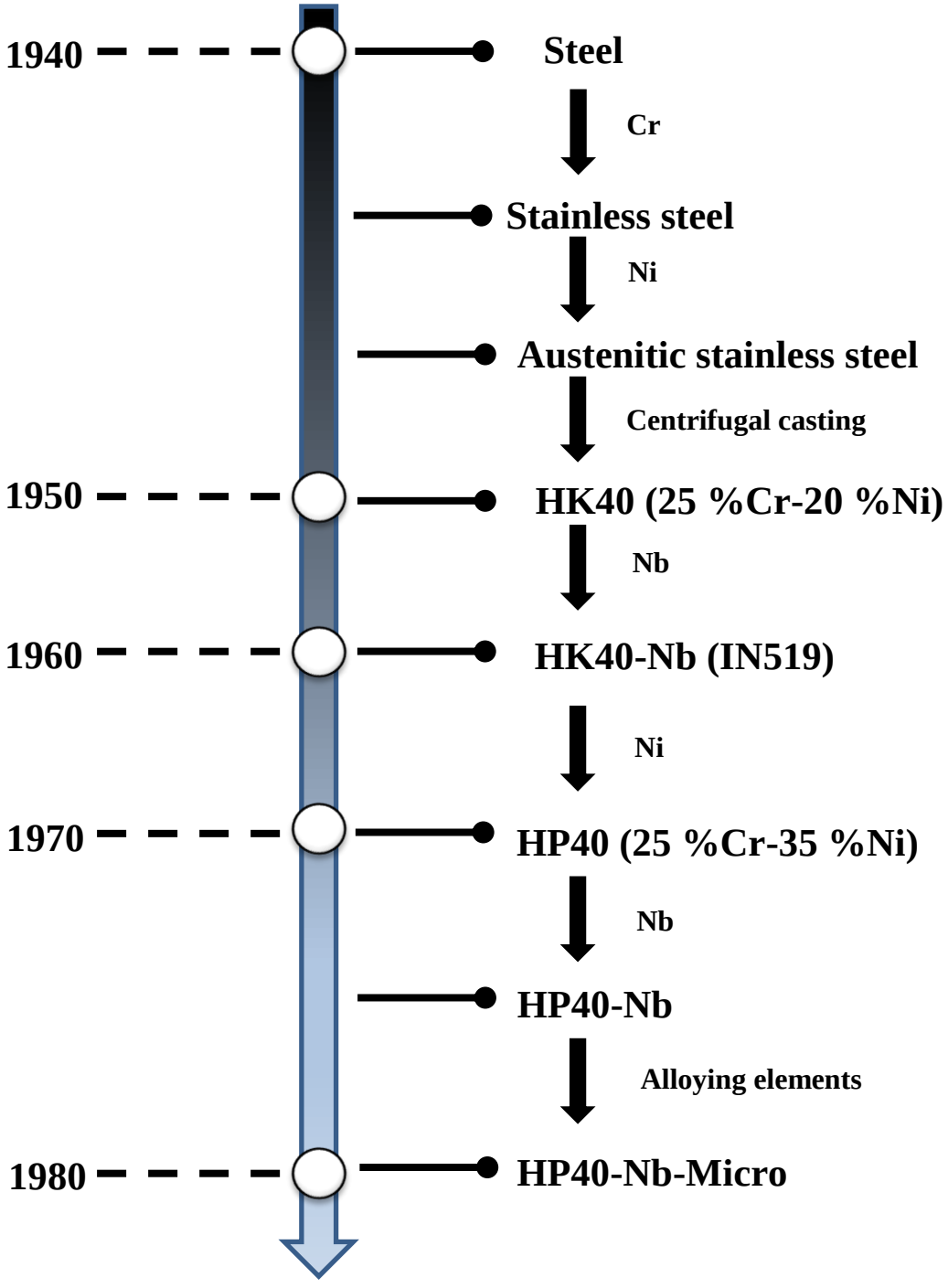

Figure 2.10 Historical development of HP40

2.3.2 Effect of chemical composition on microstructure

The elements in austenitic stainless steels can be divided into two parts: first, the basic elements Cr and Ni make the steel retain an austenitic structure at room temperature and improve oxidation and carburization resistance at elevated temperature; second, alloying elements, either interstitial such as carbon and nitrogen, or substitutional such as Mn, Nb, Ti, Si, Mo and W, are used to tailor the required microstructure.

(1) Basic elements in stainless steels (Cr-Ni)

1) Chromium (Cr)

The addition of chromium greatly improves the corrosion resistance of the steel by forming a very thin stable oxide film (Figure 2.11) on the surface. Chromium is also a 'ferrite stabiliser' and restricts the γ-loop [22]; thus Fe-Cr stainless steels have a ferritic structure, or possibly martensitic depending on the cooling process. However, when chromium is added to a steel containing nickel, it retards the kinetics of the austenite to ferrite transformation, thus making it easier to retain austenite at room temperature. The third effect of chromium is to introduce Cr-precipitates to the microstructure. The crystal structures and compositions of the main precipitates in austenitic stainless steels are listed in Table 2.3. Among these precipitates, $M_{23}C_6$ is the most significant carbide formed in HP40, primary $M_{23}C_6$ intergranularly nucleated along grain boundary [26-30] and secondary $M_{23}C_6$ intragranularly nucleated on defects, such as dislocation [31] and twinning [32]. However, the rapid cooling during production will leave M_7C_3 at room temperature. While reheating within service, M_7C_3 can transform into $M_{23}C_6$ primary and secondary carbides [33-35].

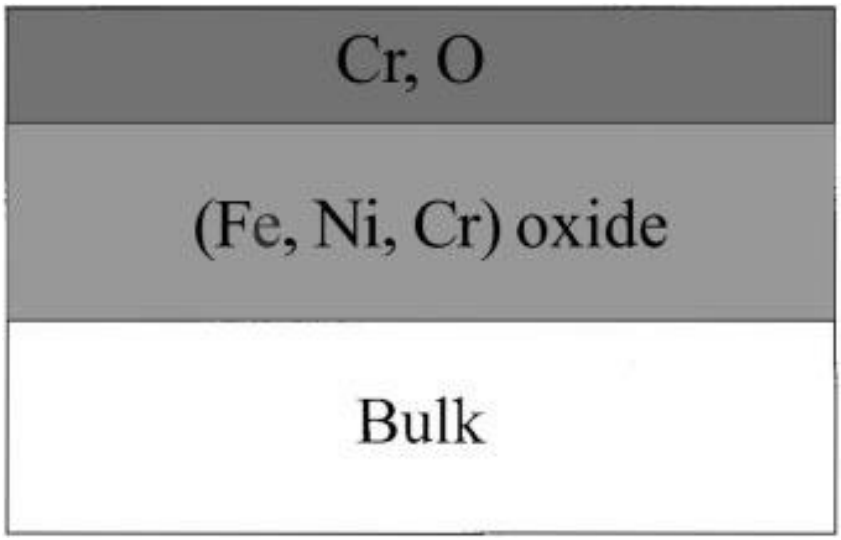

Figure 2.11 Schematic diagram of the structure of oxide film on the surface [36]

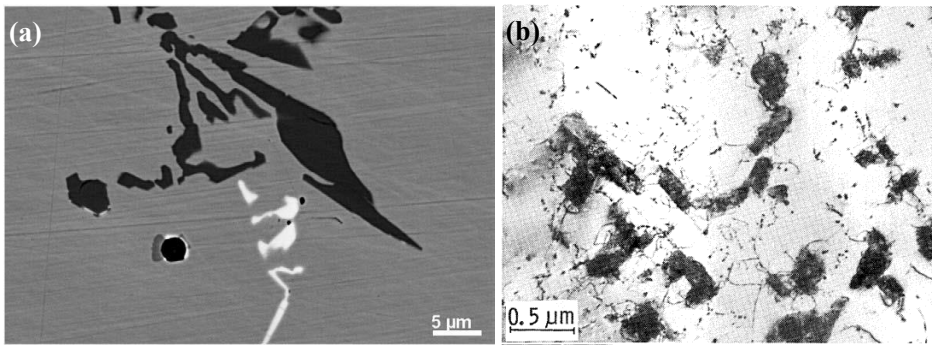

Figure 2.12 (a) BSE image of primary carbide [37] and (b) TEM bright field image of secondary $M_{23}C_6$ precipitates and dislocations [24]

Table 2.3 Structure and compositions of main precipitates in austenitic stainless steels

Precipitates	Structure	Lattice parameter / nm	Composition
$M_{23}C_6$ [38]	fcc	a = 1.06	$(Cr, Fe, Ni)_{23}C_6$
M_7C_3 [39]	Orthorhombic	a = 0.45, b = 0.70, c = 1.21	$(Cr, Fe, Ni)_7C_3$
NbC [40]	fcc	a = 0.45	NbC
NbN [40]	fcc	a = 0.44	NbN
Z-phase [41]	Tetragonal	a = 0.30, c = 0.74	CrNbN
Cr_2N [42]	hcp	a = 0.48, c = 0.44	Cr_2N
G-phase [43]	fcc	a = 1.12	$Ni_{16}Nb_6Si_7$

2) Nickel (Ni)

Nickel is added to Fe-Cr stainless steel for austenite stabilization. The equilibrium phases depend on the proportion of the three elements (Fe-Cr-Ni), as illustrated in Figure 2.13, an isothermal section of the ternary diagram for Fe-Cr-Ni at 1000 ºC. The most convenient way of representing the effect of Ni and Cr on the basic structure of stainless steel is the Schaeffler diagram. It plots the compositional limits at room temperature of austenite, ferrite and martensite in terms of nickel and chromium equivalents. In Figure 2.14, with 25 % Cr, the austenite persists to room temperature until nickel reaches 20 or more.

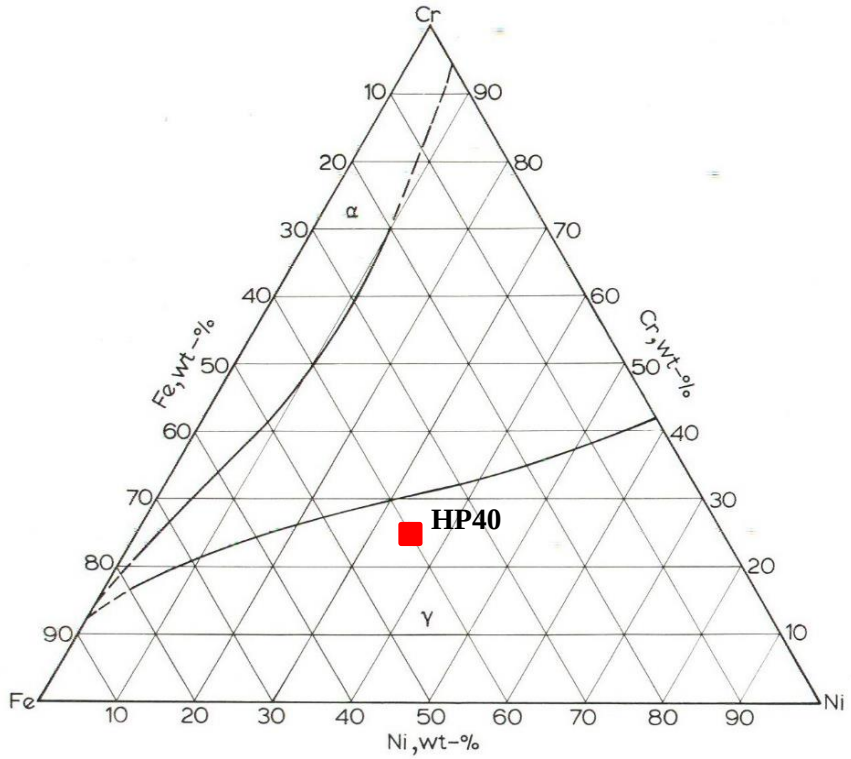

Figure 2.13 1000 ºC isotherm of Fe-Cr-Ni system [44]

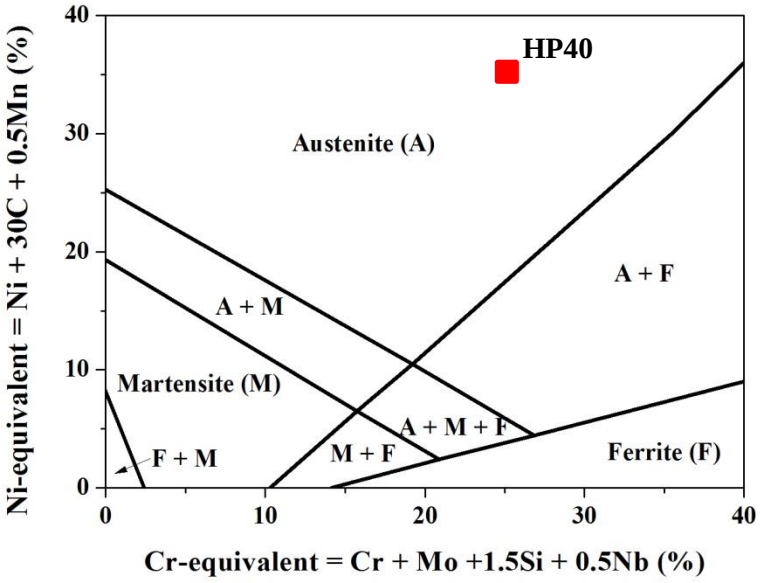

Figure 2.14 Schaeffler diagram---the basic structure of Fe-Cr-Ni stainless steels [45]

(2) Minor alloying elements:

1) Carbon (C):

Carbon is one of the few elements known since antiquity. The addition of carbon to iron is sufficient to form a steel, which was a fact known to smiths over 2500 years ago since iron heated in a charcoal fire can readily absorb carbon by solid-state diffusion [22]. Carbon has a strong influence on the microstructure of steel. Firstly, carbon, with its small atomic size relative to that of iron, can enter the iron lattice and act as an interstitial solute element which influences the lattice parameter of the austenite (Figure 2.15). Thus, strain is introduced into the lattice leading to solid-solution strengthening. As illustrated in Figure 2.16, the interstitial solutes carbon and nitrogen have the greatest solid-solution strengthening effects, followed by the ferrite-forming substitutional solutes, while the austenite-forming substitutional solutes have very little solid-solution strengthening effect.

Secondarily, carbon is a strong γ-former and enhances the formation of austenite (Figure 2.17). The addition of carbon to the binary alloy extends the γ-loop to higher chromium contents. Last but most importantly, when the concentration of carbon is above the solubility limit in iron at elevated temperature, carbide precipitation will follow in the presence of Cr, Nb or Ti. For example, as shown in Figure 2.18, for a Fe-18Cr-8Ni steel, cooling from 1000 ^{o}C will lead to the emission of excess carbon from the austenite matrix and then carbide formation.

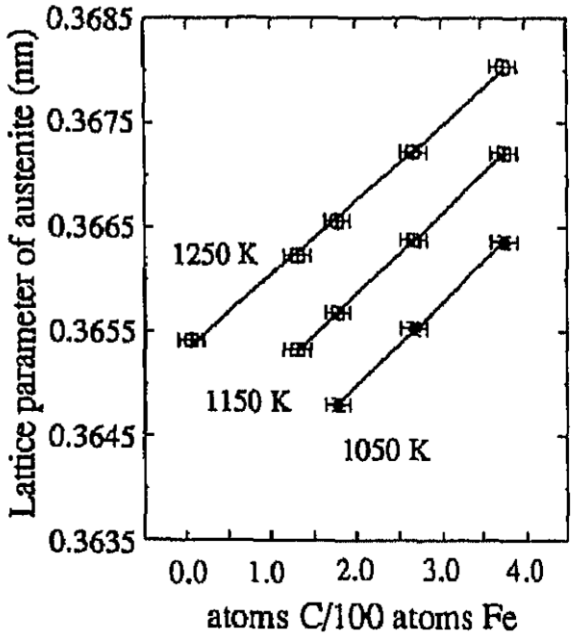

Figure 2.15 The lattice parameter of austenite as a function of the carbon concentration [46]

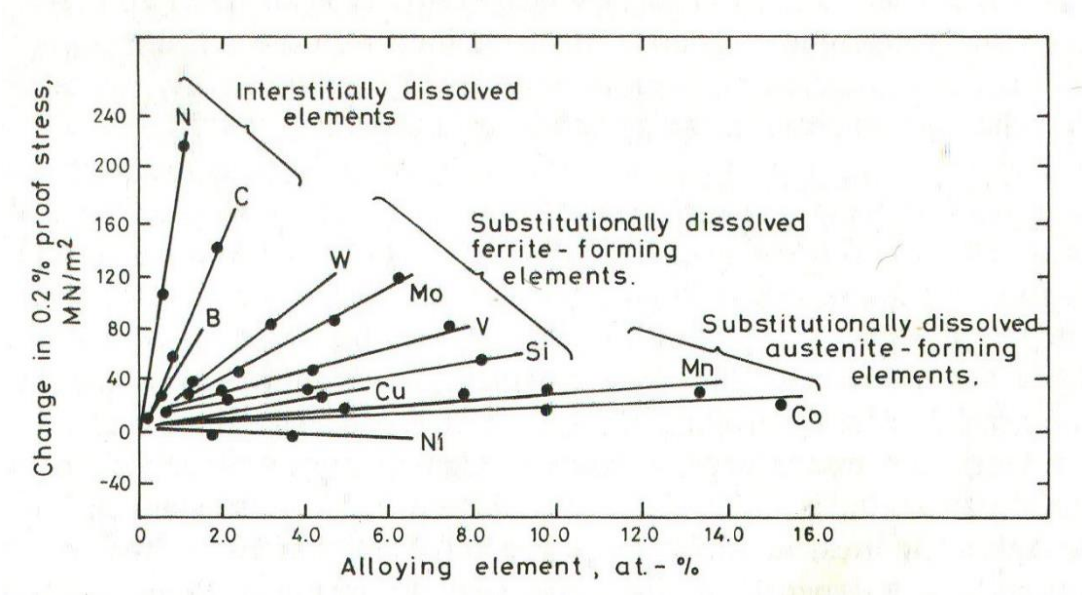

Figure 2.16 Effect of solid-solution hardening in austenite [47]

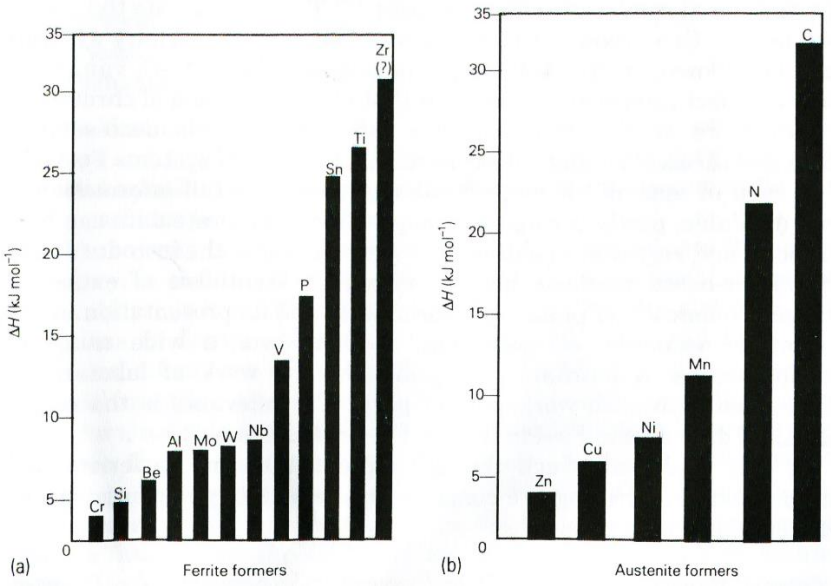

Figure 2.17 Relative strength of alloying elements as (a) ferrite formers; (b) austenite formers [22]

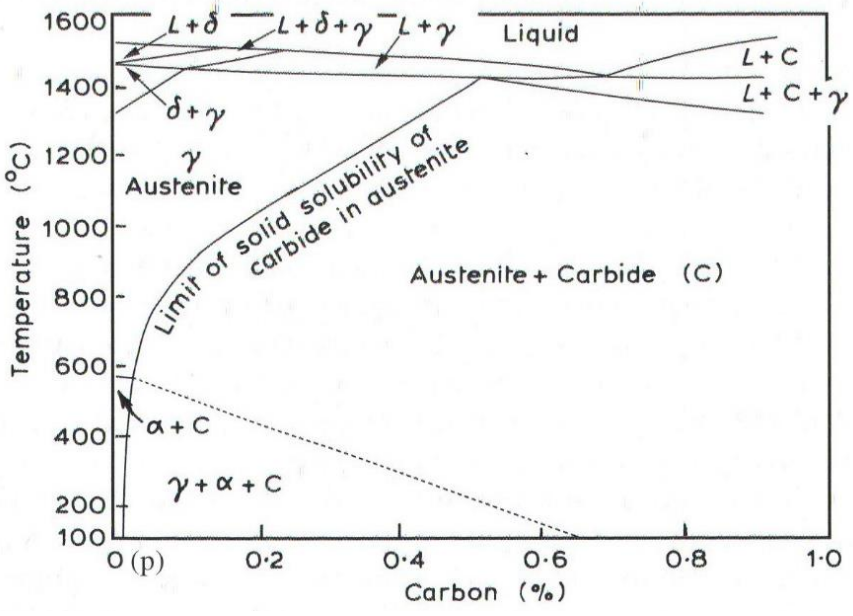

Figure 2.18 Effect of carbon on the microstructure of Fe-18Cr-8Ni steel [48]

2) Nitrogen (N)

Nitrogen is also a strong austenite stabilizer and has a high solubility in the austenite. Nitrogen can have a much greater strengthening effect than carbon (Figure 2.16). According to Lai [49] only a small amount of nitrogen is found replacing carbon in $M_{23}C_6$ to form $M_{23}(C, N)_6$. Furthermore, the presence of nitrogen is known to delay the rate of coalescence of $M_{23}C_6$ carbide in austenitic steels for two reasons: firstly, nitrogen is believed to lower the diffusivity of chromium and carbon in the matrix; secondarily, Matsuo et al. [50] proposed that nitrogen decreases the mismatch between $M_{23}C_6$ and the austenite, which reduces the interfacial energy and therefore inhibits coarsening. In the presence of stronger carbide formers, such as Nb or Ti, nitrides NbN or TiN are precipitated at high temperatures. However, with a relatively high level of nitrogen, complex nitrides can form in austenitic stainless steel, such as, Z-phase (CrNbN) [41, 51-53] or Cr_2N [42, 54], which are tetragonal and hcp structure respectively.

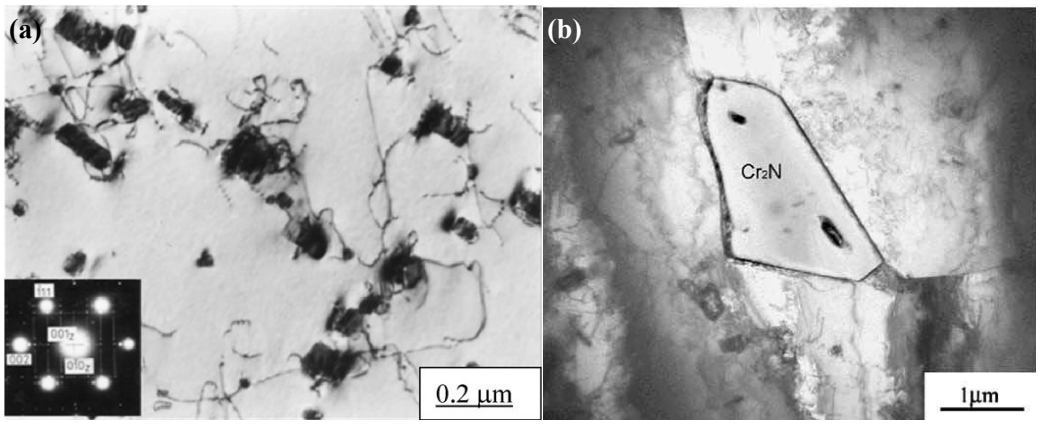

Figure 2.19 TEM bright field image of (a) Z-phase in AISI 316 LN+Nb steel [52]; (b) Cr_2N in AISI 347 steel [54]

3) Manganese (Mn)

Manganese has been introduced to austenitic stainless steels as a substitute for nickel for economic reasons. The nickel content can be halved to 4 wt% by the addition of 2-6 wt% Mn in 18-8 steel [55]. However, although the austenitic structure is achieved, such steels do not exhibit the same corrosion resistance as an 18-8 steel due to the relatively lower stability of the Mn-oxide film on the surface compared with Cr-oxide. Meanwhile, manganese is also used to increase the solubility of nitrogen in austenite to improve the solid solution strengthening. On the other hand, the addition of Mn can lead to the formation of MnS inclusions (Figure 2.20), which are detrimental to the mechanical properties of the steel.

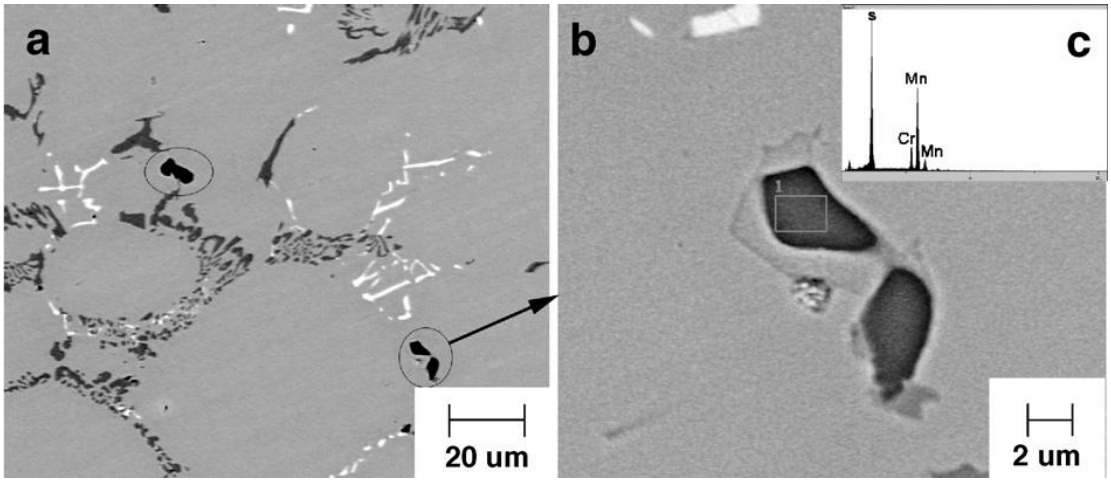

Figure 2.20 MnS particles in HP40 (a) general view, (b) enlargement of area circled in (a) and (c) EDS of rectangular area in (b) [56]

4) Niobium (Nb) and titanium (Ti)

In the 1970s, niobium and titanium were added to HP alloys to improve their high-temperature properties. Niobium carbide (NbC) and titanium carbide (TiC) form at relatively high temperature and are much more stable than chromium carbide at service temperature [57]. The formation of NbC and TiC will lead to a significant reduction in the matrix carbon level [58, 59] and thus delay the coarsening of the secondary precipitates, such as $M_{23}C_6$. Meanwhile, since Nb has a greater affinity for carbon than does Cr, replacement of the Cr-carbide formation and fragmentation of the primary carbide network are expected as the Nb concentration increases (Figure 2.21). Furthermore, low matrix carbon concentration due to additions of Nb and Ti will. However, as shown in Figure 2.22, Soares [60] found that niobium carbide (NbC) in the HP40 steel was unstable after aging at 900˚C for 1000h. The NbC can transform into G phase ($Ni_{16}Nb_6Si_7$), a nickel-niobium silicide which was first found by Beattie and Versnyder [43] in 1956. Although G phase does not appear to be intrinsically detrimental to the mechanical properties of the steel and contributes to good performance during long-term service [61], the conversion of NbC into G phase causes volume expansion and thus facilitates crack nucleation [62]. A small addition of titanium inhibits the (NbTi)C transformation to G-phase since the G-phase does not dissolve Ti, which is supported by the observation of individual TiC particles in G-phase (Figure 2.23).

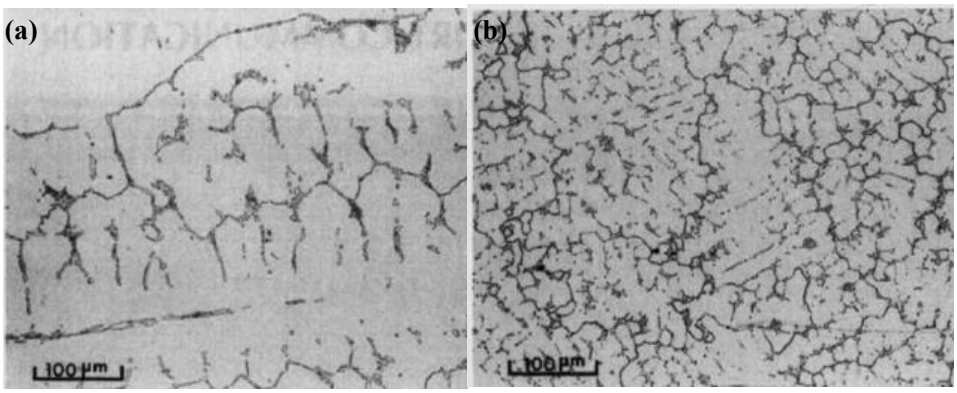

Figure 2.21 As-cast microstructures of (a) basic HP steel (b) HP steel modified with 1.97% Nb indicating that niobium can fragment the primary carbide network [63]

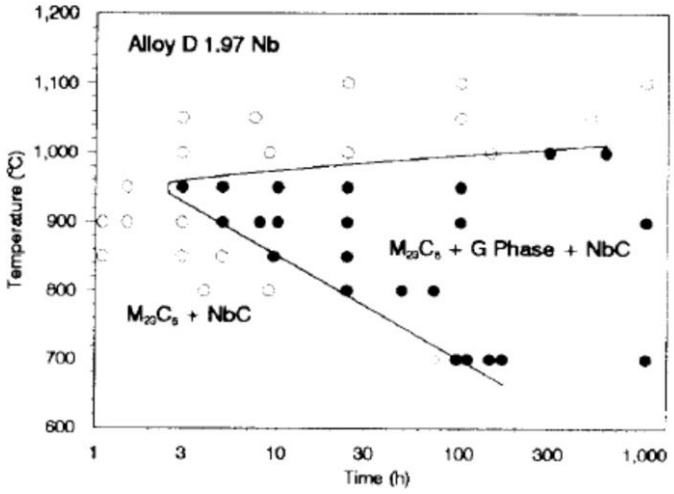

Figure 2.22 Time-temperature-precipitation curves for HP40 (1.97% Nb) showing the stability range for G phase [60]

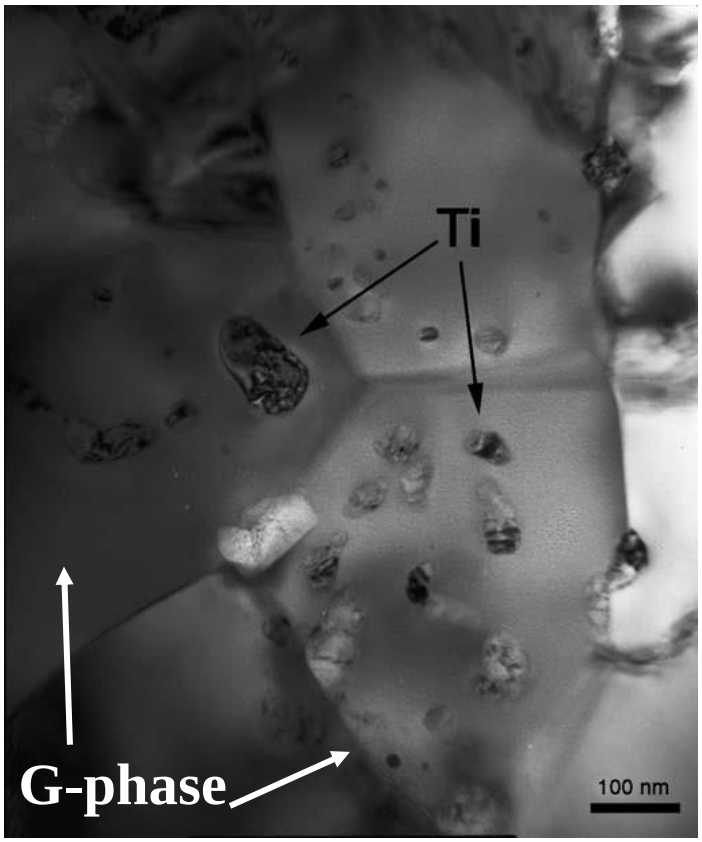

Figure 2.23 TEM bright field image of HP40-NbTi alloy. Individual TiC particles can be observed in the G-phase [64]

5) Silicon (Si)

Silicon can strength the material by solid solution. Although a silicon-oxide film (Figure 2.24) below the (Cr, Mn)-oxide film on the metal surface can improve the carburization resistance, the silicon in modified HP-steels is generally reported as 1.8 wt% to avoid the formation of ferrite phase and to retard the transformation of G-phase. In truth, modern commercial HP alloys contain 1 wt% silicon [61].

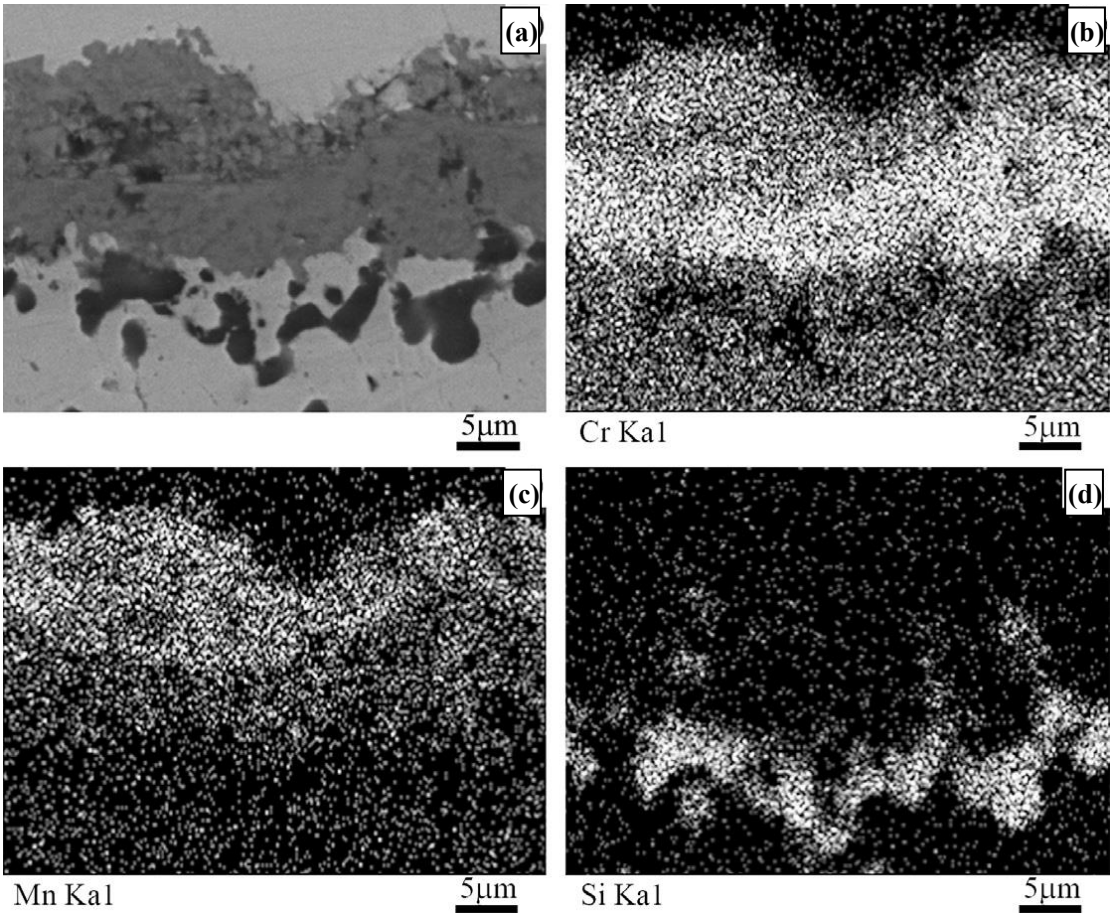

Figure 2.24 SEM elemental distribution map (a) electron image (b) chromium (c) manganese (d) silicon in HP40 alloy [65]

6) Molybdenum (Mo) and tungsten (W):

W refines the austenite grains and accelerates the carbide transformation from M_7C_3 to $M_{23}C_6$, as demonstrated by Yan [62]. In addition, W, a strong carbide former, can take away some free carbon atoms, reducing the amount of carbon dissolved in the austenitic grains (c.f. Table 2.4), and thus inhibit carbide precipitation during aging at 900 ˚C. Molybdenum will accelerate the precipitation of $M_{23}C_6$ in austenitic stainless steel since molybdenum has the effect of reducing the solubility of carbon in austenite [66]. Meanwhile, W and Mo have a relatively high solid strengthening effect on stainless steels (Figure 2.16)

Table 2.4 WDS analysis results for C in the matrices of HP40 alloys with different tungsten concentrations [62]

Specimen	Wt%		
	Sample 1	Sample 2	Sample 3
Amount of W	0.00	0.92	2.13
Amount of C in the matrix	0.288	0.251	0.187

2.3.3 Effect of solidification rate on microstructure

Currently, the dominant production technology for HP40 tubes is centrifugal casting. Centrifugal casting is used to produce cylindrical or hollow products, such as tubes and tanks. As illustrated in Figure 2.25, for a centrifugal casting process, molten steel is poured into an open-ended, water-cooled mould. Via rotation spinning at 300-3000 rpm, the centrifugal force, which can result in an acceleration of 100 times gravity [67], is in effect liquid forging or pressure casting so that molten metal is forced against the mould wall under relatively high pressure.

For horizontal centrifugal casting, the technological parameters influencing final product properties involve mould material, mould rotation speed, casting temperature, chemical composition and casting dimension.

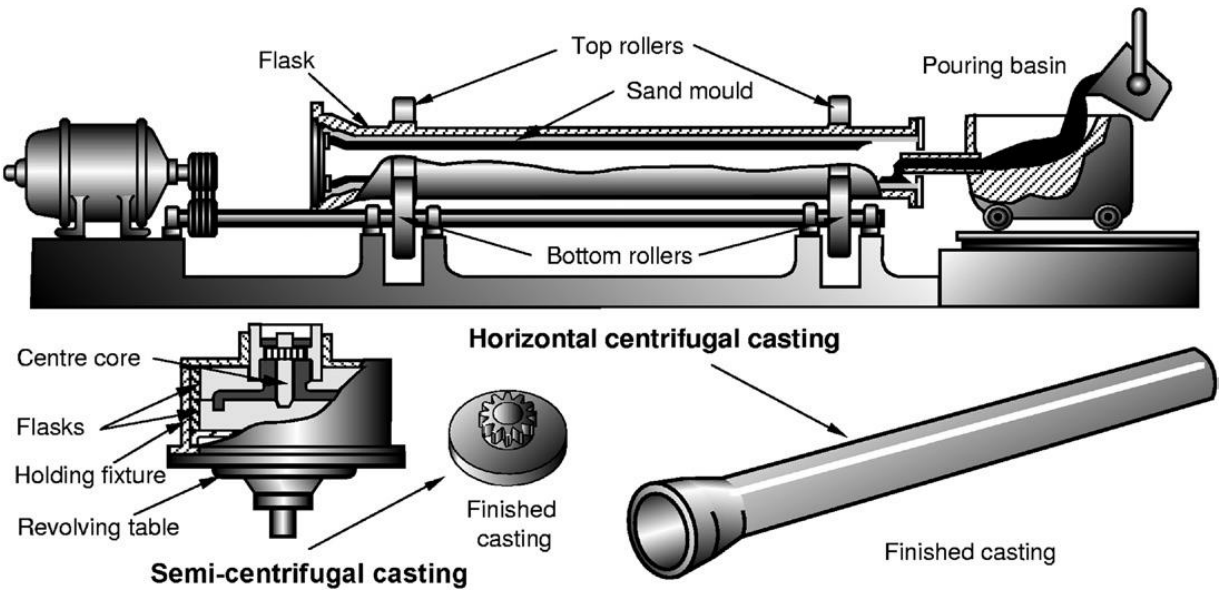

Figure 2.25 Schematic diagram of centrifugal casting [67]

Among these parameters, mould material and mould rotation speed are the most important since they have a significant influence on the solidification rate. The solidification rate is the other main effect, besides chemical composition, on the microstructure of HP40.

A higher solidification rate will refine grain morphology and grain size in HP40 tubes. Basically, as shown in Figure 2.26 (a), a cross-section through a commercial HP40 tube can be clearly divided into three zones, which demonstrates a typical structure of a quite thin outer layer of chill crystals, then columnar grains and along the inner layer equiaxed grains. The cooling rate is influenced by the mould material, such as graphite or cast iron: a cast iron mold will result in a higher cooling rate owing to its high heat capability. Wu et al. [68] found that an increase in cooling rate during centrifugal solidification diminished the barriers for the columnar grains to develop continuously along the radial direction of the cast tubes.

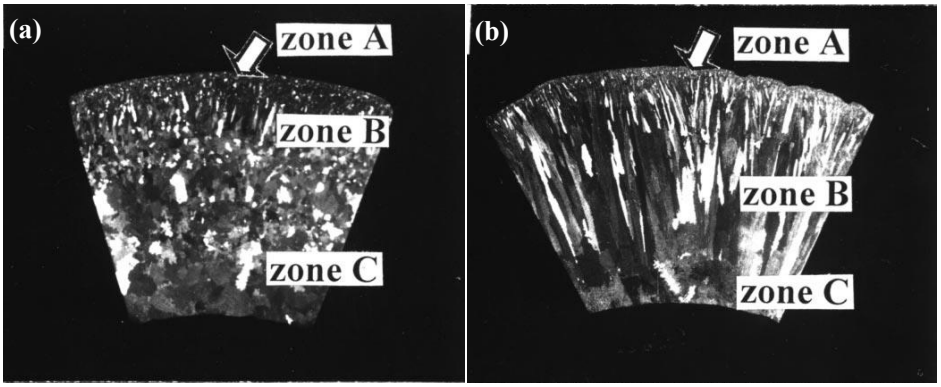

Figure 2.26 Cross-sections through centrifugally cast 25Cr20Ni heat-resistant steel tubes solidified in (a) a graphite mould and (b) a cast iron mould [68]

Table 2.5 Thickness fractions of microstructures shown in Figure 2.26 [68]

Tube type	Thickness fraction (%)		
	Chill crystal (Zone A)	Columnar grain (Zone B)	Equiaxed grain (Zone C)
Graphite mold	4	27	69
Cast iron mold	3	83	14

Pryds and Huang [69] found that increasing the cooling rate, for a ferritic steel, can lead to a refinement of grain size from 100 μm to 15 μm (Figure 2.27). This is because a higher cooling rate will lead to a larger degree of supercooling. A larger supercooling will result in a much higher rate of grain nucleation [70]. A more precise control of cooling rate (10-50 K/min) during solidification of a ferritic steel via DSC was obtained by Bleckmaan et al. [71]. In Figure 2.28, the microstructure is continuously refined with increasing cooling rate.

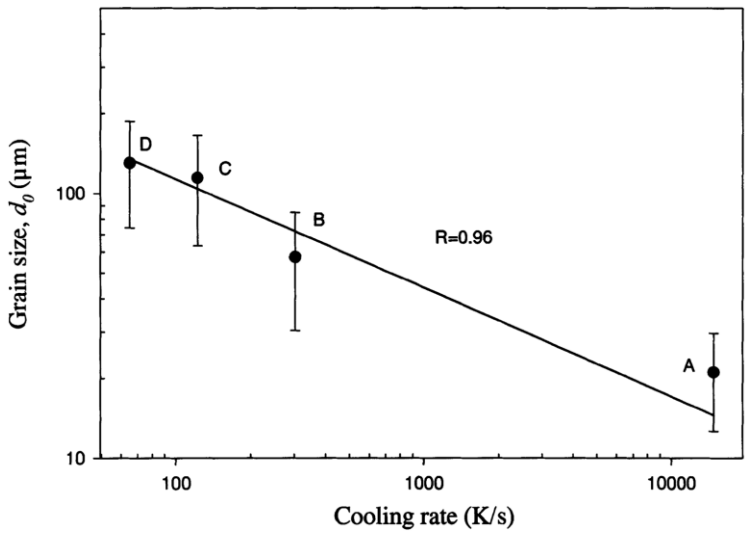

Figure 2.27 The grain size vs the average cooling rate for a ferritic steel [69]

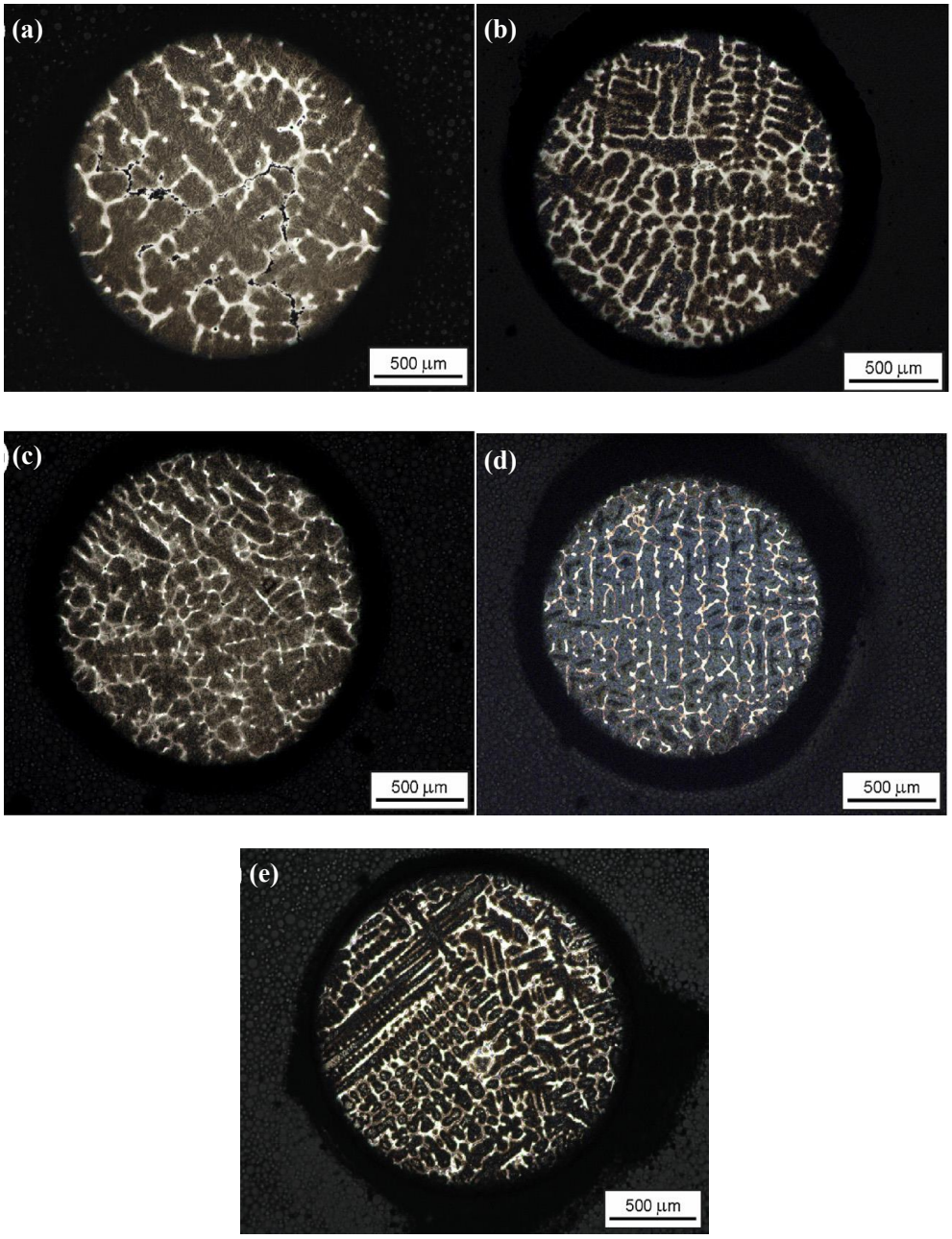

Figure 2.28 Optical microscope images of as-solidified FeCrVC samples cooled at (a) 10, (b) 20, (c) 30, (d) 40 and (e) 50 K/min [71]

Secondarily, the fraction of precipitation, such as carbides, will be strongly dependent on the solidification rate. Table 2.6 indicates that the volume fraction of the Cr-carbides in both the columnar grains and the equxied grains decreases with increase of cooling rate. This is in agreement with the research by Zhao and Yan [72] on volume fraction of Laves phase in IN718 at different solidification rates (Figure 2.29). The high cooling rate inhibits the carbide coarsening via limiting the diffusion of solute elements like Cr, even though carbon still has a relatively high diffusion rate at elevated temperature. Therefore, a higher solidification rate will lead to a lower volume fraction of carbides and a more homogeneous distribution of precipitates. However, rapid cooling will leave a supersaturated solid solution in the austenitic matrix which promotes secondary precipitation under service conditions.

Table 2.6 Volume fraction of Cr-carbides in 25Cr20Ni cast tubes [68]

Tube type	Volume fraction of the Cr-carbides in the cast tubes (%)	
	Columnar grain (Zone B)	Equiaxed grain (Zone C)
Graphite mold	8.92	13.75
Cast iron mold	7.79	10.18

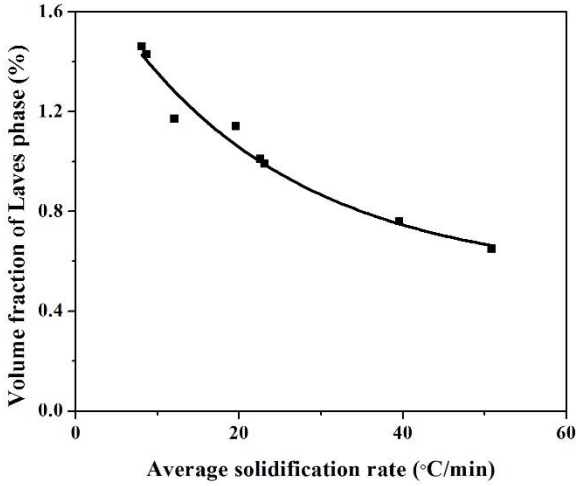

Figure 2.29 The effect of average solidification rate on volume fraction of Laves phase in IN718 [72]

Thirdly, the morphology of the precipitates will change with different solidification rates. Figure 2.30 illustrates the microstructure of Al-18Si-2.5P, solidified in a graphite mould and in a cast iron mould, respectively. With a higher solidification rate, the morphology of the particles contained in the alloy solidified in a cast iron mould appears to be plate-like and rod-like. In comparison, particles in a graphite mould solidified alloy are flake-like with a size of about 100 μm since the lower solidification rate gives the precipitates enough time to grow along a specific direction. Luan et al. [73] observed similar morphology types for MC carbides in a centrifugal cast high-speed steel, indicating that faster solidification promotes a spherical nucleus and then a chrysanthemum-like carbide after solidification. The spherical nucleus leads to smaller carbides, which are distributed evenly in the matrix and can improve wear resistance and thermal fatigue properties.

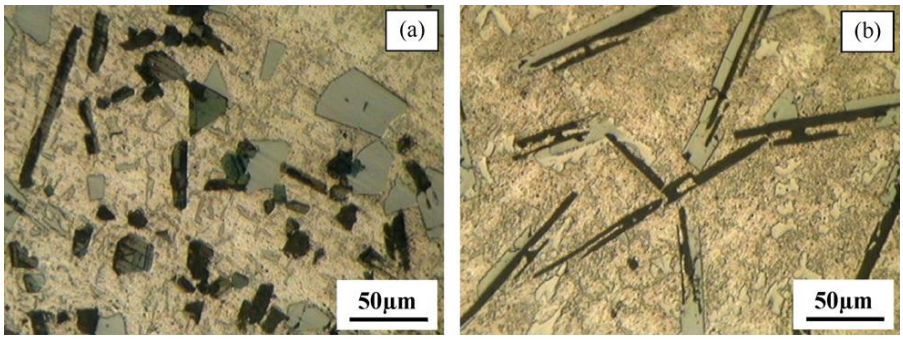

Figure 2.30 Optical diagrams illustrating the morphology of precipitates solidified with (a) graphite mould and (b) cast iron mould [74]

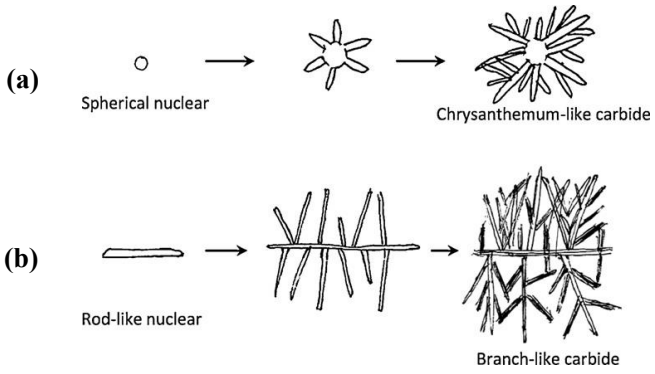

Figure 2.31 Schematic illustrations of the growth of (a) chrysanthmum-like carbide with rapid solidification and (b) branch-like carbide with slow solidification [73]

2.4 Creep behaviour

2.4.1 Fundamentals of creep deformation

In general, when the stress applied to a metal or alloy is above the yield strength of the material, it will lead to plastic deformation, which is permanent and irreversible. The deformation occurs suddenly and time-independently, since the strain is related to the value of the stress. However, the material can also deform at a constant stress below the yield strength, especially at high temperatures. In this case, the strain will accumulate continuously in a time-dependent manner. This kind of time-dependent deformation under constant stress is known as creep.

Although creep can take place at all temperatures above absolute zero Kelvin, creep is more severe in materials that are subjected to heat for long periods, and generally increases as the temperature approaches the melting point T_m [75]. Since the melting points of metals and alloys differ widely, the creep behaviour is usually considered in relationship to the homologous temperature T/T_m, where T is the creep temperature. As illustrated in Table 2.7, for austenitic iron-base high temperature alloys, creep becomes more obvious when the temperature is higher than $0.5T_m$.

Table 2.7 Temperatures at which creep becomes significant for different materials [75]

Materials	Temperatures at which creep becomes significant	
	^{o}C	T/T_m
Aluminium alloys	205	0.54
Titanium alloys	315	0.30
Low alloy steels	370	0.36
Austenitic iron-base high temperature alloys	540	0.49
Nickel and cobalt-base superalloys	650	0.56
Refractory metals	980-1540	0.40-0.45

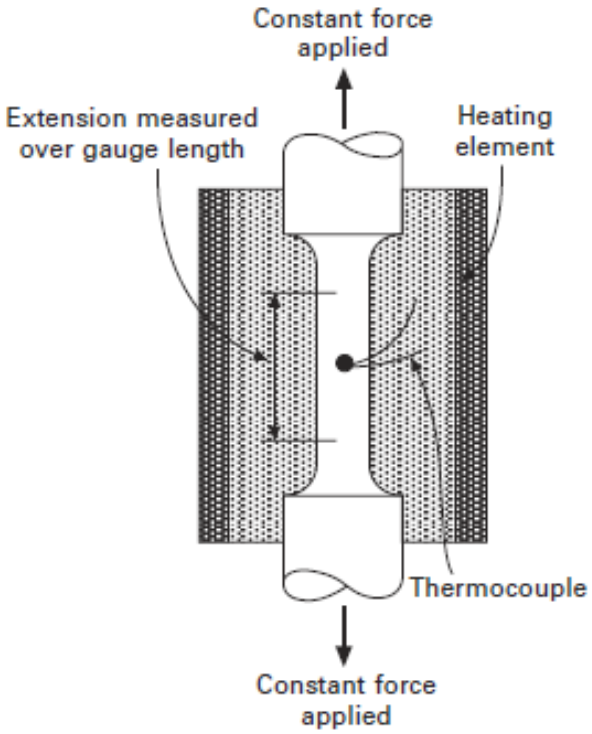

Figure 2.32 Schematic image of constant load creep test at certain temperature [76]

Practical creep test data must be acquired to predict a lifetime of components at high temperatures. The test most frequently used for determination of the creep properties of metals and alloys is on a tensile specimen maintained at a constant temperature, with a constant load or constant stress, despite the fact that non-uniform and unstable stress and temperature conditions are often encountered during service. A constant load test will have an increasing stress due to the decrease of cross-section during the tests [77]. However, constant load is more convenient. In general, creep tests conducted at constant load are used for practical engineering applications, whereas creep tests at constant stress are used for the scientific understanding of creep mechanisms [77]. To reach elevated temperatures, the specimen is heated inside a thermostatically controlled furnace attached to a creep testing machine. The actual specimen temperature is measured by a thermocouple attached to the specimen, as shown in Figure 2.32.

Creep test data are presented as a plot of strain vs time. The slope of the creep curve is $d\varepsilon/dt$. Typical creep curves are shown in Figure 2.33: a logarithmic creep curve and a normal creep curve containing three stages. ε_o in Figure 2.33 is the instantaneous elastic + plastic strain. Only the elastic strain can be recovered.

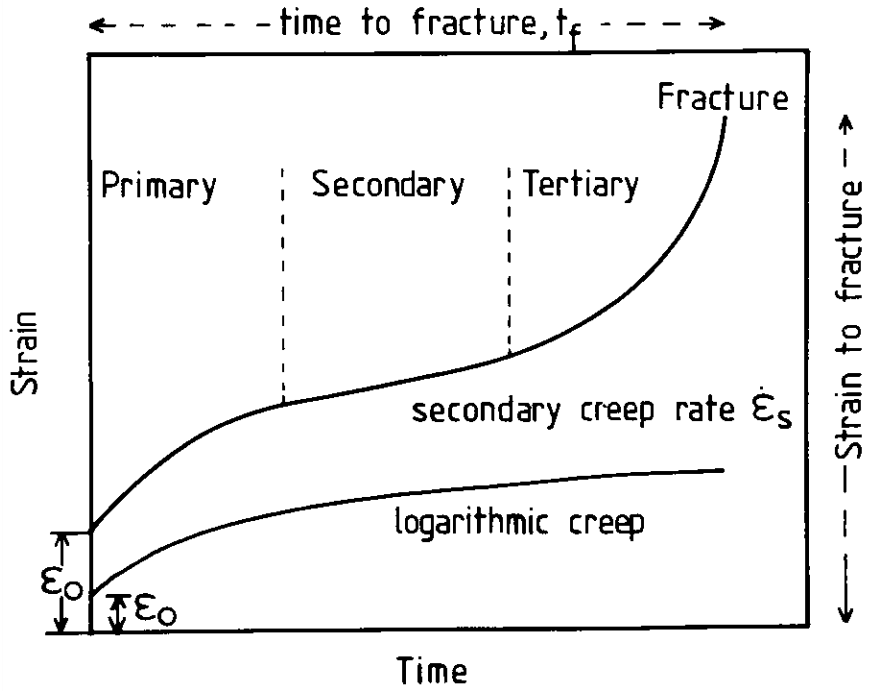

Figure 2.33 Schematic representation of creep curves. Logarithmic creep occurs at low temperature. The upper curve is for medium temperature [77]

During the initial specimen extension, the material strain hardens by the generation and movement of dislocations until the flow stress becomes equal to the applied stress. Creep subsequently occurs as a result of thermal activation helping the applied stress to continue dislocation movement. At low temperatures (0~0.3 T_m), the thermal activation enable the dislocations to overcome obstacles. Since the events which require the least thermal energy will take place most rapidly, the creep rate will decrease continuously with time. In this logarithmic or low temperature regime, only limited creep strains are encountered (usually below 1% [78]), and the deformation processes do not lead to eventual fracture.

However, as the temperature increases towards about 0.4 T_m, the shape of the creep curve departs increasingly from a logarithmic form to the 'normal' form, which contains three stages. After the initial strain on loading, the creep rate decreases gradually during the primary stage until an apparently steady-state rate is reached. This steady-state or secondary stage, is achieved via a balance between work hardening and recovery, leading to a constant creep rate. Furthermore, as illustrated in Figure 2.33, this period of constant rate does not continue indefinitely since, in most cases, the creep rate increases once again during the tertiary stage which terminates in fracture. Under these conditions, the total creep strains can be large and the rupture life is usually found to decrease rapidly with increasing stress and temperature. The change from the logarithmic form to the normal creep curve shape is attributable to the increasing importance of recovery as the temperature increases. At temperatures of about 0.4 T_m and above, recovery processes, such as climb and cross slip, allow rearrangement and annihilation of dislocations to occur. Therefore, the work hardening of the material due to generation of dislocations is balanced by these recovery processes to maintain a steady-state creep rate.

It should be emphasized that the 'normal' creep curve presented in Figure 2.33 is idealized and, in practice, the extent of the three creep stages can vary markedly for different materials and for different stress/temperature conditions (Figure 2.34). Thus, the actual creep curves recorded for metals and alloys may be dominated by either the primary or the tertiary stages. In these cases, since the strain recorded in each creep stage can vary significantly with stress and temperature, the 'steady-state' creep rate is normally chosen as the parameter most representative of the material behaviour under specified creep conditions.

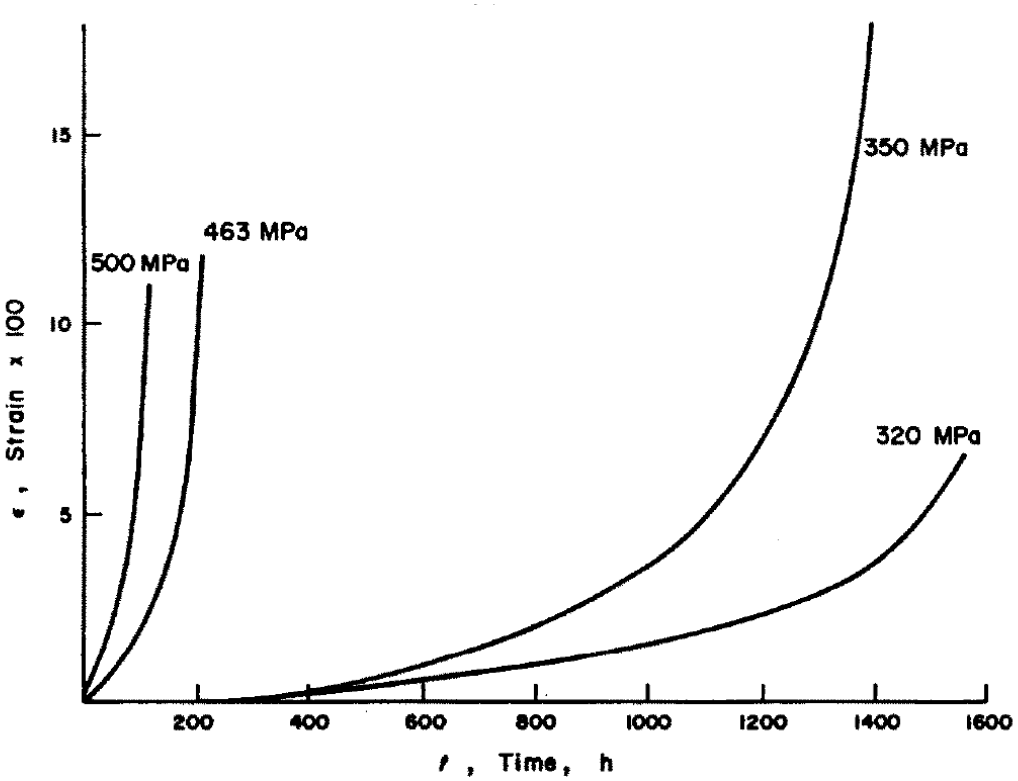

Figure 2.34 Creep curves for Mar M246 nickel base superalloy tested at different applied stresses at 1123 K [79]

Based on abundant experimental results from pure copper, Norton [80] found that, up to a life of 10000 hours, there is a straight line relationship between stress and steady-state creep rate when the curves are plotted on a logarithmic scale. This relationship can be described as $y = mx^n$, which is now known as Norton's law: $\dot{\varepsilon}_s = B\sigma^n$, where n is called the stress exponent.

Using this procedure, stress exponents for pure metals of n=1 at low stresses to n>3 at high stresses have been found (Figure 2.35). However, the stress exponent can be as high as 40 for some alloys. The change in stress exponent under different conditions has been taken as evidence for a change in the creep deformation mechanism.

Clearly, the precise mechanisms by which time-dependent deformation occurs, and therefore the actual creep characteristics exhibited, depend not only on the material but on the ranges of stress and temperature.

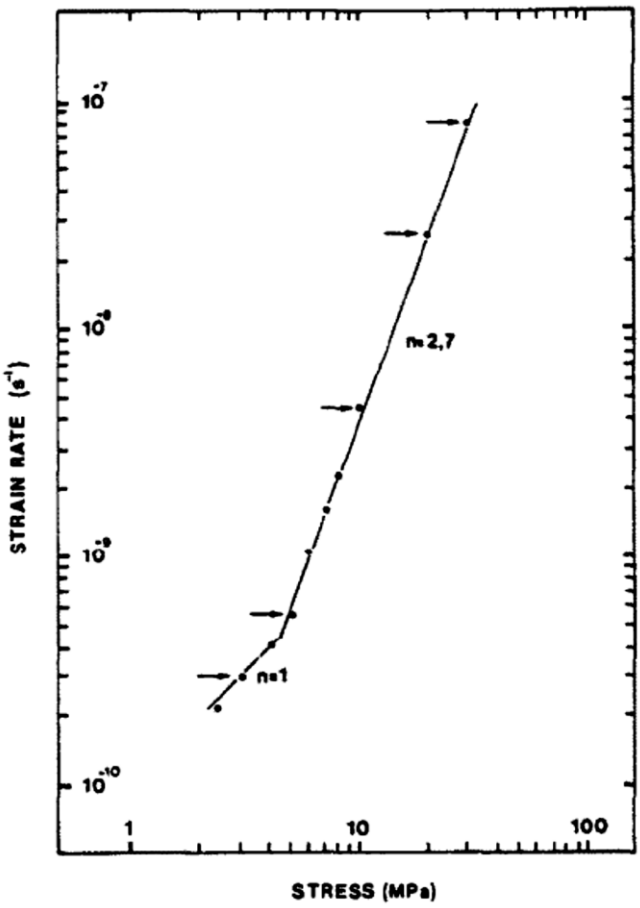

Figure 2.35 Log-log plot showing steady state creep rates as a function of the applied stress for an austenitic stainless steel. The slope of the line indicates the stress exponent, (n=1 at low stress and n=3 at high stress). [81]

As illustrated in Figure 2.33, a constant creep rate does not continue indefinitely since, in most cases, the creep rate increases once again during the tertiary stage, which terminates in trangranular/intergranular fracture. Metals undergo a transition from trangranular fracture to intergranular fracture as temperature increases. This is because slip along the slip planes is easier than grain boundary deformation at low temperatures and the opposite occurs at high temperatures [82]. Therefore, for creep-resistant steels, the main fracture mechanism will be intergranular.

There are two types of intergranular creep fracture depending on the creep conditions (Figure 2.36). One is by nucleation and growth of voids and the other is by wedge cracking at triple point grain boundary junctions [83]. Cavities (voids) generally develop at low stresses and wedge cracks are normally found at high stresses (lower temperature). Both wedge cracks and voids tend to form on grain boundaries oriented perpendicular to the applied stress. Although the wedge cracks or voids are found to develop in the early stage of creep life, in the third stage of creep the nucleation and growth of grain boundary voids occur at an accelerated rate. This leads eventually to their linkage and formation of a crack that is able to propagate under the applied tensile stress [16, 84].

Creep fracture of an intergranular mode in uniaxial tension under constant stress has been described by the Monkman-Grant relationship. This states that the creep fracture is controlled by the secondary creep rate $\dot{\varepsilon}_{ss}$ where the time to fracture (t_r) is usually found to increase linearly as $\dot{\varepsilon}_{ss}$ decreases. This is illustrated in Figure 2.37 and it is expressed as:

$$\dot{\varepsilon}_{ss}^{m} * t_r = constant\ (M)$$

where constant *m* is typically about 1.0. The value of *M* varies for different materials and larger *M* values are found in materials exhibiting larger creep ductilities [84].

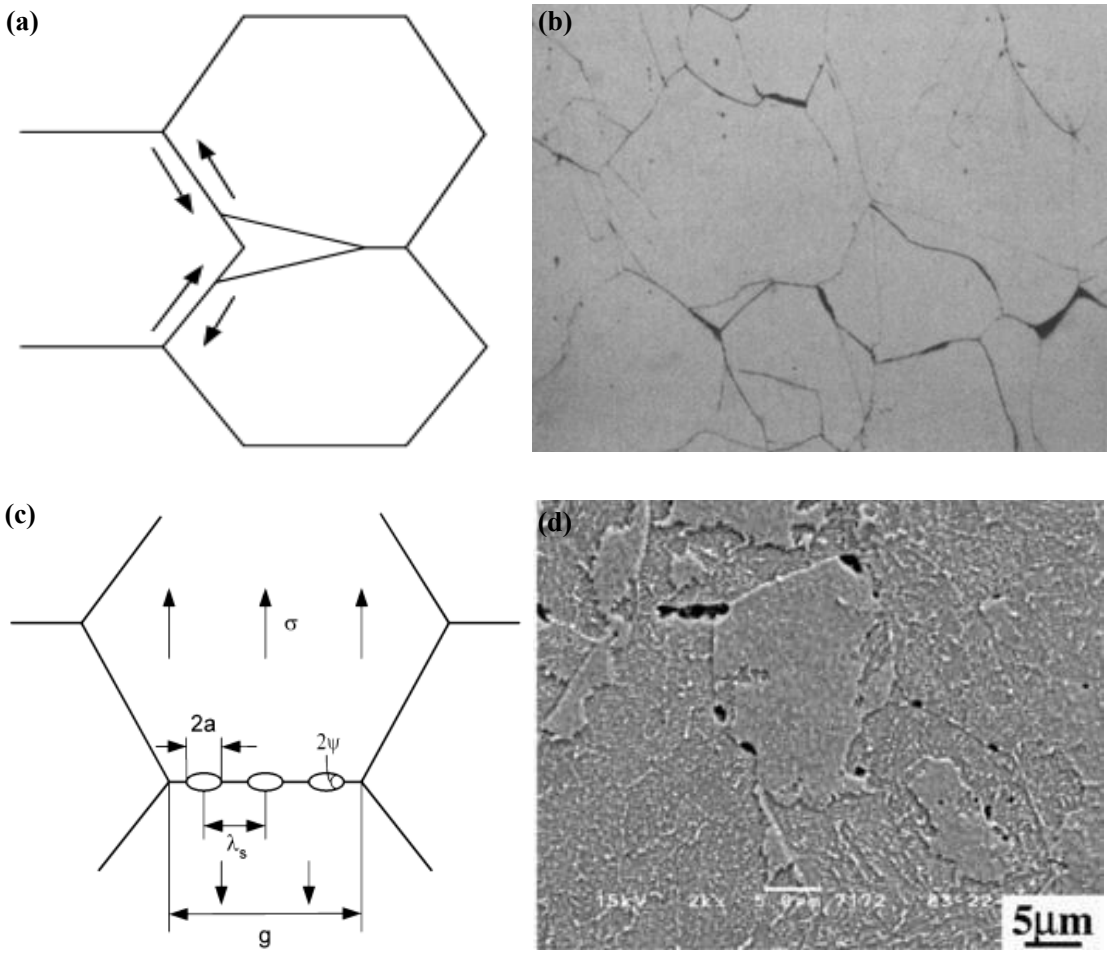

Figure 2.36 (a) Schematic illustration of wedge crack formed at the triple junctions [85]; (b) wedge crack observed in 316 stainless steel [86]; (c) Schematic illustration of voids along grain boundary [85]; (d) voids observed in 1CrMoV steel [87]

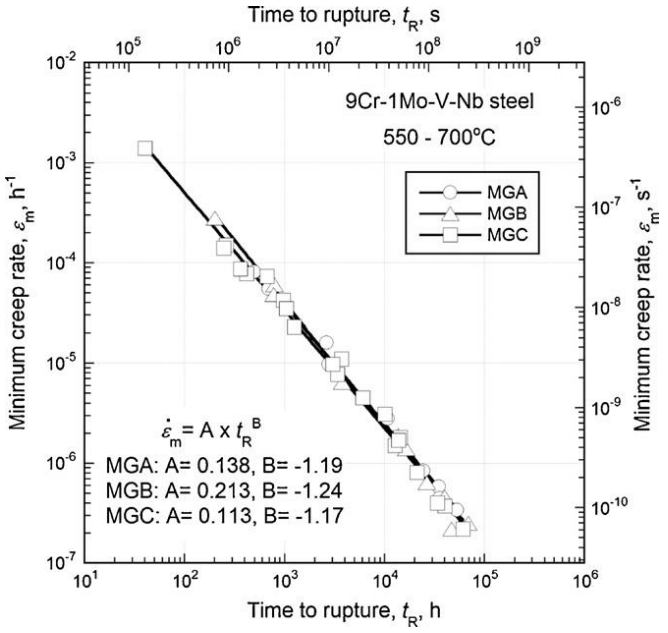

Figure 2.37 Monkman-Grant plot steel over a range of temperature from 500 to 700 °C of 9Cr-1Mo-V-Nb steel [88]

It should be emphasized that the Monkman-Grant relationship indicates that the rate of intergranular damage development must be controlled by the rate of deformation [89]. This requirement must then be integral in any micro-mechanism proposed to account for wedge-type and cavitation-type creep failures.

2.4.2 Creep deformation mechanism

At high temperatures above 0.4 T_m, if the stress is too low for dislocation movement to be significant, the accumulation of creep strain is solely attributable to diffusional transport of material as vacancies flow between sources and sinks.

This type of creep was first described by Nabarro and Herring [90]. As shown in Figure 2.38, there is a uniform equilibrium number of vacancies in a grain. When a uniaxial tensile stress is applied, vacancies and interstitial atoms are formed in pairs on the grain boundaries normal to the tensile axis. The vacancies diffuse into the bulk of the crystal, while the interstitials form additional layers of the crystal lattices on the grain boundaries. The specimen elongates to accommodate this condition thus reducing the free energy. The excess vacancies, which diffuse to other grain boundaries, are absorbed leading to a formation of concentration gradient of vacancies. This concentration gradient becomes the driving force for further vacancy migration and strain accumulation.

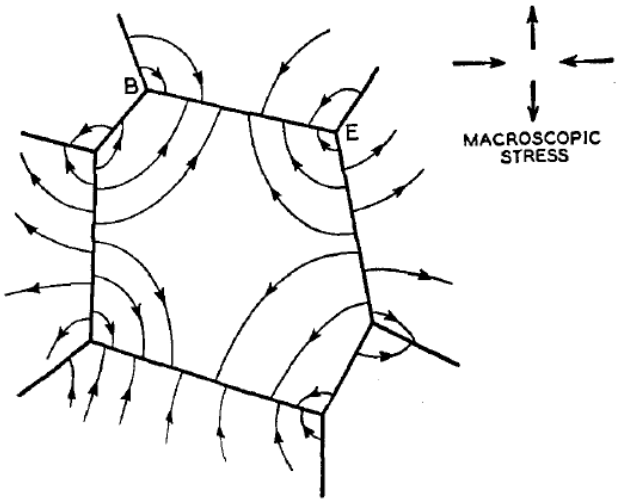

Figure 2.38 A typical grain of a polycrystalline solid showing the self-diffusion currents of vacancies to be expected when the solid is subjected to a tensile stress [90]

For Nabarro-Herring creep, only self-diffusion through the bulk of the grain is involved, while Coble [91] also considered self-diffusion along grain boundaries. For Coble creep, the bulk self-diffusion coefficient D is replaced by the grain-boundary self-diffusion coefficient D_{gb}. Since the activation energy of grain-boundary self-diffusion is roughly half that of self-diffusion through the bulk, a transition from Nabarro-Herring to Coble creep would be expected with decreasing temperature in tests undertaken at low stress levels for pure polycrystalline metals [77]. In summary, creep by self-diffusion irrespective of whether vacancy flow occurs through the bulk or along grain boundaries, is the predominant mechanism only when the stress is low and the temperature is very close to the melting point.

In comparison, when creep takes place at high stresses, the generation and movement of dislocations will be involved. With high temperature and high stress, creep is usually accomplished by dislocation glide, dislocation network growth and dislocation climb.

The creep rate can be controlled by the rate of dislocation movement within their glide planes. In this case, the speed of movement of dislocations is governed by the diffusion of solute atoms or by the motion of jogs on screw dislocations. For the latter process, Barrett and Nix [92] considered that the rate of movement of the dislocations will be fixed by the rate of emission and absorption of vacancies since the jogs on dislocations will be saturated with vacancies at high temperatures. As the rate of emission and rate of absorption are in balance, the creep rate turns out to be steady in this case.

During steady-state creep, the dislocations can join together and form a three-dimensional network. Based on the presence of this three-dimensional dislocation network, a theory of creep has been proposed by McLean [78] and refined by Davies and Wilshire [93]. The hardening obtained from the dislocation network strongly depends on its dimensions. The longest dislocations, which are also the weakest, can break free with the aid of thermal activation and move a certain distance before being joined to another network. The release of the longer dislocations shortens the average length in the network and thus refines the dimensions of the network. However, recovery at high temperature, such as via cross slip, will take place and lead to an increase of average length, which can partly offset the hardening effect via the refinement of the dislocation network. When the rate of refinement equals the rate of recovery, the creep rate will be steady-state.

At high temperatures, dislocations acquire a new degree of freedom: they can climb as well as glide. If a gliding dislocation is held up by obstacles like immobile dislocations, climb can release the pinned dislocation and allow it to glide to the next set of obstacles. The glide step is responsible for almost all of the strain, although its average velocity is determined by the climb step. Weertman [94] regards dislocation climb as the rate controlling recovery process and the general features of the analysis are illustrated in Figure 2.39. During creep, the dislocation sources in the material, Frank-Read sources in Weertman's theory, will emit dislocations which are confined to their glide planes. The leading dislocations are eventually blocked by obstacles. However, the lead dislocation can climb out of its slip plane by vacancy emission. After climbing a certain distance, the lead dislocation may either be annihilated by a dislocation of opposite sign or be free to glide in a new slip plane. In either case, a new dislocation can be emitted from the source and creep continues. The climb process represents the recovery event. The rate-controlling process, at an atomic level, is the diffusive motion of vacancies to or from the climbing dislocation. The balance between the emission rate and absorption rate will lead to a constant creep rate during the steady-state stage.

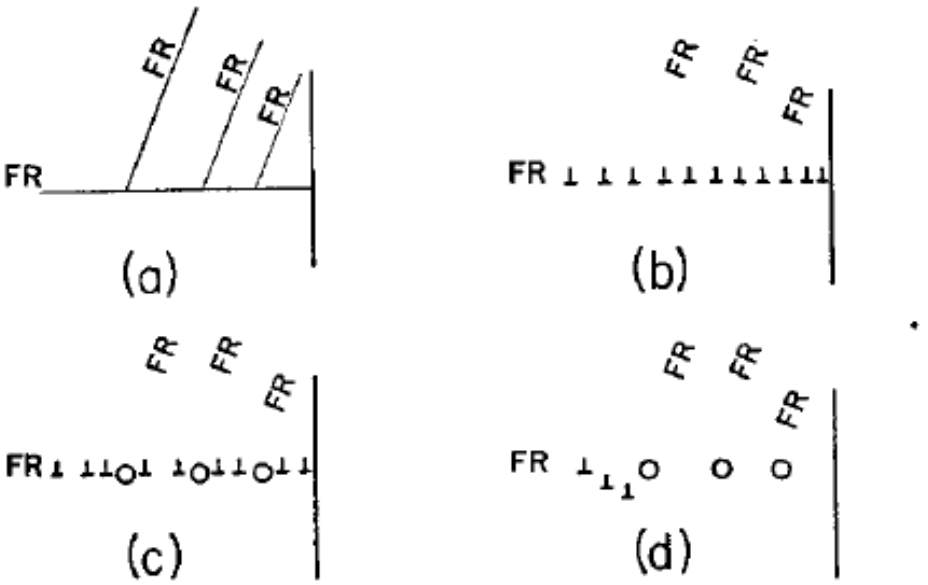

Figure 2.39 Processes leading up to a Frank-Read source being blocked by obstacles [94]

Since diffusional and dislocation processes are relatively independent, one of these creep mechanisms described above can be dominant, when the contribution to the overall creep rate made by the other independent processes is so small that it can be ignored.

Moreover, the dominant creep mechanism, and hence the creep properties displayed by the materials, would be expected to vary in different stress and temperature ranges. For this reason, considerable emphasis has been placed on the development of ‘Deformation mechanism maps’, which presents the deformation mechanism of a material in the form of a stress and temperature diagram and was invented by Ashby [95].

Ashby [95, 96] proposed that there are five deformation mechanisms, which are mutually independent and operate in a parallel way:

(1) Defect-less flow: material can deform plastically by body movement of planes of atoms in the crystal, when the stress is sufficiently high and close to the theoretical shear stress;

(2) Dislocation glide: in practice, all crystals will contain dislocations and deform via dislocation glide when the stress is above the yield strength of material;

(3) Diffusional creep: Nabarro-Herring creep by lattice diffusion and Coble creep by grain boundary diffusion;

(4) Dislocation creep: controlled by dislocation glide at relatively low temperature or controlled by dislocation climb at higher temperatures;

(5) Other mechanisms: under specific conditions, material can deform by other mechanisms, such as twinning or super-plastic flow, which are generally ignored in deformation maps.

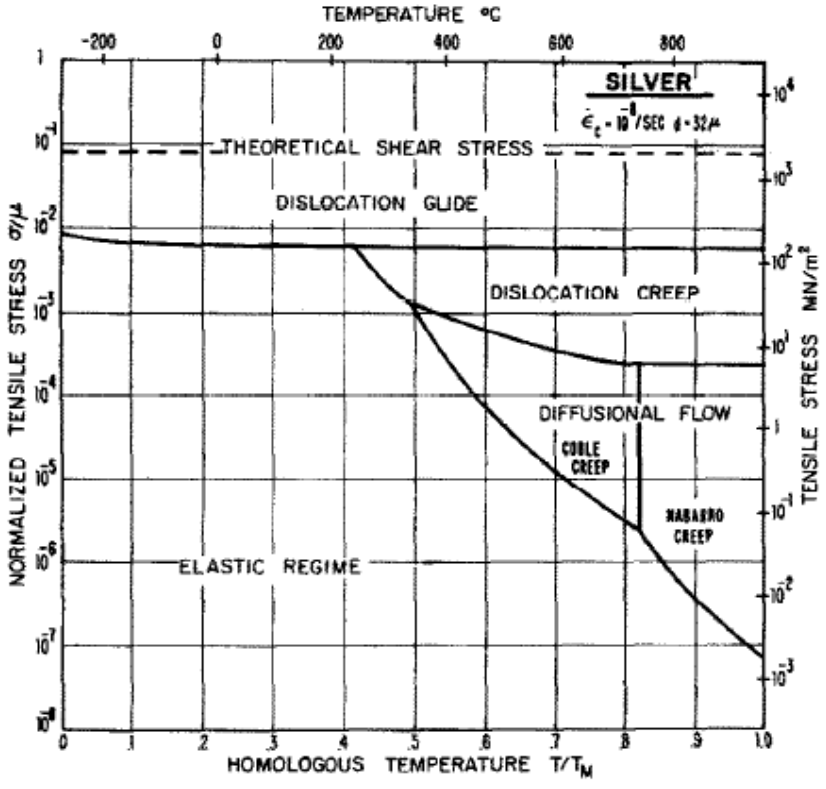

Figure 2.40 A deformation mechanism map for pure silver [95]

Figure 2.40 illustrates a typical deformation mechanism map obtained from pure silver with a grain size of 32 μm and a strain rate of 10^{-8}/s. The deformation mechanism map is constructed with axes of normalized stress σ/G, where G is the shear modulus, and homologous temperature T/T_m. The upper limit of the boundary is set by a theoretical strength ranging from $G/20$ to $G/30$. Within a field in the deformation mechanism map, one mechanism is dominant and will supply a greater strain rate than any other mechanism. Meanwhile, the boundaries between adjacent fields indicate the conditions under which two mechanisms contribute equally to the overall creep rate. The ranges of stress and temperature over which each mechanism predominates can then be identified.

Deformation mechanism maps can be constructed using actual creep data or by deriving the steady-state creep rate using appropriate theoretical equations for a given process. Figure 2.41 is an example of the construction of a deformation mechanism map. Each field, where a certain deformation mechanism is dominant, can be described by theoretical equations. The field boundaries are the loci of points at which two mechanisms have equal steady-state creep rates. Furthermore, from the appropriate constitutive equations, the steady state creep rate can be calculated and contours of constant strain-rate can be superimposed on the original deformation mechanism maps. (Figure 2.42)

The map displays the relationship between the three macroscopic variables: stress, temperature and strain-rate. If any pair of these variables is specified, the map can be used to determine the third.

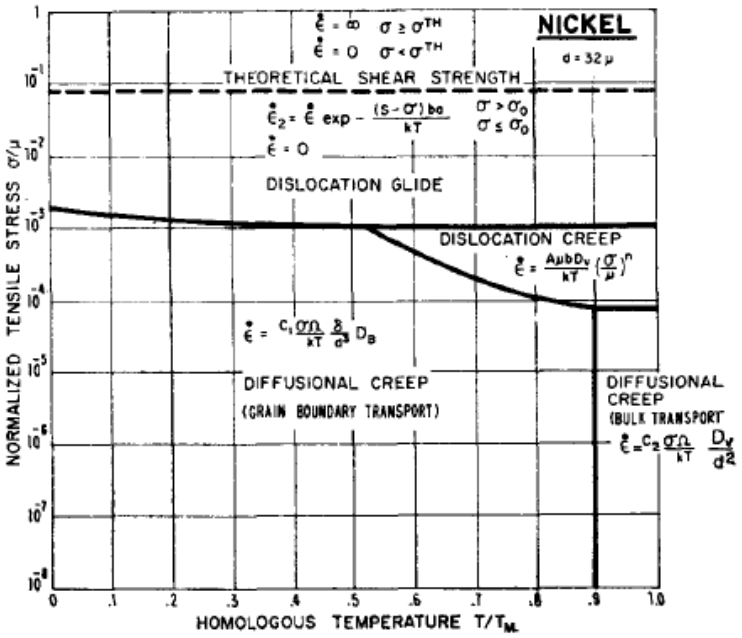

Figure 2.41 Mechanism fields for pure nickel with a grain size of 32 μm. The fields are labelled with the appropriate constitutive equation [95]

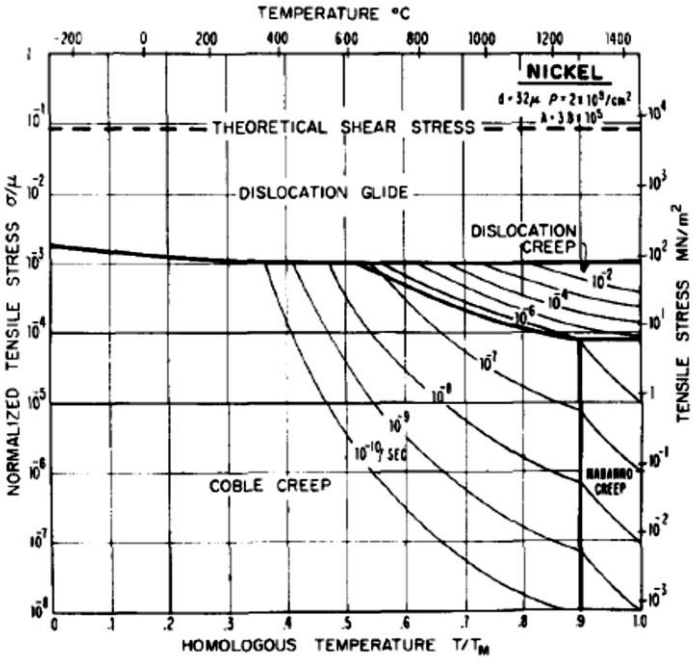

Figure 2.42 A deformation mechanism map for pure nickel with a grain size of 32 μm with superimposed contours of constant strain-rate [95]

The exact locations of the boundaries between adjacent creep regimes obviously differ for different materials. However, even for the same material, the stress/temperature ranges over which a particular mechanism is dominant can be dependent on such microstructural variables as grain diameter. When creep occurs by diffusion–controlled generation and movement of dislocations, evidence has been obtained which suggests that the secondary creep rate is independent of grain size. Thus diffusional creep is strongly dependent on grain size whereas dislocation creep is insensitive to grain size.

Figure 2.43 illustrates the deformation mechanism map for pure silver with grain sizes from 10 to 100 μm. As the grain size increases, the field of diffusional creep contracts and shifts to higher temperatures. Meanwhile, increasing the grain size has a small effect only on the dislocation creep field, which moves to lower stress: there is no change in the dislocation glide field by changing the grain size.

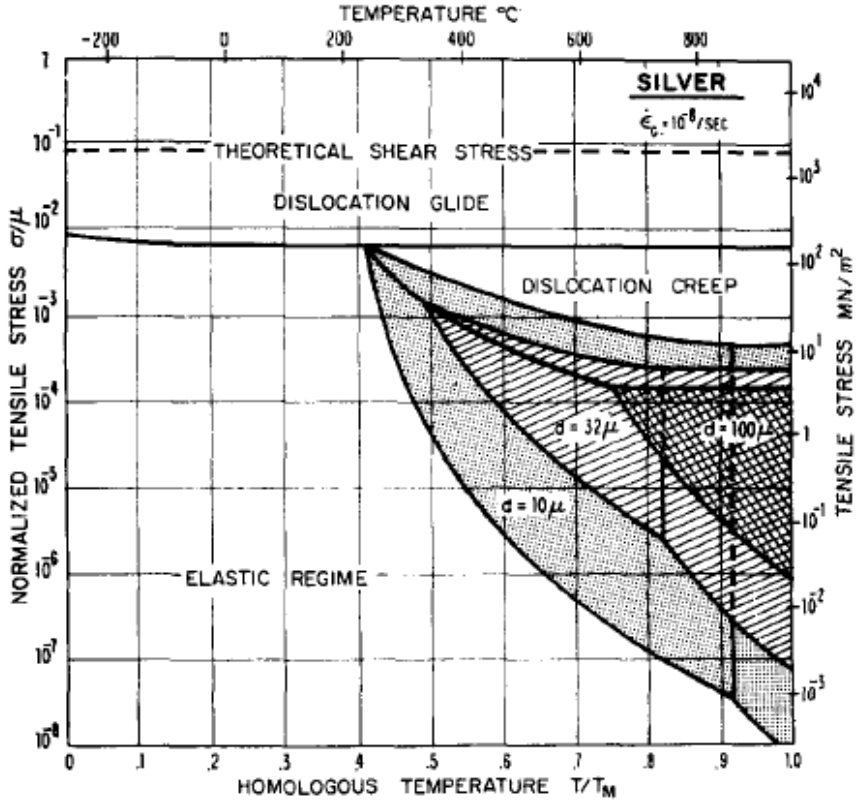

Figure 2.43 Deformation mechanism maps for pure silver with grain sizes of 10, 32 and 100 μm at a strain rate of 10^{-8} / s [95]

The main application of deformation mechanism maps is to identify the mechanism by which a component or structure deforms in given service conditions. For example, Figure 2.44 illustrates a deformation mechanism map for 25Cr-20Ni austenitic stainless steel. When this kind of steel is used for steam reforming, dislocation creep is the dominant mechanism with little contribution from diffusional creep. Therefore, the analysis and design of 25Cr-20Ni for steam reforming can be based on the theory of dislocation creep and other mechanisms can be ignored.

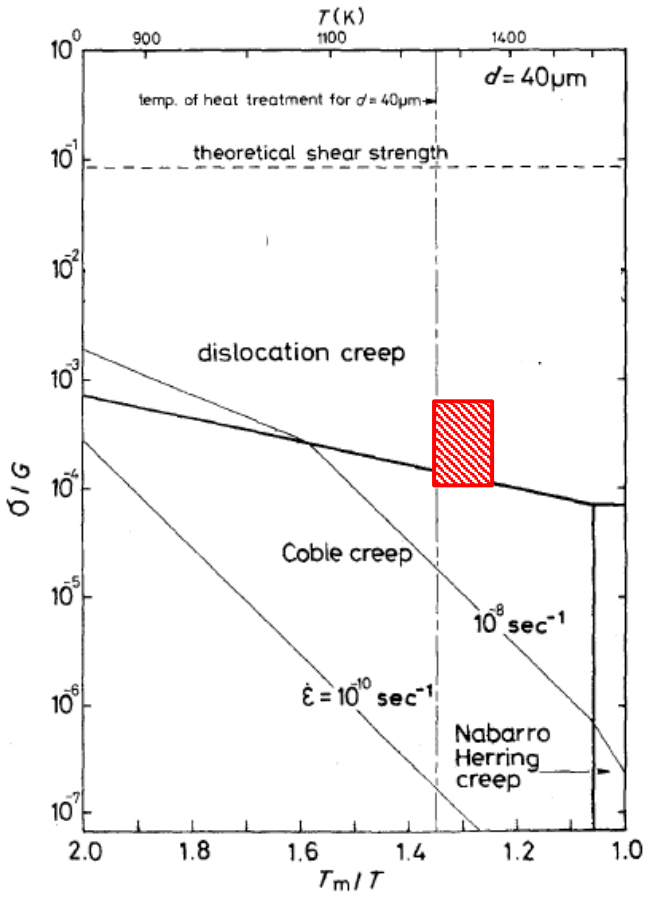

Figure 2.44 Deformation mechanism map of 25Cr-20Ni austenitic stainless steel. The service conditions for steam reforming are shown as the rectangle [97] (G is equivalent to μ in Figure 2.40-43)

2.4.3 Strengthening mechanisms for creep

Austenitic stainless steels can be highly strengthened by various methods. Precipitation strengthening is one of the most effective ways to increase the high temperature creep resistance required for heat-resisting steels. Based on the nucleation position, the precipitates in austenitic stainless steel can be divided into intergranular and intragranular. However, at high temperatures where recovery takes place rapidly, this main strengthening mechanism loses its effectiveness during long exposure, due to precipitation coarsening. In such cases, the intrinsic strength of the matrix determines the creep resistance. The creep resistance of the austenitic matrix depends on its grain size and on solid solution strengthening during creep deformation.

(1) Grain size

In the regime of diffusional creep, the creep rate is inversely proportional to the square or cube of the mean grain size, depending on whether the diffusion of the vacancies is via the lattice or the grain boundary. However, for dislocation creep, the effect of grain size on creep rate is controversial, although a larger grain size is generally preferred for higher creep strength. Kondo [98] investigated the effect of the grain size on the steady state creep rate in a single-phase 17Cr-14Ni austenitic steel at 850 and 900 ºC (Figure 2.45). The steady state creep rate decreased to a minimum at an average grain diameter of 100 μm and then increased with increasing original grain size. For some heat-resisting alloys, such as Cr-Mo-V rotor steel (Figure 2.46) [99], Hastelloy X [100] and 316 stainless steel [101], this relation between the steady state creep rate and the original grain size holds true.

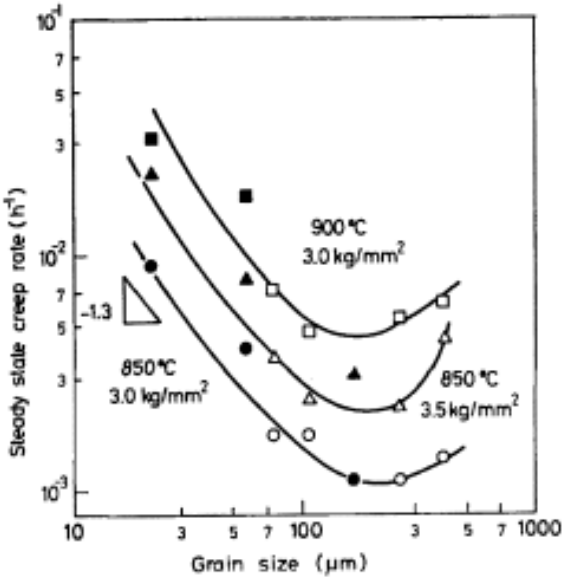

Figure 2.45 Variation of steady state creep rate with grain size of 17Cr-14Ni austenitic steel at 850 and 900 °C [98]

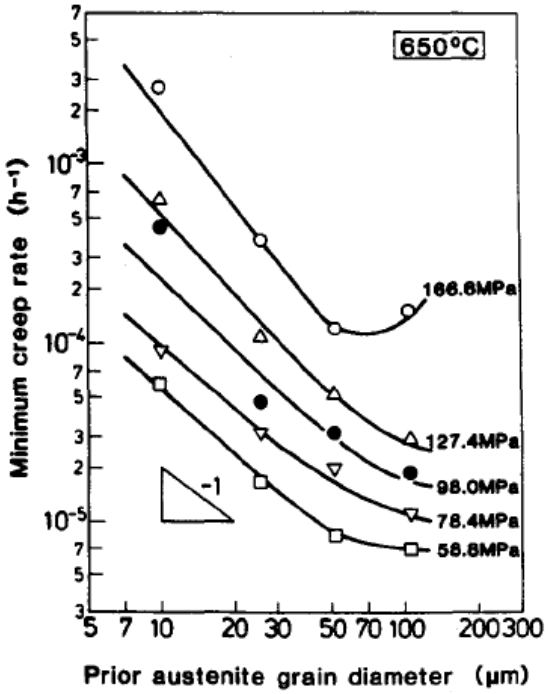

Figure 2.46 Minimum creep rate as a function of prior austenite grain diameter of Cr-Mo-V rotor steel under five different applied stresses at 650 °C [99]

(2) Solid solution strengthening

Nelmes and Wilshire [102] compared solid solution strengthening due to zinc, silicon and germanium in single-phase copper alloys at 700 ºC. A decrease in the steady state creep rate of two orders of magnitude was found on going from zinc to germanium. Furthermore, the stress exponent rises from 4.5 to 7.5 (Figure 2.47), which was explained by a decrease in stacking fault energy and a strong dislocation-solute interaction.

Kondo et al. [103] investigated the effect of substitutional solutes, such as molybdenum, tungsten, manganese, titanium and niobium, on creep behaviour in a 25Cr-35Ni austenitic steel at 1000 ºC. Through heat treatments, the grain size was controlled to be the same in all the specimens. The creep curves for different solutes are compared in Figure 2.48. The specimen with tungsten shows the longest creep life, which is due to the relatively larger change of lattice parameter of the matrix with tungsten addition. Furthermore, within the solubility limit, the strengthening effect increases with the increase of amount of alloy addition. Research by Takeyama et al. [104] found that the effect of solid solution strengthening is stress dependent. Creep tests on Ni-20Cr austenitic steels strengthened with molybdenum, tungsten, niobium and tantalum confirmed that increasing the applied stress will lead to a larger effect of a solid solution strengthening.

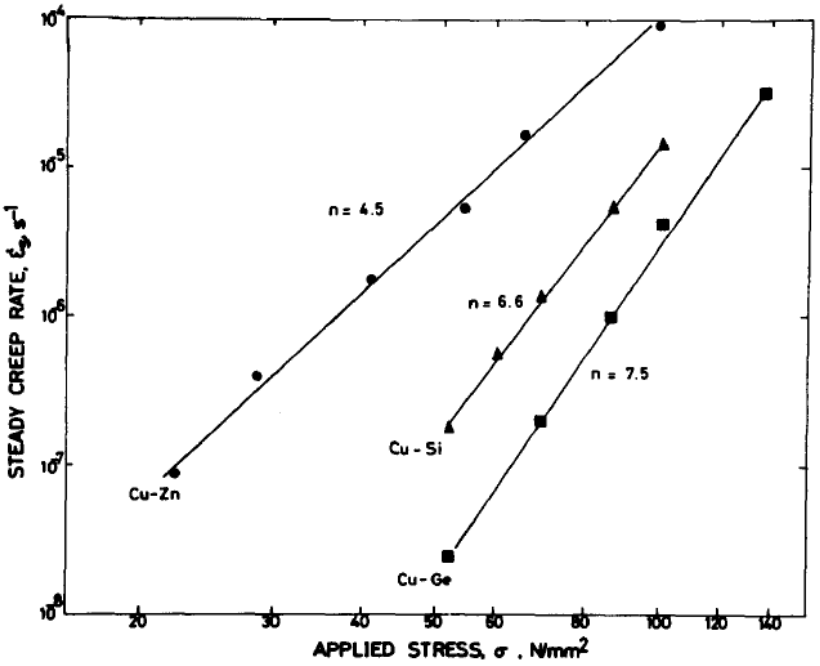

Figure 2.47 The stress dependence of the steady-state creep rate of Cu-Zn, Cu-Si and Cu-Ge alloys at around 400 °C [102]

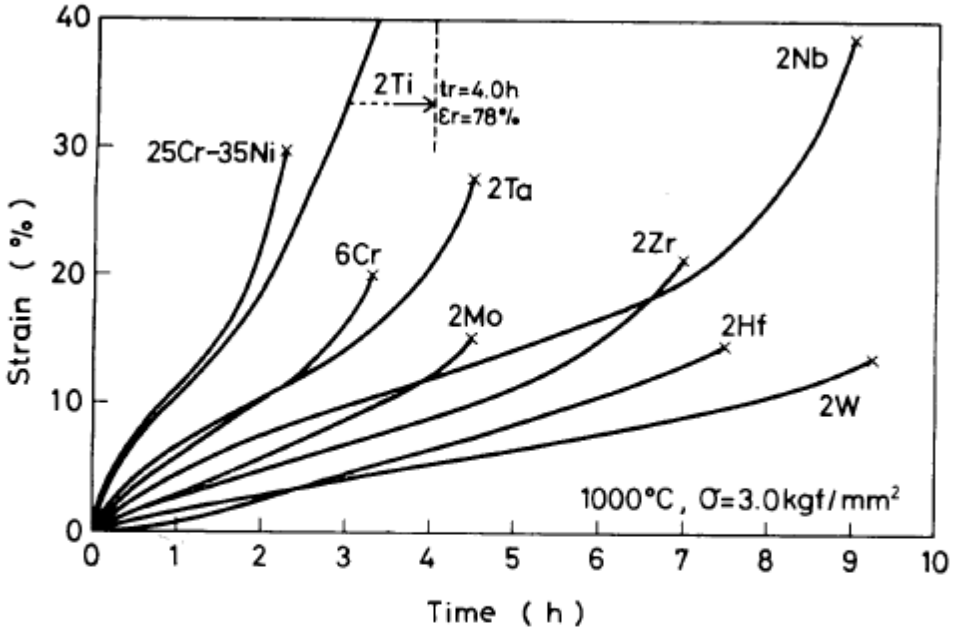

Figure 2.48 Creep curves of 25Cr-35Ni steels with addition of 6Cr, 2Mo, 2W, 2Nb, 2Ta, 2Ti, 2Zr and 2Hf at 1000 °C [103]

Turning now to interstitial solutes, Mathew [105] performed a constant-stress creep test on two 316 austenitic stainless steels, named as 316 SS with 0.03 wt.% nitrogen and 316 LN SS with 0.09 wt.% nitrogen. The results demonstrated that the solid solution strengthening due to nitrogen was quite effective at 700 ºC, as shown in Figure 2.49 where with an increase of nitrogen concentration the steady state creep rate of the steels decreases, and that the strengthening effect via nitrogen was independent of carbon concentration. The decrease of steady state creep rate due to increasing nitrogen content is explained as the combined contributions from solid solution strengthening by nitrogen itself and its influence of carbide coalescence. The presence of nitrogen is known to delay the rate of coalescence of $M_{23}C_6$ carbides in austenitic stainless steels since nitrogen can reduce the interfacial energy between the carbides and the austenite matrix. The suppression of coalescence of carbides due to the nitrogen addition is the predominant factor in the solid solution strengthening. Furthermore, Tanaka et al. [106] pointed out that nitrogen can prevent the formation of the subgrains during creep deformation and thus decrease the creep rate.

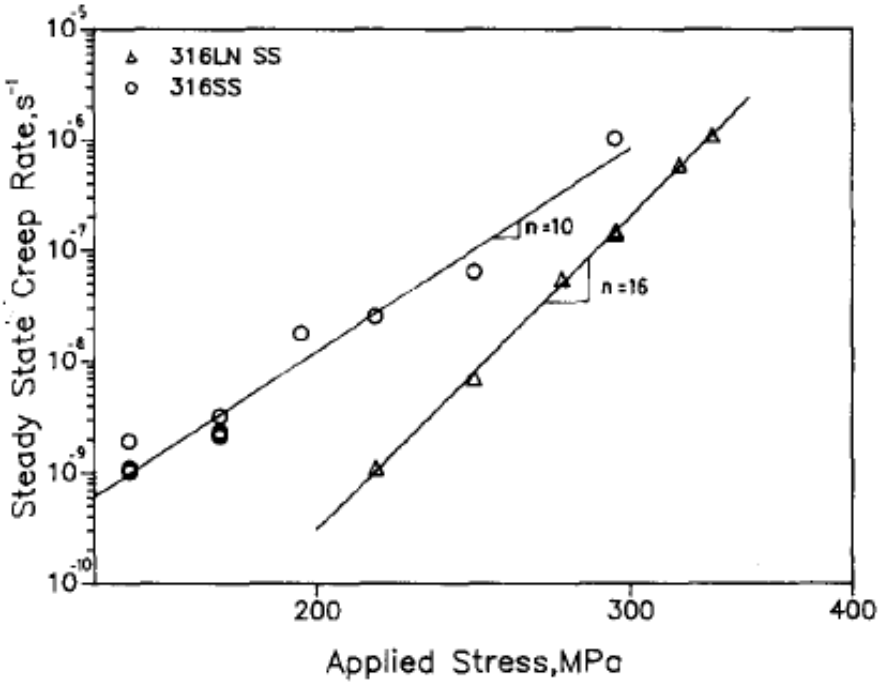

Figure 2.49 Effect of N on steady state creep rate at 700 ºC of the 316 SS (0.03 wt.% nitrogen) and 316 LN SS (0.08 wt.% nitrogen) austenitic stainless steels [105]

(3) Intergranular precipitation strengthening

Grain boundaries tend to become weakeners rather than strengtheners at higher temperatures so that grain boundary strengthening should always be accompanied by intergranular precipitation strengthening. Integranular precipitates are effective in suppressing the nucleation of intergranular voids and cracks by reducing the stress concentration via reduced grain boundary sliding.

Takeyama et al. [104] have found a semiquantitative relation between the creep rate and the density of intergranular precipitates. Specimens of Ni-20Cr-20W alloys with different amounts of intergranular tungsten precipitates were prepared by pre-heating treatments at 1000 ^{o}C. The minimum creep rate of a specimen with intergranular precipitates to that of a specimen without intergranular precipitates was proportional to the grain boundary area free from precipitates.

In a 15Cr-25Ni austenitic steel, Zhang et al. [107] reported the contribution of the intergranular $M_{23}C_6$ to its creep resistance. The grain boundary carbide precipitation leads to a dramatic decrease in creep rate. However, above a certain matrix strength, intergranular precipitation strengthening can become totally ineffective. Based on the review by Matsuo [108], when more than 90% of the grain boundary area is covered by precipitates, the creep rate can only decrease by one order of magnitude via intergranular precipitation strengthening. This strengthening mechanism is especially useful at high temperatures, since the slow coarsening rate of intergranular precipitates obtaining over a long period.

(4) Intragranular precipitation strengthening

Intragranular precipitation strengthening is one of the most important strengthening mechanisms in creep-resistant steels at elevated temperatures. To achieve enough strengthening using this effect, engineering creep-resistant steels usually contain several kinds of precipitate particles in the matrix. Among these precipitates, $M_{23}C_6$ is the favourite particle in austenitic stainless steels to enhance strengthening.

A dispersion of fine precipitates can prevent movement of dislocations in the matrix and stabilize the sub-grain structure formed during creep deformation. Considerable efforts have been made to increase the density of carbide precipitate and to control its size in order to achieve enough strengthening. However, the coarsening of the precipitates at elevated temperatures makes it difficult to retain the density and size of carbides over a long period. Furthermore, the dissolution of fine precipitates sometimes takes place preferentially in the vicinity of grain boundaries during creep, which promotes the formation of a localized weak zone and thus creep deformation near the grain boundaries.

A decrease in creep rate of one order of magnitude cannot easily be achieved by increasing the grain size. Solid solution strengthening is a stable creep resistance mechanism at high temperatures. However, even a very effective strengthener such as nitrogen can decrease the creep rate by only one and half orders of magnitude. Intergranular precipitation strengthening is a promising method at high temperatures, but the creep rate only decreases by one order of magnitude with more than 90% of the grain boundary area covered by precipitates. Although the carbides easily coagulate and lose their role as an effective strengthening dispersion at very high temperatures, intragranular precipitation strengthening due to carbides is still the most effective and widely adopted way to increase the high temperature creep resistance of austenitic heat-resisting steels. In this way, a decrease in creep rate of more than three orders of magnitude can easily be achieved. Therefore, the creep behaviour of intragranular precipitation strengthened alloys needs to be understood.

2.4.4 Creep in intragranular precipitation strengthened alloys

As mentioned in Chapter 2.4.1, the steady-state or secondary creep rate maintains a constant minimum value over most of the creep life through a balance of recovery and work hardening. Based on abundant experimental results, Norton [80] found that there is a straight line relationship between stress and creep rate when the curves are plotted on a logarithmic scale. This relationship can be described as

$\dot{\varepsilon} = A\sigma^n$--- Equation 2.1

where $\dot{\varepsilon}$ is creep rate, A is a constant, σ is the applied stress and n is called the stress exponent.

By including in A a term involving the activation energy of creep, Equation 2.1 represents the creep rate as a function of stress and temperature:

$\dot{\varepsilon} = A'\sigma^n exp\left(-\frac{Q}{kT}\right)$ --- Equation 2.2

where A' is a constant, Q is the activation energy of creep (roughly equal to the self-diffusion activation energy), k is Boltzmann's constant and T is the temperature.

Equation 2.2 is known as the Power Law, and is the most commonly invoked constitutive law to describe creep behaviour. For precipitate-free materials, n generally varies from 1 to 10 [75]. Weertman [94] showed that n should be 4 for steady-state creep by dislocation climb.

Although the power law fits well for pure metals and single-phase alloys, it becomes inadequate for complex engineering alloys, such as nickel-based superalloys and intragranular precipitation strengthened steels. The creep behaviour of such materials deviates from the power law in two main ways:

(i) The values of n and Q are higher than those observed in pure materials: n can be above 20 and Q three times the expected value;

(ii) An established steady state is rarely observed; the creep rate, after a decrease during the primary creep stage, progressively increases from a minimum value until fracture occurs.

To correct these two problems, the concept of "back-stress" σ_b is invoked. The back-stress is the threshold stress to overcome the interactions between dislocations and intragranular precipitates, such as via Orowan looping, cutting and bypass by climb [109]. These interactions oppose the glide of the dislocations, leading to a decrease in the effective applied stress on the material.

$\sigma_{eff} = \sigma - \sigma_b$ --- Equation 2.3

where σ_{eff} is the effective stress

Incorporating Equation 2.3 into 2.2, results in the modified power law equation

$\dot{\varepsilon} = A''(\sigma - \sigma_b)^n exp\left(-\frac{Q}{kT}\right) = A''{\sigma_{eff}}^n exp\left(-\frac{Q}{kT}\right)$ --- Equation 2.4

Threadgill and Wilshire [110] studied a two-phase copper-cobalt alloy and found that, for Equation 2.2, n=5 and Q=140 kJ/mol at low stress and n=12 and Q=210 kJ/mol at high stress. However, Parker and Wilshire [111] applied Equation 2.4 to the same alloy with an experimentally determined back stress σ_b, resulting in Q=110 kJ/mol and n=4 at all stresses; the self-diffusion activation energy for pure copper Q=115 kJ/mol.

In the case of high temperatures (above 0.5 T_m) and relatively low stress (below the threshold stresses of Orowan looping and cutting), bypass by climb becomes the main interaction between the dislocations and intragranular precipitates. The climb process will involve a dislocation line length increase and hence an increase of elastic strain energy, which is the origin of the threshold stress of climb. However, climb can be divided into two types: local climb, where most of dislocations remain in the glide plane and general climb, where most of the dislocations move out of the glide plane (Figure 2.50). For local climb, the increase of the dislocation line length is dependent on the precipitate size while, for general climb, the precipitate spacing will contribute to the increase in the dislocation line length.

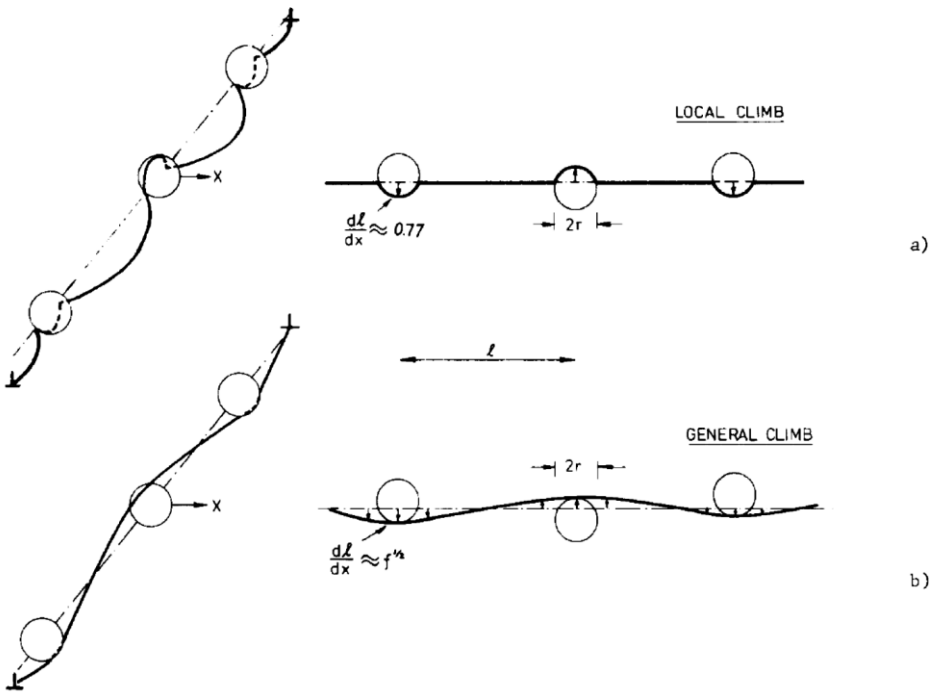

Figure 2.50 Schematic image of a dislocation bypassing precipitates via (a) local climb and (b) general climb [112]

Several models have been developed for dislocation bypass by climb to predict the creep behaviour of alloys. Stevens and Flewitt [109] described a bypass climb model for IN718 based on the geometry of climb at spherical precipitates while Arzt and Ashby [112] pointed out that the threshold stresses for dislocations bypassing spherical precipitates are 0.3 Orowan stress for local climb and 0.04 Orowan stress, respectively. For alloys strengthened by cubic precipitates, climb models have also been presented by Lagneborg [113] for a Ni_3Al strengthened Ni-Cr-Al alloy, Evans and Knowles [114] for a TiN strengthened 20Cr/25Ni stainless steel and McLean [115] for a γ' strengthened IN738LC alloy. However, TEM observations [116, 117] indicate that the dislocations can be held by an attractive force on the departure side after climb is completed, as shown in Figure 2.51. This attraction or detachment process will lead to a larger threshold stress and hence a stronger barrier to dislocations bypassing precipitates than that of climb itself [118-120].

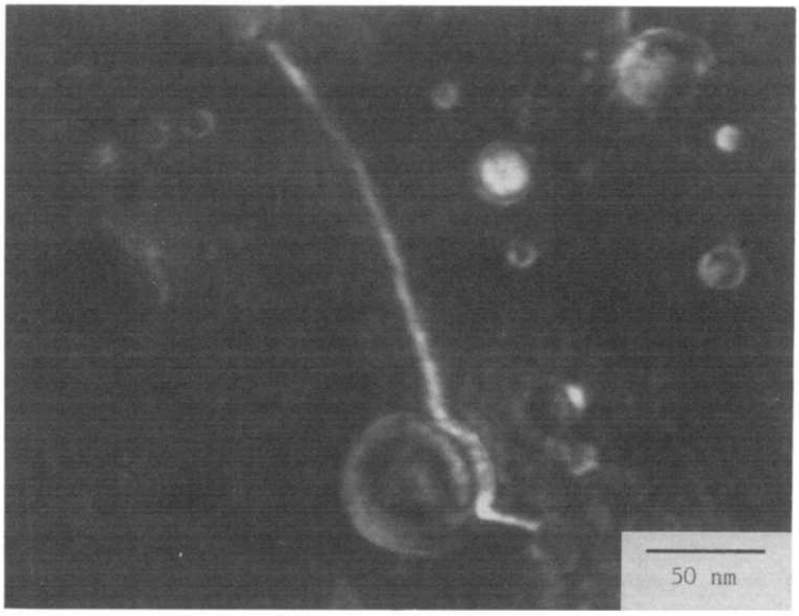

Figure 2.51 Bright field image of a dislocation at an oxide dispersoid. The dislocation contrast at the dispersoid remains ambiguous [117]

For all of the climb models described above, the value of threshold stress or the back stress σ_b will depend on the microstructural parameters of the precipitate. The threshold stress thus will not be constant but will vary with temperature, stress and time due to coarsening of the precipitates [121, 122]. For example, by introducing the time-dependent coarsening of precipitates, Dyson and McLean [79] established a time-dependent creep model for precipitate-strengthened IN597. This approach is now known as continuum damage mechanics (CDM). Similar approaches have been developed by Stevens and Flewitt [109, 123] for IN738, Williams and Cane [124] for 0.5Cr0.5Mo0.25V steel and Rosler and Arzt [120] for aluminium alloys and strengthened tungsten.

However, the above approaches (based on Equation 2.4) to presenting the creep behaviour of complex engineering alloys are generally empirical and lack physical justification for the stress exponent n and constant A. Furthermore, these models have no immediate quantitative relationship to microstructural parameters such as dislocation density, precipitate volume fraction, precipitate size and precipitate interspacing. Basoalto et al. [125, 126] were the first to derive a creep equation for nickel-based superalloys including a consideration of microstructural parameters. A refinement of this model had been presented by Dyson [127], which is a microstructure-based climb bypass model linking microstructural evolution to creep rate. Coakley et al. [128] pointed out that Dyson's model is only suitable for a unimodal particle size distribution while some nickel-based superalloys have a bimodal particle size distribution. Oruganti et al. [129] presented a similar model for 9-10% Cr ferritic steels assuming that creep occurs by the thermally activated release of dislocations from pinning. Zhu et al. [130] made the spherical particles into cubic ones for CMSX-4 and introduced an effective diffusivity D_{eff} to account for the dependence of creep deformation on alloy chemistry.

Based on models of climb, which is the main creep mechanism in intragranular precipitation strengthened alloys, the microstructural parameters of precipitates and thus the back stress exerted by the dislocation climb process are the key factor for the creep properties of alloys. Therefore, the microstructural characterisation of HP40 alloys is important for understanding the creep and improving resistance to it.

2.4.5 Creep behaviour of HP40

The creep behaviour of HP40 austenitic stainless steel has been investigated from different aspects, both practically and theoretically. Whittaker et al. [131] compared the creep rupture properties of HK40 and HP40 based on an analysis of the National Institute for Materials Science (NIMS) data sheets which records the creep rupture strength, the creep ductility and the reduction in area at fracture. From Figure 2.52, the creep rupture strength of HP40 is greater than that of HK40. For example, at 1000 °C, the 100000 hours creep rupture strength of HK40 is 3.5 MPa while that of HP40 is 6.9 MPa. The creep ductility of HK40 decreases to around 5 % as the applied stress decreases at temperatures approaching 1000 °C, whereas that of HP40 is fairly constant at around 15% (Figure 2.53).

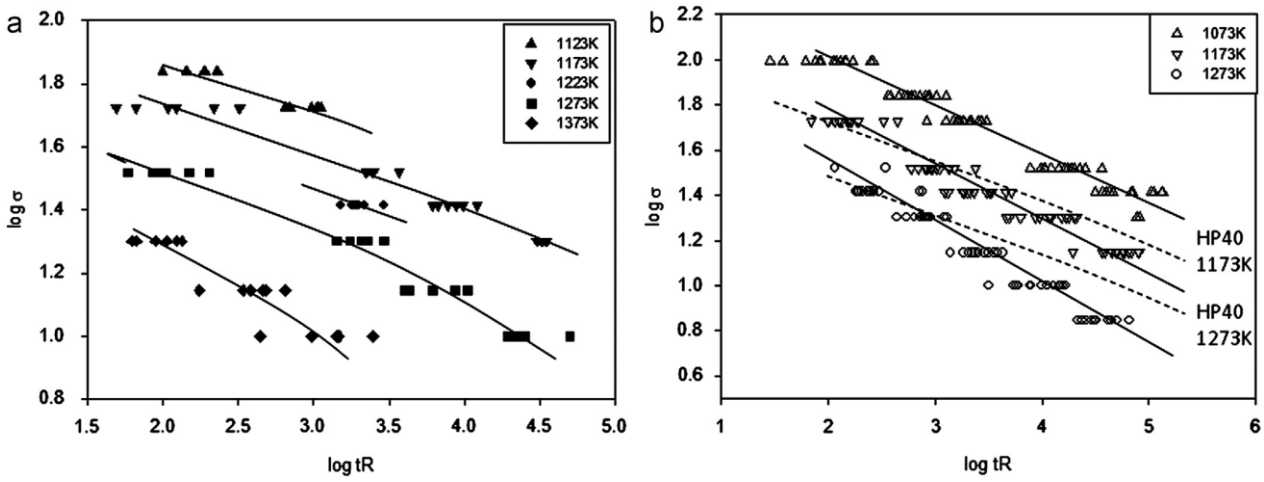

Figure 2.52 The creep rupture stresses of (a) HK40 and (b) HP40 at different temperatures [131]

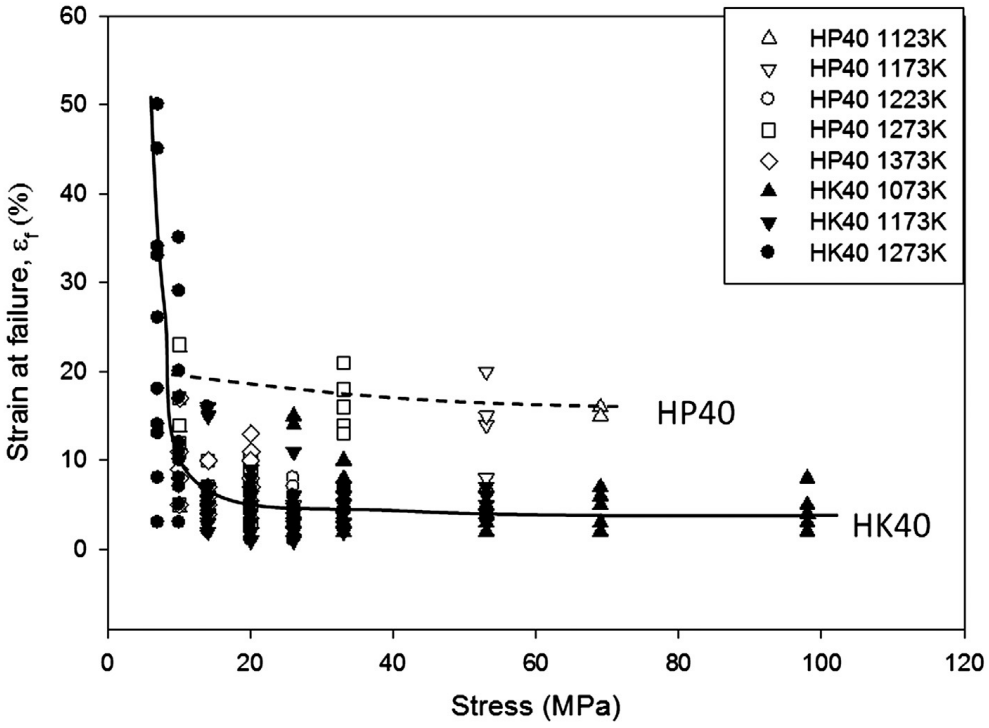

Figure 2.53 The creep ductility (%) of HK40 and HP40 at various temperatures and stresses [131]

However, the National Institute for Materials Science (NIMS) data sheets do not include properties such as the minimum creep rate and the times to various creep strains (creep curves). Nowak et al. [17] has undertaken creep tests in air on as-cast HP40 austenitic stainless steel at temperatures of 880, 900 and 950 ^{o}C to obtain the minimum creep rate and creep curve analysis. From Figure 2.54, the creep curves were found to consist of a relatively short primary stage leading to a minimum strain rate and then an extended tertiary stage. There was no convincing evidence of a period of steady-state creep (Figure 2.55). The best-fit lines for the Norton equation through the experimental data are shown in Figure 2.56 and the corresponding values of stress exponent n were found to be 9.6 at both 880 and 900 ^{o}C while a higher value of 11.5 was found at 950 ^{o}C.

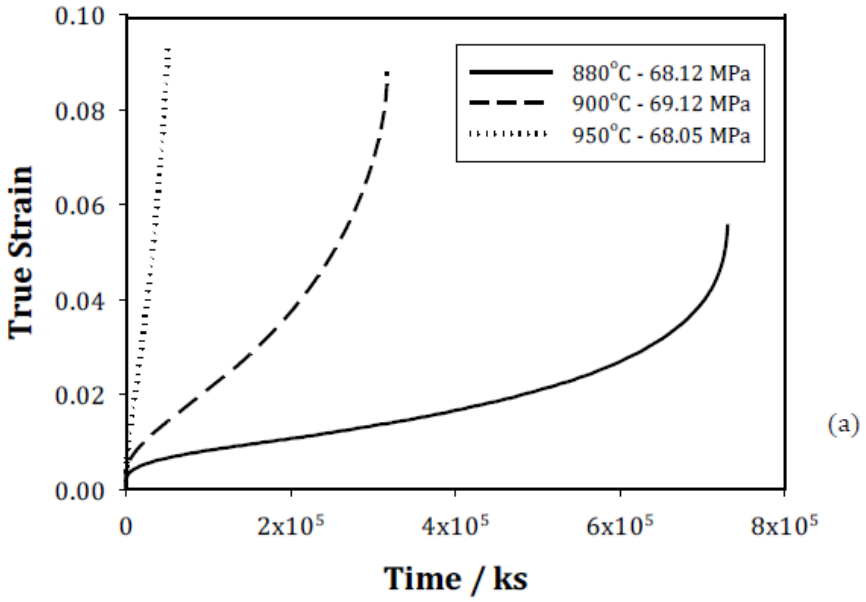

Figure 2.54 Creep curves of the constant stress creep tests at 880, 900 and 950 °C for HP40 [17]

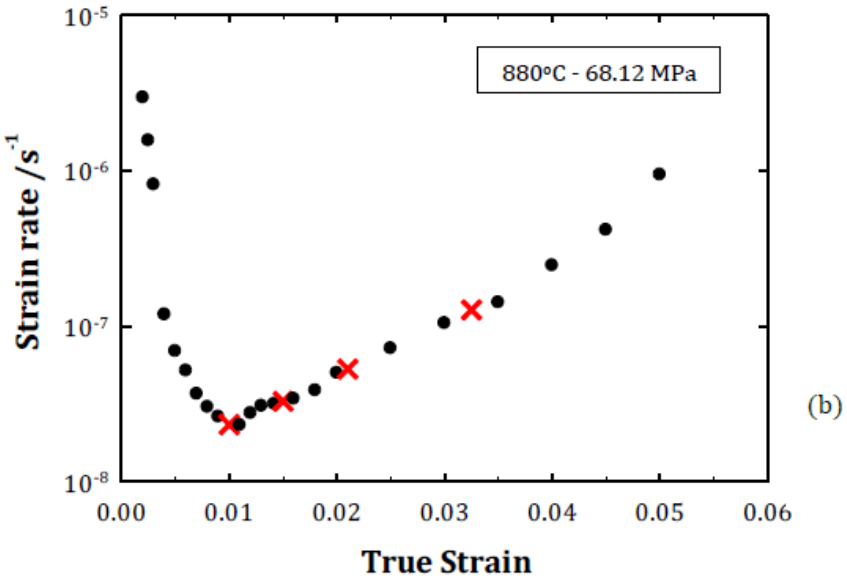

Figure 2.55 The strain rate-strain curve obtained from the creep test at 880 °C and 68.12 MPa for HP40 [17]

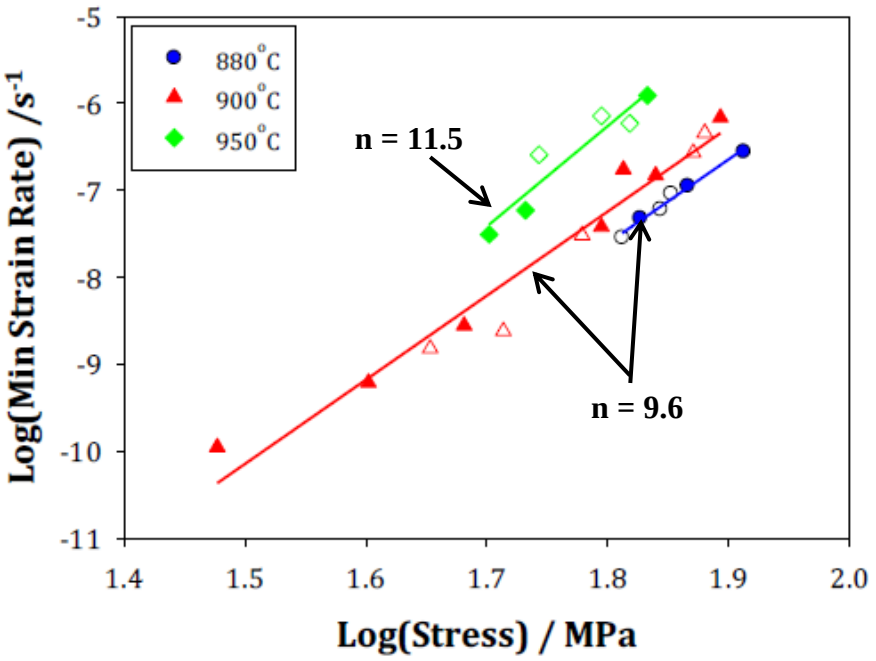

Figure 2.56 The dependence of minimum creep rate on the applied stress at 880, 900 and 950 °C [17]

In this PhD project, three different types of HP40 austenitic stainless steels, which are named as Alloy A, Alloy B and Alloy C, were supplied by Doncasters Paralloy Ltd. Creep experiments for each alloy had previously been carried out using an ATS Paralloy creep machine at a temperature of 1000˚C and stress of 40MPa by Nowak. Creep curves, as well as strain rate-strain curves were obtained and are presented in Figure 2.57 and Figure 2.58, respectively. For all three alloys, the creep curves are similar and consist of the primary and tertiary stages but with no substantial steady-state stages. Immediately after the primary creep stage the tertiary creep stage begins at t_m as shown in Figure 2.58. In this case, the minimum creep rate instead of the steady-stage creep rate is used, which can be explained as a process where hardening in the primary stage is balanced by softening in the tertiary stage. The creep properties for the HP40 alloys studied in this study are summarized in Table 2.8.

Table 2.8 Creep properties for HP40 alloys in this study

Specimen	Alloy A	Alloy B	Alloy C
Minimum creep rate / s^{-1}	4.50×10^{-8}	2.45×10^{-8}	2.40×10^{-8}
Creep life / hour	104	124	154
t_m / hour	12	14	13

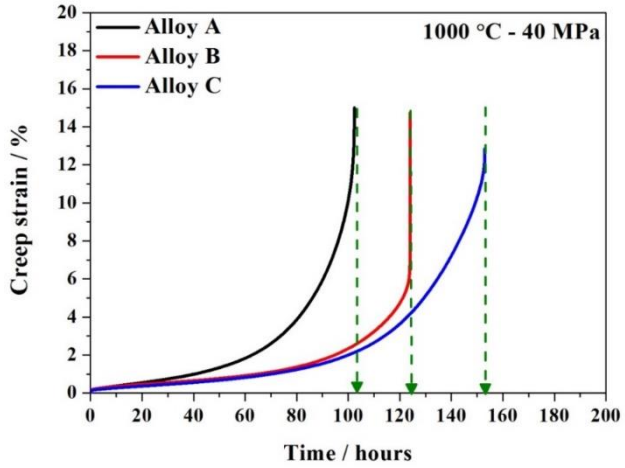

Figure 2.57 The creep curve for the alloys under constant stress at 1000˚C and 40MPa

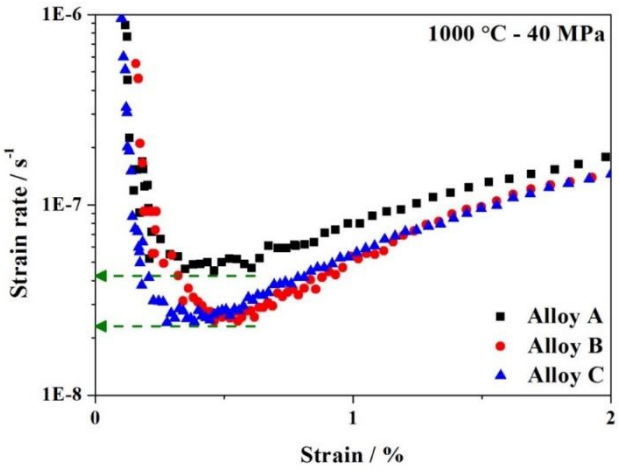

Figure 2.58 The strain rate-strain curves obtained from the creep test at 1000 ºC and 40 MPa

Chapter 3 Materials and experimental procedure

3.1 Materials

The HP40 austenitic stainless steels investigated in this PhD project were produced by Doncasters Paralloy Ltd. via a centrifugal casting process. In this process, molten metal is heated to around 1600°C and then poured into a horizontally spinning mould which is machined from a carbon steel billet, as shown in Figure 2.25. The inner diameter of the mould controls the outer diameter of the tube and the inside surface of the mould is coated with a refractory to prevent the molten metal fusing into the mould. Furthermore, by changing the refractory composition, the desired solidification rate of the molten metal can be controlled. The mould is spun to produce a centrifugal force between 80 to 100 times gravity, which will distribute the liquid metal uniformly over the entire inner surface of the mould. Residual refractory on the outside of the tube is removed by blasting with stainless steel shot and the unsound shrinkage porosity existing on the inside surface is removed by deep hole boring. The tubes commercially sold by Paralloy typically consist of a combination of columnar and equiaxed grains (Figure 3.1). The columnar to equiaxed depth ratio is often driven by specifications and varies with customer preferences.

Three as-cast HP40 steels, named Alloy A, Alloy B and Alloy C, were supplied by Doncasters Paralloy Ltd. The chemical compositions of the alloys were measured by the supplier using the optical emission spectrometry (OES) and are shown in Table 3.1 in both weight percent and atomic percent.

The Alloy A represents the typical HP40 steel while Alloy B has been chemically modified, for example by adding tungsten and increasing niobium content. The solidification rates of Alloy A and Alloy B were controlled to be the same, then the main reason of the microstructural difference between Alloy A and Alloy B is due to their chemical composition difference. Furthermore, to find out the effect of solidification rate on the microstructure of HP40, another type alloy, Alloy C, was produced. The chemical compositions of Alloys B and C fell into the same HP40 modified alloy range while the solidification rate of Alloy B was lower than that of Alloy C.

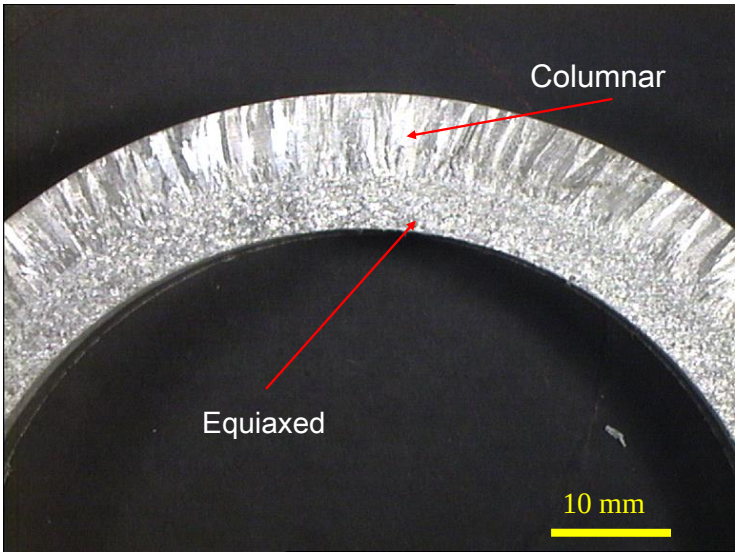

Figure 3.1 Macrostructure of a centrifugally cast HP40 tube consisting of about 50% columnar and 50% equiaxed grains [17]

Table 3.1 The chemical compositions of the as-cast Alloys A, B and C

Element / Specimen		C	N	Si	Mn	Ni	Cr	Mo	Nb	W	Ti	Zr	Fe
Alloy A	wt %	0.46	0.08	1.42	1.01	35.88	24.25	0.05	0.97	0	0.05	0.02	35.81
	at %	2.08	0.29	2.74	1.00	33.13	25.27	0.03	0.57	0.00	0.06	0.01	34.82
Alloy B	wt %	0.41	0.11	0.97	0.74	34.74	24.66	0.01	1.11	0.05	0.05	0.03	37.12
	at %	1.86	0.43	1.88	0.73	32.26	25.85	0.01	0.65	0.03	0.06	0.02	36.22
Alloy C	wt %	0.41	0.10	0.92	0.75	36.12	23.49	0.02	1.39	0.05	0.05	0.01	36.69
	at %	1.86	0.39	1.79	0.74	33.66	24.71	0.01	0.82	0.01	0.06	0.01	35.94

Cross-sections from the as-cast tubes were cut and prepared for microstructural observation and further heat treatment (Figure 3.2). Cylindrical creep specimens with a gauge diameter of 6 mm and gauge length of 31.75 mm were machined from the columnar region of the wall (3 mm from outside diameter) of an as-cast tube with the stress axis parallel to the tube axis (Figure 3.3). Creep tests were carried out at 1000 ˚C and 40 MPa on Alloy A for 12 hours, Alloy B for 14 hours and Alloy C for 13 hours which times correspond to the minimum strain rates (c.f. Figure 2.56). After the creep tests, the creep specimens were cut into two halves; the heads of the cut creep specimen were used for further microstructural observation. All the microstructural observations of as-cast, heat treated and crept specimens were carried out at the 3 mm from the outside diameter of tubs (Figure 3.2 (b)).

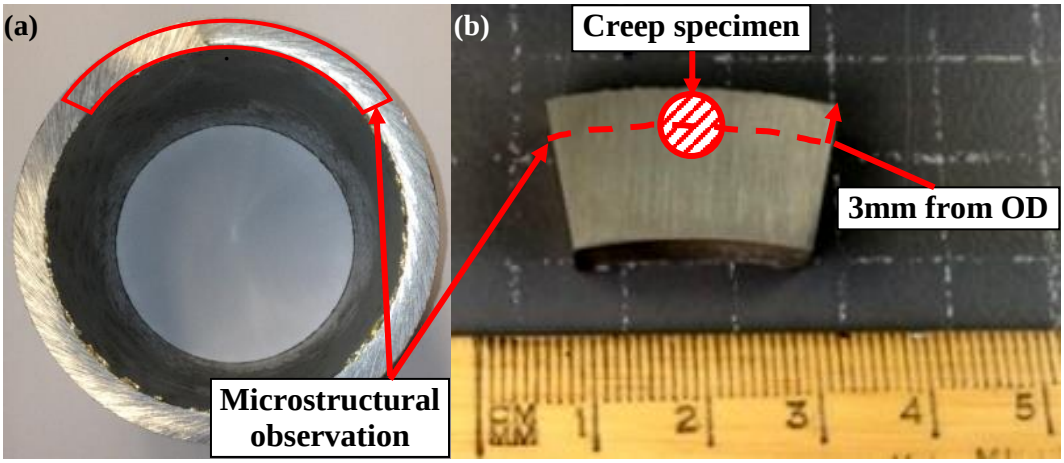

Figure 3.2 (a) and (b) Schematic diagrams of the cross-section through an as-cast cast tube for microstructural observation

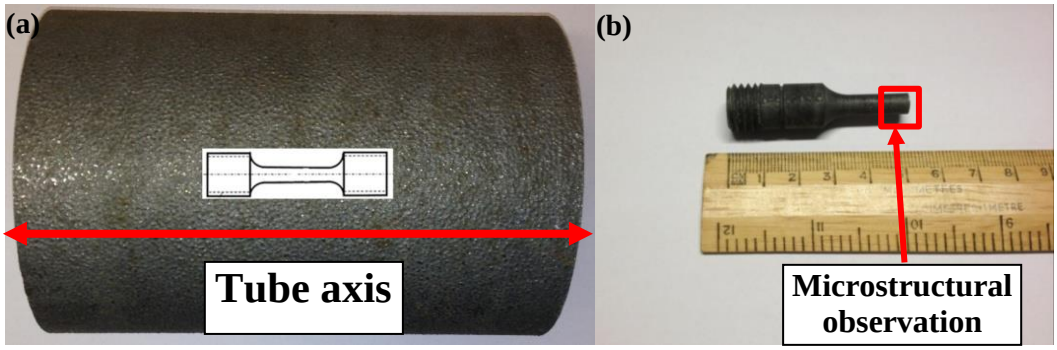

Figure 3.3 (a) and (b) Schematic diagrams of the creep specimens obtained from as-cast cast tubes

3.2 Heat treatment

In order to determine the effect of stress on microstructural evolution, Alloy A kept 12 hours at 1000 ºC without stress was compared with crept Alloy A (i.e. with stress). The specimens for heat treatment were put into a muffle furnace in air and heated up to 1000˚C at 5 ºC/min. After holding for 12 hours, the specimens were cooled down in the furnace to mimic creep tests.

For Alloys B and C, heat treatments at 1000 ºC for 1 to 150 hours were used to understand the microstructural evolution during long-term service. After holding for the designated period time, the specimens were quenched into water. The detailed heat treatment process is shown in Figure 3.4 and the specimens are listed in Table 3.2. For example, HT-10 indicates that the specimen was hold at 1000 ºC for 10 hours.

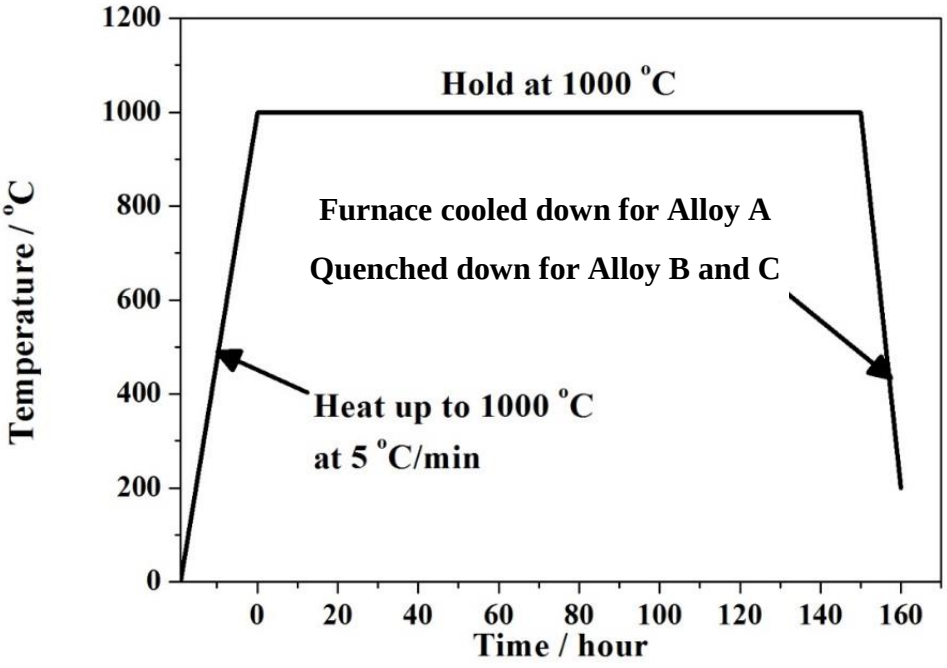

Figure 3.4 Schematic figure for heat treatment process (150 hours in this case)

Table 3.2 List of heat treatment specimens

Specimen		Heat treatment condition		
		Time / hours	Temperature / ºC	Cool down method
Alloy A	HT-12	12	1000	Furnace cooled
Alloy B & Alloy C	HT-1	1	1000	Quenched
	HT-2	2	1000	Quenched
	HT-5	5	1000	Quenched
	HT-10	10	1000	Quenched
	HT-20	20	1000	Quenched
	HT-30	30	1000	Quenched
	HT-40	40	1000	Quenched
	HT-50	50	1000	Quenched
	HT-100	100	1000	Quenched
	HT-150	150	1000	Quenched

3.3 Metallurgical observations

The specimens were firstly mounted in bakelite with an EZ-mat Opal 400 hot mounting machine. The specimens were mechanically ground using SiC papers up to #2500 on a Struers Labopol-5. The specimens were then polished on the same machine using an MD Mol cloth (Struers Ltd.) with a 3 μm liquid diamond suspension (Kemet Ltd.). An MD Nap polishing cloth (Struers Ltd.) with 1 μm liquid diamond suspension (Metprep Ltd.) was then used. The final polishing used an MD Chem polishing cloth with 0.25 μm diamond compound (Metprep Ltd.). The specimens were ultrasonically rinsed in ethanol and dried in cool air.

3.4 Optical microscopy

An optical microscope was used to obtain the macrostructure of the alloys. The specimens were firstly etched in a water-based solution containing 40% hydrochloric acid (HCl) and 40% nitric acid (HNO_3). Optical observations were conducted on a Zeiss Axioskop 2 optical microscope using Axio vision image capture and analysis software.

3.5 Scanning electron microscopy

Scanning electron microscopes (SEM) equipped with Energy Dispersive X-ray (EDX) detectors were used for microstructural observation and chemical analysis of the alloys. In this study, two field emission gun SEMs: JEOL JSM-7000F SEM and TESCAN MIRA3, were employed for the microstructure observation. The EDX detector on the JSM-7000F SEM is a Si-Li detector operated with INCA software while that on the TESCAN MIRA3 is a new generation silicon drift detector (SDD) with AZtecEnergy software. Generally, the microstructural characterization was performed at an operating voltage of 20 keV. The chemical analysis using EDX, including spot analysis, line scans and maps also were carried out at 20keV. All microstructural observations were made in areas approximately three millimetres from the outside diameter (OD) of the tubes.

3.6 Transmission electron microscopy

For preparation of TEM samples, thin slices of about 1 mm in thickness were cut from bulk samples using a Struers Accutom 5 cutting machine with a SiC blade. TEM discs 3 mm in diameter were punched from these thin slices and manually ground to 150 ~ 180 μm thick using the #800 SiC grinding paper. The foils were prepared by twin-jet electro-polishing (Struers TenuPol-3) using a solution of 20% perchloric acid and 80% methanol at 0 °C. Transmission electron microscope (TEM) examination was performed on a JEOL-2100HT TEM operating at 200 kV to obtain bright field (BF) images, dark field (DF) images and diffraction patterns. Furthermore, scanning transmission electron microscopy (STEM) using high angle annular dark field (HAADF) imaging was performed on a Philips Tecnai F20 equipped with an Oxford Instruments X-Max 80 silicon drift detector for chemical analysis.

3.7 Focused ion beam scanning electron microscope

A focused ion beam scanning electron microscope (FIB/SEM, FEI Quanta 3D FEG) equipped with a focused gallium ion beam and a conventional field-emission gun electron beam was used to prepare TEM specimens at specific positions where specimens would be difficult to produce via twin jet polishing, for example a particular precipitate or grain boundary. Firstly, the area of interest was coated with tungsten in order to protect it from ion milling. Then, the specific area was thinned to 1 μm using the ion beam at 30 kV with the beam current gradually decreased from 65 nA down to 5 nA. This thin slice was cut off and mounted on an Omniprobe (tungsten needle), followed by welding onto a copper grid. Finally, this slice was ion beam thinned to around 200 nm and cleaned at a very low beam current.

3.8 X-ray diffraction

X-ray diffraction (XRD) was carried out on a Philips D62-WSC X-ray diffractometer operating at 40 kV and 40 mA. X-ray diffraction (XRD) spectra were recorded in the 2θ range of 20-100° with a step rate of 1°/second using Cu-K_α radiation (λ=1.541Å) for phase determination purposes. The peak matching was performed using XPert software equipped with the database of the Joint Committee for Powder Diffraction Standards (JCPDS).

3.9 Differential scanning calorimetry

Thermal analysis was performed using differential scanning calorimetry (DSC) in a Netzsch STA-449F3 Jupiter equipped with Proteus software. The DSC experiments were conducted under a static atmosphere of nitrogen of 99.99 vol.% purity to prevent both the de-nitrogenation of the steel and to minimize the surface oxidation. The empty corundum crucible was used as a reference. The specimens were also cut from areas approximately three millimetres from the outside diameter (OD) of the tubes; the samples weighed 50~80 mg. The detailed DSC process for dynamic measurements is shown in Figure 3.5 and two cooling rates, 10 °C/min and 100 °C/min, were used. The DSC process in Figure 3.5 is chosen to simulate the solidification process during centrifugal casting with different solidification rates.

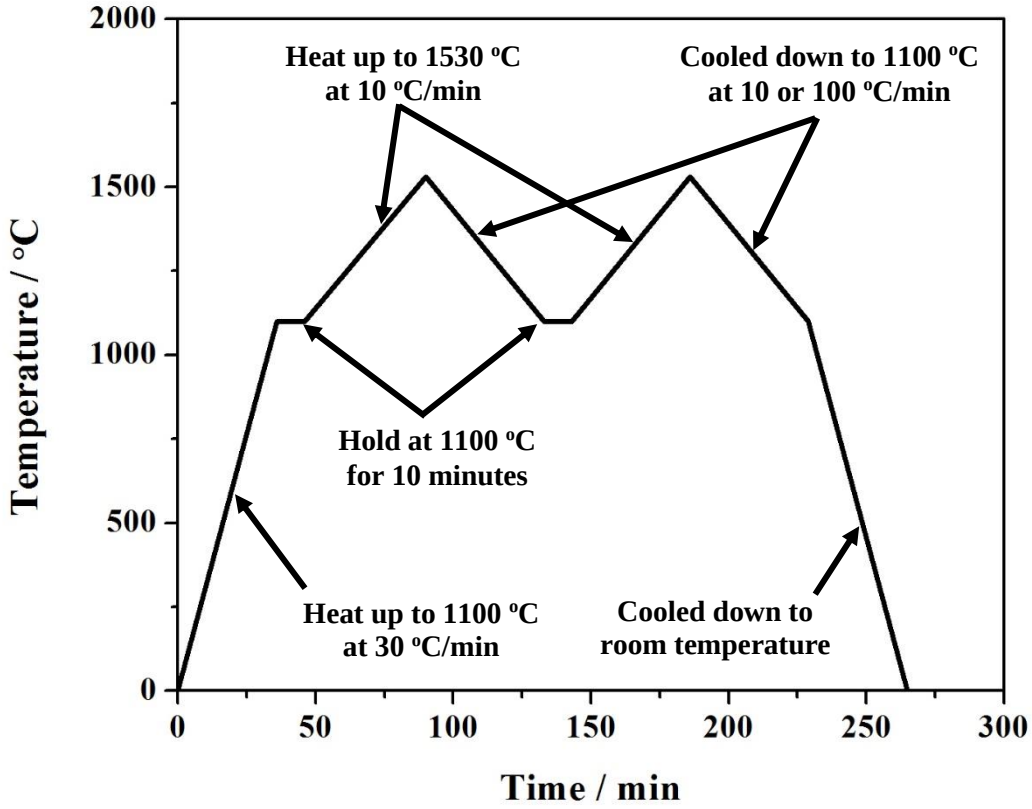

Figure 3.5 Schematic figure for DSC tests

3.10 Thermodynamic calculation

JMat Pro 6.2, commercial software utilizing core minimization routines developed for the PMLFKT program [132], was used for the thermodynamic calculations for the alloys following the CALPHAD method (CALculation of PHAse Diagrams). The CALPHAD method provides a consistent description of the phase diagram and the thermodynamic properties so as to reliably predict the set of stable phases and their thermodynamic properties in regions without experimental information during simulations of phase transformations [133]. In this study, the TCNI7 database was selected.

3.11 Microstructural parameter measurement

The microstructural parameters of the precipitates, like their area fraction, interspacing and size, were measured in this study. The area fractions of precipitates in the as-cast, heat treated and crept specimens were evaluated using ImageJ software. Ten measurements for each specimen were obtained.

When the precipitates are of non-spherical form, such as the $M_{23}C_6$, various measurement methods have been reported. Aghajani et al. [134] and Prat et al. [135] defined the precipitate size as the average value of the two perpendicular axes across the particle. However, Qin et al. [136] determined the size of the precipitates by drawing the circumference of each precipitate by hand and automatically determining the corresponding diameter of a circle of equal area via ImageJ. According to Zhu et al. [122], the average precipitate sizes measured by these two methods are close, but both smaller than the Feret's diameter.

In this study, the interspacing and precipitate size measurements were carried following Aghajani's method (see Figure 3.6):

Firstly, fifty TEM bright field images were taken from each specimen at a magnification of 6000. The area of each image, A, was 1824 × 1824 nm^2. The number of precipitates, n, in each image was recorded: for example in Figure 3.6 n is 5. The interspacing λ_p was calculated following equations 3.1 and 3.2:

$\lambda_{p,i} = \sqrt{A/n}$ --- Equation 3.1

$\lambda_p = \frac{1}{m}\sum_{i=1}^{m} \lambda_{p,i}\,, m = 50$ --- Equation 3.2

For precipitate size, two perpendicular sizes d_1 and d_2 through each precipitate, were measured. Five hundred precipitates were analysed in each condition and the average precipitate size was calculated using equations 3.3 and 3.4.

$d_{p,i} = (d_{1,i} + d_{2,i})/2$ --- Equation 3.3

$d_p = \frac{1}{m}\sum_{i=1}^{m} d_{p,i}, m = 500$ --- Equation 3.4

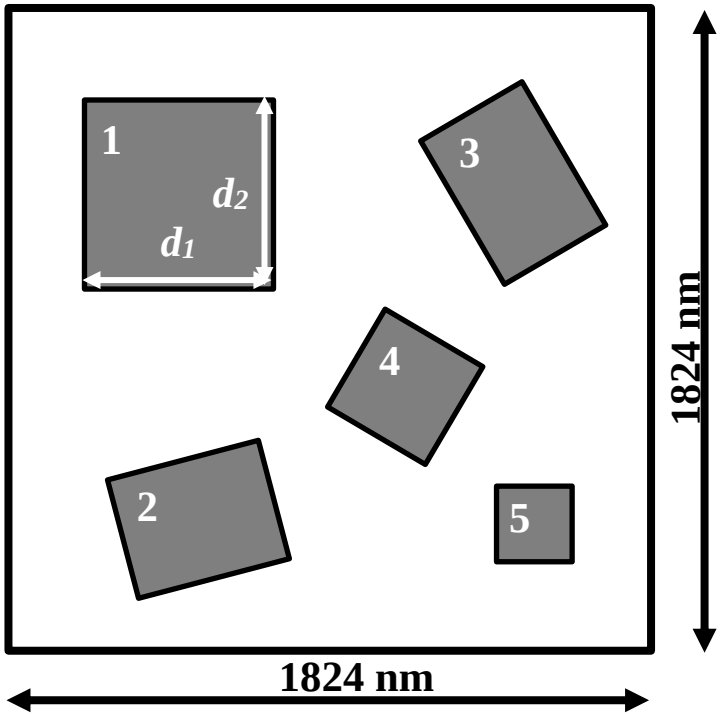

Figure 3.6 Schematic figure illustrating the measurement of the microstructural parameters --- precipitate interspacing and size

3.12 Foil thickness measurement

To quantify accurately the extent of interfacial segregation from the measured data in accounting for the effect of beam spreading, it is necessary to measure the foil thickness, *t*. Many techniques are available. The most accurate measurements are obtained using convergent beam electron diffraction (CBED).

The technique makes use of the intensity oscillations present in convergent beam patterns. An equation from the two-beam dynamical theory of electron diffraction, which shows the relation between ξ_g, t and the positions of the minima in intensity oscillations in the diffraction disc is as follows:

$$\left(\frac{s_i}{n_i}\right)^2 + \left(\frac{1}{n_i}\right)^2 \left(\frac{1}{\xi_g}\right)^2 = \frac{1}{t^2}$$ --- Equation 3.5

where S_i is the deviation parameter of the minimum for the reflection *g*. S_i can be measured directly from the spacing of the fringes in the convergent beam pattern and n_i is the number of the fringes counting outwards from the mid-line. ξ_g is the extinction distance for the reflection. The values of S_i can be determined by:

$$S_i = \frac{\lambda}{d^2}\left(\frac{\Delta\theta_i}{2\theta_d}\right)$$ --- Equation 3.6

where *d* is the plane spacing of the operating reflection and λ is the electron wavelength (200 kV). $\Delta\theta_i$ is the distance to the chosen minimum from the mid-line and $2\theta_d$ is the distance from the bright field disc to the diffracted disc. Plotting $(S_i/n_i)^2$ versus $(1/n_i)^2$, the foil thickness is given by the intercept of the resulting straight line with the $(S_i/n_i)^2$ axis if n gives a straight line. The method described above to determine the foil thickness is illustrated in Figure 3.7

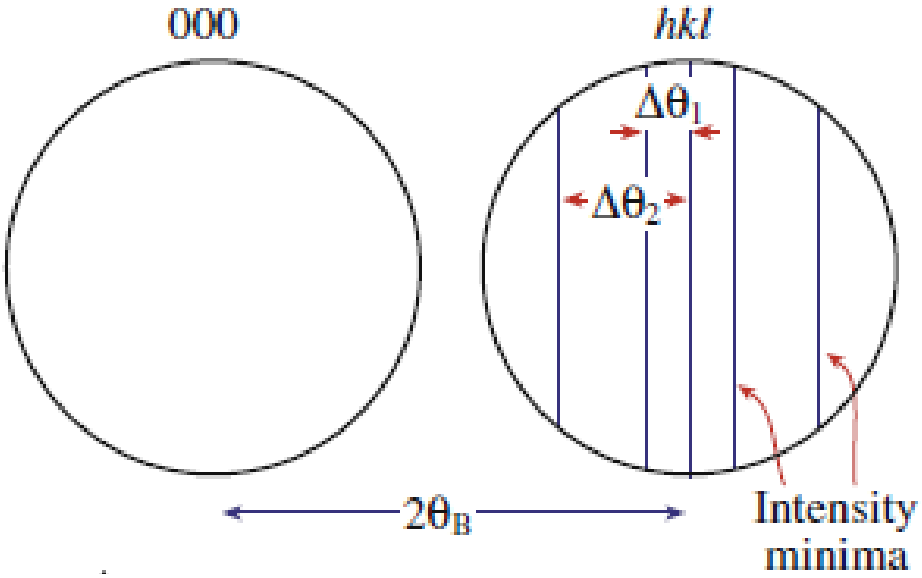

(a)

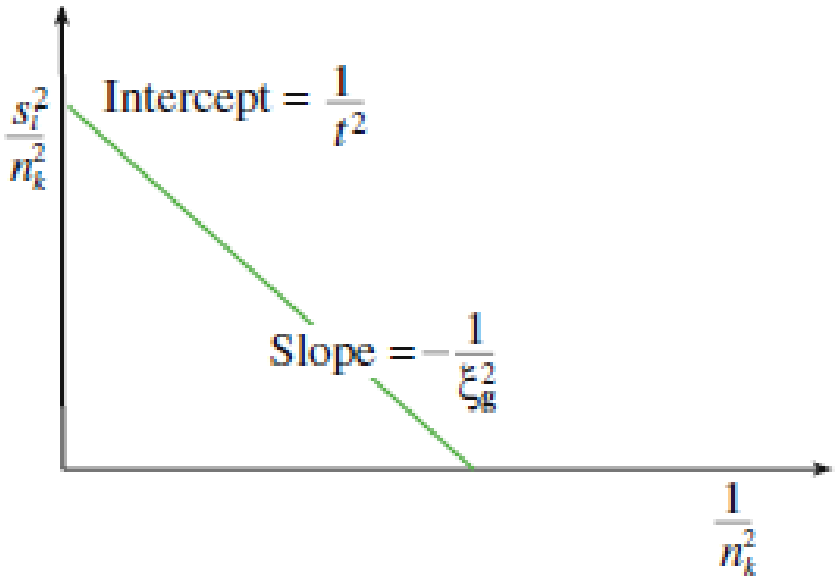

(b)

Figure 3.7 Schematic drawing showing the foil thickness measurement using a two-beam condition convergent beam electron diffraction (CBED) pattern: (a) the measurements necessary to extract thickness (t) from K-M fringes. From n_i measure spacing of $\Delta\theta_i$ determine the deviation parameters S then (b) plot $(S_i/n_i)^2$ against $(1/n_i)^2$ [137]

Chapter 4 Microstructural characterisation of HP40 (Alloy A)

4.1 Microstructure of as-cast Alloy A

A cross section through the Alloy A as-cast tube wall is shown in Figure 4.1. The macrostructure consists of a combination of columnar and equiaxed grains. The tube wall thickness is 13 mm, while the columnar grain region is 10 mm across and the equiaxed grain region is 3 mm. The columnar to equiaxed depth ratio (~ 3:1) is typical of commercial HP40 tubes produced by Paralloy Ltd.

However, the creep specimen of Alloy A was cut from a different tube with the one where as-cast and heat treated Alloy A were cut. Since these two tubes share the same chemical composition and solification rate, all the microstructural observations carried out in as-cast and heat treated Alloy A (3 mm from the outside diameter of tubs) can be compared with the microstrcuture of the central region of creep specimens.

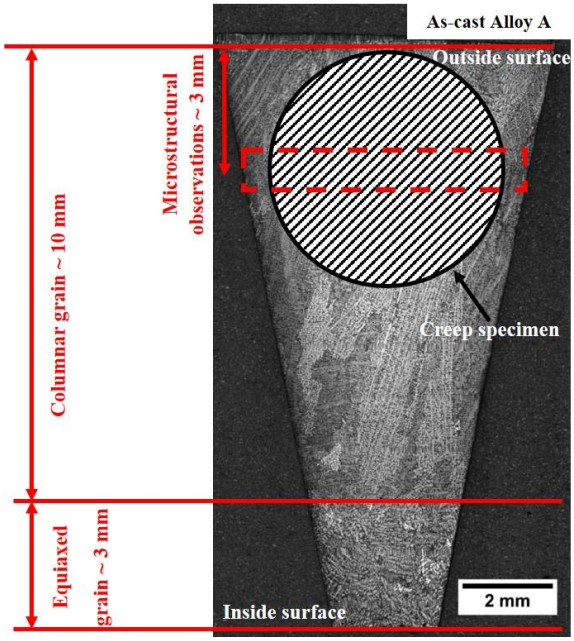

Figure 4.1 Optical image illustrating the macrostructure of as-cast Alloy A tube; There are 75% columnar and 25% equiaxed grains over the wall thickness

Figure 4.2 shows, at higher magnifications, the microstructure of as-cast Alloy A obtained by BSE. Austenitic matrix is surrounded by dark and bright precipitates which form a fragmented network. The dark precipitates are of mixed granular and acicular shapes, which is described as eutectic or 'Chinese-script' structure (Figure 4.3). Most of the bright precipitates have a rod-like morphology (Figure 4.4). From the EDS results (Table 4.1), the precipitates in bright contrast correspond to primary Nb-carbides while the dark precipitates correspond to primary Cr-carbides. Furthermore, almost all the Nb is confined to the primary carbide network, whereas Si and Fe remain in solid solution in the Ni-rich matrix. Cr appears both to be dissolved in the matrix and to form part of the primary carbides. However, as shown in Table 2.3, austenitic stainless steel can contain different kinds of precipitates. XRD analysis confirms that the Cr- and Nb-carbides are M_7C_3 and MC, respectively (Figure 4.5). Furthermore, some NbC carbides were observed within the eutectic structure as shown in Figure 4.3. The area fractions of primary Cr-carbide and primary Nb-carbide are also measured and listed in Table 4.2: 3.89 % for M_7C_3 and 1.40 % for NbC.

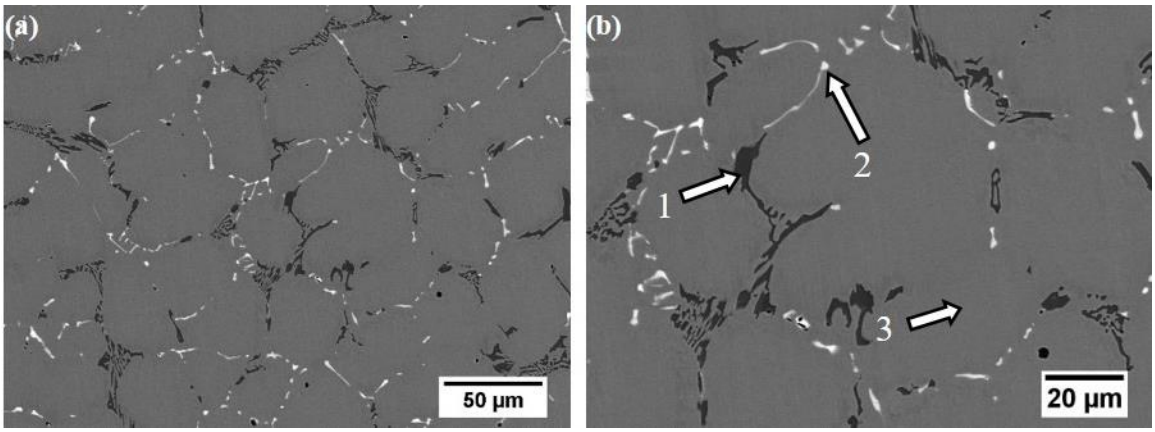

Figure 4.2 (a) Low magnification and (b) high magnification BSE images obtained from as-cast Alloy A

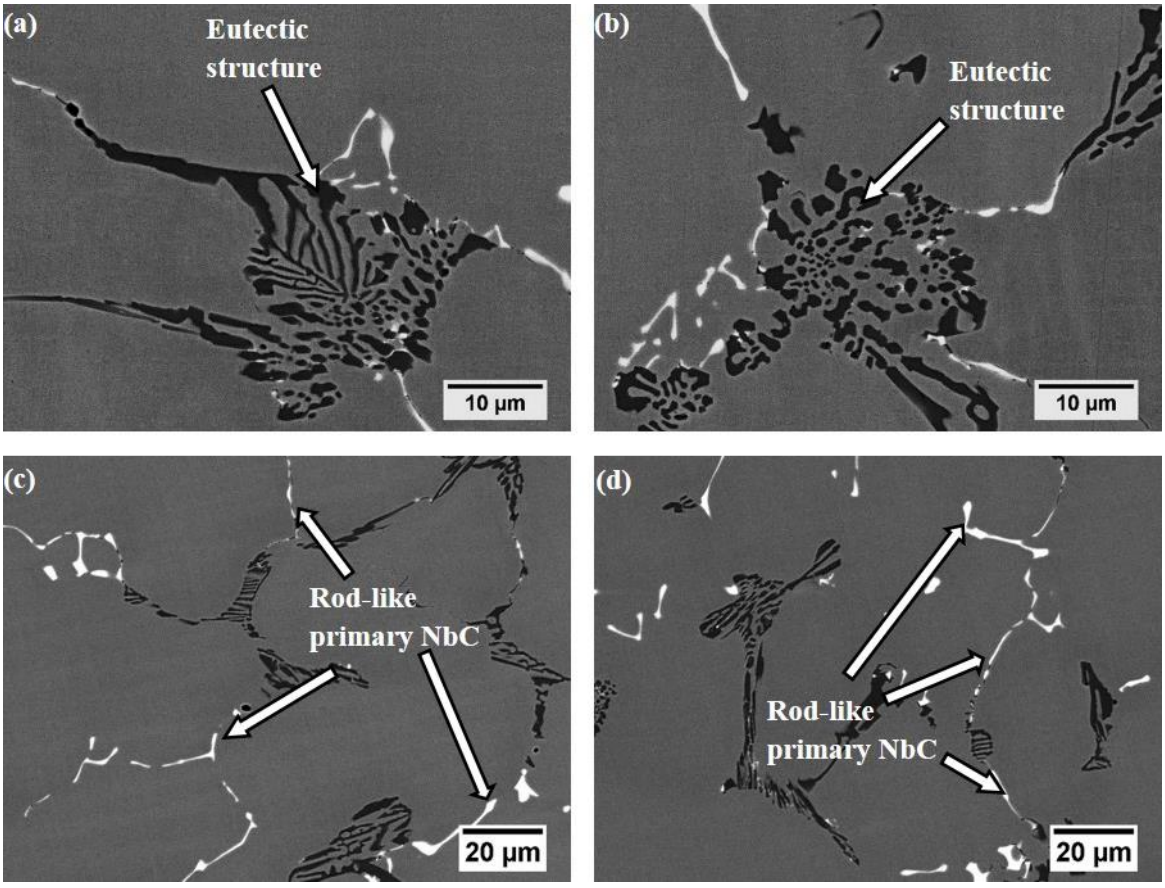

Figure 4.3 BSE images of as-cast Alloy A illustrating (a) and (b) eutectic or "Chinese script" structure between austenite and M7C3; (c) and (d) rod-like primary NbC

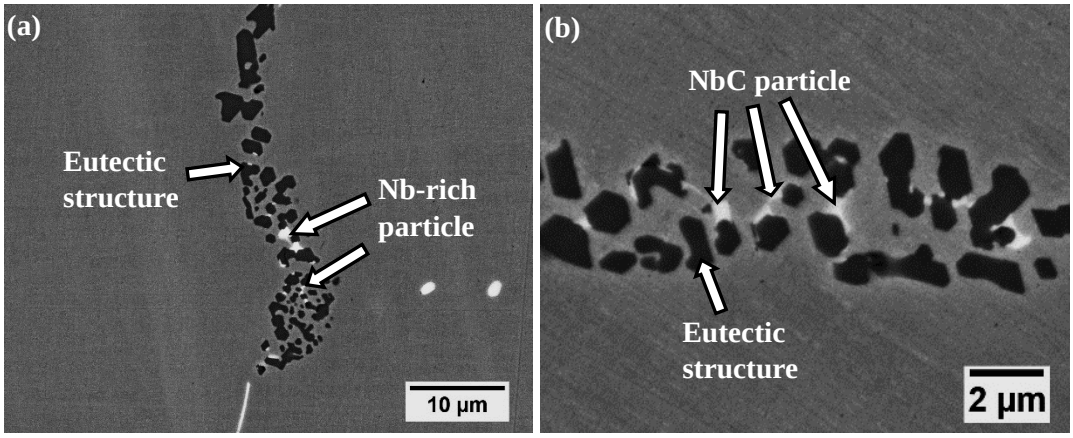

Figure 4.4 (a) Low magnification and (b) high magnification BSE images of as-cast Alloy A illustrating NbC carbides observed within the eutectic $\gamma + M_7C_3$

Table 4.1 EDS analyses obtained from the points shown in Figure 4.2 (b)

Points	Atomic %						
	C	Si	Cr	Fe	Ni	Mn	Nb
1	31.85±0.72	---	59.63±1.13	7.30±0.68	1.21±0.22	0.59±0.02	---
2	41.73±0.81	---	9.56±1.33	3.46±0.52	2.67±0.14	0.22±0.02	42.36±0.33
3	6.99±0.67	2.12±0.54	22.41±1.04	35.77±0.43	31.94±0.20	0.78±0.02	---

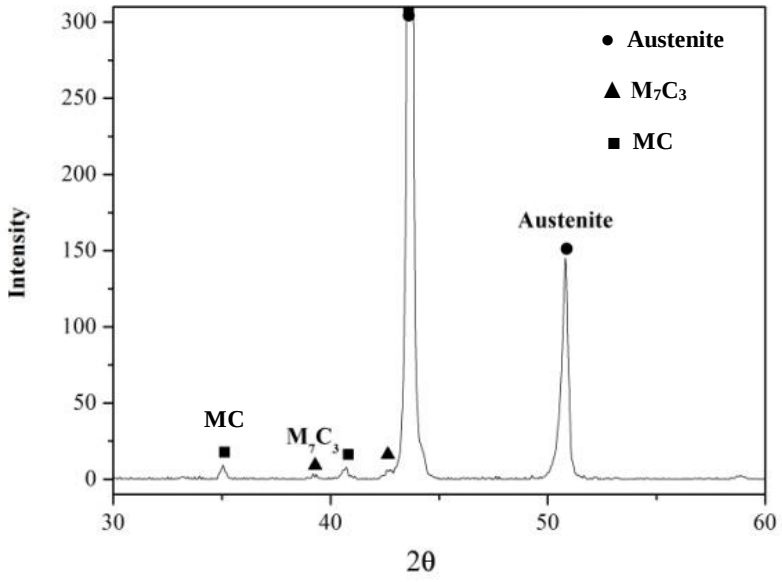

Figure 4.5 XRD spectrum obtained from as-cast Alloy A illustrating that the primary precipitates are M_7C_3 and MC

4.2 Microstructure of crept Alloy A

After creep at 1000 ˚C and 40 MPa for 12 hours as described in Section 3.1. The microstructure of crept Alloy A is illustrated in Figure 4.6 (a). After creep, the morphology of the primary precipitates shows no significant difference. The area fraction of primary Cr-carbides increased from 3.89 % to 5.25 % during creep whilst that of the primary Nb-carbides shows only a slight increase from 1.40 % to 1.60 % (Table 4.2). Furthermore, the XRD spectrum obtained from crept Alloy A shows peaks for NbC and $M_{23}C_6$, indicating the transformation of the primary Cr-carbides from M_7C_3 to $M_{23}C_6$ (Figure 4.6 (b)).

Notably, secondary precipitation can be observed within the matrix. The secondary precipitates result from the supersaturated solid solution of carbon and chromium in the austenite originally formed during non-equilibrium solidification. These secondary precipitates are cubic and the maximum size is below half a micron, making them difficult to analyse via SEM.

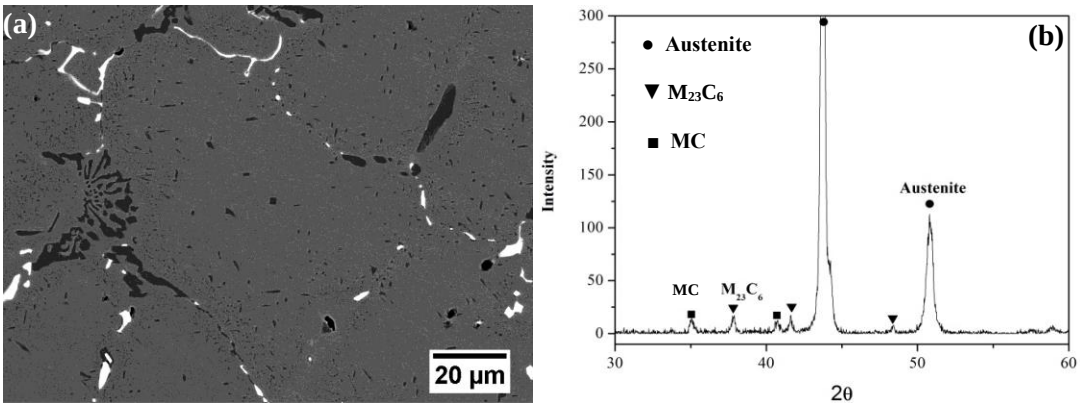

Figure 4.6 (a) BSE image and (b) XRD spectrum obtained from crept Alloy A

Table 4.2 Area fractions of various carbides in as-cast and crept Alloy A

Specimen	Area fraction%		
	Primary Cr-carbide	Secondary Cr-carbide	Primary Nb-carbide
As-cast Alloy A	3.89±0.17	---	1.40±0.07
Crept Alloy A	5.25±0.26	1.75±0.14	1.60±0.07

TEM was used to identify the secondary precipitates and measure the microstructural parameters. A specimen was cut using FIB/SEM. Figure 4.7 illustrates the TEM bright field image. There is a strip of primary Cr-carbides and fine cuboid secondary Cr-carbides. A higher magnification bright field (BF) image (Figure 4.7 (b)) shows secondary Cr-carbides. The selected area diffraction (SAD) pattern (Figure 4.7 (c)) obtained from the secondary Cr-carbide in Figure 4.7 (b) shows that it is $M_{23}C_6$ type with an orientation relationship $\{110\}_\gamma \parallel \{110\}_{M_{23}C_6}$ and $\langle 110\rangle_\gamma \parallel \langle 110\rangle_{M_{23}C_6}$. The primary Cr-carbide however does not show such a relationship with the matrix. Some finely sized intragranular particles, also observed in the matrix as shown in Figure 4.7 (d), are confirmed to be rich in Nb (Figure 4.10).

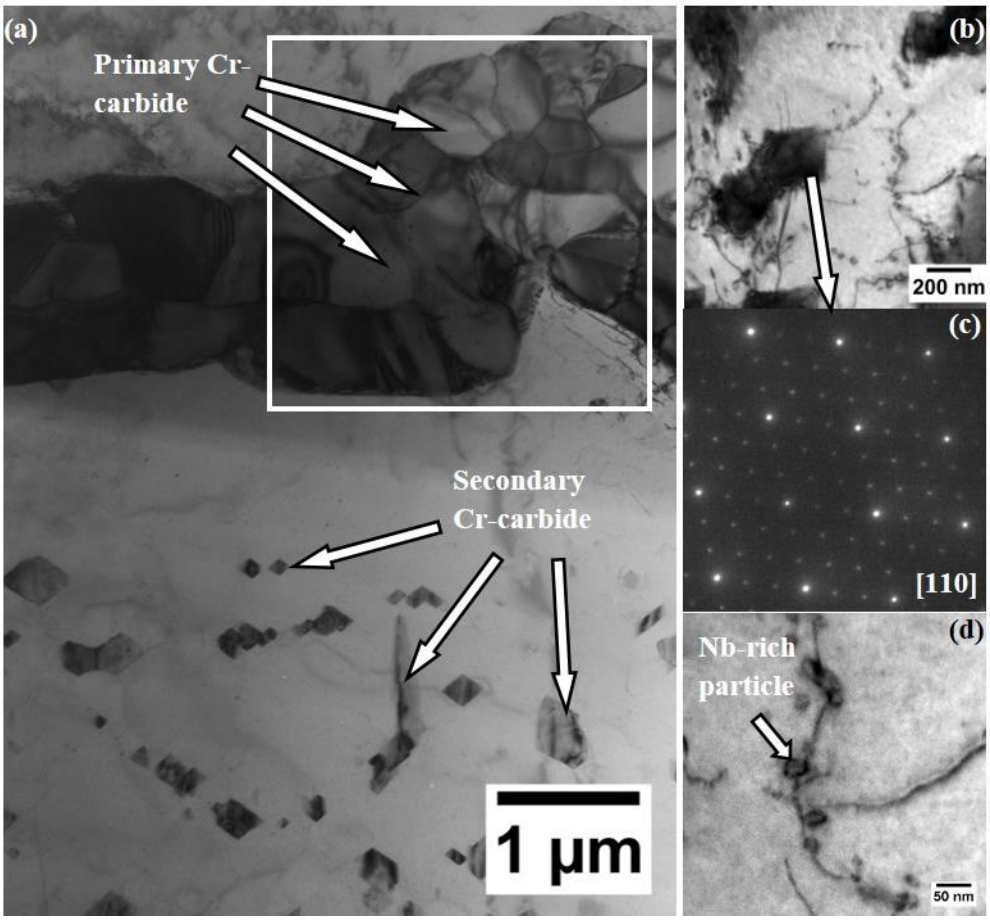

Figure 4.7 (a) TEM BF image obtained from crept Alloy A showing Cr-carbides (rectangle is investigated further in Figure 4.6); (b) BF image showing secondary Cr-carbides; (c) SAD pattern obtained from a secondary Cr-carbide in (b); (d) BF image of intragranular Nb-rich particle

Figure 4.8 (b)-(e) show TEM EDS maps of an area selected from Figure 4.7 including primary Cr-carbides. Besides the primary Cr-carbide, two different precipitates were found. Firstly, fine Nb-rich particles (Figure 4.8 (c) & (e)) were observed, not only at the interface between the primary Cr-carbide and the matrix (particle 1 in Figure 4.8 (e)), but also at the interfaces between the primary Cr-carbides (particle 2 in Figure 4.8 (e)). Meanwhile, Nb-Ni-Si particles are found to be associated with the primary Cr-carbide (Figure 4.8 (a), (d), (e) & (f)). The diffraction patterns in Figure 4.9 obtained from the Nb-Ni-Si particle (that labelled in Figure 4.8 (a)) indicate that the precipitate has an fcc structure with a lattice parameter of 1.13nm. This is G-phase ($Ni_{16}Nb_6Si_7$) which is fcc with a parameter 1.1~1.14 nm.

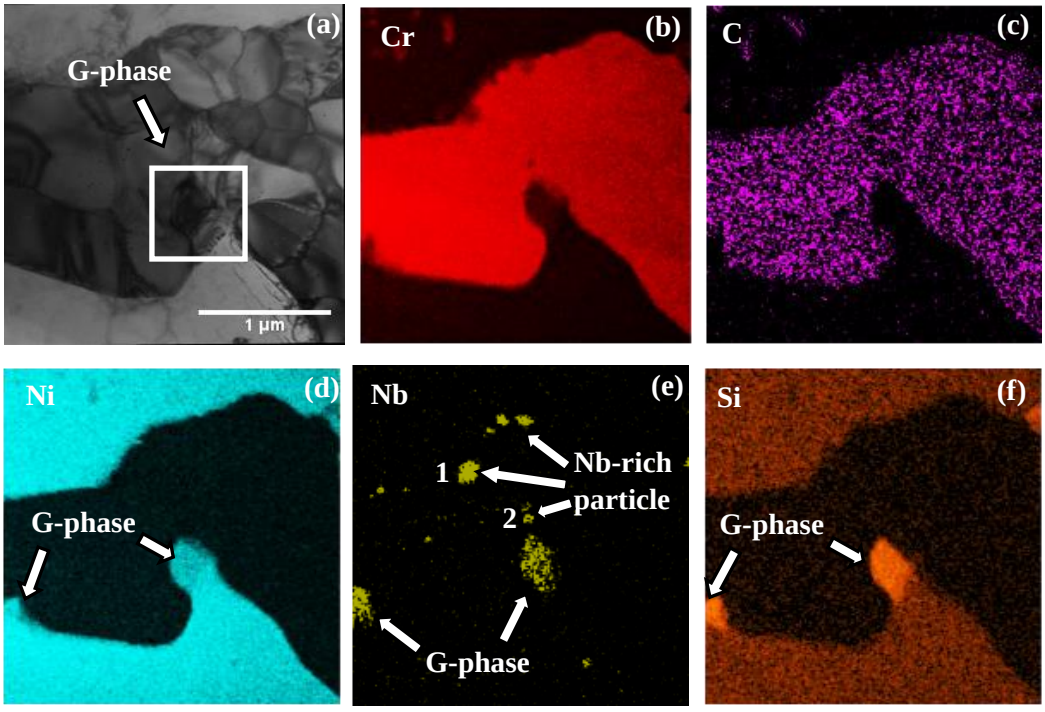

Figure 4.8 (a) BF image from rectangle outlined in Figure 4.7; (b)-(f) TEM-EDS maps of selected area illustrating the appearances of Nb-rich particle and Nb-Ni-Si precipitate (G-phase)

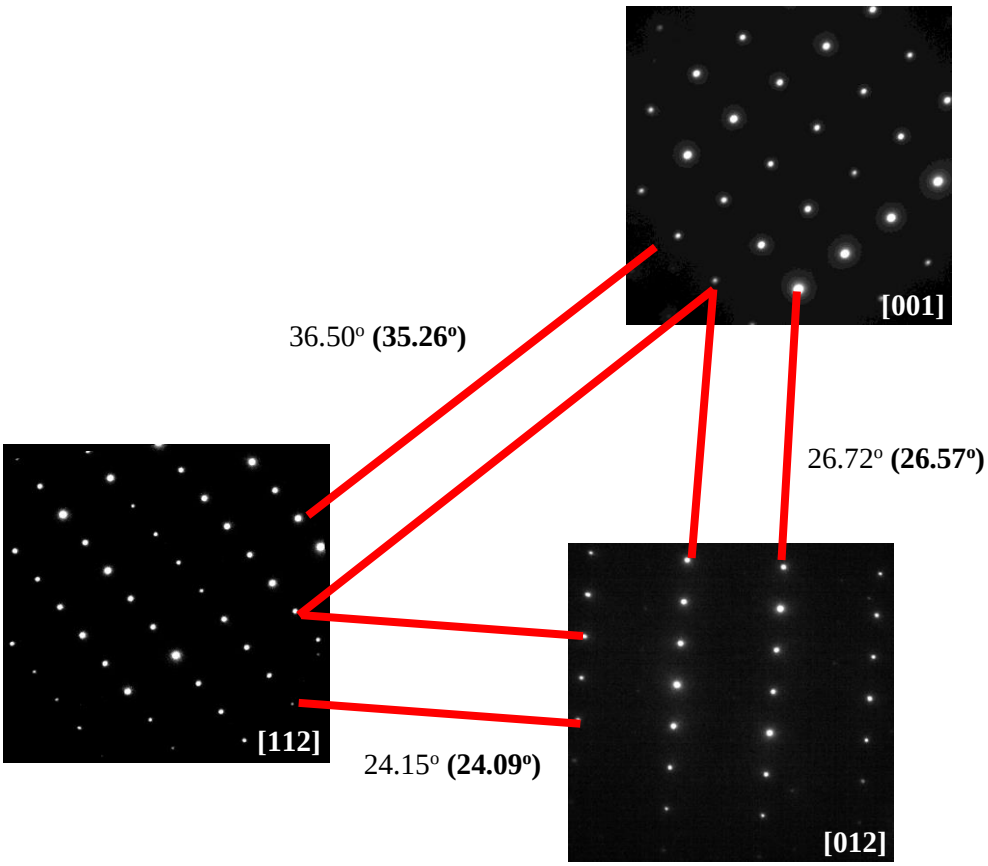

Figure 4.9 SAD patterns obtained from the G-phase precipitate labelled in Figure 4.8 (a); the angles between three zone-axes agree with those angles calculated theoretically (bold numbers)

Some finely sized particles, around 20~50 nm in diameter, also appear within the matrix and are observed to be associated with dislocations (Figure 4.7 (d)). EDS mapping of such particles indicated they are rich in Nb, as shown in Figure 4.10 (e). However, since the diameter of such particles is much smaller than the thickness of the FIB-TEM sample (~200 nm), the light elements such as carbon or nitrogen are difficult to distinguish as illustrated in Figure 4.10 (c). Accurate chemical information concerning the Nb-rich particle cannot therefore be identified from this FIB-TEM specimen.

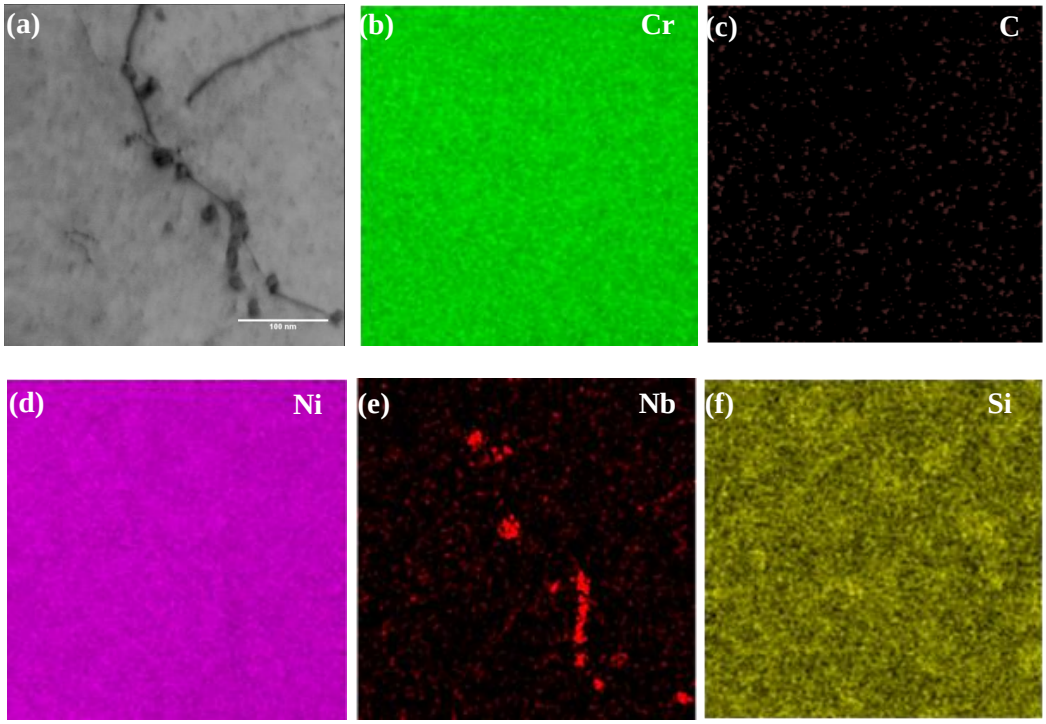

Figure 4.10 Nb-rich particles in association with dislocations (a) BF image; (b)-(f) TEM-EDS maps of selected area. The particles are Nb-rich (e) while carbon distribution shows no fluctuation at any point

To solve this problem, another TEM specimen from crept Alloy A was prepared via twin jet polishing. A measurement of thickness was carried out via convergent beam electron diffraction (CBED) patterns following the method described in section 3.12.

Figure 4.11 (b) shows a CBED pattern taken at a two-beam condition with $g = 3\bar{1}\bar{1}$. As shown in Table 4.3, the guessed values of n are shown in column 1. The values of s_2, s_3 and s_4 were calculated with Equation 3.6 and listed in column 2. The values of $(s_i/n_i)^2$ were listed in column 3. A straight line for $(s_i/n_i)^2$ against $(1/n_i)^2$ was obtained for n=3 as shown in Figure 4.12. The intercepts of the straight line with the ordinate $(s_i/n_i)^2$ is $1/t^2$, and this equals 2.10569×10^{-4} nm^{-2}. The extinction distance (ξ_g) for {311} equals 28 nm and the foil thickness is therefore 69 nm, which is much thinner than the FIB-TEM specimen.

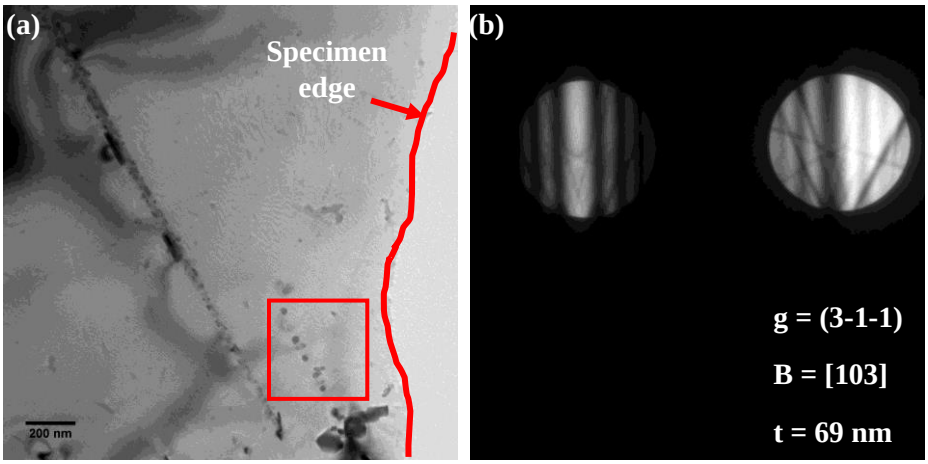

Figure 4.11 (a) BF image of crept Alloy A; (b) CBED pattern obtained from selected area in (a) close to the specimen edge (i.e. thin)

Table 4.3 CBED data for thickness determination

n_i	s_i (nm^{-1})	s_i^2/n_i^2 (nm^{-2})
3	0.111	8.291×10^{-5}
4	0.063	1.194×10^{-4}
5	0.040	1.739×10^{-4}

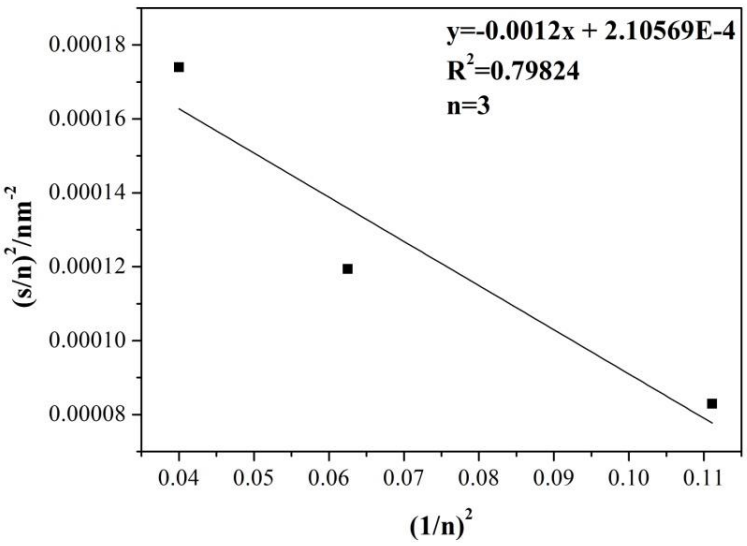

Figure 4.12 A straight line of $(S_i/n_i)^2$ vs. $(1/n_i)^2$ for Figure 4.11 (b)

A Nb-rich particle was chosen from the rectangle outlined in Figure 4.11. The size of this particle is around 30 nm, which is half the specimen thickness in this area. Figure 4.13 (b) illustrates the EDS spectra obtained from the selected particle and from the surrounded matrix as a comparison. It is obvious that the particle is rich in niobium combined with nitrogen. Other elements, such as chromium, nickel and iron are lower than in the matrix.

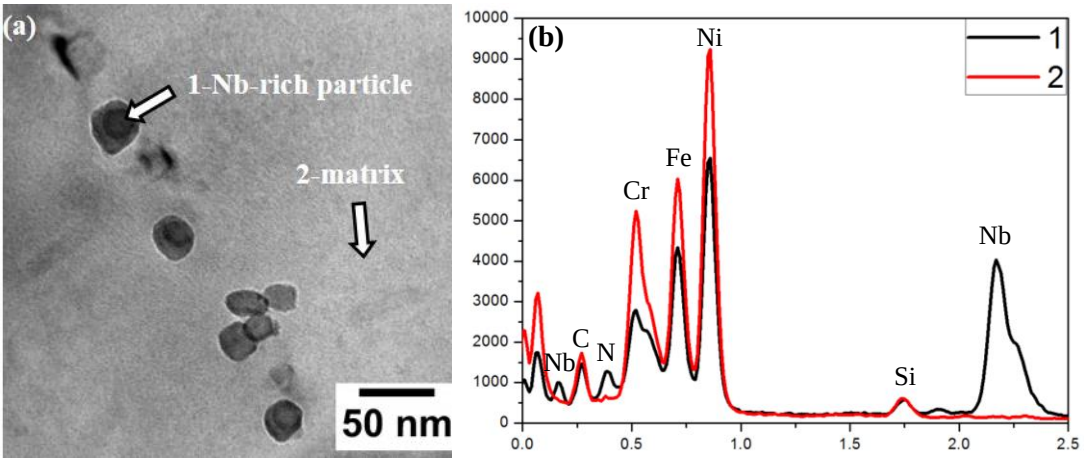

Figure 4.13 (a) BF image from rectangle outlined in Figure 4.11; (b) EDS spectra obtained from selected Nb-rich particle and from the matrix as shown in (a)

To confirm the nature of the Nb-rich particles, SAD patterns (Figure 4.14 (b)-(d)) were obtained from a selected particle (Figure 4.14 (a)). Due to the size limit of the selected area aperture, diffraction patterns were obtained from both the particle and the matrix. As shown in Figure 4.14, two sets of spots can be observed. The brighter spots are from the γ-Fe matrix which has an fcc structure. The weaker diffraction spots are from the selected particle, can be indexed as fcc with a lattice parameter of 0.43 nm. As listed in Table 2.3, the lattice parameter of NbC is 0.44 nm while the lattice parameter of NbN is 0.45 nm. Therefore, using also the EDS result, the Nb-rich particle is identified as an NbN precipitate.

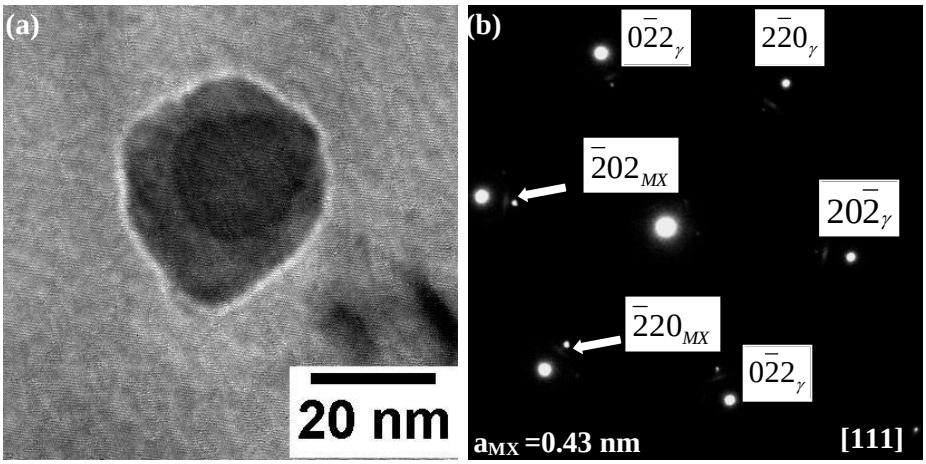

Figure 4.14 (a) BF image of selected Nb-rich particle; (b) SAD pattern from selected particle where the brighter spots are from γ-Fe matrix and the weaker spots are from the MX particle

As discussed in Sections 2.4.3 and 2.4.4, intragranular precipitation is the most effective creep strengthening method. The microstructural parameters for intragranular precipitates will have a strong influence on the creep rate and need to be measured.

However, in crept Alloy A, two types of intragranular precipitates have been identified, secondary Cr-carbide $M_{23}C_6$ and fine NbN. Although the NbN precipitates are smaller than the $M_{23}C_6$ precipitates, the content of NbN is too low to achieve a strengthening effect compared with that of $M_{23}C_6$. The measurement of microstructural parameters therefore focused on secondary Cr-carbide $M_{23}C_6$.

The measurement area (Figure 4.15) was selected to be close to primary carbides and to have a width of 2 μm for the following reasons:

(i) From Figure 4.15 (a), most of the secondary precipitates are in the area 0~2μm from primary carbides, indicating that this area has the highest particle density;

(ii) The particle size in the area of 0~2μm from primary carbides is around 100 nm, which is suitable for dislocation-precipitate interactions. However, the size of the precipitates beyond this area can be several microns (particles 1 and 2 in Figure 4.15 (b)) making them unlikely to act as effective obstacles to dislocation movement;

(iii) Primary carbides can be potential sites for dislocation generation during creep. This will lead to a greater possibility for dislocation-precipitate interactions in the area close to primary carbides.

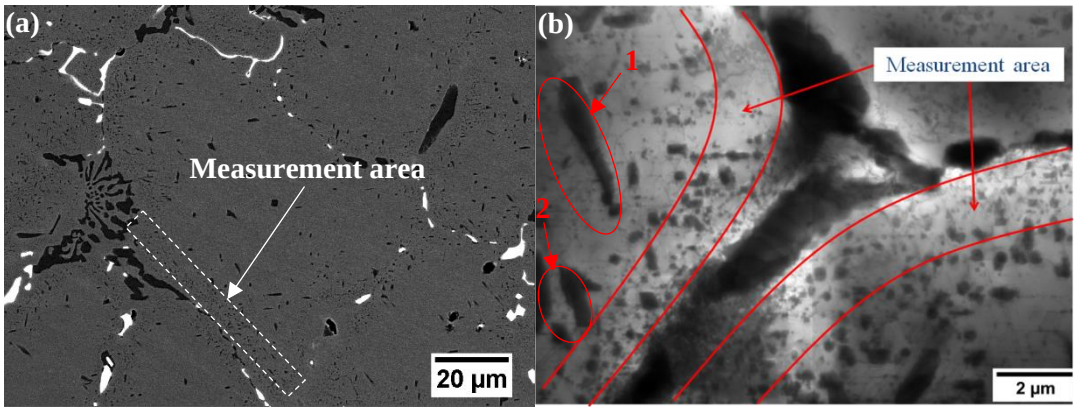

Figure 4.15 (a) SEM-BSE image and (b) TEM-BF image illustrating the measurement area of microstructural parameters in crept Alloy A

The measurement of microstructural parameters followed the method described in Section 3.11. 50 TEM BF images were taken to calculate the interspacing and 500 secondary precipitates were analysed to calculate average precipitate size. In crept Alloy A, the average precipitate size is 159 ± 58 nm and interspacing is 565 ± 66 nm. However, Figure 4.16 illustrates the precipitate size distribution obtained from crept Alloy A which is a unimodal particle distribution. Half of the precipitates fall into the range of 50~150 nm while a few precipitates have a size above 400 nm. The average precipitate size may not adequately present the true size distribution. A Gaussian fit was applied to the particle size distribution in Figure 4.16; the mean was 126 nm and the full width at half maximum (FWHM) was 109 nm. Although the large precipitates (300~500 nm) have low frequency, they have a significant influence on the value of average precipitate size leading to the difference between the average precipitate size and the Gaussian mean.

Table 4.4 Microstructural parameters of secondary Cr-carbide $M_{23}C_6$ in crept Alloy A

Precipitate size		Interspacing
Average precipitate size	Gaussian mean	565 ± 66 nm
159 ± 58 nm	126 nm	

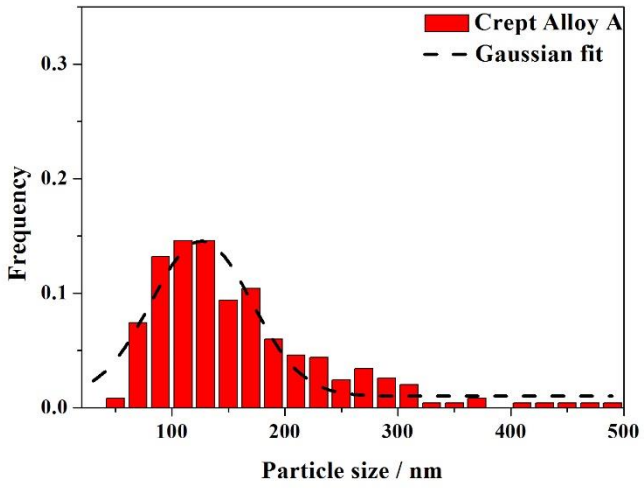

Figure 4.16 Particle size distribution for crept Alloy A

4.3 Microstructure of heat treated Alloy A

To determine the effect which stress plays in microstructural evolution during creep, Alloy A was heat treated for 12 hours at 1000 ^{o}C. The resulting specimen is referred to as HT-12 Alloy A. The heat treatment process is described in Section 3.2. Figure 4.17 illustrates the BSE images obtained from as cast Alloy A, crept Alloy A and HT-12 Alloy A. The microstructure of HT-12 shows no significant difference from crept Alloy A. The area fractions for the various carbides in HT-12 Alloy A are listed in Tables 4.5. The evolution of the area fraction of primary carbides from as cast Alloy A to HT-12 Alloy A shows the same tendency from as cast Alloy A to crept Alloy A. The area fraction of primary Cr-carbide increased from 3.89 % to 4.76 % while the area fraction of primary Nb-carbide increased from 1.40 % to 1.46 %. However, for secondary Cr-carbide, the area fractions in crept Alloy A and HT-12 Alloy A are quite close, i.e. 1.75 % in crept Alloy A and 1.72 % in HT-12 Alloy A, respectively.

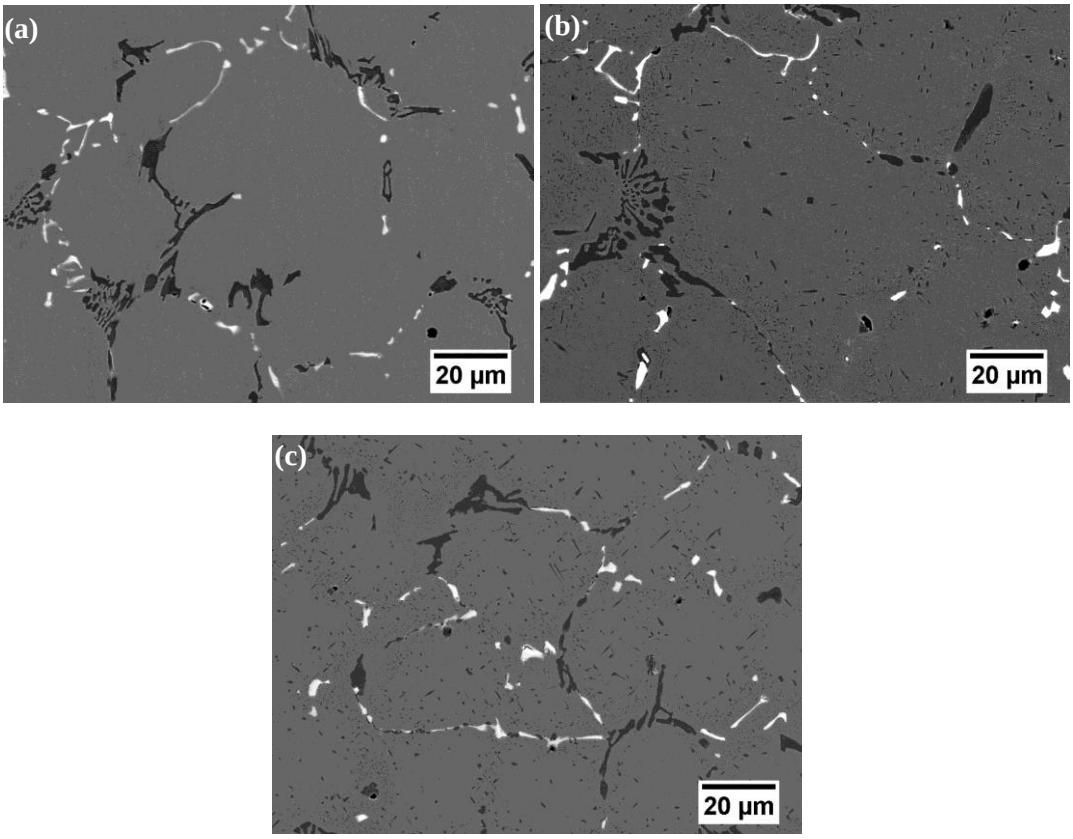

Figure 4.17 BSE images obtained from (a) as-cast; (b) crept; (c) HT-12 Alloy A

Table 4.5 Area fractions of various carbides in as-cast, crept and HT-12 Alloy A

Specimen	Area fraction%		
	Primary Cr-carbide	Secondary Cr-carbide	Primary Nb-carbide
As-cast Alloy A	3.89±0.17	---	1.40±0.07
Crept Alloy A	5.25±0.26	1.75±0.14	1.60±0.07
HT-12 Alloy A	4.76±0.33	1.72±0.12	1.46±0.08

The microstructural parameters of HT-12 Alloy A were also measured. In HT-12 Alloy A, the average precipitate size is 125 nm and the interspacing 405 nm, which are both smaller than those of crept Alloy A. Meanwhile, as shown in Figure 4.16, more than 60 % of precipitates are below 100 nm. The largest precipitate size found in HT-12 Alloy A is around 350 nm. A Gaussian fit applied to Figure 4.18 also indicates that HT-12 Alloy A has a narrower particle distribution, where the full width at half maximum is 78 nm and the mean is 94 nm.

Table 4.6 Microstructural parameters of secondary Cr-carbide $M_{23}C_6$ in crept Alloy A and HT-12 Alloy A

Specimens	Precipitate size		Interspacing
	Average precipitate size	Gaussian mean	
Crept Alloy A	159 ± 58 nm	126 nm	565 ± 66 nm
HT-12 Alloy A	125 ± 49 nm	94 nm	405 ± 80 nm

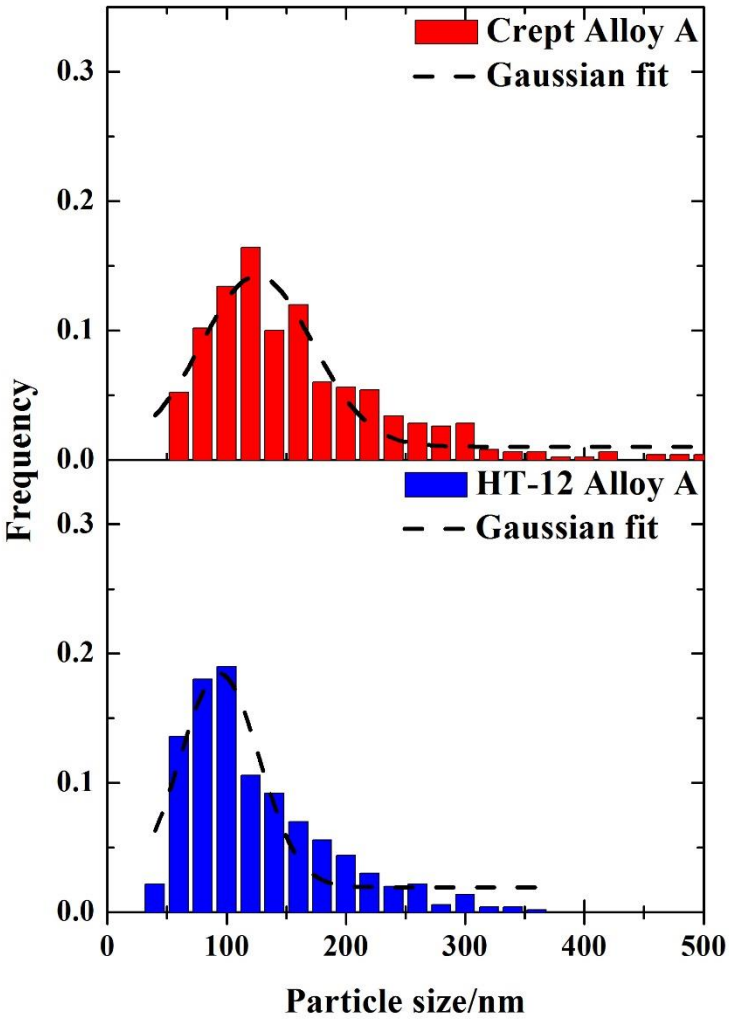

Figure 4.18 Particle size distributions for crept Alloy A and HT-12 Alloy A

4.4 Summary of results

1. The microstructure of as-cast Alloy A contains austenitic matrix and a primary precipitation network, which is a combination of primary Cr-carbides (M_7C_3) and primary Nb-carbides (NbC);

2. In crept Alloy A, the primary Cr-carbides transformed from M_7C_3 to $M_{23}C_6$ while the primary Nb-carbides remain NbC type. Area fractions of primary Cr-carbides and primary Nb-carbides both increased after creep;

3. After creep, secondary precipitation was observed within the matrix, which are identified as secondary Cr-carbides ($M_{23}C_6$) and finely sized particles (NbN). Furthermore, the secondary Cr-carbides $M_{23}C_6$ has an orientation relationship with austenite $\{110\}_\gamma \parallel \{110\}_{M_{23}C_6}$ and $\langle 110\rangle_\gamma \parallel \langle 110\rangle_{M_{23}C_6}$;

4. The microstructural parameters of secondary Cr-carbides ($M_{23}C_6$) were measured, i.e. the average precipitate size is 159 ± 58 nm and interspacing is 565 ± 66 nm. The precipitate size distribution of secondary Cr-carbides ($M_{23}C_6$) shows a unimodal distribution with a Gaussian mean of 126 nm and a full width at half maximum of 109 nm;

5. G-phase, which is likely transformed from NbC, was observed in crept Alloy A at the interface between the primary Cr-carbide and the matrix;

6. In HT-12 Alloy A (without stress), the area fractions of various carbides and the average precipitate size of secondary Cr-carbides are both smaller than those of crept Alloy A (with stress), indicating that the stress can enhance the coarsening of precipitate.

4.5 Discussion

4.5.1 Microstructure of Alloy A

As shown in Table 3.1, the HP 40 austenitic stainless steels contain up to approximately 0.45 wt% carbon. However, the solubility of carbon in austenite is strongly dependent on the temperature. The solid solubility curve for carbon in Fe-18Cr stainless steels is shown in Figure 4.19, indicating that the carbon solubility in austenite decreases rapidly as the temperature decreases. In addition, a high Ni content also decreases the carbon solubility.

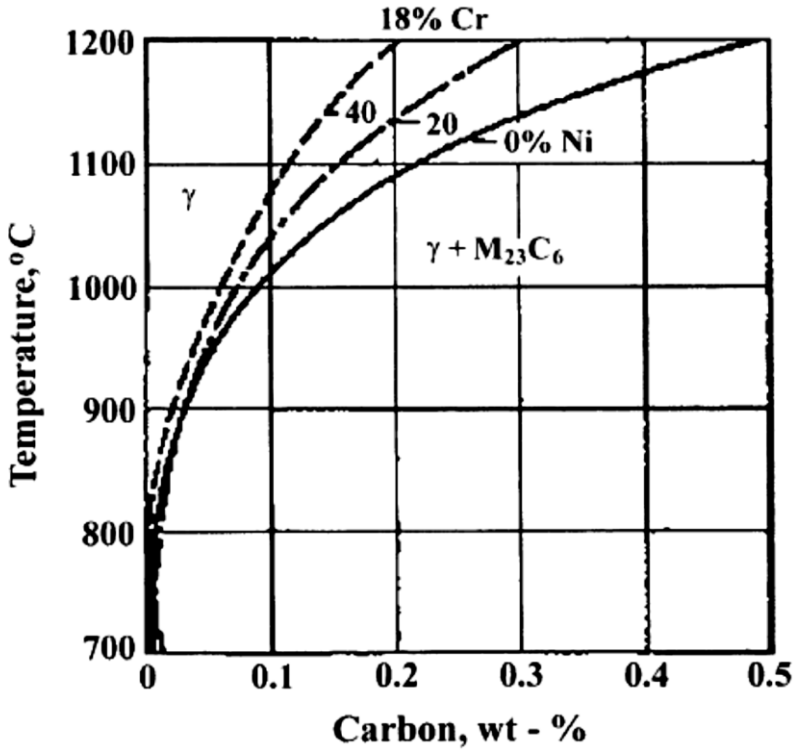

Figure 4.19 Influence of temperature and nickel content on the carbon solubility in Fe-18Cr austenite stainless steels [138]

The carbon solubility in equilibrium with Cr-carbide [139] and Nb-carbide [47] in AISI316 stainless steels (18Cr-12Ni) was determined experimentally as:

$$log([C]) = 7.771 - \frac{6272}{T}$$ --- Equation 4.1

$$log[Nb][C] = 4.55 - \frac{9350}{T}$$ --- Equation 4.2

These relations give the solubility of chromium carbide as 0.069 wt% and that of niobium carbide as 0.0016 wt% at 1000 °C. Although these values are based on AISI316 austenitic stainless steels and will be different from the values in HP40 austenitic stainless steels, it is obvious that the solubility of carbides in austenite (0.069 wt%) is much smaller than the carbon content in Alloy A (0.46 wt%). Meanwhile, the thermodynamic calculation by JMat Pro shows that the solubility of carbon in HP40 at 1000 °C is 0.103 wt%. Therefore, the rapid solidification to room temperature during casting will lead to the formation of a carbide network, which is in agreement with the observations on as-cast Alloy A, shown in Figure 4.2.

The presence of NbC in austenitic stainless steels is expected even for very low carbon content since Nb is such a strong carbide former. NbC generally forms at high temperature directly from the liquid and is quite stable after solidification to room temperature.

As discussed in Section 2.3.2, several Cr-carbides can be present in austenitic stainless steels, such as M_2C, M_7C_3, $M_{23}C_6$ and M_6C (with increasing M/C ratio). Figure 4.20 demonstrates the solubility of carbon and the effect of nickel in Fe-18Cr based austenitic stainless steels, indicating that the predominant carbide is $M_{23}C_6$ while M_7C_3 can form at very high carbon levels. This is because the formation of M_7C_3 needs more carbon than $M_{23}C_6$ at the same Cr concentration i.e. the atomic M/C ratios are 2.33/1 and 2.83/1 for M_7C_3 and $M_{23}C_6$ respectively.

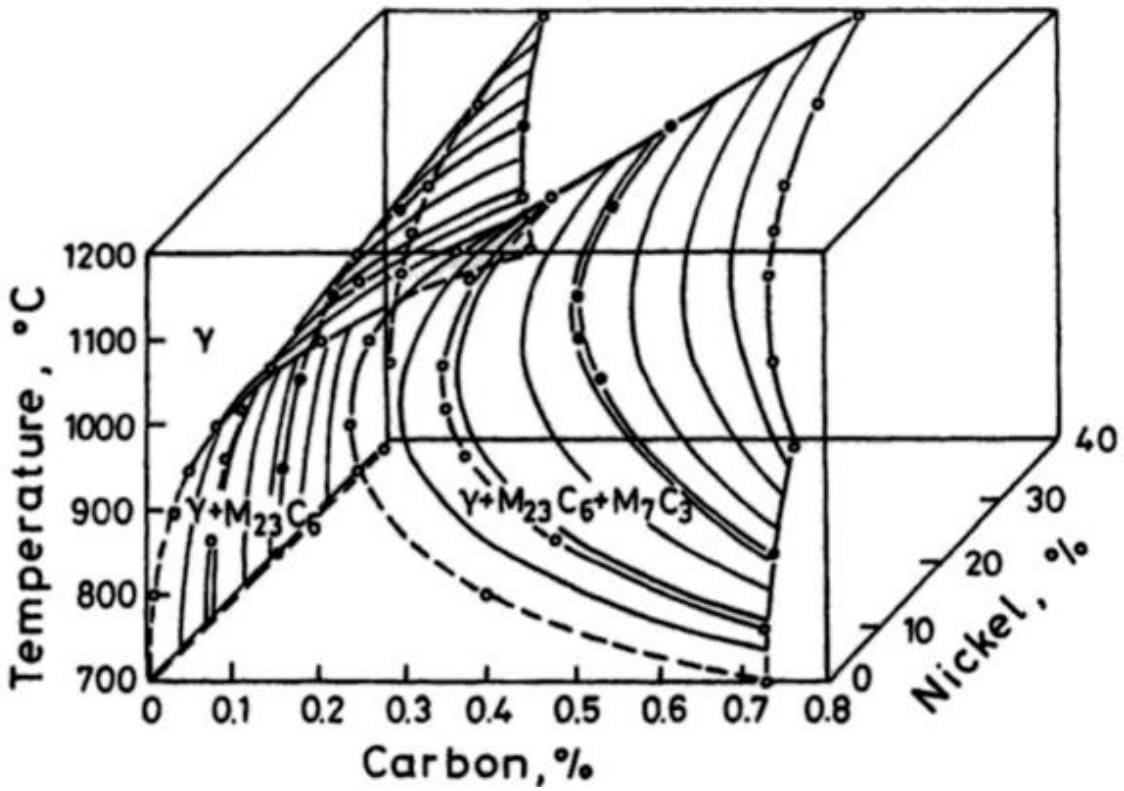

Figure 4.20 Solid solubility of carbon in Fe-18Cr steels showing that $M_{23}C_6$ is the predominant carbide while M_7C_3 can form at high carbon levels [47]

Gregolin and Alcantara [140] developed a solidification model for Fe-Cr-Nb-C alloys in the white cast iron range. Experimental measurements yield the precipitation sequence shown in Figure 4.21. According to them, NbC is the first phase formed from the liquid, followed by M_7C_3. Then a reaction $L \rightarrow \gamma + M_7C_3$ leads to a eutectic or so-called 'Chinese script' structure, which was also observed in a white iron containing 2.1 wt% C, 14.7 wt% Cr and 1.0 wt% Nb and is shown in Figure 4.22. The same eutectic structure was found in as-cast Alloy A as shown in Figure 4.3 (a) & (b), indicating that the reaction $L \rightarrow \gamma + M_7C_3$ takes place during the solidification of HP40.

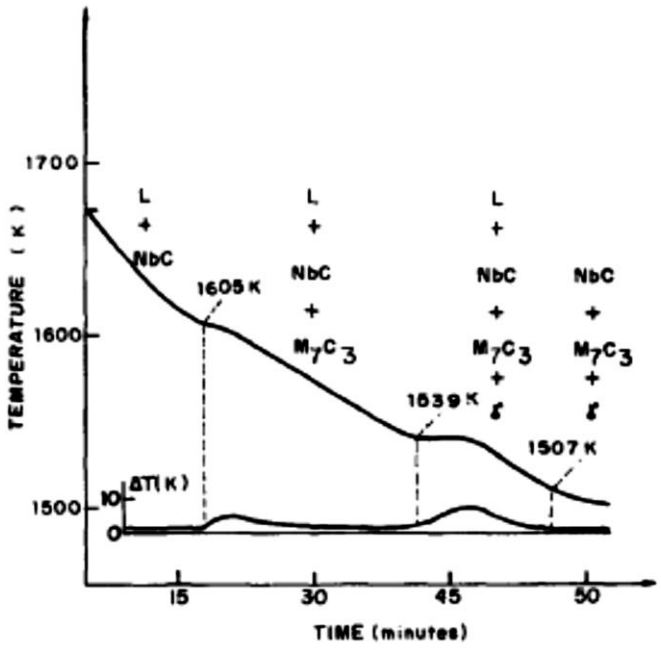

Figure 4.21 Precipitation sequence in a white iron containing 3.42 wt% C, 21.6 wt% Cr and 5.4 wt% Nb [140]

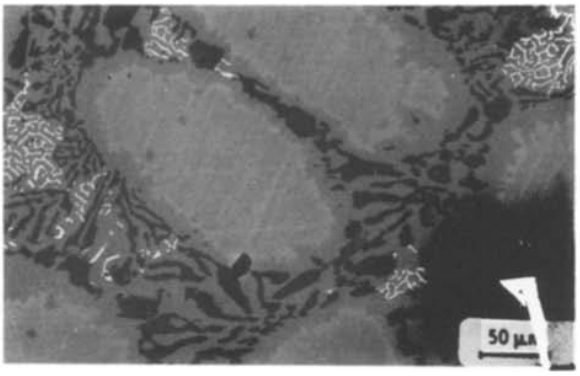

Figure 4.22 SEM of a white iron containing 2.1 wt% C, 14.7 wt% Cr and 1.0 wt% Nb illustrating a eutectic or "Chinese script" structure involving austenite and M_7C_3 [141]

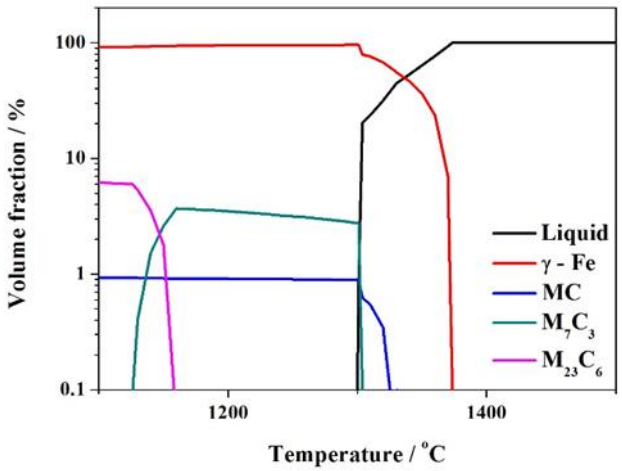

Figure 4.23 Thermodynamic simulation of Alloy A by JMat Pro

A thermodynamic simulation using JMat Pro is shown in Figure 4.23. There is one main difference between the results shown in Figure 4.21 and the JMat Pro simulation: the austenite forms in the liquid before NbC due to the high concentration of nickel, which is an austenite stabiliser.

Therefore, the solidification sequence of HP40 alloys during casting is:

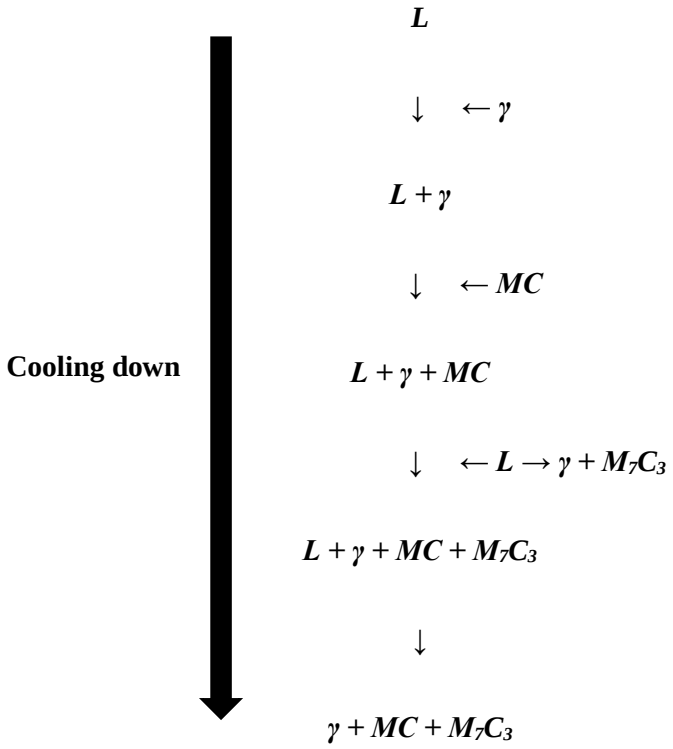

The austenite is the first to solidify from the liquid and forms the primary dendrite cells. The next precipitation is of MC, which prefers to nucleate around the cell boundaries; most of the MC-carbides have a rod-like morphology as shown in Figure 4.3 (c) and (d). When the temperature further decreases, the reaction $L \rightarrow \gamma + M_7C_3$ also occurs along the austenite cell boundaries and leads to a eutectic structure (Figure 4.3 (a) & (b)). At the end of solidification, the as-cast microstructure of Alloy A will be austenitic matrix surrounded by primary Cr-carbides (M_7C_3) and primary Nb-carbides (NbC), which form a fragmented network.

Although the primary Cr-carbide after rapid solidification is of the M_7C_3 type, a transformation from M_7C_3 to $M_{23}C_6$, which was found in crept Alloy A by XRD (Figure 4.6 (b)), has also been found in 17Cr-0.5C ferritic steel [142], 25Cr-0.45C-Co superalloy [33], 29Cr-0.33C ferritic steels [34] and 30Cr-2.3C cast iron [35]. $M_{23}C_6$ is more thermodynamically stable than M_7C_3 since the free energies of carbide formation are ~15 kJ/mol for $M_{23}C_6$ [143] and ~40 kJ/mol for M_7C_3 [144] respectively in the Fe-Cr-C system at 1000 ºC. Therefore, when alloys are heated to service temperature (1000 ºC), the primary Cr-carbide will transform from metastable M_7C_3 to stable $M_{23}C_6$ to reduce the system free energy.

In as-cast Alloy A, some NbC carbides were observed within the eutectic $\gamma + M_7C_3$ as shown in Figure 4.4. Vardavoulias et al. [34] found that the transformation from $M_{23}C_6$ carbides to M_7C_3 carbides introduced an increase in volume, which was 20~25% as determined by quantitative metallography. As a consequence of the volume increase and further particle growth, the $M_{23}C_6$ carbides will cluster together and form a continuous primary carbide along the austenite cell boundaries as observed in crept Alloy A (Figure 4.7 (a)). When the $M_{23}C_6$ carbides cluster together, the NbC which is originally within the eutectic structure will be surrounded by $M_{23}C_6$, like the particle 2 observed in Figure 4.8 (e).

The instability of the NbC, which are at the interface between the primary carbides and the matrix, has been found in niobium alloyed steels, like 20/25 Nb steel [57] and HP40 [60, 61, 63], i.e. a transformation from NbC to G-phase will take place at elevated temperature, which is in agreement

with the observations in crept Alloy A (Figure 4.8 & 4.9). Normally, this transformation takes place when the temperature is above 700 ^{o}C. However, Soares et al. [60] found there was no G-phase in a HP40 steel held at 1100 ^{o}C, indicating that the maximum temperature for the stability of G-phase is around 1000 ^{o}C. Furthermore, the increase in Si content will enhance the transformation of G-phase [61]. Since the Si concentrates around the grain boundaries during solidification [17], the formation of G-phase is preferred at the interface between the primary carbides and the matrix.

Although niobium is a strong carbide former and precipitation of primary NbC drastically reduces the matrix carbon content, some carbon remains available for later secondary precipitation during creep. This is because the minimum niobium content required to stabilize all the carbon is normally eight times the carbon content [22], while in Alloy A the niobium content is 0.97 wt% and carbon is 0.46 wt%, i.e. available carbon content is around 0.3 wt%. Therefore, when as-cast Alloy A was heated up and held at 1000 ^{o}C, the available carbon combined with the high Cr concentration in the austenite matrix leads to the formation of secondary Cr-carbide, which is $M_{23}C_6$ type due to its relatively low formation energy. This is confirmed by the TEM analysis in Figure 4.7 (c) on secondary Cr-carbide in crept Alloy A. The precipitation of NbN (Figure 4.13 & 4.14) follows the same mechanism on the formation of secondary Cr-carbide, which is the combination of available nitrogen and niobium in the matrix.

With a beam direction of <110> as shown in Figure 4.24, the secondary $M_{23}C_6$ carbides in the matrix are all rhombic with interfacial angles of 70^{o} and 110^{o}. Beckett and Clark [31] determined that the $M_{23}C_6$ has surfaces of {110} and {111}[61] planes as illustrated in Figure 4.25. There are four rectangular faces of {111} type with side: length ratio 1.154:1.000. The other two faces are {110} and are rhombic with angles of 70.53^{o} and 109.47^{o}. Therefore, when the {110} interface is perpendicular to the electron beam, the precipitate will be rhombic and the interfacial angles will be 70.53^{o} and 109.47 ^{o}, which are close to the values measured from Figure 4.24.

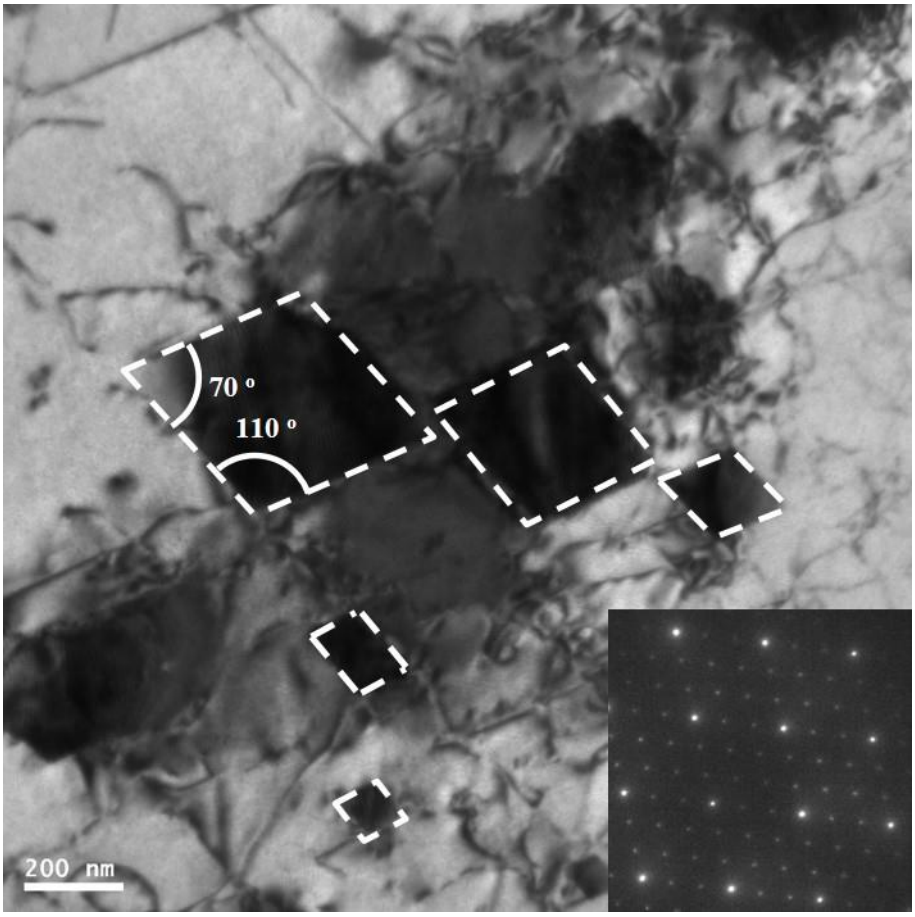

Figure 4.24 TEM BF image of crept Alloy A from a <110> zones illustrating that the secondary $M_{23}C_6$ carbides in the matrix are all rhombic with interfacial angles of 70° and 110°

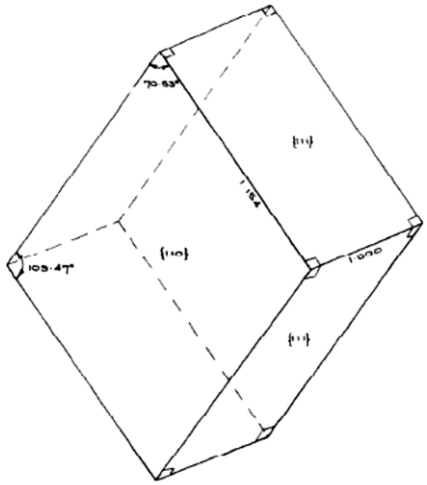

Figure 4.25 Schematic image of a $M_{23}C_6$ particle formed in the austenite matrix [31]

4.5.2 Effect of stress on precipitation

The difference between crept Alloy A and HT-12 Alloy A is the external stress. It is apparent that, for the same temperature and time, the area fractions of the various carbides and the average size of the secondary Cr-carbides are greater in crept Alloy A, as described in Section 4.3. It is concluded that the stress can enhance coarsening of Alloy A precipitate during creep. A similar observation of the coarsening of $M_{23}C_6$ carbides being accelerated by creep was found by Hattestrand and Andren [145] in a 9% Cr steel.

The coarsening behaviour of the precipitates follows diffusion controlled Ostwald ripening theory, where the smaller precipitates will decompose and their mass will transport to the larger precipitates by diffusion. Based on the analysis by Lifshitz and Slyozov [146], the coarsening rate, *K*, can be calculated by Equation 4.3:

$$K = 8\gamma V_p / \sum_{i=1}^{n} \frac{9(C_i^p - C_i^m)^2}{C_i^m D_i / RT} \quad \text{--- Equation 4.3}$$

K – – – Coarsening rate coefficient
γ – – – Interfacial energy
V_p – – – Molar volume of precipitate
C_i^p – – – Concentration of element in the precipitate
C_i^m – – – Concentration of element in the matrix
D_i – – – Diffusion coefficent of element in the matrix

For equation 4.3 at elevated temperature and stress, the interfacial energy, molar volume and concentration of element can be considered as constants. Therefore, the most important parameter controlling the effect of stress on precipitation is the element diffusion coefficient *D*.

Diffusion is controlled by vacancy migration. An external stress on the material will lead to a distortion of the crystal symmetry. For example, an external tensile stress on a fcc crystal produces a strain along the tensile direction, which results in lattice distortion. The uniaxial tensile stress distorts the crystal symmetry, turning a cubic crystal into a slightly tetragonal one, as illustrated in Figure 4.26. Consequently, the vacancy migration rate becomes different due to the distortion of the crystal and its reduction of symmetry, which alter the vacancy jump distance and the diffusion energy barrier. Based on this idea that the distortion of the crystal symmetry by stress will lead to a change in vacancy migration, Chen et al. [147] proposed a simple model which predicts the effect of an applied stress parallel to [001] on *D* in the age forming of a 7XXX alloy. Figure 4.27 illustrates that the diffusion coefficient ratios of age forming (with stress) to traditional aging (without stress) changed with stress. This image suggests that the diffusion coefficient rises quickly with increasing stress. For instance, with a stress of 40 MPa, the diffusion coefficient with stress is about 1.15 of that without stress.

.

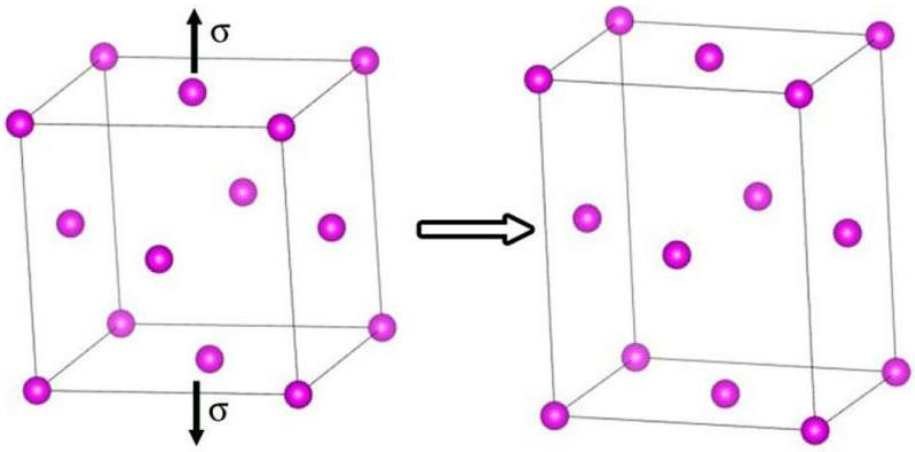

Figure 4.26 Schematic image of crystal distortion of a fcc structure with applied tensile stress

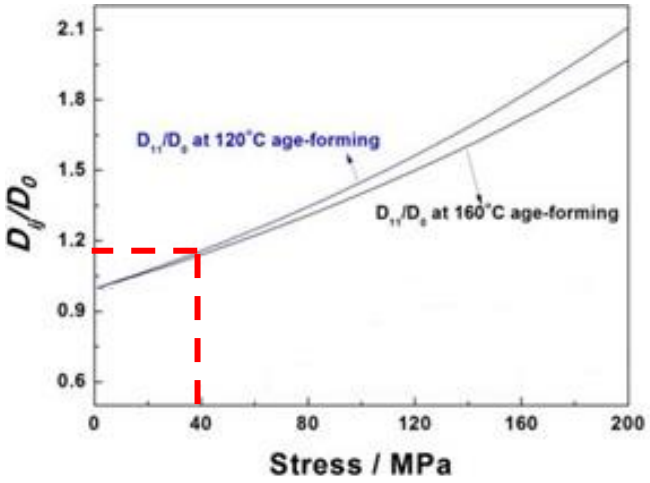

Figure 4.27 Variation of ratio of diffusion coefficient with stress to that without stress as a function of stress [147]

Another method whereby stress can have an influence on the diffusion coefficient is via the activation energy of diffusion. With an increase of tensile stress, both the vacancy formation enthalpy and the migration activation enthalpy decrease [148], as shown in Figure 4.28. This indicates that stress will reduce the energy barrier to vacancy diffusion and furthermore enhance diffusion and the coarsening of precipitates.

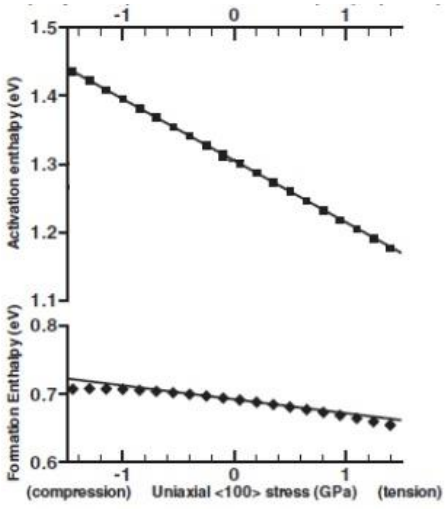

Figure 4.28 The vacancy activation enthalpy and vacancy formation enthalpy as a function of uniaxial stress [148]

An alternative explanation involves pipe diffusion along dislocation. During creep, plastic deformation involves the production and movement of dislocations. Dislocations can provide easier diffusion paths since pipe diffusion through the dislocations is much faster than lattice diffusion through the matrix. It has been suggested by Eggeler [149] that a higher dislocation density is maintained during creep as compared to during isothermal ageing. It is clear that a higher dislocation density obtained by stress could increase the coarsening rate of the precipitates via this route.

However, Spigarelli et al. [150] found that acceleration via pipe diffusion does not describe with sufficient accuracy the experimental variation of the coarsening constant with applied stress on T91 steel (9Cr-Mo-Nb-V-N). For this reason, an empirical equation was developed.

$K = K_o exp[k(\sigma/E)^p]$ --- Equation 4.4

K – – – Coarsening rate coefficient with stress
K_o – – – Coarsening rate coefficient without stress
σ – – – Applied stress
E – – – Young' s modulus
k, p – – – Temperature dependent parameters

Although there are no explanations of the temperature dependent parameters *k* and *p* in Equation 4.4, the corresponding curve calculated via Equation 4.4 gave good agreement with experimental coarsening rates (Figure 4.29). It is obvious that the coarsening rate is not linearly dependent on applied stress.

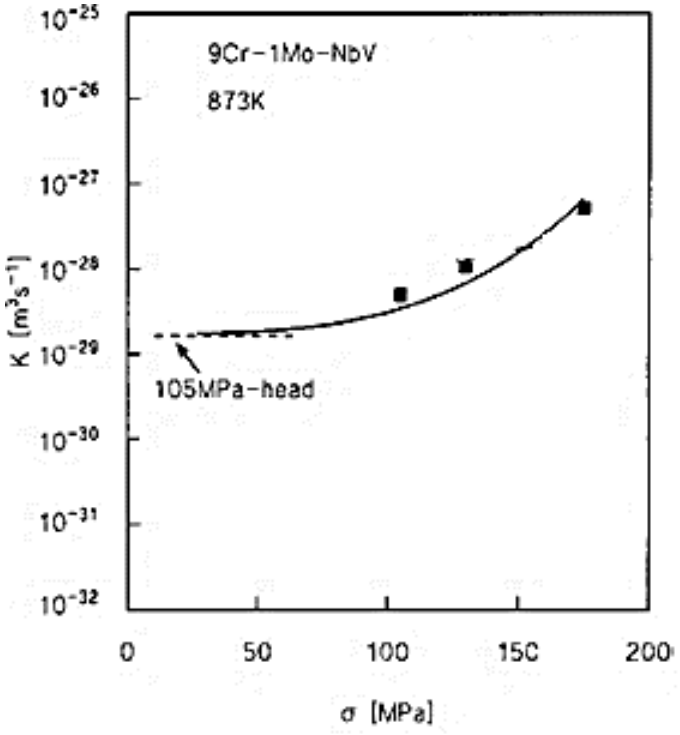

Figure 4.29 Variation of coarsening constant K with stress at 873 K and the curve calculated by Equation 4.4 [150]

In summary, the stress can enhance the precipitate coarsening behaviour of Alloy A during creep. The actual mechanism of how the applied stress accelerates the coarsening rate of the precipitates probably involves a combination of different effects of stress: distortion of the crystal symmetry, reduction of diffusion activation energy and increase of dislocation density.

4.6 Conclusions

1. During casting of HP40, austenite is the first to solidify from the liquid and forms primary dendrite cells followed by the precipitation of NbC and eutectic reaction $L \rightarrow \gamma + M_7C_3$. This solidification sequence leads to the as-cast microstructure of Alloy A, which contains austenitic matrix and a primary precipitation network (primary Cr-carbides (M_7C_3) and primary Nb-carbides (NbC));

2. In crept Alloy A, the primary Cr-carbides transformed from metastable M_7C_3 to stable $M_{23}C_6$ to reduce the system free energy. G-phase, which is likely transformed from NbC, was observed in crept Alloy A at the interface between the primary Cr-carbide and the matrix due to the instability of the NbC. Area fractions of primary Cr-carbides and primary Nb-carbides both increased after creep due to the growth of precipitates;

3. After creep, secondary precipitation was observed within the matrix due to the supersaturation of the matrix solid solution, which are identified as secondary Cr-carbides ($M_{23}C_6$) and fine particles (NbN). The microstructural parameters of secondary Cr-carbides ($M_{23}C_6$) were measured, i.e. the precipitate size distribution of secondary Cr-carbides ($M_{23}C_6$) shows a unimodal distribution with a Gaussian mean of 126 nm and a full width at half maximum of 109 nm;

4. In HT-12 Alloy A (without stress), the area fractions of various carbides and the average precipitate size of secondary Cr-carbides are both smaller than those of crept Alloy A (with stress), indicating that the stress can enhance the coarsening of precipitate by accelerating the diffusion coefficient (distortion of the crystal symmetry and reduction of diffusion activation) and providing easier diffusion paths (increase of dislocation density).

Chapter 5 Effect of chemical composition on microstructure of HP40 (Alloy B c.f. Alloy A)

5.1 Microstructure of as-cast Alloy B

Figure 5.1 shows the microstructure of as-cast Alloy B obtained by BSE. Primary Cr-carbide (M_7C_3) and primary Nb-carbide (NbC) form a fragmented network, which surrounds the austenitic matrix. The primary Cr-carbide and primary Nb-carbide are both composed of granular and acicular morphologies.

The area fractions of primary Cr-carbide and primary Nb-carbide are also measured and listed in Table 5.1: 2.75 % for M_7C_3 and 1.34 % for NbC. Although the Cr concentrations in Alloy A and Alloy B are quite similar (24.25 wt.% in Alloy A and 24.66 wt.% in Alloy B (Table 3.1)), as-cast Alloy B contains much less M_7C_3 than as-cast Alloy A. The amounts of primary Nb-carbide in as-cast Alloy A and as-cast Alloy B are, however, similar (1.40 % and 1.34 % respectively).

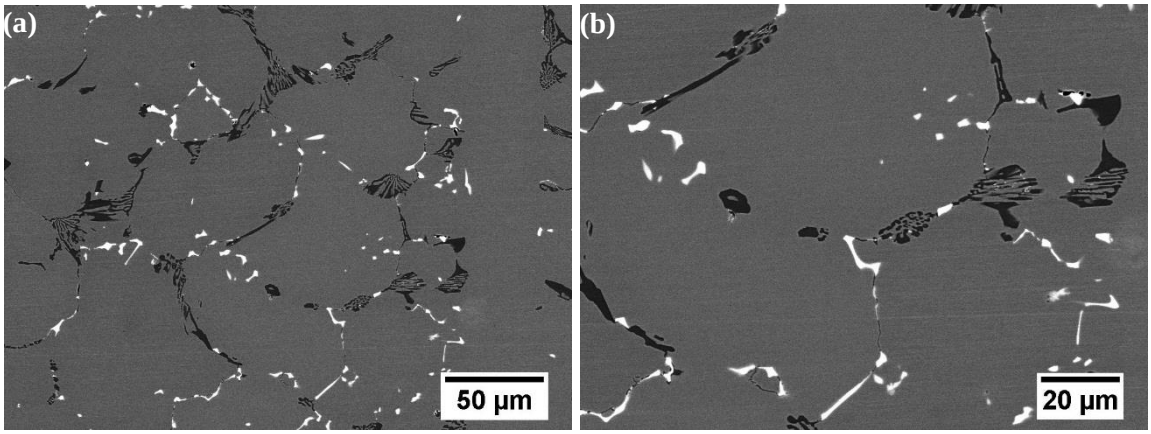

Figure 5.1 (a) low magnification and (b) high magnification BSE images obtained from as-cast Alloy B

Table 5.1 Area fractions of various carbides in as-cast and crept Alloy A and Alloy B

Specimen	Area fraction%		
	Primary Cr-carbide	Secondary Cr-carbide	Primary Nb-carbide
As-cast Alloy A	3.89±0.17	---	1.40±0.07
As-cast Alloy B	2.75±0.08	---	1.34±0.11
Crept Alloy A	5.25±0.26	1.75±0.14	1.60±0.07
Crept Alloy B	2.82±0.51	0.86±0.12	1.34±0.10

5.2 Microstructure of crept Alloy B

The microstructure of crept Alloy B (1000 ˚C and 40 MPa for 14 hours) is illustrated in Figure 5.2. After creep, the primary Cr-carbide transformed from M_7C_3 to $M_{23}C_6$ while the primary Nb-carbide remained as NbC type. The primary network of chromium carbides also coalesced and enlarged during creep. The area fraction of primary Cr-carbides increased from 2.75 % to 2.82 % during creep whilst that of the primary Nb-carbides remained as 1.34 %, (Table 5.1).

Secondary precipitation, $M_{23}C_6$, is also observed within the matrix and most of these secondary precipitates are found 0~2μm from the primary carbides. The area fraction of secondary Cr-carbide in crept Alloy B is 0.86 %, only half that observed in crept Alloy A. The precipitate size of secondary Cr-carbide ($M_{23}C_6$) in crept Alloy B was measured. The average precipitate size in crept Alloy B was 136 nm. A Gaussian fit applied to the particle size distribution indicated that a mean of 110 nm and FWHM of 97 nm, both of which are smaller than those of crept Alloy A.

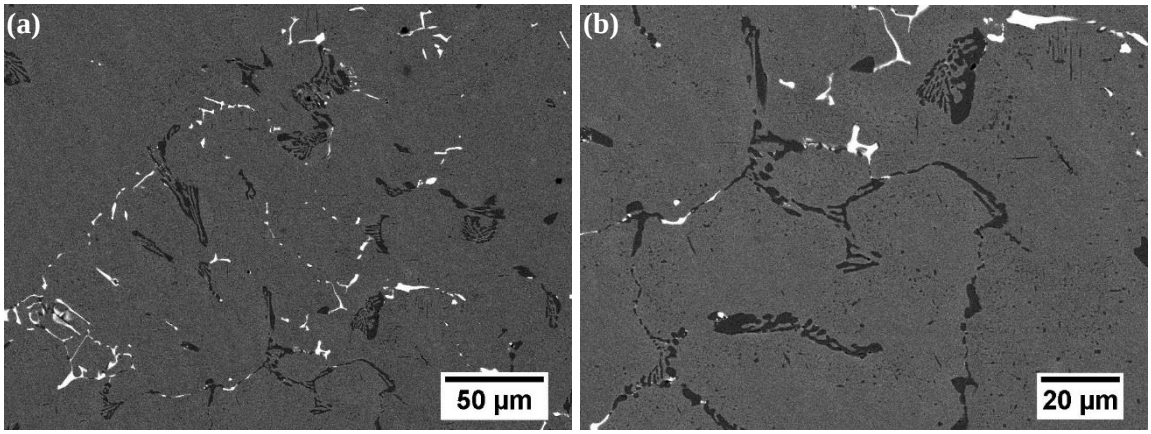

Figure 5.2 (a) Low magnification and (b) high magnification BSE images obtained from crept Alloy B

Table 5.2 Microstructural parameters for secondary Cr-carbide $M_{23}C_6$ in crept Alloy A and crept Alloy B

Specimens	Precipitate size		Interspacing
	Average precipitate size	Gaussian mean	
Crept Alloy A	159 ± 58 nm	126 nm	565 ± 66 nm
Crept Alloy B	136 ± 68 nm	110 nm	497 ± 149 nm

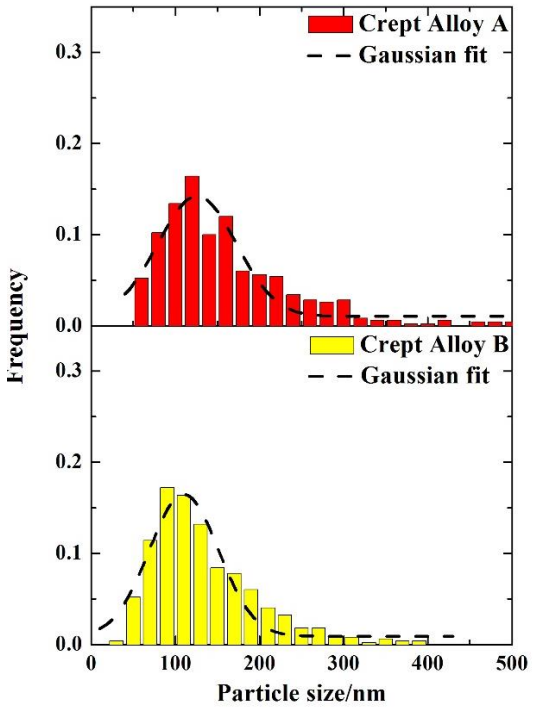

Figure 5.3 Particle size distributions for crept Alloy A and crept Alloy B

5.3 Thermodynamic simulation of microstructure of HP40 using JMat Pro

To determine the effect of chemical concentration on the microstructure, thermodynamic simulation via JMat Pro 6.2 was carried out and compared with the experimental results, indicating which phases were present and their amounts.

Figure 5.4 illustrates the volume fractions of the equilibrium phases of Alloy A, Alloy B and Alloy C as a function of temperature. At the creep test temperature (1000 ^{o}C), four phases, i.e. austenite, MC (M = Nb), MN (M = Nb) and $M_{23}C_6$ (M = Cr, Fe, Ni and Mn), exist in all three alloys. The simulation is substantially in agreement with experimental observation with one main difference. The simulation could not distinguish primary $M_{23}C_6$ from secondary $M_{23}C_6$.

Table 5.3 Phases in Alloy A and Alloy B via simulation and experiment

Phases at 1000 ^{o}C		
Simulation	Alloy A	γ-Fe, $M_{23}C_6$, MC, MN
	Alloy B	γ-Fe, $M_{23}C_6$, MC, MN
	Alloy C	γ-Fe, $M_{23}C_6$, MC, MN
Experiment	Alloy A	γ-Fe, $M_{23}C_6$, MC, MN, G-phase
	Alloy B	γ-Fe, $M_{23}C_6$, MC, MN, G-phase
	Alloy C	γ-Fe, $M_{23}C_6$, MC, MN, G-phase

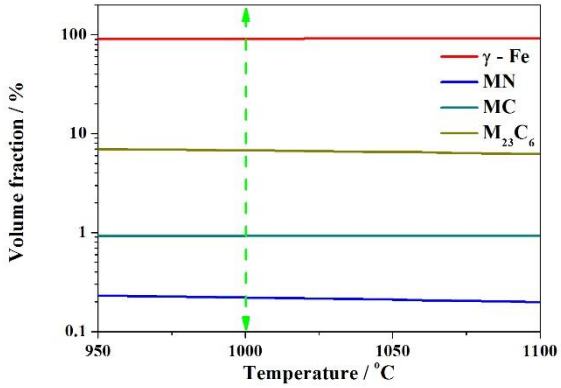

(a)

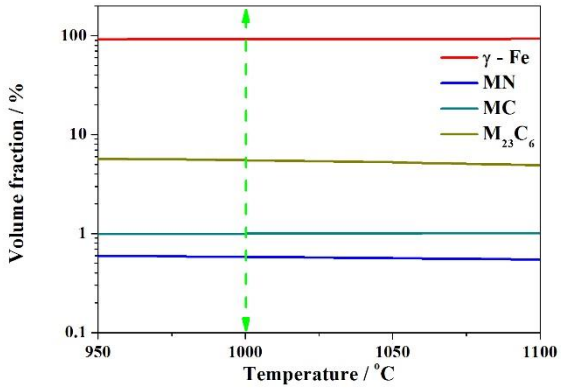

(b)

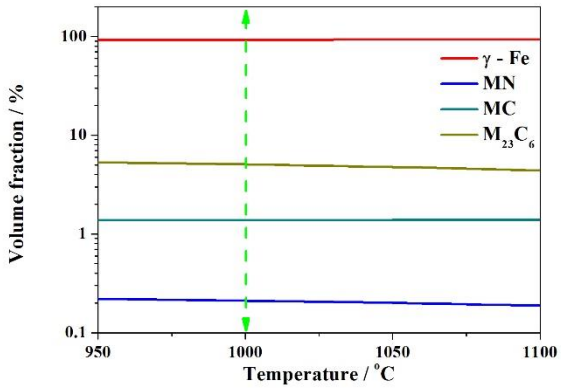

(c)

Figure 5.4 Phase simulations for (a) Alloy A, (b) Alloy B and (c) Alloy C

The volume fractions of carbides at 1000 ^{o}C are listed in Table 5.4. The simulated volume fractions were compared with area fractions measured from crept Alloy A, crept Alloy B and crept C since the area fraction is equal to the volume fraction. From Table 5.4, simulation indicates that Alloy A contains more Cr-carbide than Alloy B which is in agreement with experimental measurements. The fractions of Cr-carbides for Alloys B and C from both simulated and experimental measurements are quite close since Alloy B and Alloy C have similar chemical compositions. However, for Nb-carbide, there is a contradiction between simulation and measurement. This contradiction can be explained by an inhomogeneous distribution of elements during the production process or by an insufficient holding time to reach equilibrium.

Table 5.4 Fractions of various phases in crept Alloy A, crept Alloy B and crept Alloy C via simulation and experimental measurement

Specimen	Fractions of various phases %	
	Cr-carbide	Nb-carbide
Crept Alloy A	7.00 ± 0.40	1.60 ± 0.07
Simulation Alloy A	6.77	1.14
Crept Alloy B	3.68 ± 0.63	1.34 ± 0.10
Simulation Alloy B	5.51	1.58
Crept Alloy C	3.76 ± 0.59	1.93 ± 0.06
Simulation Alloy C	5.06	1.59

5.4 Microstructure of heat treated Alloy B

As discussed in Section 2.4.4, at a temperature of 1000˚C and stress of 40MPa, the creep life of Alloy B is 124 hours. However, the current observations of the microstructure are for Alloy B crept for only 14 hours i.e. 10% of the whole creep life. To understand the microstructural evolution during long-term creep, heat treatments for Alloy B at 1000 ºC from 1 to 150 hours were carried out; the detailed heat treatment process was described in Section 3.2.

Figure 5.5 illustrates BSE images of heat treated Alloy B, from HT-1 Alloy B to HT-150 Alloy B. The primary carbide network has enlarged and become more globular in morphology with the increase of heat treatment time. More Cr-carbide nucleated and grew. For example, in HT-150 Alloy B, the gaps between primary Nb-carbide were filled by Cr-carbides and most of the dendrite cell boundaries were covered by the continuous carbide network.

Secondary Cr-carbides were observed in all ten heat treated specimens, even in HT-1 Alloy B. During the heat treatments, the secondary Cr-carbide coarsened: the smallest precipitates decompose and their mass is transported towards the larger precipitates by diffusion. This coarsening process will continue until all the secondary precipitates have dissolved and their mass absorbed by the primary chromium network. A typical over-aged microstructure is presented in Figure 5.6 where the material had been prolonged service. The secondary phases have dissolved and the precipitates at the cell boundaries or within the matrix are large and globular.

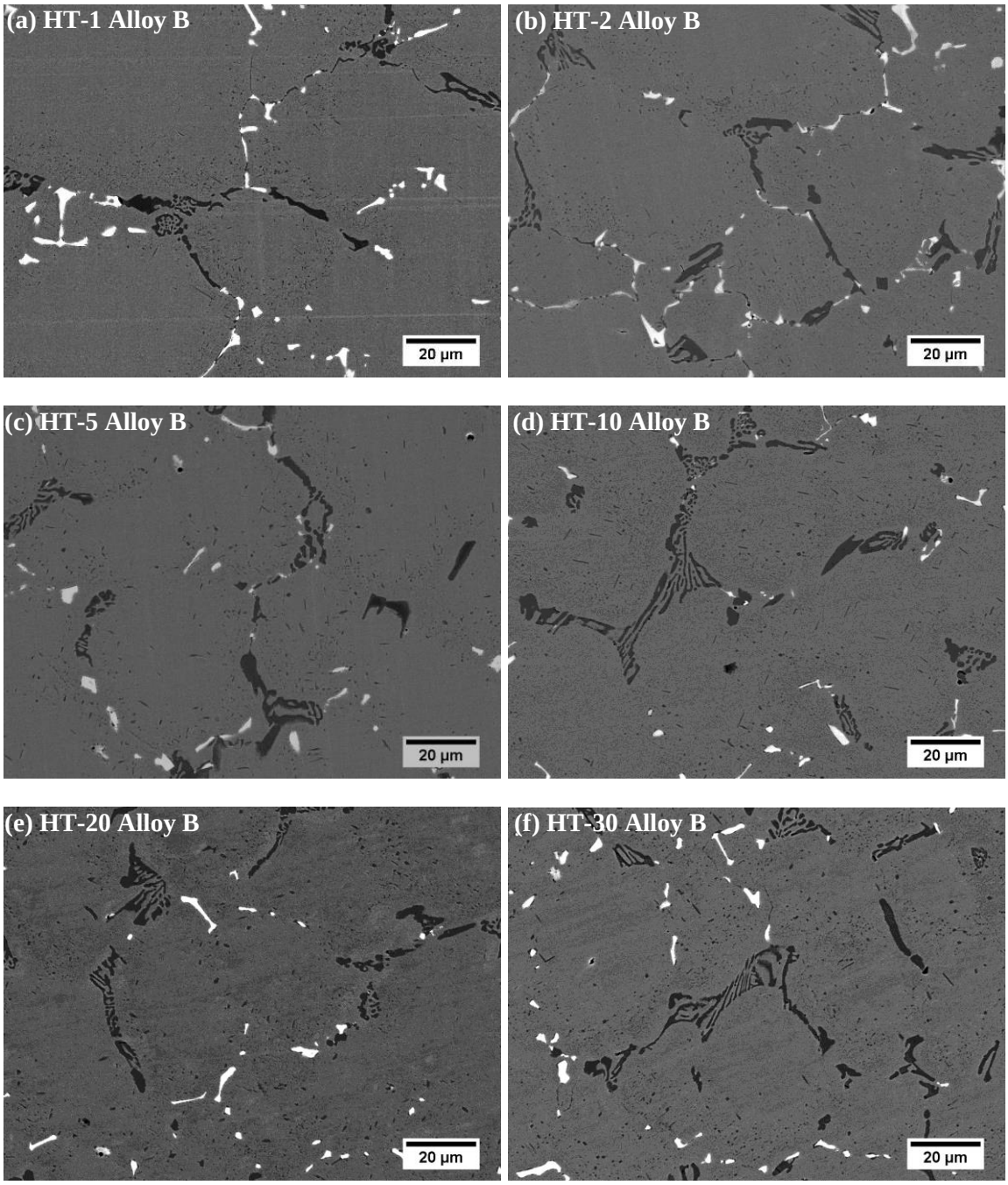
(a) HT-1 Alloy B
20 µm
(b) HT-2 Alloy B
20 µm
(c) HT-5 Alloy B
20 µm
(d) HT-10 Alloy B
20 µm
(e) HT-20 Alloy B
20 µm
(f) HT-30 Alloy B
20 µm

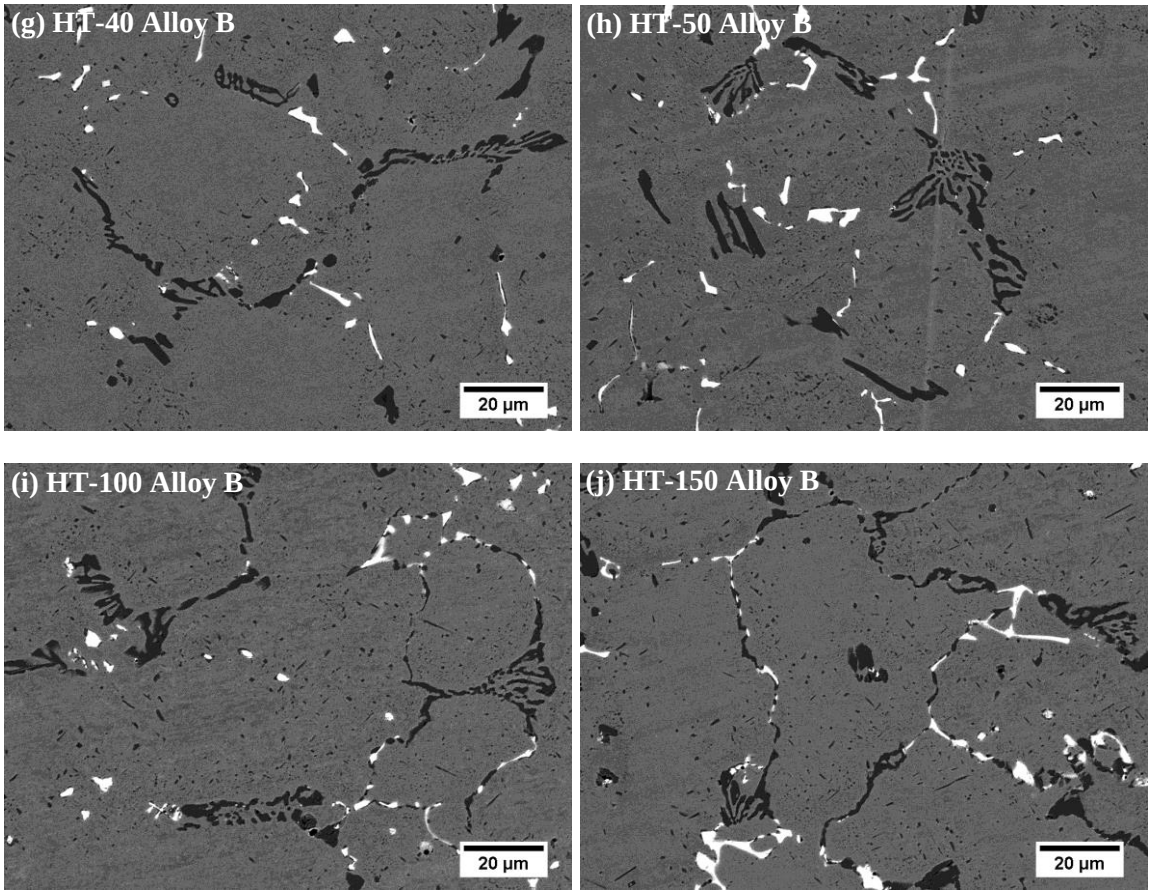

Figure 5.5 BSE images (a)-(j) obtained from Alloy B, HT-1 to HT-150

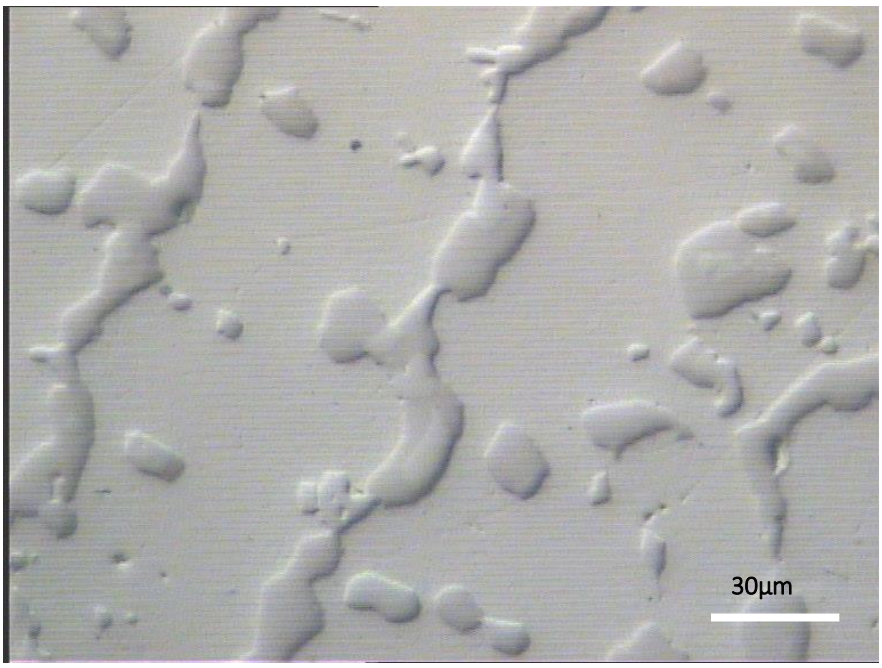

Figure 5.6 Optical micrograph of HP40 alloy after service of 150000 hours at 950°C [17]

The area fractions for primary Cr-carbide, primary Nb-carbide and secondary Cr-carbide in heat treated specimens were also measured (Table 5.5 and Figure 5.7) while the fourth column in Table 5.5, area fraction of Cr-carbide, is the combination of the area fractions of primary and secondary Cr-carbide. The area fraction of primary Cr-carbide fluctuates at first and then increases continuously from 20 hours; after heat treating for 50 hours, the coarsening rate becomes slightly lower. The area fraction of secondary Cr-carbide started to increase from the beginning by about three times from 0.83 % to 2.34 % after holding at 1000 ^{o}C for 150 hours. The area fraction of primary Nb-carbide becomes nearly constant for 100 hours and 150 hours after showing a significant increase between 1 hour and 50 hours. Furthermore, as shown in Table 5.4, the simulated fraction of Cr-carbide in Alloy B is 5.47%, which is close to the area fraction of Cr-carbide obtained from HT-150 Alloy B (5.55%), indicating that the microstructure is approaching the equilibrium condition after 150 hours' heat treatment.

Table 5.5 Area fractions of various carbides in heat treated Alloy B

Specimen	Area fraction%			
	Primary Cr-carbide	Secondary Cr-carbide	Cr-carbide (Total)	Primary Nb-carbide
As-cast	2.75±0.08	---	2.75±0.08	1.34±0.11
HT-1	2.40±0.06	0.83±0.43	3.23±0.37	1.35±0.03
HT-2	2.10±0.16	1.04±0.37	3.14±0.21	1.46±0.07
HT-5	3.05±0.28	1.08±0.41	4.13±0.13	1.51±0.08
HT-10	2.77±0.06	1.34±0.20	4.11±0.26	1.49±0.09
HT-20	2.43±0.19	1.66±0.40	4.09±0.21	1.50±0.06
HT-30	2.47±0.09	1.83±0.27	4.30±0.18	1.54±0.09
HT-40	2.66±0.08	1.93±0.36	4.59±0.28	1.56±0.10
HT-50	2.82±0.05	1.94±0.18	4.76±0.23	1.56±0.10
HT-100	2.92±0.11	2.18±0.20	5.10±0.31	1.59±0.05
HT-150	3.20±0.07	2.34±0.36	5.54±0.29	1.58±0.12

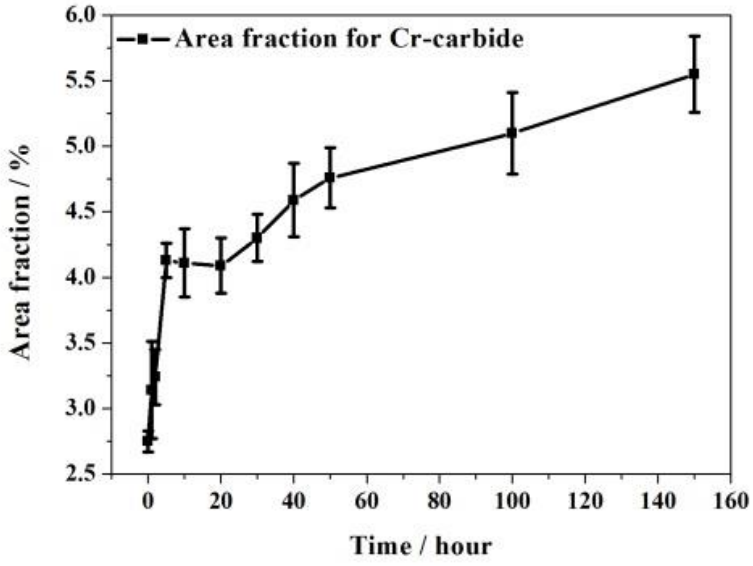
Area fraction for Cr-carbide
Area fraction / %
Time / hour
6.0
5.5
5.0
4.5
4.0
3.5
3.0
2.5
0
20
40
60
80
100
120
140
160

(a)

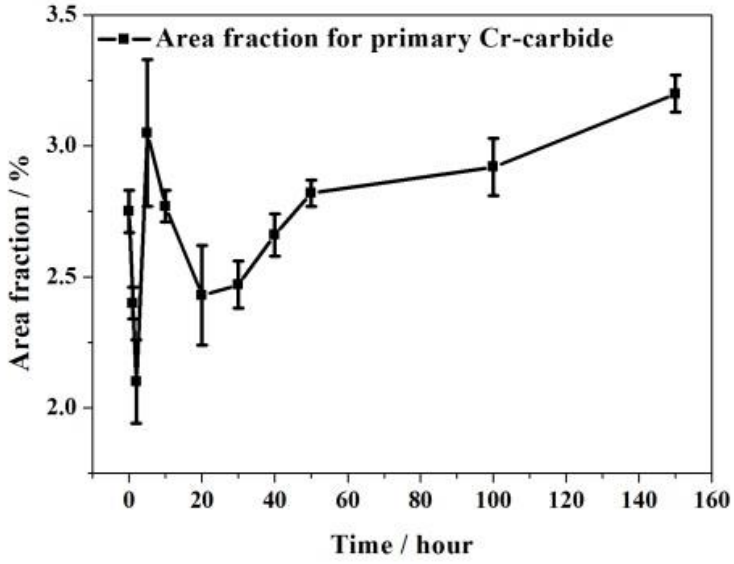
Area fraction for primary Cr-carbide
Area fraction / %
Time / hour
3.5
3.0
2.5
2.0
0
20
40
60
80
100
120
140
160

(b)

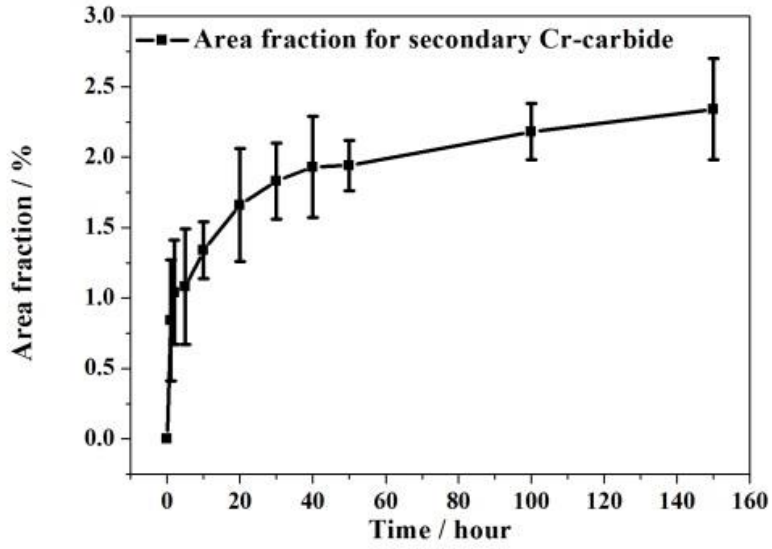

(c)

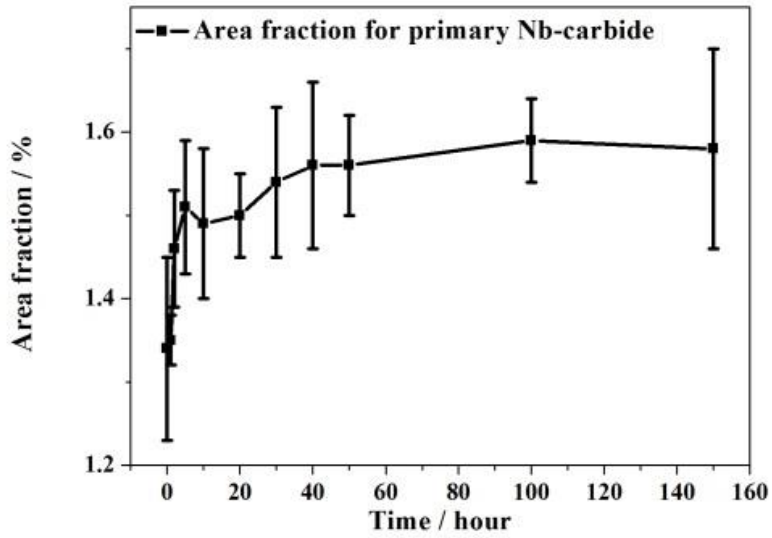

(d)

Figure 5.7 Area fractions of (a) Cr-carbide; (b) primary Cr-carbide, (c) secondary Cr-carbide and (d) primary Nb-carbide for Alloy B as a function of heat treatment time

The precipitate sizes of the secondary Cr-carbide in the heat treated specimens were measured and are listed in Table 5.6. The size of the secondary Cr-carbide precipitates increased rapidly to 76 nm after only 1 hour heat treatment. Then the precipitates continue to grow to 135 nm at 150 hours. It is obvious that the coarsening rate of the secondary Cr-carbides from HT-1 Alloy B to HT-40 Alloy B is much larger than that from HT-40 Alloy B to HT-150 Alloy B, as shown in Figure 5.8. The precipitate sizes for HT-100 and HT-150 are close: 134 nm for HT-100 and 135 nm for HT-150, indicating that the coarsening of secondary Cr-carbide is nearly complete at around 100 hours at 1000 ^{o}C.

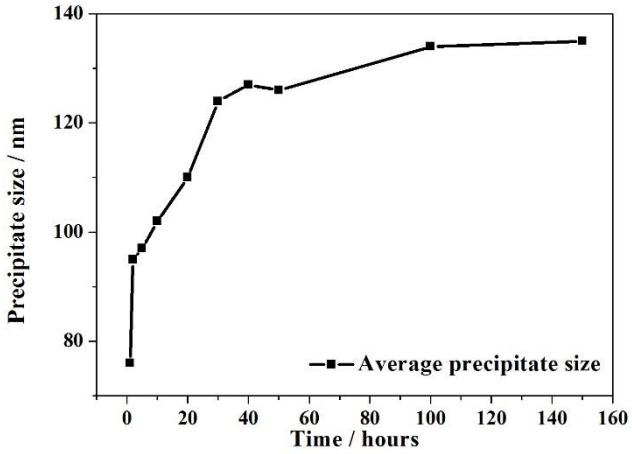

Figure 5.8 Secondary Cr-carbide precipitate size in Alloy B as a function of heat treatment time at 1000 ^{o}C (scatters are shown in Table 5.6)

Table 5.6 Microstructural parameters of secondary Cr-carbide $M_{23}C_6$ in heat treated Alloy B

Specimens	Precipitate size		Interspacing
	Average precipitate size	Gaussian mean	
Alloy B HT-1	76 ± 37 nm	64 nm	267 ± 60 nm
Alloy B HT-2	95 ± 38 nm	81 nm	300 ± 54 nm
Alloy B HT-5	97 ± 52 nm	78 nm	335 ± 79 nm
Alloy B HT-10	102 ± 59 nm	84 nm	379 ± 63 nm
Alloy B HT-20	110 ± 52 nm	93 nm	416 ± 91 nm
Alloy B HT-30	124 ± 74 nm	90 nm	414 ± 108 nm
Alloy B HT-40	127 ± 74 nm	94 nm	440 ± 87 nm
Alloy B HT-50	126 ± 71 nm	99 nm	467 ± 90 nm
Alloy B HT-100	134 ± 84 nm	102 nm	497 ± 106 nm
Alloy B HT-150	135 ± 82 nm	103 nm	499 ± 111 nm

The precipitate size distributions of the secondary Cr-carbide in heat treated Alloy B are shown in Figure 5.9. The distributions for HT-1, HT-2 and HT-5 Alloy B are narrow. For example, the full width at half maximum (FWHM) of HT-1 Alloy B is 58 nm, while the FWHM of HT-150 Alloy B is nearly twice that (99 nm). Meanwhile, the highest frequency in the distributions decreases with increasing heat treatment time, from around 0.30 in HT-1 Alloy B to around 0.15 in HT-150 Alloy B. To present succinctly the time dependence of precipitate size distribution, the fitted Gaussian from HT-1, HT-10 and HT-100 Alloy B are compared in Figure 5.10.

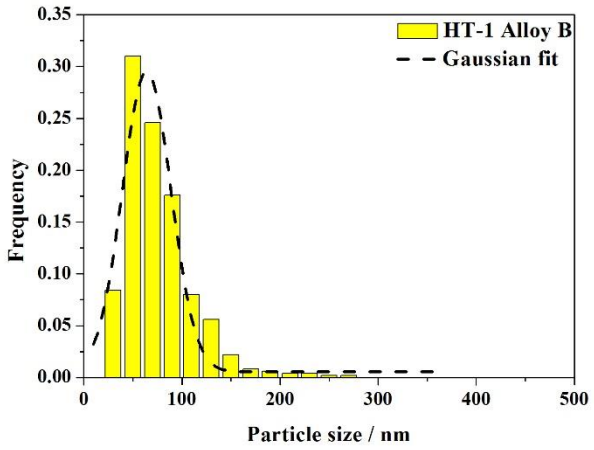

(a)

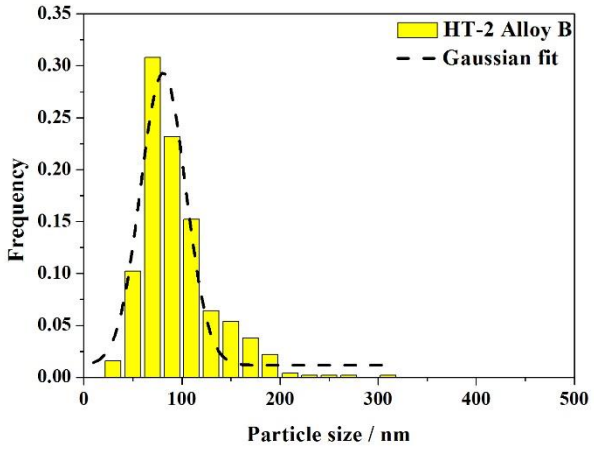

(b)

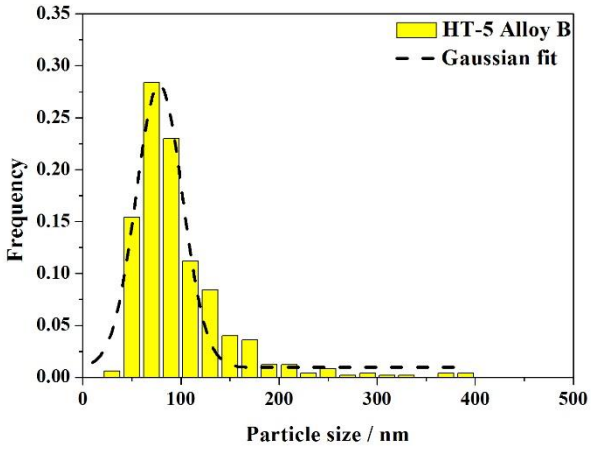
HT-5 Alloy B
Gaussian fit
Frequency
Particle size / nm
0.35
0.30
0.25
0.20
0.15
0.10
0.05
0.00
0
100
200
300
400
500

(c)

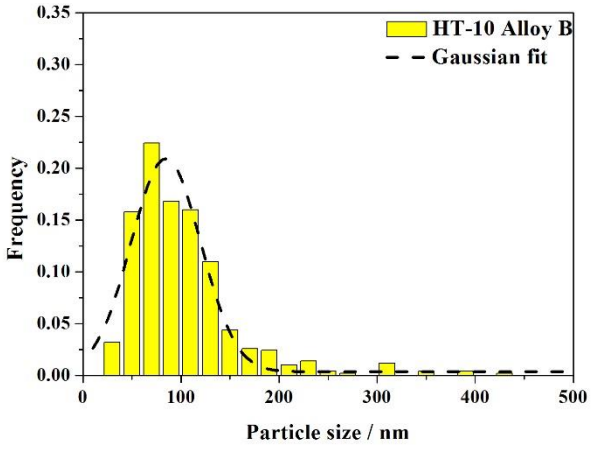
HT-10 Alloy B
Gaussian fit
Frequency
Particle size / nm
0.35
0.30
0.25
0.20
0.15
0.10
0.05
0.00
0
100
200
300
400
500

(d)

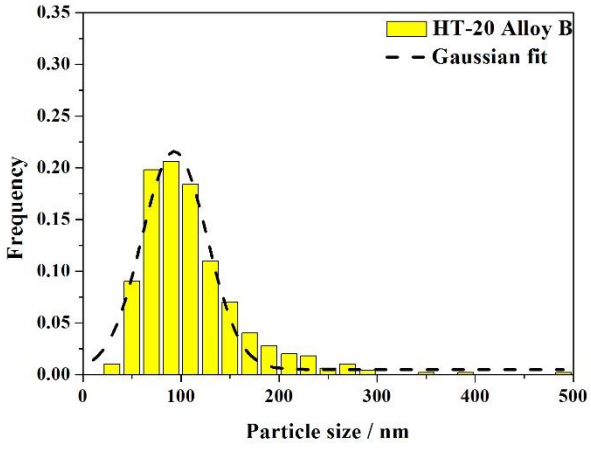
HT-20 Alloy B
Gaussian fit
Frequency
Particle size / nm
0.35
0.30
0.25
0.20
0.15
0.10
0.05
0.00
0
100
200
300
400
500

(e)

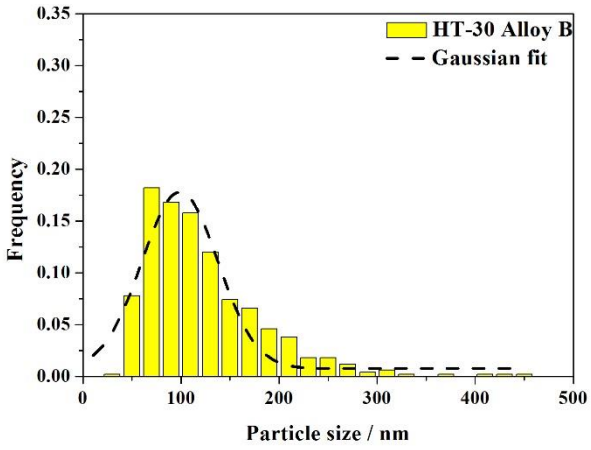
HT-30 Alloy B
Gaussian fit
Frequency
Particle size / nm
0.35
0.30
0.25
0.20
0.15
0.10
0.05
0.00
0
100
200
300
400
500

(f)

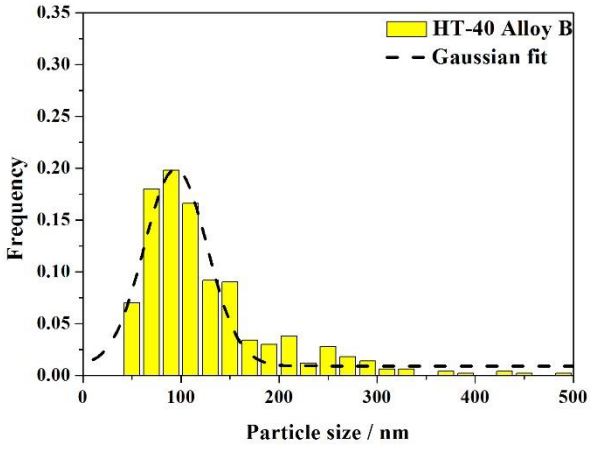
HT-40 Alloy B
Gaussian fit
Frequency
Particle size / nm
0.35
0.30
0.25
0.20
0.15
0.10
0.05
0.00
0
100
200
300
400
500

(g)

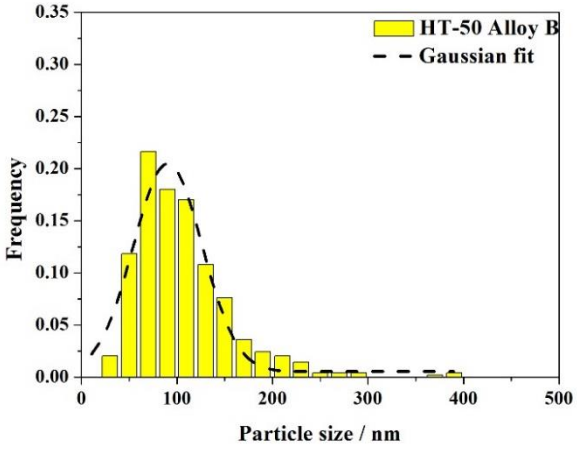
HT-50 Alloy B
Gaussian fit
Frequency
Particle size / nm
0.35
0.30
0.25
0.20
0.15
0.10
0.05
0.00
0
100
200
300
400
500

(h)

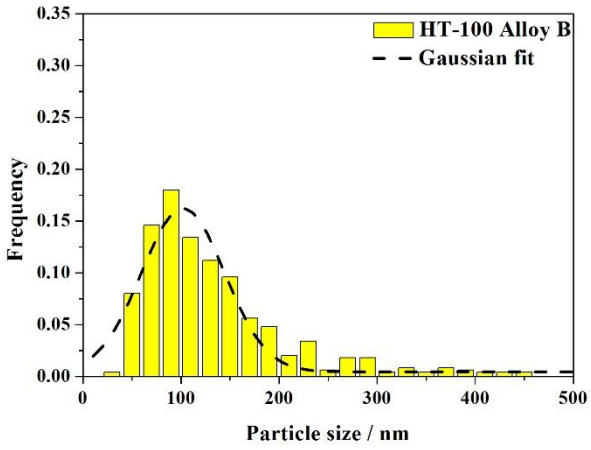

(i)

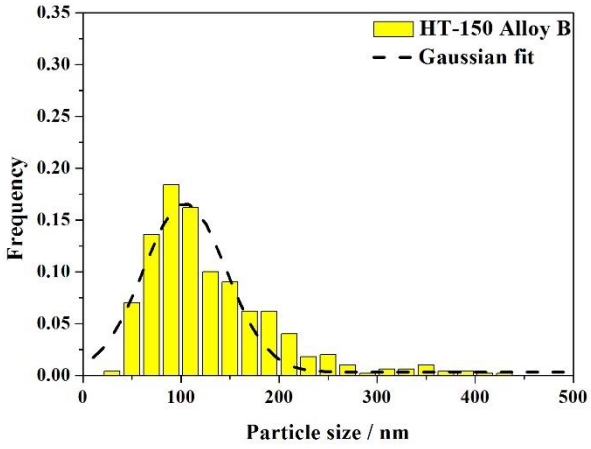

(j)

Figure 5.9 Particle size distributions of the secondary Cr carbide obtained from HT-1 Alloy B to HT-150 Alloy B

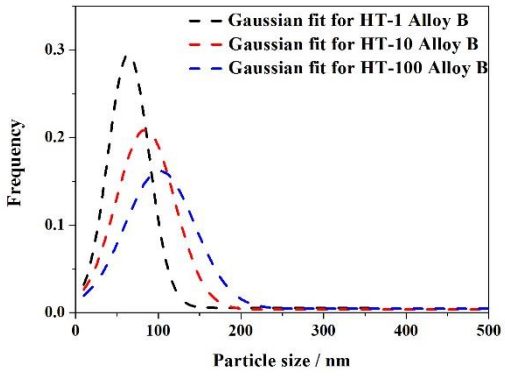

Figure 5.10 Gaussian fits for Alloy B, HT-1, 10 and 100

The coarsening behaviour of secondary Cr-carbide follows Ostwald ripening theory, where the smaller precipitates will decompose and their mass will transport to the larger precipitates by diffusion. The coarsening rate of secondary Cr-carbide can be calculated by Equation 5.2:

$R^3 - R_o^3 = Kt$ --- Equation 5.2

where *t* is the heat treatment time, *K* is the coarsening rate R_o and *R* are the precipitate sizes at certain heat treatment time.

(Precipitate size)^3 was plotted against *(time)* in Figure 5.11 (a) and a linear fit regressed. The linear fit shows a slope of 3.4, which suggests that the coarsening rate *K* is 3.4 $nm^{-3}s^{-1}$. However, as illustrated in Figure 5.11 (a), the linear fit is not very good and R-square is only 0.68. Since the theory of Ostwald ripening is based on the assumption that the solute content in the matrix is nearly at equilibrium; in the initial stage a longer holding time is needed to fulfil this assumption. In the early stage of heat treatment, only part of the precipitates can be considered as coarsening while some of the precipitates are still in nucleation or growth stage.

A log plot was applied to (*precipitate size)* - (*time)* with a quite good fit (R-square of 0.93), as shown in Figure 5.11 (b), indicating that at the beginning of heat treatment the secondary Cr-carbides still grew and coarsened after 40 hours. The linear fit was then restricted to Alloy B HT-40 to HT-150 (Figure 5.11 (c)), leading to a much better fit ($R^2 = 0.81$) and a much smaller coarsening rate of 1.2 $nm^{-3}s^{-1}$.

Table 5.7 Coarsening rates of secondary Cr-carbide in heat treated Alloy B

Coarsening rate	Secondary Cr-carbides	
	HT-1 to HT-150	HT-40 to HT-150
Calculation / $nm^{-3}s^{-1}$	3.4	1.2
R-square	0.68	0.81

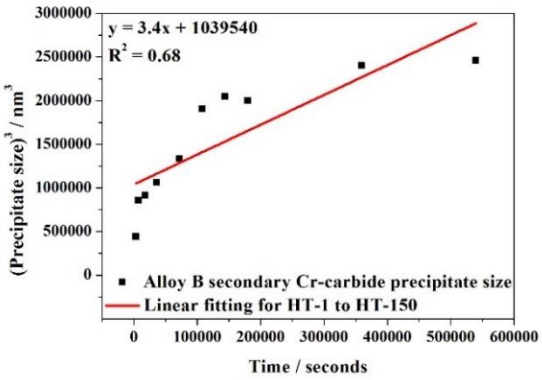

(a)

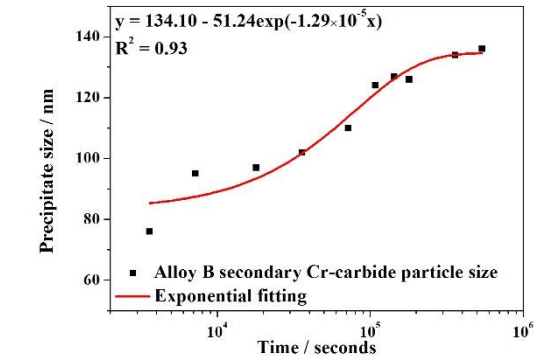

(b)

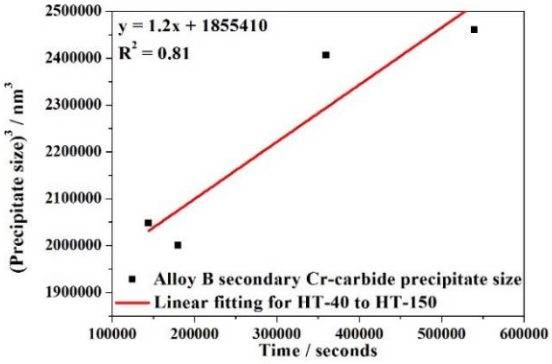

(c)

Figure 5.11 (a) (Precipitate size)^3 - (time) linear fit for Alloy B HT-1 to HT-150; (b) (Precipitate size) – (time) log fit for Alloy B HT-1 to HT-150 and (c) (Precipitate size)^3 - (time) linear fit for Alloy B HT-40 to HT-150

5.5 Summary of results

1. Larger area fractions of primary Cr-carbide (3.89 %) and primary Nb-carbide (1.40 %) were observed in as-cast Alloy A compared with as-cast Alloy B (2.75 % for primary Cr-carbide and 1.34 % for primary Nb-carbide);

2. Secondary Cr-carbides ($M_{23}C_6$) were also observed in crept Alloy B, which has a smaller area fraction (0.86%) compared with that in crept Alloy A (1.75%). Meanwhile, the secondary Cr-carbides in crept Alloy B has a smaller average precipitate (136 ± 68 nm) than crept Alloy A (159 ± 58 nm);

3. During heat treatment of Alloy B at 1000 ^{o}C from 1 to 150 hours, the area fraction of primary Cr-carbide fluctuates at first and then increases from 20 hours while the area fractions of primary Nb-carbide increases continuously from the beginning of heat treatment. The coarsening rate of primary Nb-carbide is lower than that of primary Cr-carbide;

4. Secondary Cr-carbides were observed in heat treated specimens, even in HT-1 Alloy B. During the heat treatments, the size of the secondary Cr-carbide increased rapidly to 76 nm after only 1 hour heat treatment and then continued to grow to 135 nm at 150 hours. The precipitate sizes for HT-100 and HT-150 are close: 134 nm for HT-100 and 135 nm for HT-150;

5. The precipitate size distributions of the secondary Cr-carbide for HT-1, HT-2 and HT-5 Alloy B are much narrower. For example, the full width at half maximum (FWHM) of HT-1 Alloy B is 58 nm, while the FWHM of HT-150 Alloy B is nearly twice that (99 nm). Meanwhile, the highest frequency in the distributions decreases with increasing heat treatment time, from around 0.30 in HT-1 Alloy B to around 0.15 in HT-150 Alloy B;

6. The coarsening rate of secondary Cr-carbide was obtained by the linear fit of $(Precipitate\ size)^3$-$(time)$ based on Ostwald ripening theory. The coarsening rate from HT-40 to HT-150 is 1.2 $nm^{-3}s^{-1}$.

5.6 Discussion

5.6.1 Effect of chemical composition on microstructure of HP40

From Table 3.1, the differences in chemical composition between Alloys A and B are that Alloy A contains more carbon (C), silicon (Si), manganese (Mn), nickel (Ni) and molybdenum (Mo) than Alloy B while Alloy B contains more nitrogen (N), chromium (Cr), niobium (Nb), tungsten (W) and iron (Fe) than Alloy A.

As shown in Table 5.1, as-cast Alloy A contains more primary Cr-carbide and primary Nb-carbide than as-cast Alloy B. The precipitation of primary carbides mainly depends on the content of carbon in the material, and Alloy A contains more carbon (0.46 wt%) than that of Alloy B (0.41 wt%). Meanwhile, some alloying elements have the effect of enhancing carbide precipitation. For example, as shown in Figure 4.19, the carbon solubility in Fe-18Cr austenitic stainless steel decreases with increasing nickel content [138]. Kawabe et al. [151] found that Mo has the effect of reducing the solubility of carbon and enhancing precipitation in AISI316 steel. The concentrations of Ni and Mo are both higher in Alloy A than in Alloy B, leading to an acceleration in carbide precipitation. Therefore, even though the concentrations of Cr and Nb in Alloy A are both less than those in Alloy B, larger area fractions of primary Cr-carbide (3.89 %) and primary Nb-carbide (1.40 %) were observed in as-cast Alloy A compared with as-cast Alloy B (2.75 % for primary Cr-carbide and 1.34 % for primary Nb-carbide).

The effects of Ni and Mo in decreasing the carbon solubility and enhancing carbide precipitation can also explain the different contents of secondary Cr-carbide between two alloys after creep, where the area fraction of secondary Cr-carbide in crept Alloy A is 1.75 % and that in crept Alloy B is only 0.86 %. Furthermore, Yan et al. [62] found that the addition of tungsten to HP40 can take away free carbon atoms and inhibit precipitation from the matrix. Thus, the existence of tungsten in crept Alloy B can suppress the formation of secondary Cr-carbide in the matrix and give rise to a smaller area fraction as compared with crept Alloy A.

Although the primary Cr-carbides in both Alloys A and B coarsened after creep (Table 5.1), the coarsening rates between two alloys appear to be different. It is obvious that the Alloy A coarsens more quickly, i.e. the ratio of primary Cr-carbide area fractions in as-cast and crept Alloy A is 1.35 (5.25/3.89) while that ratio in Alloy B is only 1.02. This faster coarsening behaviour in Alloy A is also supported by the measurements of secondary Cr-carbide precipitate size, which are 159 nm in crept Alloy A and 136 nm in crept Alloy B.

As mentioned in Section 4.5.2, the coarsening behaviour of the precipitates follows diffusion controlled Ostwald ripening theory, where the smaller precipitates decompose and their mass transported to the larger precipitates by diffusion. The coarsening rate *K*, which is strongly dependent on the concentrations and diffusion rates of different elements in the carbide and matrix, can be calculated by Equation 4.3:

$$K = 8\gamma V_p / \sum_{i=1}^{n} \frac{9(C_i^p - C_i^m)^2}{C_i^m D_i / RT}$$ --- Equation 4.3

K – – – Coarsening rate coefficient
γ – – – Interfacial energy
V_p – – – Molar volume for precipitate
C_i^p – – – Concentration of element in the precipitate
C_i^m – – – Concentration of element in the matrix
D_i – – – Diffusion coefficent of element in the matrix

The concentrations of different elements in $M_{23}C_6$ and the matrix at 1000 ^oC were obtained from simulation via JMat Pro. In this calculation, γ is 0.2 J/m^2 [152] and the molar volume of $M_{23}C_6$ is 6×10^{-6} m^3/mol [153].The diffusion coefficients of the various elements are listed in Table 5.9.

Table 5.8 The chemical compositions of $M_{23}C_6$ and matrix in Alloys A and B predicted by JMat Pro

Elements / at %	Alloy A		Alloy B	
	$M_{23}C_6$	Matrix	$M_{23}C_6$	Matrix
C	20.69	0.09	20.69	0.10
N	---	0.05	---	0.08
Si	---	3.02	---	2.05
Fe	10.06	37.42	10.13	38.84
Cr	66.21	22.03	66.57	23.39
Mn	0.32	1.07	0.24	0.78
Mo	0.24	0.01	0.05	0.01
Nb	6.55×10^{-4}	0.03	7.88×10^{-4}	0.03
Ni	2.47	36.27	2.31	34.73
Ti	5.78×10^{-7}	7.38×10^{-5}	1.02×10^{-6}	1.13×10^{-4}
W	---	---	0.12	0.01

Table 5.9 Diffusion coefficients of different elements in pure γ-Fe [154]

Elements	D_o / m^2s^{-1}	Q_v / KJ/mol	D_v / m^2s^{-1}
C	2×10^{3}	254	7.55×10^{-8}
N	0.70×10^{-4}	166	1.08×10^{-11}
Si	0.07×10^{-4}	243	7.48×10^{-16}
Fe	4.08×10^{-4}	311.1	7.03×10^{-17}
Cr	10.8×10^{-4}	291.8	1.15×10^{-15}
Mn	0.16×10^{-4}	261.7	2.91×10^{-16}
Mo	25.1×10^{-4}	323.7	1.32×10^{-16}
Nb	0.75×10^{-4}	264	1.11×10^{-15}
Ni	3.0×10^{-4}	314	3.90×10^{-17}
Ti	2100×10^{-4}	293.2	1.96×10^{-13}
W	0.509×10^{-4}	272	3.51×10^{-16}

Table 5.10 Calculated coarsening rates of secondary Cr-carbide $M_{23}C_6$ in Alloy A and B

Coarsening rate	Secondary Cr-carbides	
	Alloy A	Alloy B
Calculation / $m^{-3}s^{-1}$	8.64×10^{-27}	8.48×10^{-27}

The calculated coarsening rates of secondary Cr-carbide $M_{23}C_6$ in Alloy A and Alloy B based on Equation 4.3 are listed in Table 5.10. The calculated coarsening rates of the two alloys show that Alloy A has a slightly larger coarsening rate in agreement with the experimental measurements. Even though the larger concentration of Mo and its low diffusion rate in Alloy A can delay the coarsening of Cr-carbides, the combined effects of more iron, titanium and tungsten in Alloy B lead to a smaller coarsening rate for $M_{23}C_6$.

However, two things may influence the accuracy of the calculation. Firstly, the concentrations of elements from the JMat Pro simulation are for equilibrium, while the as-cast alloys originally formed via non-equilibrium solidification leading to a supersaturated solid solution of elements in the matrix. Also, the niobium and titanium can reduce the matrix carbon content and retard the growth of $M_{23}C_6$ due to the formation of intragranular Nb(C, N) [22]. Secondly, the diffusion coefficients involved in the calculation are those for pure γ-Fe and in reality some elements [155], such as nitrogen, will have a strong influence on the diffusion behaviour of other alloying elements in the austenite. Thier et al. [156] found that nitrogen reduces the diffusivity of carbon and chromium and therefore delays the coarsening rate of $M_{23}C_6$. Furthermore, another effect of nitrogen on coarsening rate is to decrease the mismatch between $M_{23}C_6$ and austenite [50], which can reduce the interfacial energy between $M_{23}C_6$ and austenite and thus inhibit coarsening.

5.6.2 Precipitation evolution in Alloy B

As shown in Section 5.4, to understand the microstructural evolution during long-term creep, heat treatments for Alloy B at 1000 °C from 1 to 150 hours were carried out. The area fractions for primary Cr-carbide, primary Nb-carbide and secondary Cr-carbide for heat treated Alloy B (HT-1 to HT-150) were measured (Table 5.5 and Figure 5.7).

It is interesting that the area fractions of both the primary Nb-carbide and secondary Cr-carbide increase continuously from the beginning of heat treatment while the area fraction of primary Cr-carbide fluctuates at first and then increases from 20 hours. As discussed in Section 4.5.1, for the as-cast condition, the primary Cr-carbide in HP40 is M_7C_3 type which transforms to $M_{23}C_6$ during creep, indicating that the M_7C_3 is relatively unstable at 1000 °C. Therefore, besides the transformation from M_7C_3 to $M_{23}C_6$, the dissolution of primary M_7C_3-carbide is also expected to progress during the heat treatments.

Dissolution of M_7C_3 has been widely observed in ferritic and austenitic steels during heat treatments [33, 66, 157-160]. However, the dissolution temperature of M_7C_3 can be anywhere over a large temperature range due to the different chemical compositions in steels. Based on the analysis of four different alloyed 18Cr steels heat treated at 1100 °C, Kuzucu et al. [66] found that the initial temperatures of dissolution of these phases is about 850 °C, but the final temperatures for the completion of M_7C_3 dissolution vary from 1000 to 1098 °C. Jiang et al. [157] gave a similar initial dissolution temperature of M_7C_3, which is around 900 °C in a 0.45C-25Cr-11Ni-Co superalloy. However, the dissolution was not detected above 1100 °C in a 6.8Cr tool steel [158] and the maximum temperature for dissolution in a 23Cr-N steel was found to be 1050 °C [159]. In summary, the temperature range of M_7C_3 dissolution is 850~1100 °C while the holding temperature for heat treated Alloy B is 1000 °C, suggesting the possibility of M_7C_3 dissolution during heat treatment.

The dissolution of M_7C_3 will lead to a progressive reduction in the area fraction of the carbides, as confirmed by an in situ observation of dissolution of carbides in a Fe-1.72Cr-2.54C steel [161]. The temperature will change significantly the time to complete the dissolution. However, the time to complete the dissolution is dependent on the temperature. For example, according to simulation of Fe-Cr-C by John Argen [160], at 1200 ^oC, complete dissolution of M_7C_3 in austenite requires about 15 min whereas 1.5 min is sufficient at 1260 ^oC (Figure 5.12). This difference is mainly due to the temperature dependence of the Cr diffusion coefficient.

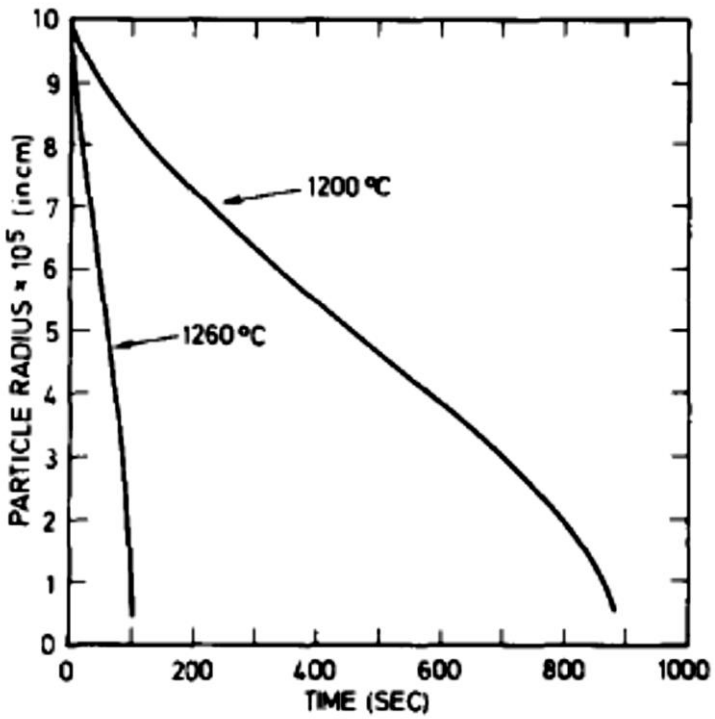

Figure 5.12 The dissolution of high chromium M_7C_3 in austenite at two temperatures [160]

Based on the work of Masoumi et al. [162], the dissolution of a spherical precipitate under diffusion controlled conditions can be formulated as:

$\frac{dr}{dt} = -\frac{kD}{2}\left[\frac{1}{r} + \frac{1}{\sqrt{\pi Dt}}\right]$ --- Equation 5.1

The solution to Equation 5.1 is:

$r_t = r_o - \frac{kDt}{2r_o} - \frac{k\sqrt{Dt}}{\sqrt{\pi}}$ --- Equation 5.2

where r_t is the particle radius after 't' seconds, r_o is the initial precipitate radius (in as-cast Alloy B). The time when r_t decreases to zero is the completion of dissolution. D is the diffusion coefficient of Cr in γ-Fe at temperature T. k is the supersaturation and is given by

$k = \frac{2(C_o - C_i^e)}{C_p^e - C_i^e}$ --- Equation 5.3

where c_o is the solute concentration in the matrix, c_i^e and c_p^e are equilibrium solute concentrations at the precipitate-matrix interface and in the precipitate respectively. The values c_o, c_i^e and c_p^e were determined by JMat Pro, leading to a k of 0.16.

The diffusion coefficient of Cr in γ-Fe at 1000 °C is listed in Table 5.9, as 1.15×10^{-15} m^2/s. However, this model is based on the assumption that the precipitate is spherical while in Alloy B the primary M_7C_3 is granular and acicular. To solve this problem, the areas of fifty primary M_7C_3-carbides in as-cast Alloy B were measured to define an equivalent radius r_e based on Equation 5.4:

$A = \pi(r_e)^2$ --- Equation 5.4

The average area for primary M_7C_3-carbides (fifty measurements) in as-cast Alloy B is 16.41 μm^2, leading to an equivalent radius r_e of 2.29 μm.

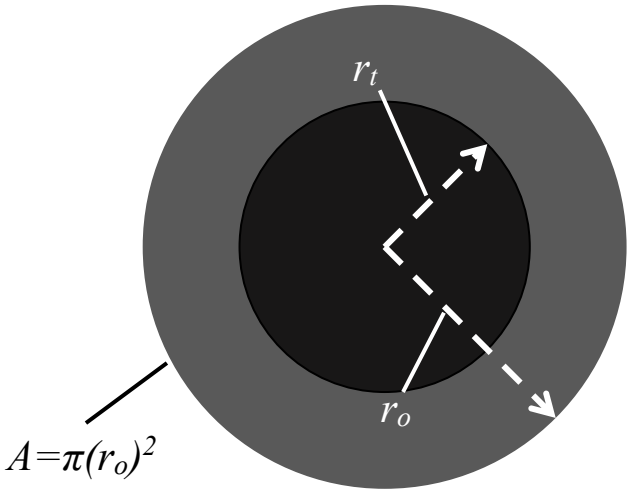

Figure 5.13 Schematic of the radius evolution during dissolution

Importing all the necessary values into Equation 5.2, the predicted time to complete the dissolution of M_7C_3 in Alloy B is 41830 seconds (11.6 hours) while the experimental measurement shows that the minimum area fraction of primary M_7C_3-carbide was observed in HT-2 Alloy B (2 hours). However, the area fraction increases again from HT-2 to HT-5. Jiang et al. [33] found the dissolution of M_7C_3 provided the precipitation of $M_{23}C_6$ with essential carbon. The carbon leads to a rapid nucleation and growth of $M_{23}C_6$, which is faster than the dissolution of M_7C_3. The combination of M_7C_3 dissolution and $M_{23}C_6$ growth is reflected: the re-increase in area fraction of primary Cr-carbide from HT-2 to HT-5 Alloy B.

However, the in situ transformation of primary Cr-carbides from M_7C_3 to $M_{23}C_3$ cannot change the non-equilibrium condition of chemical concentration close to grain boundaries. Some of the primary $M_{23}C_6$ is expected to dissolve when there are insufficient elements for further growth, i.e. after the completion of M_7C_3 dissolution (11.6 hours). Therefore, another reduction in area fraction of primary Cr-carbide was found between 5 and 20 hours for Alloy B. The calculation of a dissolution time based on Equation 5.2 is not applied to $M_{23}C_6$ due to the lack of an initial particle radius. The area fraction of primary Cr-carbide then increases continuously from 20 hours indicating that the dissolution of $M_{23}C_6$ has finished before 20 hours and that then there are only growth and coarsening of primary Cr-carbides. The microstructural evolution of primary Cr-carbide is summarized in Figure 5.14.

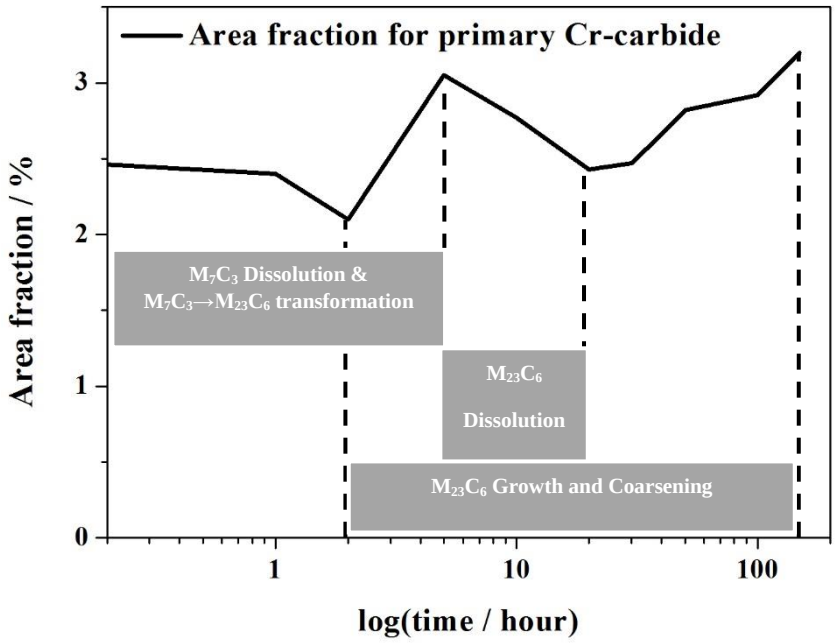

Figure 5.14 Microstructural evolution of primary Cr-carbides

The fluctuation in area fraction of primary Cr-carbide only occurs due to its dissolution. In comparison, the area fractions of secondary Cr-carbide and primary Nb-carbide increase continuously from the beginning of the heat treatment. However, the coarsening rate of Nb-carbide is much smaller than that of the Cr-carbides since there is very little niobium left in the austenitic matrix for further coarsening. The insufficient solute content and slow diffusion rate of niobium in the matrix lead to the lower coarsening rate of Nb-carbide.

The secondary Cr-carbides precipitated from supersaturated solid solution grow rapidly at the expense of matrix solutes. The average precipitate size will gradually increase and the number of precipitates will decrease, i.e. they will coarsen. Precipitate coarsening is driven by the difference of solute concentrations at the precipitate-matrix interfaces.

According to the Gibbs-Thomson effect, the solute concentration at the particle/matrix interface varies with the curvature of the interface. This variation can be quantitatively described:

$C_r = C_\infty \exp(\frac{2\gamma V_m}{RTr})$ --- Equation 5.5

where C_r is the concentration of solute at outside of the precipitate-matrix interface, C_∞ is the equilibrium concentration of solute atoms, V_m is the molar volume of the precipitate, γ is the interfacial energy and r is the precipitate radius.

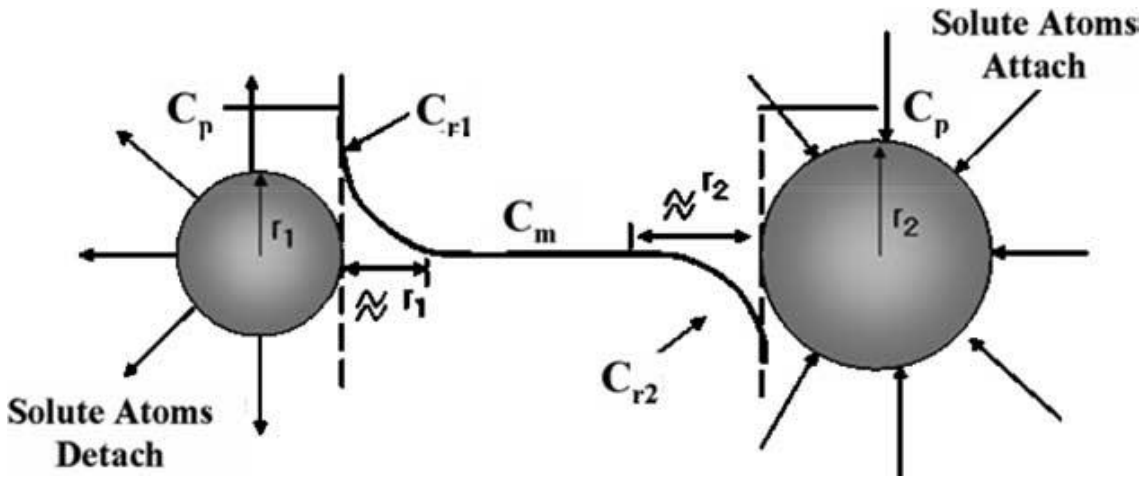

Figure 5.15 Schematic concentration profile between large and small particles [163]

This indicates that a smaller particle has a higher solute concentration at the precipitate-matrix interface. Figure 5.15 illustrates schematically the concentration profile between a small (r_1) and a large (r_2) precipitate. C_{r1} and C_{r2} are solute concentrations determined by Equation 5.5 at the precipitate-matrix interface. C_m is the mean solute concentration in the matrix. As shown in Figure 5.15, the solute concentration at the small (more highly curved) precipitate-matrix interface is higher than that of the large one. Therefore, solute atoms will detach into the matrix from a small precipitate and then attach onto a large precipitate until the small particle disappears. There will be a critical particle size r_c when C_r is equal to C_m and no transport of solute atoms occurs. By this process, the precipitates smaller than r_c will dissolve and the precipitates larger than r_c will coarsen.

As shown in Figure 5.10, at the beginning of heat treatment (HT-1 Alloy B), most of the precipitates are around 70 nm in diameter leading to quite a sharp distribution. With increase in holding time, the smaller precipitates continuously dissolved into the matrix while the larger precipitates coarsened. This makes the average precipitate size shift to a larger value and the precipitate size distribution to become flatter. This tendency will remain until all the precipitates achieve the critical size.

(Precipitate size)^3 was plotted against *(time)* in Figure 5.11 (a) to determine the coarsening rate. The linear fit shows a slope of 3.4, which suggests that the coarsening rate K is 3.4 $nm^{-3}s^{-1}$. However, the linear fit is not very good and R-square is only 0.68. The fit was then restricted to Alloy B HT-1 to HT-40 (Figure 5.11 (b)), leading to a much better fit ($R^2 = 0.93$) and the much larger coarsening rate of 10.4 $nm^{-3}s^{-1}$. The coarsening rate from HT-40 Alloy B to HT-150 Alloy B has also been calculated to be 1.2 $nm^{-3}s^{-1}$.

A similar coarsening behaviour of Mo_6C carbide at three different temperatures was found by Wey et al. [121] (Figure 5.15). The graph appears to be linear from the initial stage at 1373 K, but not at 1273 K and 1173 K. The growth of carbide at 1273 and 1173 K initially takes place at a higher rate until several tens of hours and then it occurs at a lower rate.

The theory of Ostwald ripening is based on the assumption that the solute content in the matrix is nearly at equilibrium; in the initial stage a longer holding time or a higher holding temperature is needed to fulfil this assumption. In the early stage of heat treatment, only part of the precipitates can be considered as coarsening while some of the precipitates are still growing. Therefore, the rate obtained from relatively longer holding times, HT-40 to HT-150, is the coarsening rate well described by Ostwald ripening. The calculated coarsening rate (8.4 $nm^{-3}s^{-1}$) of Alloy B (Table 5.10) falls into the same magnitude range as the coarsening rate (1.2 $nm^{-3}s^{-1}$) obtained by fitting to experimental measurements. The smaller coarsening rate obtained by fitting to experimental measurements indicates that the diffusion rates of solute elements used in the calculation (Table 5.9) are not accurate. Diffusion will be much slower in highly alloyed austenite compared with pure γ-Fe.

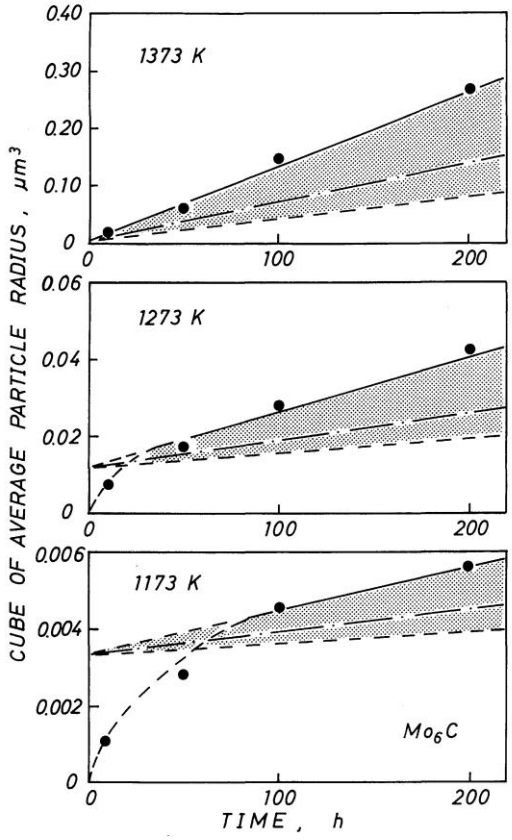

Figure 5.16 A plot of the cube of average particle radius of Mo_6C carbides vs heating time [121]

5.6.3 Creep behaviour of Alloy A and Alloy B

The creep behaviours of Alloys A and B have been compared in Section 2.4.5; Alloy B shows a better creep performance, i.e. a longer creep life (Figure 2.53) and a smaller minimum creep rate (Figure 2.54). As discussed in Section 2.4.4, in intragranular precipitation strengthened alloys like HP40, the microstructural parameters of the precipitates and thus the back stress obtained from the dislocation climb process are the key factor for the creep properties.

The back-stress σ_b is the threshold stress to overcome the interactions between dislocations and intragranular precipitates, bypass by climb in this case. These interactions oppose the glide of the dislocations, leading to a decrease in the effective applied stress on the material and, furthermore, a reduction in the creep rate, based on Equations 2.3 and 2.4.

$\sigma_{eff} = \sigma - \sigma_b$ --- Equation 2.3

$\dot{\varepsilon} = A''(\sigma - \sigma_b)^n \exp(-\frac{Q}{kT})$--- Equation 2.4

The threshold stress of climb can be calculated using Equation 5.6 [164].

$\sigma_{climb} = \frac{0.32Gb}{\lambda_p}$--- Equation 5.6

where G is the shear modulus, b is the Burgers vector and λ_p is the average precipitate interspacing.

The back stress contributed by climb can be considered as the same as threshold stress

$\sigma_{b(climb)} = \sigma_{climb}$--- Equation 5.7

The average precipitate interspacings of Alloy A and B have been measured and are listed in Table 5.2: 565 nm for crept Alloy A and 497 nm for crept Alloy B. The shear moduli and Burgers vectors of Alloys A and B, which are needed for calculations of the climb threshold stress using Equation 5.6, are listed in Table 5.11:

Table 5.11 Calculations of climb CRSS, back stress and effective stress of Alloy A and B

		Alloy A	Alloy B
Creep properties	Creep life / hour	104	124
	Minimum creep rate / s^{-1}	4.50×10^{-8}	2.45×10^{-8}
Microstructural parameters for crept specimens	Average precipitate size / nm	159 ± 58	136 ± 68
	Average precipitate interspacing / nm	565 ± 66	497 ± 149
Parameters for calculations	Shear modulus / GPa [165]	45.27	45.27
	Burgers vector / nm [166]	0.25	0.25
Calculation results based on Equation 2.3, 5.6 and 5.7	Climb threshold stress / MPa	6.41	7.29
	Back stress / MPa	6.41	7.29
	Effective applied stress / MPa	33.69	32.71

Although the accuracy of the equations for critical shear stress are approximate, it is obvious that the climb threshold stress in Alloy B is much larger than that in Alloy A due to the relatively small precipitate interspacing. The larger threshold stress will contribute more to back stress in Alloy B.

Based on Equations 2.3 and 2.4, with the same applied stress of 40 MPa during the creep tests, there is a smaller effective stress and thus a smaller creep rate in Alloy B, which is in agreement with the minimum creep rates measured. This smaller minimum creep rate helps lead to a longer creep life for Alloy B (124 h) than that for Alloy A (104 h).

5.7 Conclusions

1. The additions of W and Nb in Alloy B suppressed the formation of carbides by reducing free carbon in the matrix, leading to a smaller area fraction of primary Cr-carbide (2.75 %) and primary Nb-carbide (1.34 %) in as-cast Alloy B compared with as-cast Alloy A (3.89 % for primary Cr-carbide and 1.40 % for primary Nb-carbide);

2. The combined effects of Ti and W led to a slower coarsening behaviour of secondary Cr-carbides in Alloy B than in Alloy A, which is in agreement with experimental observation, i.e., a smaller area fraction and a smaller average precipitate size in crept Alloy B than in crept Alloy A;

3. The area fractions of primary and secondary carbides, precipitate size and interspacing of secondary $M_{23}C_6$ in heat treated Alloy B were also characterised. During heat treatment of Alloy B at 1000 ^{o}C from 1 to 150 hours, the area fractions of primary Nb-carbide and secondary Cr-carbide and the average size of secondary $M_{23}C_6$ increases continuously from the beginning of heat treatment due to the growth and coarsening of precipitates;

4. The combination of M_7C_3 dissolution, $M_7C_3 \rightarrow M_{23}C_6$ transformation and $M_{23}C_6$ growth leads to a fluctuation in area fraction of primary Cr-carbide up to 20 hours in heat treated Alloy B. After 20 hours, the area fraction of primary Cr-carbide increase continuously with a faster rate than that of primary Nb-carbide due to the insufficient solute content and slow diffusion rate of niobium in the matrix.;

5. It is the back stress exerted by the smaller precipitate size of secondary $M_{23}C_6$ that leads to a smaller creep rate and thus a longer creep life for Alloy B as compared with Alloy A.

Chapter 6 Effect of solidification rate on microstructure of HP40 (Alloy C c.f. Alloy B)

6.1 Microstructure of as-cast Alloy C

In Chapter 5, the effect of chemical composition on microstructure of HP40 has been discussed by comparison between Alloy A and B. In this chapter, another effect, solidification rate, on microstructure of HP40 will be described based on the observations between Alloy B and C, which are in the same HP40 modified alloy range but produced under different solidification rate.

Although the actual solidification rate during production is impossible to be measured, it is definite that the Alloy B has a lower solidification rate than that of Alloy C due to different refractory compositions coated on casting moulds.

Figure 6.1 shows the microstructure of as-cast Alloy C obtained by BSE. The morphologies of primary Cr-carbide and primary Nb-carbide are both composed of granular and acicular types, which are similar to the morphologies found in Alloy B. The area fractions of primary Cr-carbide and primary Nb-carbide were measured and are listed in Table 6.1: 2.12 % for M_7C_3 and 1.80 % for NbC. As-cast Alloy C contains less M_7C_3 and more NbC as compared with as-cast Alloy B.

The dendrite cell size (DCS) and secondary dendritic arm spacing (SDAS) are widely used as parameter for correlating solidification rate and the microstructures. Therefore, the dendrite cell sizes and secondary dendritic arm spacings of as-cast Alloy B and C were measured. From Table 6.2, both of DCS and SADS in Alloy C are smaller than those in Alloy B.

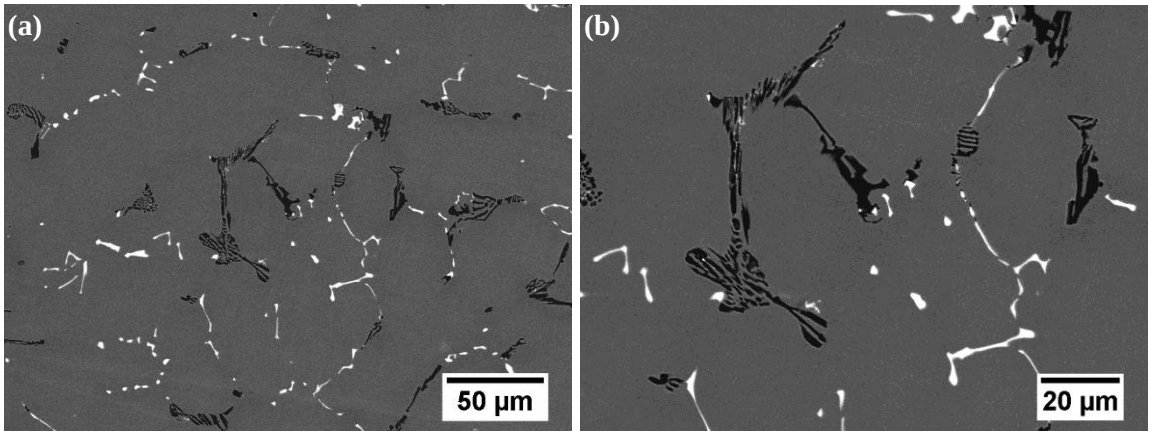

Figure 6.1 (a) low magnification and (b) high magnification BSE images obtained from as-cast Alloy C

Table 6.1 Area fractions of various carbides in as-cast and crept Alloy B and Alloy C

Specimen	Area fraction%		
	Primary Cr-carbide	Secondary Cr-carbide	Primary Nb-carbide
As-cast Alloy B	2.75±0.08	---	1.34±0.11
As-cast Alloy C	2.12±0.18	---	1.80±0.10
Crept Alloy B	2.82±0.51	0.86±0.12	1.34±0.10
Crept Alloy C	2.94±0.41	0.82±0.18	1.93±0.06

Table 6.2 Dendrite cell sizes and secondary dendritic arm spacings in as-cast Alloy B and Alloy C

Specimen	DCS / µm	SDAS / µm
As-cast Alloy B	66.62 ± 20.90	30.11 ± 5.34
As-cast Alloy C	51.66 ± 20.10	25.48 ± 3.52

6.2 Microstructure of crept Alloy C

The microstructure of crept Alloy C (1000 ˚C and 40 MPa for 13 hours) is illustrated in Figure 6.2. After creep, the primary Cr-carbide transformed to $M_{23}C_6$ type while the primary Nb-carbide remained as NbC type. The primary network of chromium carbides also coalesced and enlarged during the creep test. The area fraction of primary Cr-carbides increased from 2.12 % to 2.94 % during creep whilst that of the primary Nb-carbides increased to 1.93 %.

The area fraction of secondary Cr-carbide in crept Alloy C is 0.82 %, quite close to that in crept Alloy B. The precipitate size and interspacing of secondary Cr-carbide ($M_{23}C_6$) in crept Alloy C were measured and compared with those in crept Alloy B. The average precipitate size in crept Alloy C is 108 nm. Meanwhile, a Gaussian fit was applied to the particle size distribution resulting a mean of 94 nm and a FWHM of 86 nm, both of which are both smaller than those of crept Alloy B.

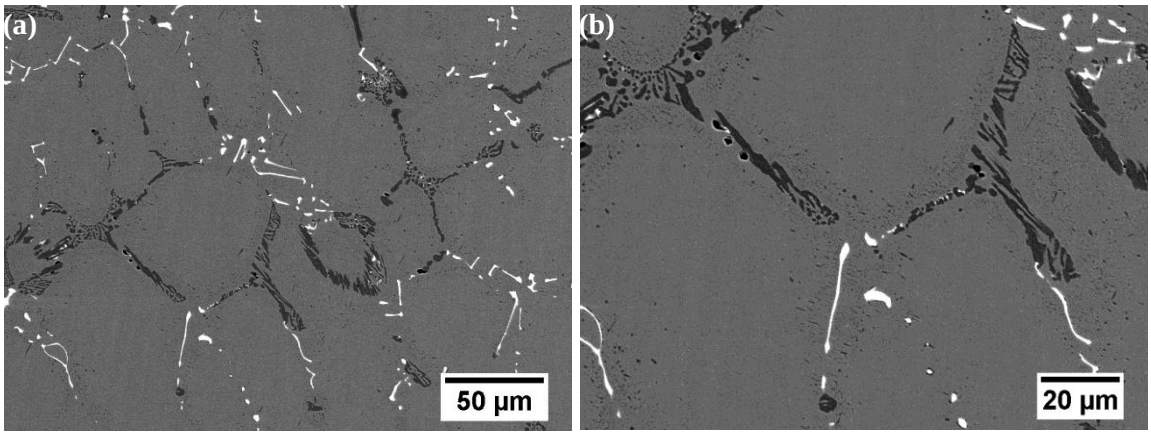

Figure 6.2 (a) Low magnification and (b) high magnification BSE images obtained from crept Alloy C

Table 6.3 Microstructural parameters of secondary Cr-carbide $M_{23}C_6$ in crept Alloy B and crept Alloy C

Specimens	Precipitate size		Interspacing
	Average precipitate size	Gaussian mean	
Crept Alloy B	136 ± 68 nm	110 nm	497 ± 149 nm
Crept Alloy C	108 ± 37 nm	94 nm	399 ± 64 nm

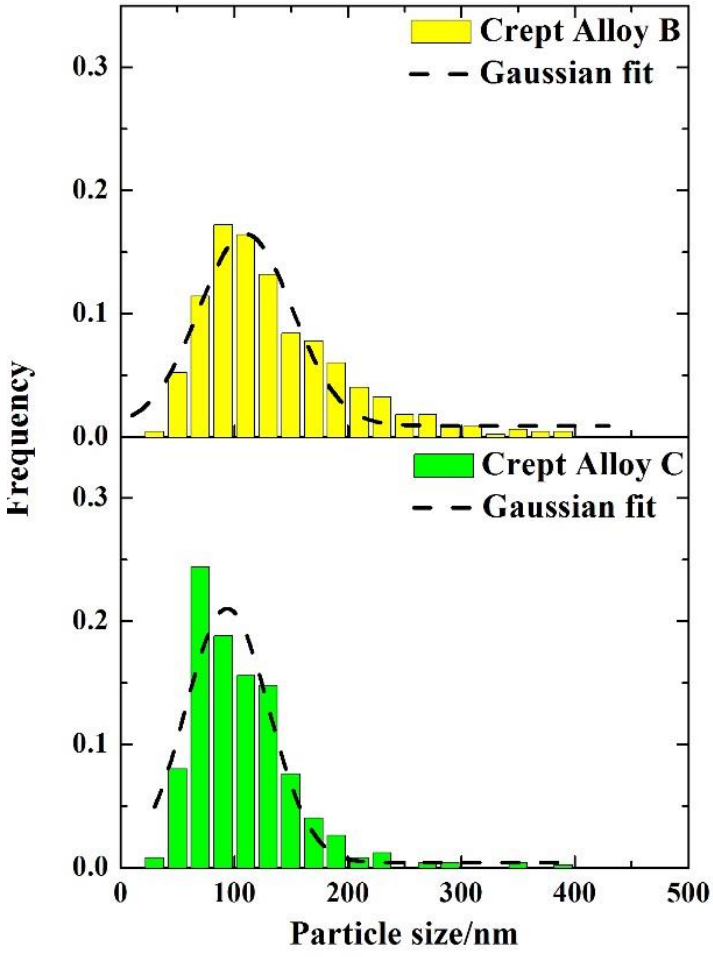

Figure 6.3 Particle size distributions for crept Alloy B and crept Alloy C

6.3 Microstructure of heat treated Alloy C

To understand the microstructural evolution during the long-term creep, heat treatments for Alloy C at 1000 ºC from 1 to 150 hours were applied, since the creep life of Alloy C at a temperature of 1000˚C and a stress of 40MPa is 150 hours. The detailed heat treatment process was the same as for heat treated Alloy B and was described in Section 3.2.

Figure 6.4 shows the BSE images obtained from heat treated Alloy C, from Alloy C HT-1 to HT-150. The primary carbide network has enlarged and become more globular with the increase of heat treatment time. Furthermore, the coalescence of the primary carbides and the nucleation and growth of more carbides make the carbide network more continuous. The area fraction of primary Cr-carbide increases continuously; after heat treating for 50 hours, the coarsening rate becomes slightly lower. The area fractions of Nb-carbide and secondary Cr-carbide become nearly constant for HT-100 and HT-150 after a significant increase from HT-1 to HT-50.

The area fractions for primary Cr-carbide, primary Nb-carbide and secondary Cr-carbide were also measured (Table 6.4 and Figure 6.5) while the fourth column in Table 6.5, area fraction of Cr-carbide, is a combination of the area fractions of the primary and secondary Cr-carbides. The area fraction of primary Cr-carbide fluctuates at first and then increases continuously from 20 hours to 50 hours while after heat treating for 50 hours, the area fraction of primary Cr-carbide decreases slightly. The area fraction of secondary Cr-carbide started to increase from the very beginning and increases about twice from 0.97 % for HT-1 to 1.76 % for HT-150, which is much smaller than for heat treated Alloy B (2.34 %). However, the area fraction of primary Nb-carbide becomes nearly constant at around 2 % after a significant increase between 1 hour and 30 hours.

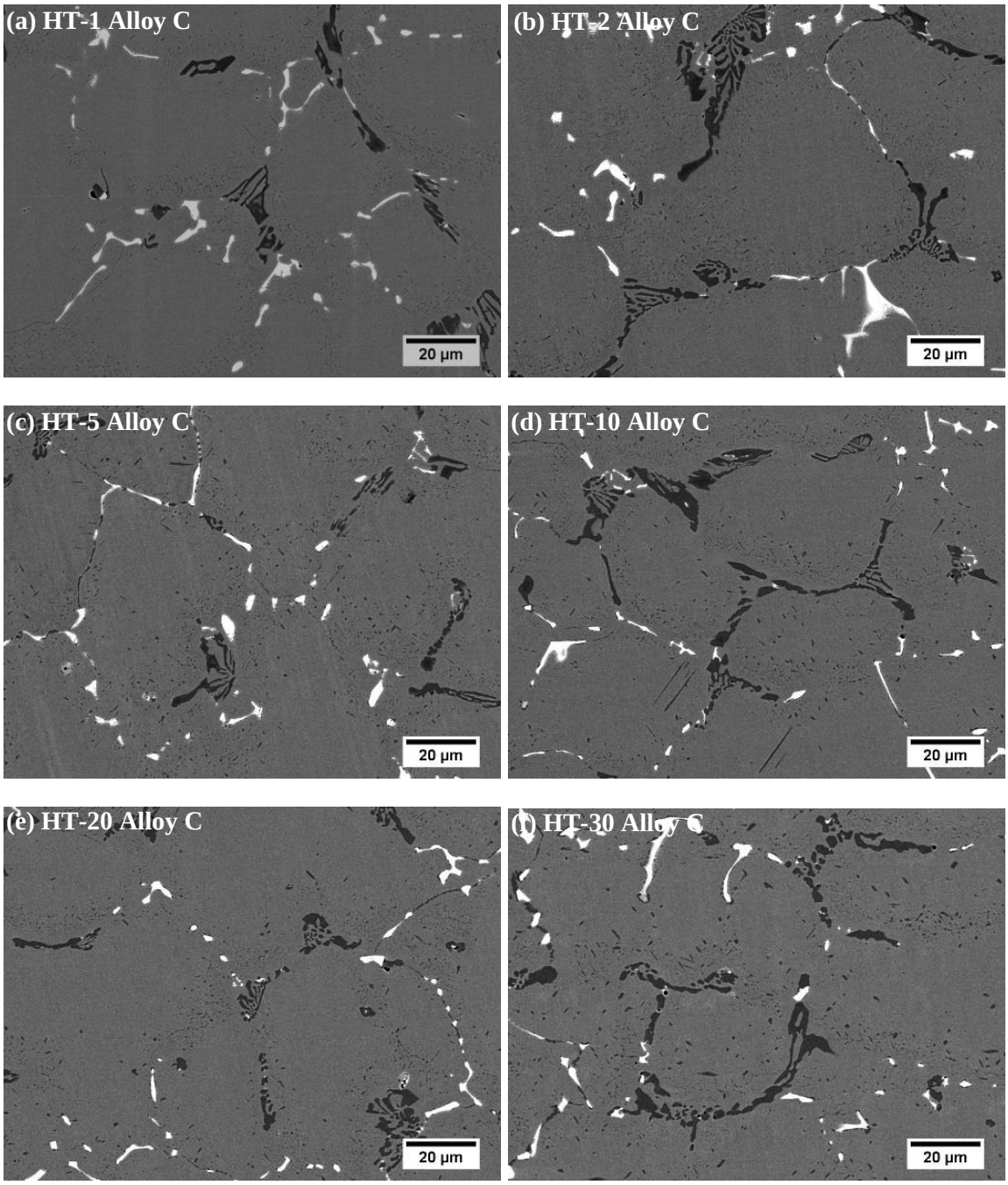
(a) HT-1 Alloy C
20 µm
(b) HT-2 Alloy C
20 µm
(c) HT-5 Alloy C
20 µm
(d) HT-10 Alloy C
20 µm
(e) HT-20 Alloy C
20 µm
(f) HT-30 Alloy C
20 µm

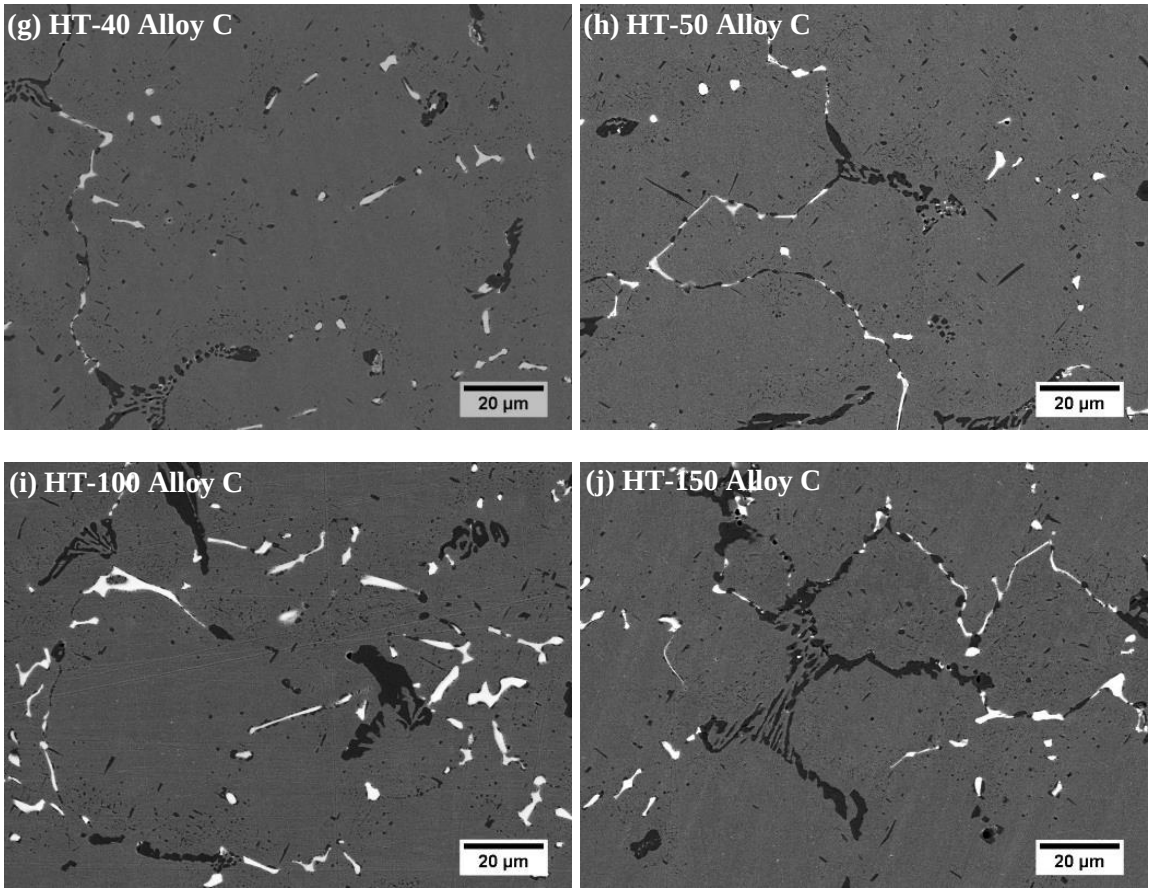

Figure 6.4 BSE images (a)-(j) obtained from Alloy C, HT-1 to HT-150

Table 6.4 Area fractions of various carbides in heat treated Alloy C

Specimen	Area fraction%			
	Primary Cr-carbide	Secondary Cr-carbide	Cr-carbide (Total)	Primary Nb-carbide
As-cast	2.12±0.18	---	2.12±0.18	1.80±0.10
HT-1	1.23±0.03	0.97±0.29	2.20±0.26	1.79±0.11
HT-2	1.35±0.06	1.06±0.24	2.41±0.30	1.86±0.08
HT-5	1.97±0.14	1.05±0.26	3.02±0.40	1.95±0.06
HT-10	1.86±0.05	1.21±0.35	3.07±0.30	1.95±0.07
HT-20	1.95±0.04	1.39±0.28	3.34±0.24	1.96±0.12
HT-30	2.53±0.12	1.39±0.26	3.92±0.14	1.99±0.11
HT-40	2.51±0.11	1.47±0.21	3.98±0.20	1.99±0.07
HT-50	2.60±0.13	1.54±0.38	4.14±0.25	2.00±0.12
HT-100	2.43±0.07	1.75±0.15	4.18±0.22	1.97±0.10
HT-150	2.42±0.28	1.76±0.47	4.18±0.19	2.00±0.11

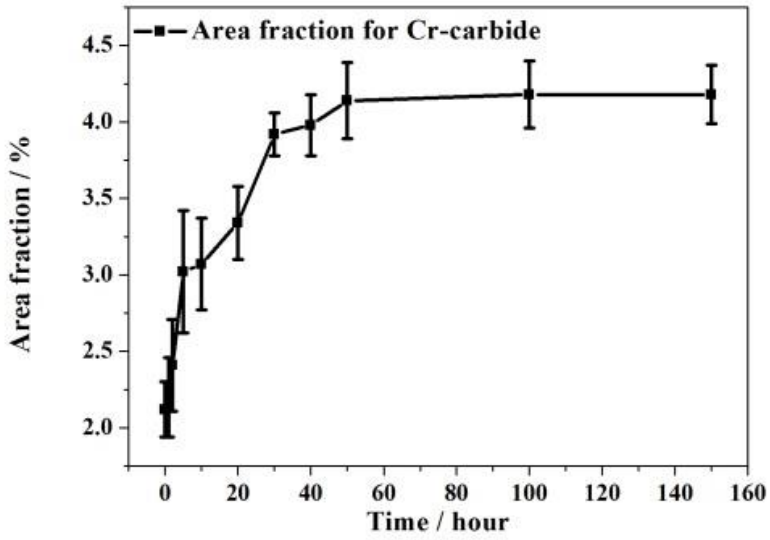
Area fraction for Cr-carbide
Area fraction / %
Time / hour
4.5
4.0
3.5
3.0
2.5
2.0
0
20
40
60
80
100
120
140
160

(a)

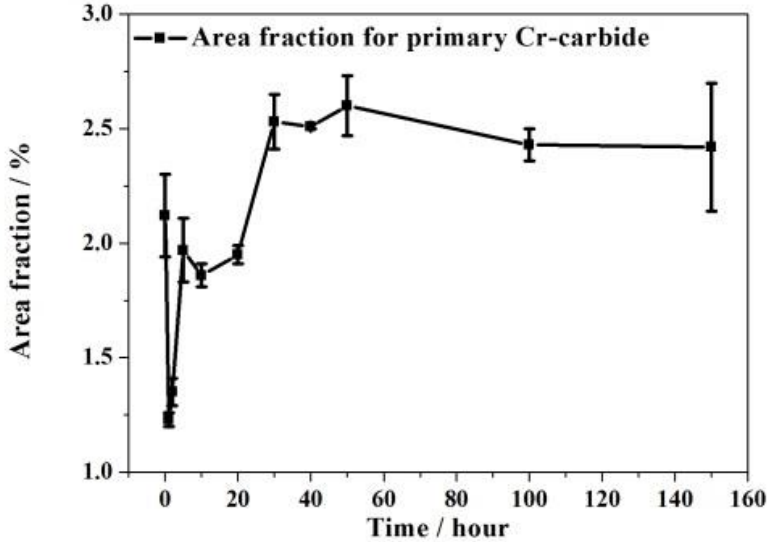
Area fraction for primary Cr-carbide
Area fraction / %
Time / hour
3.0
2.5
2.0
1.5
1.0
0
20
40
60
80
100
120
140
160

(b)

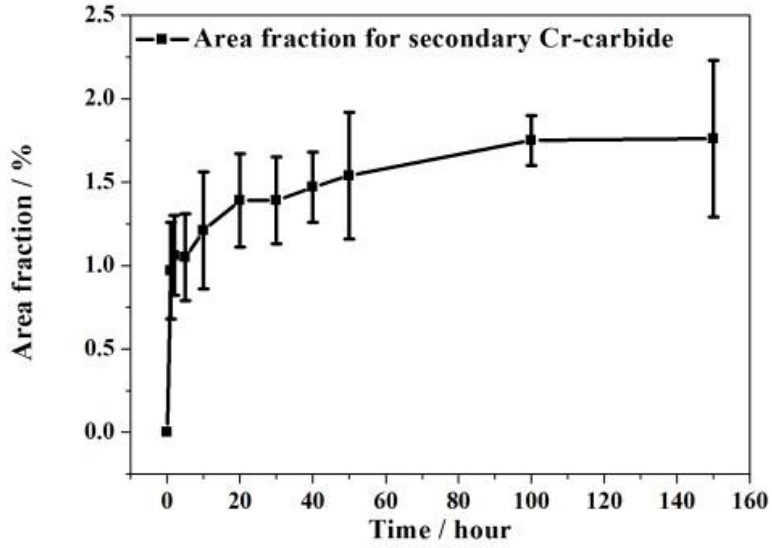

(c)

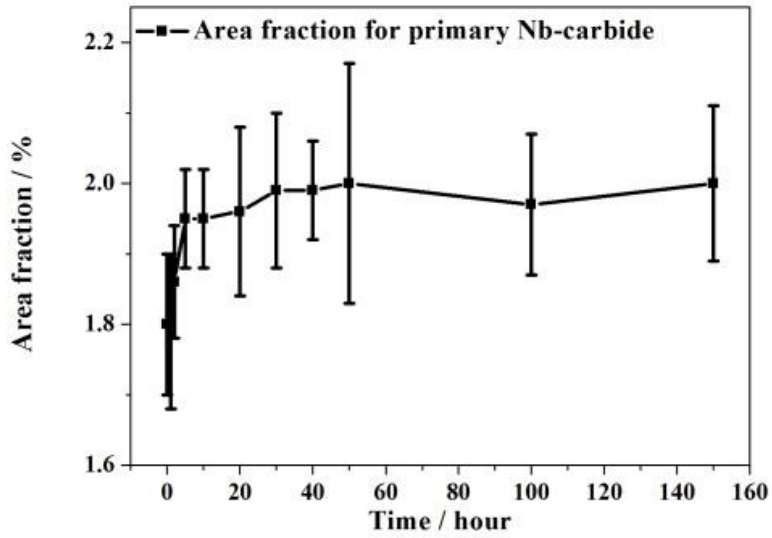

(d)

Figure 6.5 Area fractions of (a) Cr-carbide; (b) primary Cr-carbide, (c) secondary Cr-carbide and (d) primary Nb-carbide for Alloy C as a function of heat treatment time

In Alloy C HT-1, HT-2 and HT-5, different contrast was observed in the BSE images of primary Cr-carbide (Figure 6.6), illustrating the transformation of primary Cr-carbide. EBSD mapping (Figure 6.7) of primary Cr-carbide in HT-5 Alloy C confirms that the outside shell is $M_{23}C_6$ carbide and that the core is M_7C_3 type carbide. Meanwhile, the orientation mapping (Figure 6.7 (c)) illustrates that the $M_{23}C_6$ has a similar orientation with austenite matrix.

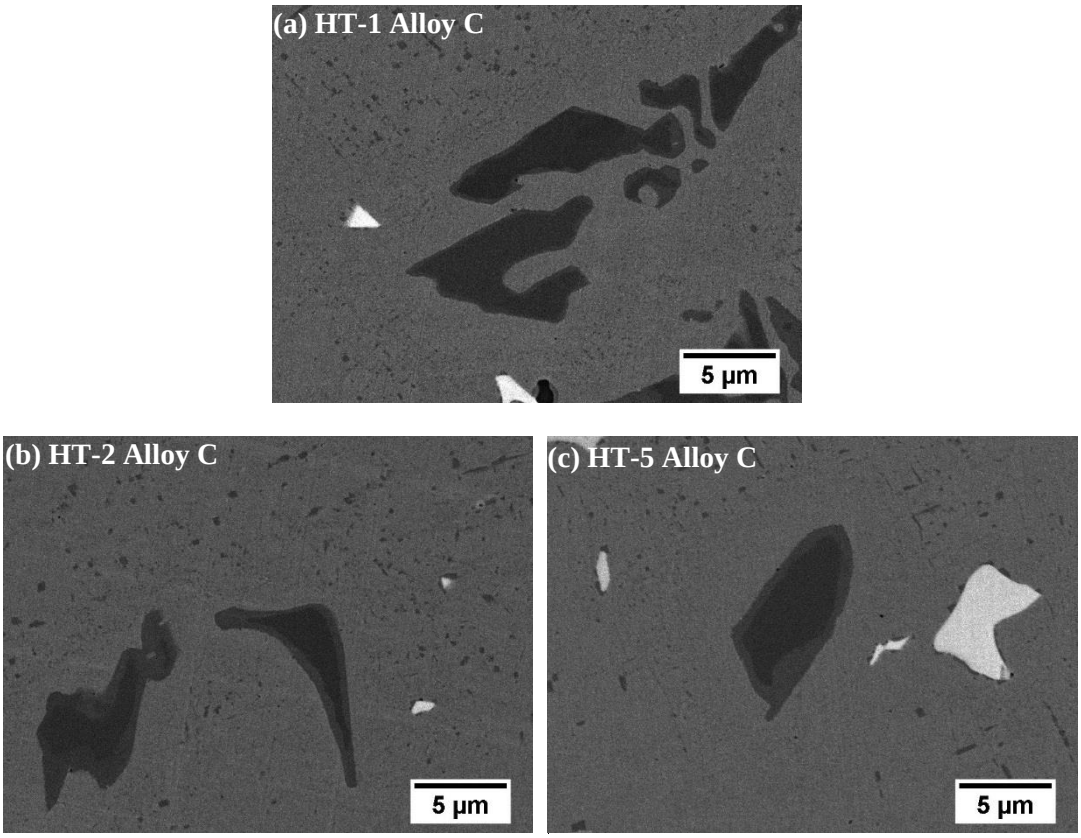

Figure 6.6 BSE image obtained from (a) Alloy C HT-1; (b) Alloy C HT-2 and (c) Alloy C HT-5 illustrating primary Cr-carbides with different contrast

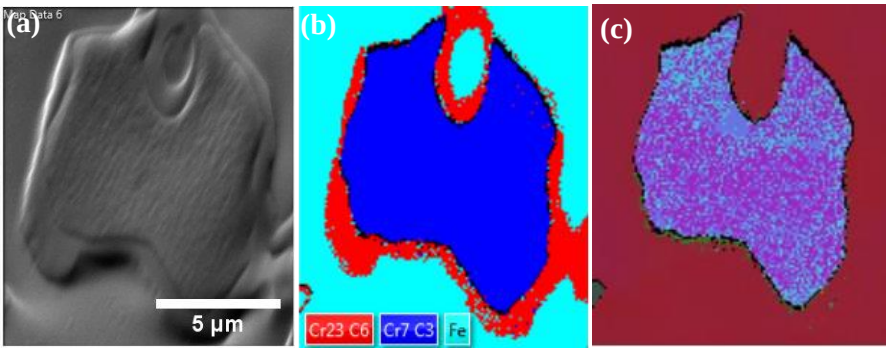

Figure 6.7 Primary Cr-carbide in HT-5 (a) SE image; (b) phase map; (c) orientation map

A primary Cr-carbide in HT-5 Alloy C (Figure 6.8 (a)) was selected for a TEM specimen to be prepared via focused ion beam (FIB), as shown in Figures 6.8 (b) and (c). A TEM bright field image of the FIB-TEM specimen cut from the selected primary Cr-carbide is shown in Figure 6.9 (a). It is clear that the M_7C_3 is covered by a shell of $M_{23}C_6$. An EDS line scan was carried out across the M_7C_3, the $M_{23}C_6$ and the austenitic matrix; the line scan direction is shown in Figure 6.9 (a). As shown in Figure 6.9 (b), the atomic ratio of carbon decreases from around 30 % in M_7C_3 to around 20 % in $M_{23}C_6$ while the $M_{23}C_6$ contains more Fe, Cr and Ni. Furthermore, the SAD patterns obtained from the M_7C_3 confirm that it has an orthorhombic structure, as shown in Figure 6.10. Figure 6.11 (b)-(f) are TEM EDS maps of Figure 6.11 (a). Nb-rich particles (Figure 6.11 (b)) were found at the interface between the $M_{23}C_6$ and the matrix, similar to the observation in crept Alloy A (Figure 4.6). However, one difference from crept Alloy A is that a MnS particle was found as shown in Figure 6.11 (e) and (f), probably from contamination during casting.

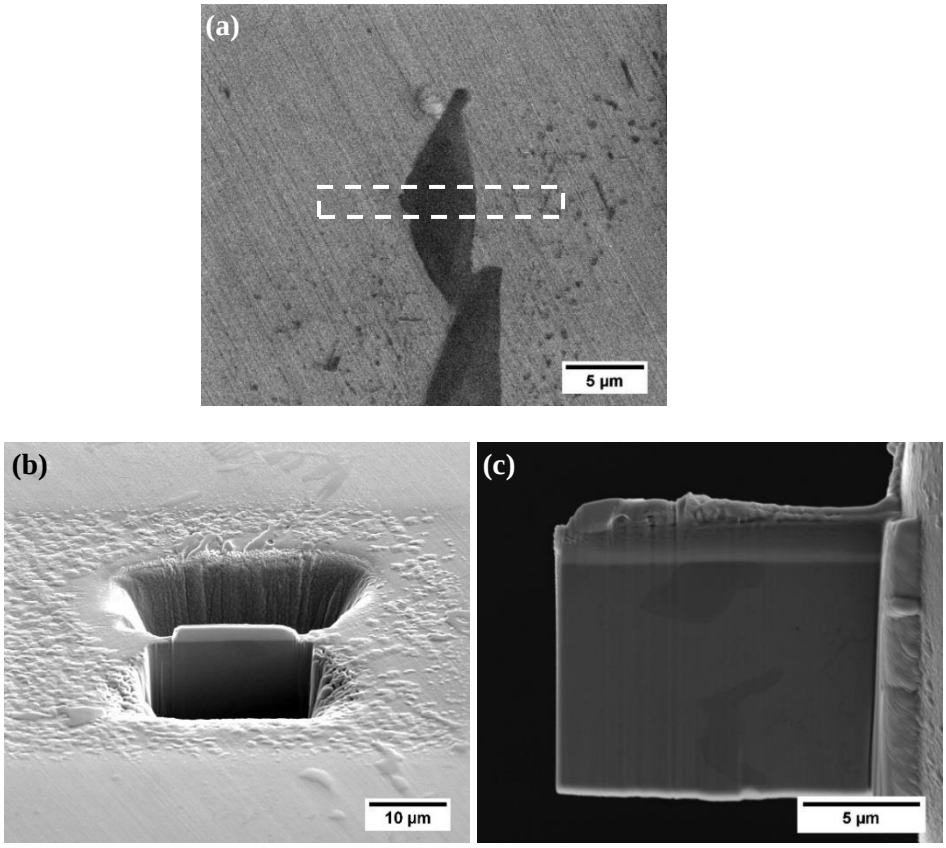

Figure 6.8 (a) BSE image of selected primary Cr-carbide in Alloy C HT-5; (b) and (c) secondary eleatron images illustrating the FIB preparation of TEM specimen

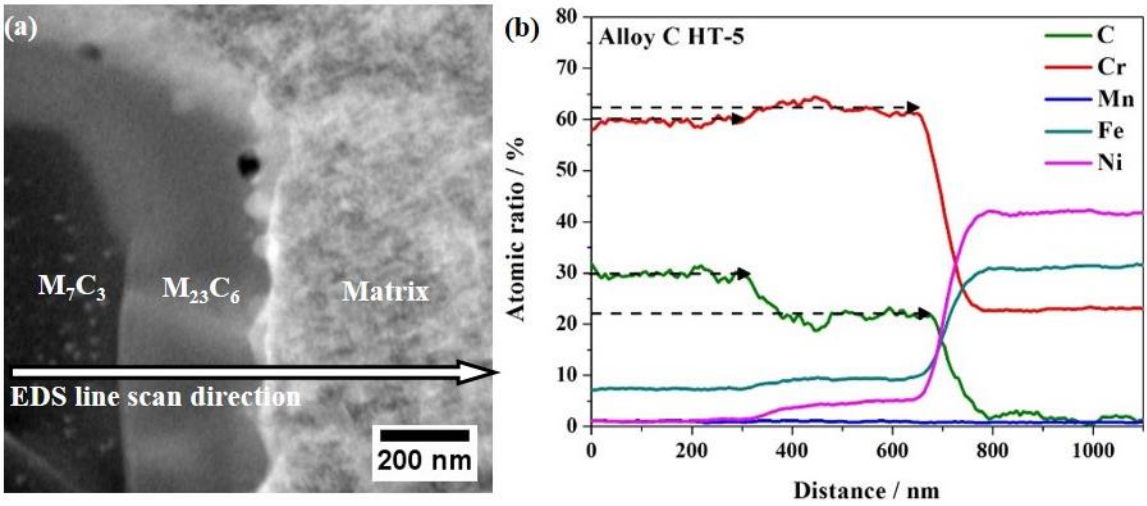

Figure 6.9 (a) BF image obtained from the FIB-TEM specimen; (b) EDS line scan from the position shown in (a)

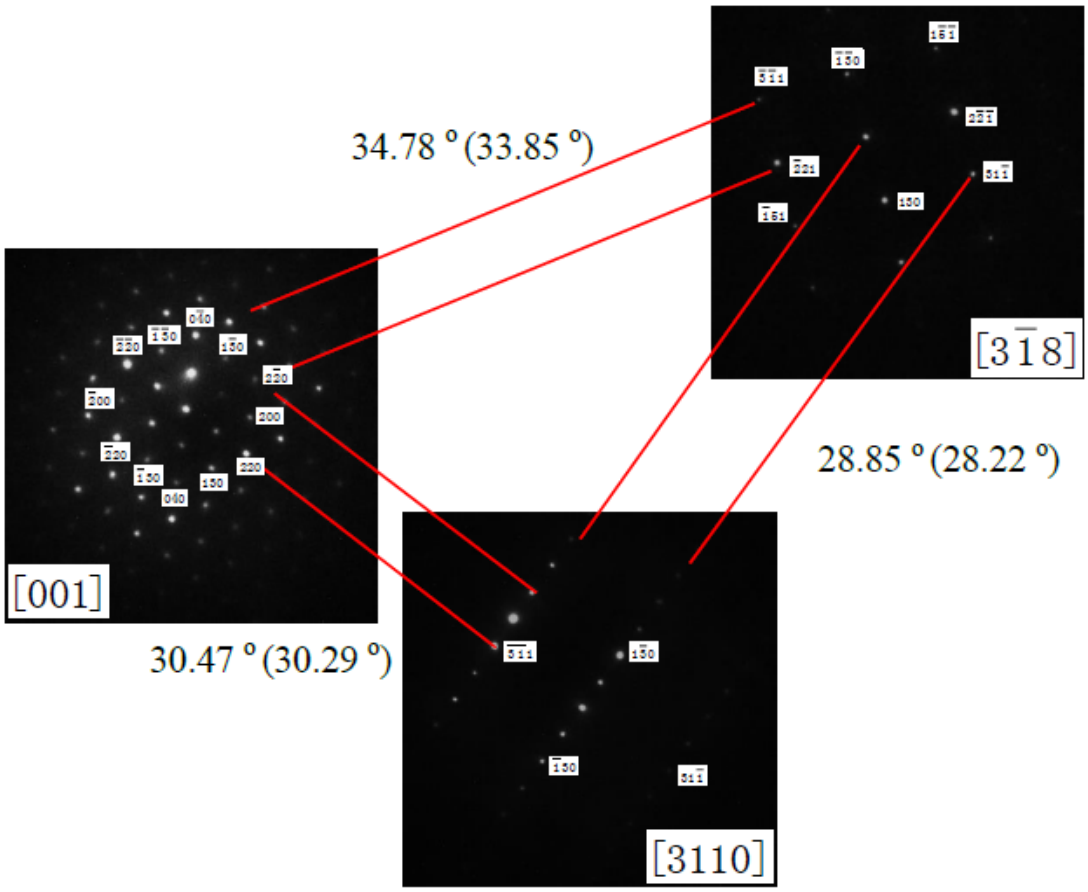

Figure 6.10 SAD patterns identifying the M_7C_3 precipitate labelled in Figure 6.11 (a); the angles between the three zone-axes agree with those calculated for an orthorhombic structure (numbers in brackets)

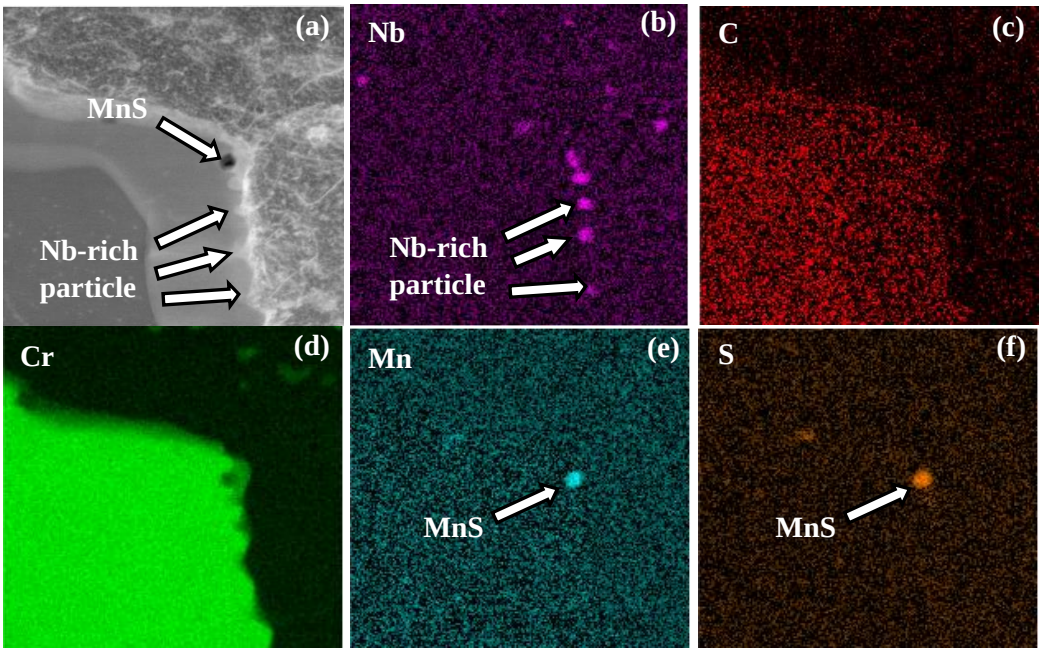

Figure 6.11 (a) BF image of primary Cr-carbide in Alloy C HT-5; (b)-(f) TEM-EDS maps of (a) illustrating Nb-rich particles and MnS

In the BSE images obtained from Alloy C HT-50, 100 and 150, different contrast was observed around the primary carbide network, as shown in Figure 6.12 (a), indicating that new precipitates formed during heat treatment. EDS maps illustrate that the new precipitates are rich in Nb, Ni and Si, suggesting G-phase, which nucleated firstly at the interfaces between the primary carbides and the matrix and then grew up to several microns during long time heat treatment.

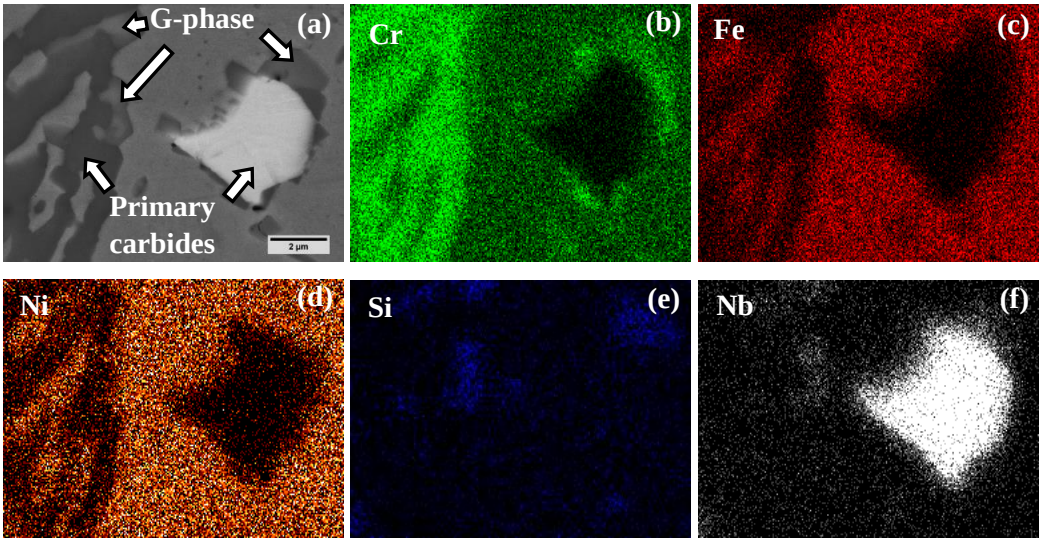

Figure 6.12 (a) BSE image of Alloy C HT-50 (b-f) EDS maps of (a) showing micron-scale G-phase surrounding the primary carbides

The precipitate sizes of the secondary Cr-carbide in heat treated specimens were measured and are listed in Table 6.5. The size of the secondary Cr-carbides increased rapidly to 74 nm after only 1 hour heat treatment. The precipitate size fluctuates around 80 nm for HT-2, HT-5 and HT-10 Alloy C and then increases continuously to 148 nm after 150 hours. As shown in Figure 6.13, the precipitate size of Alloy C is smaller than that of Alloy B until 50 hours while the secondary Cr-carbides in Alloy C continue growing and become larger than those in Alloy B after 100 hours. The coarsening rate of the secondary Cr-carbides in Alloy C HT-1 to HT-40 is much larger than that from HT-40 to HT-150, which is similar to the precipitate size evolution behaviour found in Alloy B.

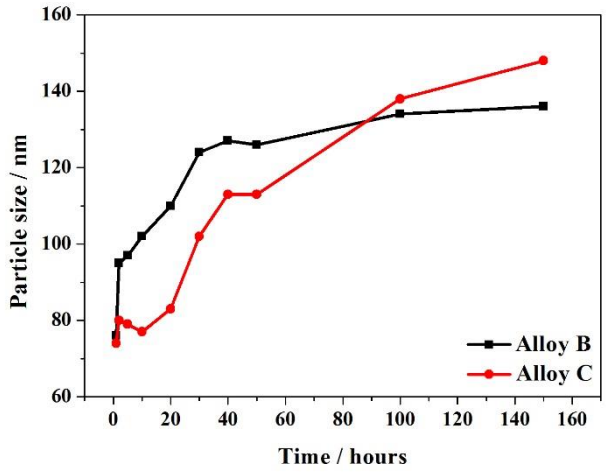

Figure 6.13 Secondary Cr-carbide precipitate sizes in Alloys B and C as a function of heat treatment time at 1000 °C (scatters are shown in Table 6.5)

The precipitate size distributions for heat treated Alloy C are shown in Figure 6.14. The distributions for Alloy C HT-1, HT-2. HT-5 and HT-10 (FWHM ~ 65 nm) are much narrower than those for HT-100 and HT-150 (FWHM ~ 90 nm). Meanwhile, the highest frequency in the distributions decreases with increasing heat treatment time, from around 0.30 for HT-1 to around 0.15 for HT-150.

The Gaussian fits of precipitate size distributions from Alloy B and C were compared in Figure 6.15. At the beginning of heat treatment, HT-1 and HT-5, Alloy C has a much narrower and sharper distributions while the distributions from HT-100 and HT-150 are quite close between Alloy B and C.

Table 6.5 Microstructural parameters of secondary Cr-carbide $M_{23}C_6$ in heat treated Alloy C

Specimens	Precipitate size		Interspacing
	Average precipitate size	Gaussian mean	
Alloy C HT-1	74 ± 42 nm	60 nm	275 ± 72 nm
Alloy C HT-2	80 ± 40 nm	64 nm	281 ± 72 nm
Alloy C HT-5	79 ± 42 nm	70 nm	281 ± 68 nm
Alloy C HT-10	77 ± 40 nm	65 nm	321 ± 114 nm
Alloy C HT-20	83 ± 39 nm	73 nm	324 ± 73 nm
Alloy C HT-30	102 ± 50 nm	89 nm	371 ± 92 nm
Alloy C HT-40	113 ± 47 nm	94 nm	413 ± 107 nm
Alloy C HT-50	113 ± 56 nm	96 nm	423 ± 96 nm
Alloy C HT-100	138 ± 65 nm	117 nm	505 ± 107 nm
Alloy C HT-150	148 ± 65 nm	122 nm	532 ± 126 nm

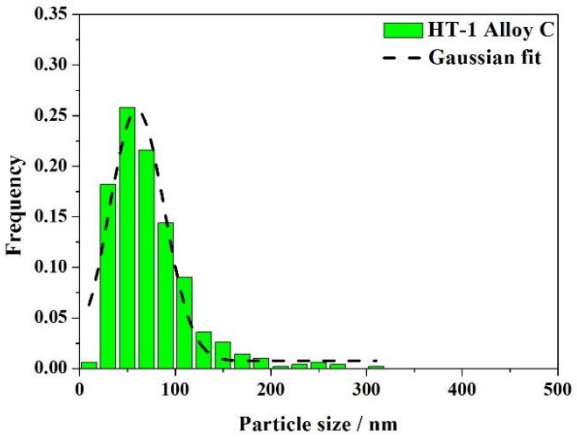

(a)

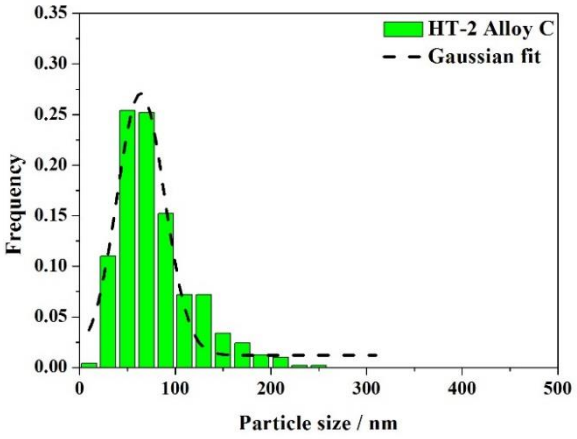

(b)

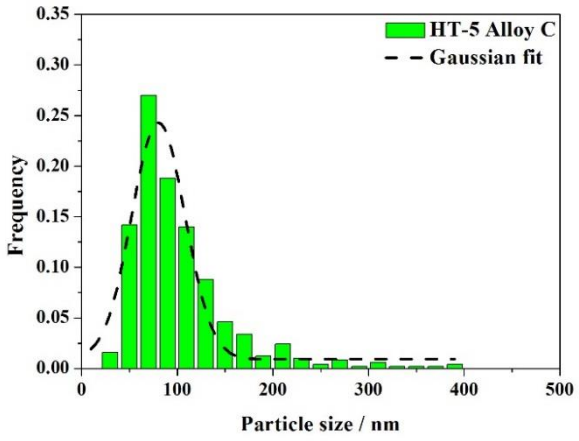
HT-5 Alloy C
Gaussian fit
Frequency
Particle size / nm
0.35
0.30
0.25
0.20
0.15
0.10
0.05
0.00
0
100
200
300
400
500

(c)

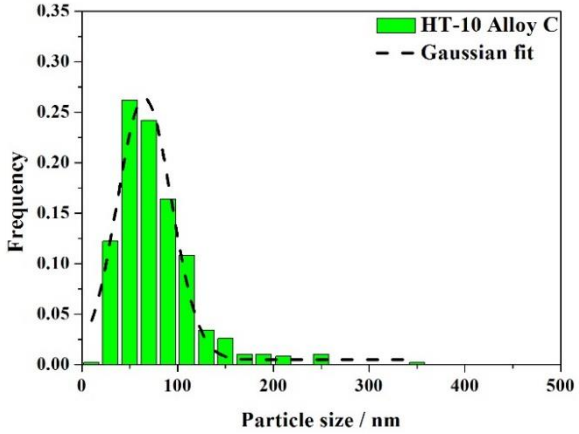
HT-10 Alloy C
Gaussian fit
Frequency
Particle size / nm
0.35
0.30
0.25
0.20
0.15
0.10
0.05
0.00
0
100
200
300
400
500

(d)

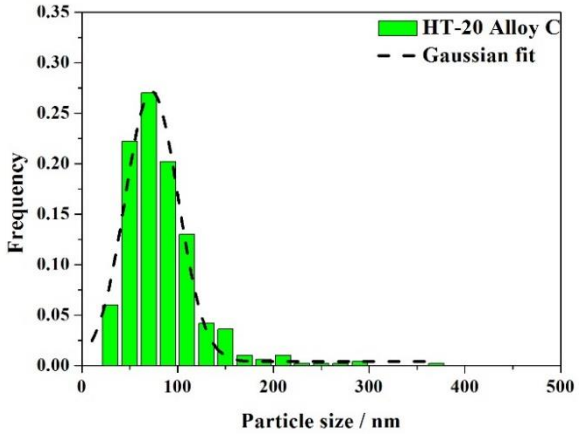
HT-20 Alloy C
Gaussian fit
Frequency
Particle size / nm
0.35
0.30
0.25
0.20
0.15
0.10
0.05
0.00
0
100
200
300
400
500

(e)

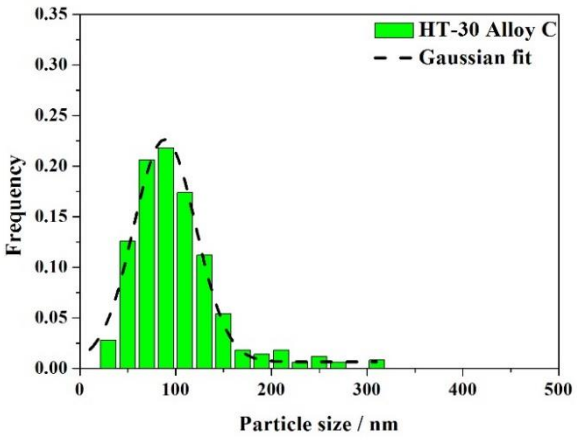
HT-30 Alloy C
Gaussian fit
Frequency
Particle size / nm
0.35
0.30
0.25
0.20
0.15
0.10
0.05
0.00
0
100
200
300
400
500

(f)

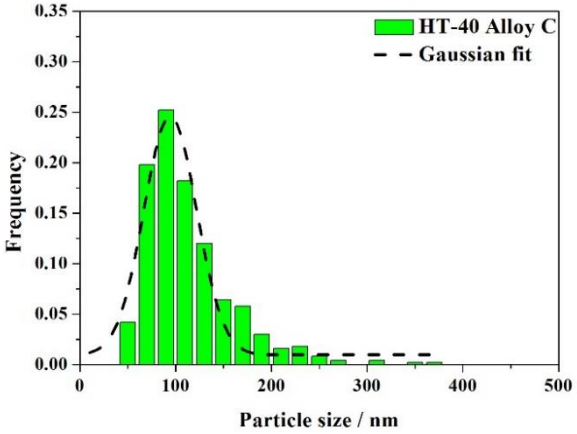
HT-40 Alloy C
Gaussian fit
Frequency
Particle size / nm
0.35
0.30
0.25
0.20
0.15
0.10
0.05
0.00
0
100
200
300
400
500

(g)

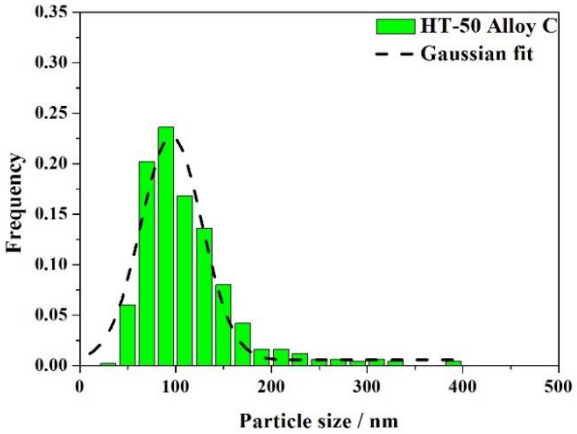
HT-50 Alloy C
Gaussian fit
Frequency
Particle size / nm
0.35
0.30
0.25
0.20
0.15
0.10
0.05
0.00
0
100
200
300
400
500

(h)

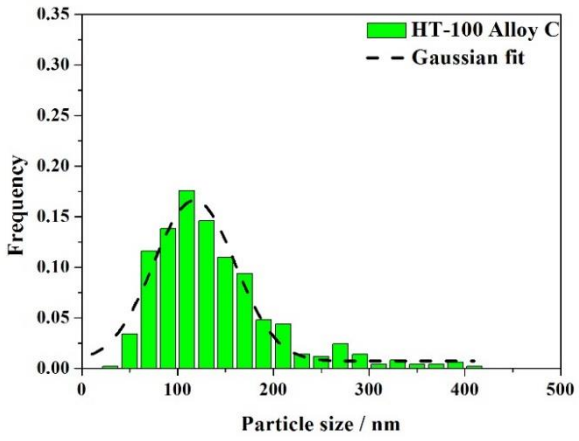

(i)

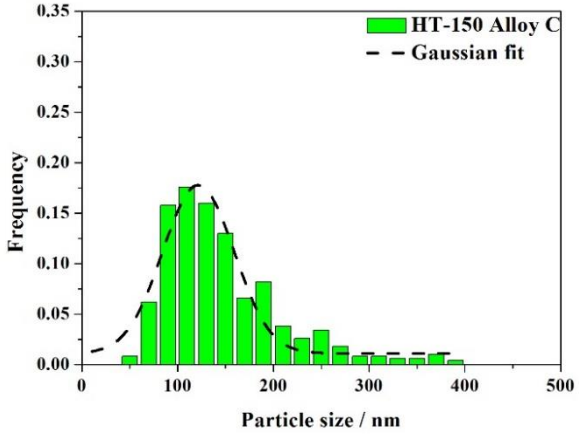

(j)

Figure 6.14 Particle size distributions of the secondary Cr carbide obtained from HT-1 Alloy C to HT-150 Alloy C

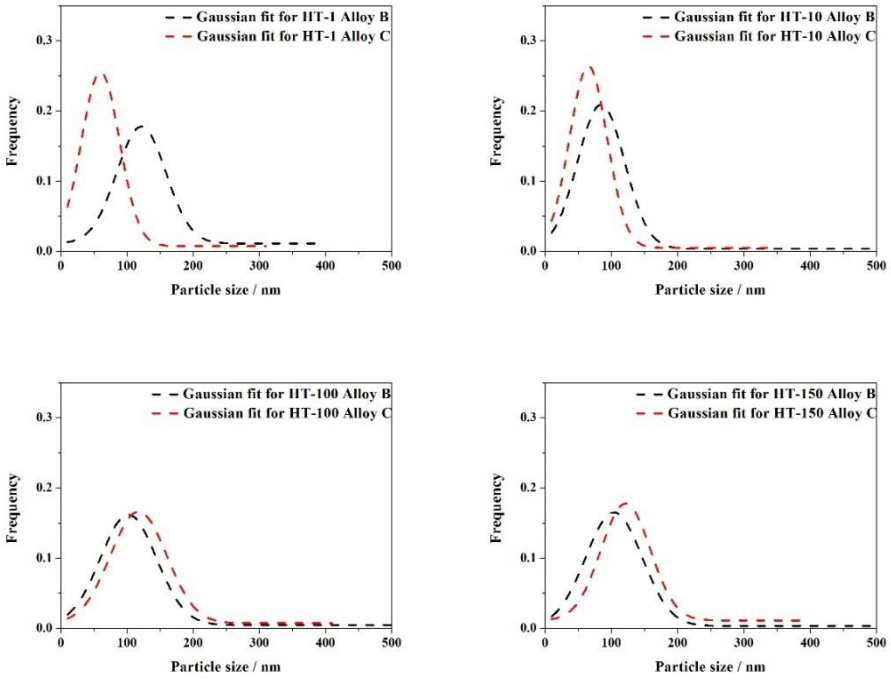

Figure 6.15 Gaussian fits for Alloy B and C for 1, 5, 100 and 150 hours heat treatment

To compare the coarsening rates of Alloy B and Alloy C, the *(Precipitate size)*^{3} vs *(time)* are plotted in Figure 6.16 (a) and a linear fit applied. The linear fit shows the coarsening rate *K* of secondary Cr-carbide in Alloy C is 5.6 $nm^{-3}s^{-1}$, with quite a good fit (R^2 = 0.97). However, this coarsening rate is larger than that of Alloy B (K = 3.4 $nm^{-3}s^{-1}$) as illustrated in Table 6.6.

A log fit was applied to (*precipitate size)* - (*time)* plot (R^2=0.97), Figure 6.16 (b), indicating that the evolution of secondary Cr-carbide in Alloy C involves both growth and coarsening. Then the linear fit was applied to HT-40~HT-150 (Figure 6.16 (c)). From 40 to 150 hours, the coarsening rate of secondary Cr-carbides in Alloy C (4.9 $nm^{-3}s^{-1}$) is four times that of Alloy B (1.2 $nm^{-3}s^{-1}$).

Table 6.6 Coarsening rates of secondary Cr-carbide in heat treated Alloy B and Alloy C

Coarsening rate		Secondary Cr-carbides	
		HT-1 to HT-150	HT-40 to HT-150
Alloy B	Calculation / $nm^{-3}s^{-1}$	3.4	1.2
	R-square	0.68	0.81
Alloy C	Calculation / $nm^{-3}s^{-1}$	5.6	4.9
	R-square	0.97	0.96

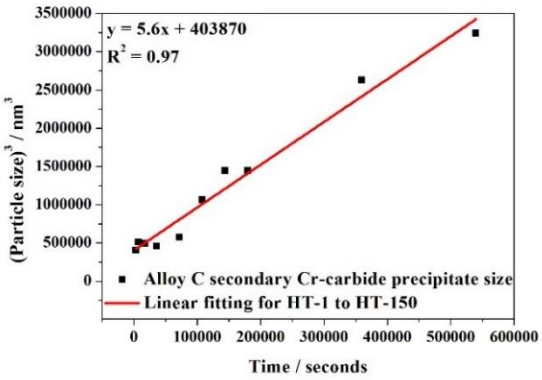

(a)

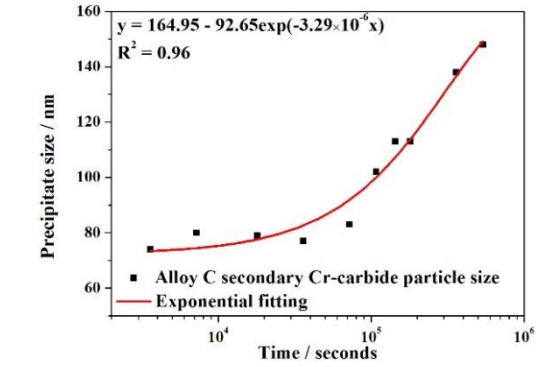

(b)

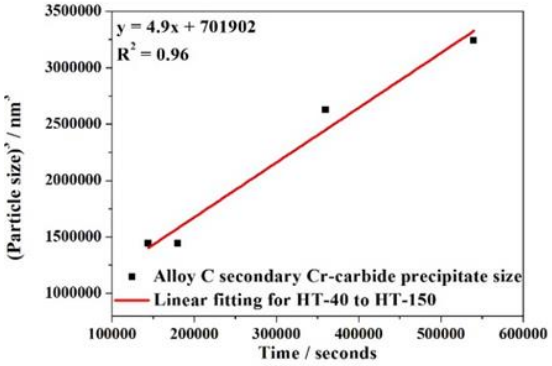

(c)

Figure 6.16 (a) (Precipitate size)^3 - (time) linear fit for Alloy C HT-1 to HT-150; (b) (Precipitate size) – (time) log fit for Alloy C HT-1 to HT-150 and (c) (Precipitate size)^3 - (time) linear fit for Alloy C HT-40 to HT-150

6.4 DSC tests for Alloy B and Alloy C

To determine the effect of solidification on microstructure, DSC was used to simulate the solification process. The detailed DSC process for dynamic measurements has already been shown in Figure 3.5. Two cooling rates, 10 ºC/min and 100 ºC/min, were selected to simulate the solidification rates during centrifugal casting.

The DSC curves during second cycle cooling from 1530 ºC to 1100 ºC of Alloy B and Alloy C with two cooling rates are shown in Figure 6.17. A large exothermic peak was observed in all four curves indicating the solidifiation of γ-Fe. However, there are three exothermic peaks on slow cooling Alloy B (10 ºC/min) and two exothermic peaks on fast cooling Alloy B (100 ºC/min). In contrast, two peaks were found on slow cooling Alloy C (10 ºC/min) while three peaks were found on fast cooling Alloy C (100 ºC/min). The undercoolings and enthalpies were measured and are listed in Table 6.7. The undercoolings in both alloys became much larger with increase of cooling rate. Meanwhile, a larger cooling rate leads to a smaller measured enthalpy of solidification as shown in Table 6.7.

Table 6.7 Undercoolings and enthalpies obtained from the DSC specimens using slow cooling and fast cooling of Alloy B and Alloy C

Specimen		Thermal properties			
		Undercooling / ºC			Total enthalpy / (J/s)
		NbC	M_7C_3	γ-Fe	
Alloy B	10 ºC/min	67	34	107	941.88
	100 ºC/min	109	77	125	176.93
Alloy C	10 ºC/min	71	37	96	732.66
	100 ºC/min	111	80	115	169.08

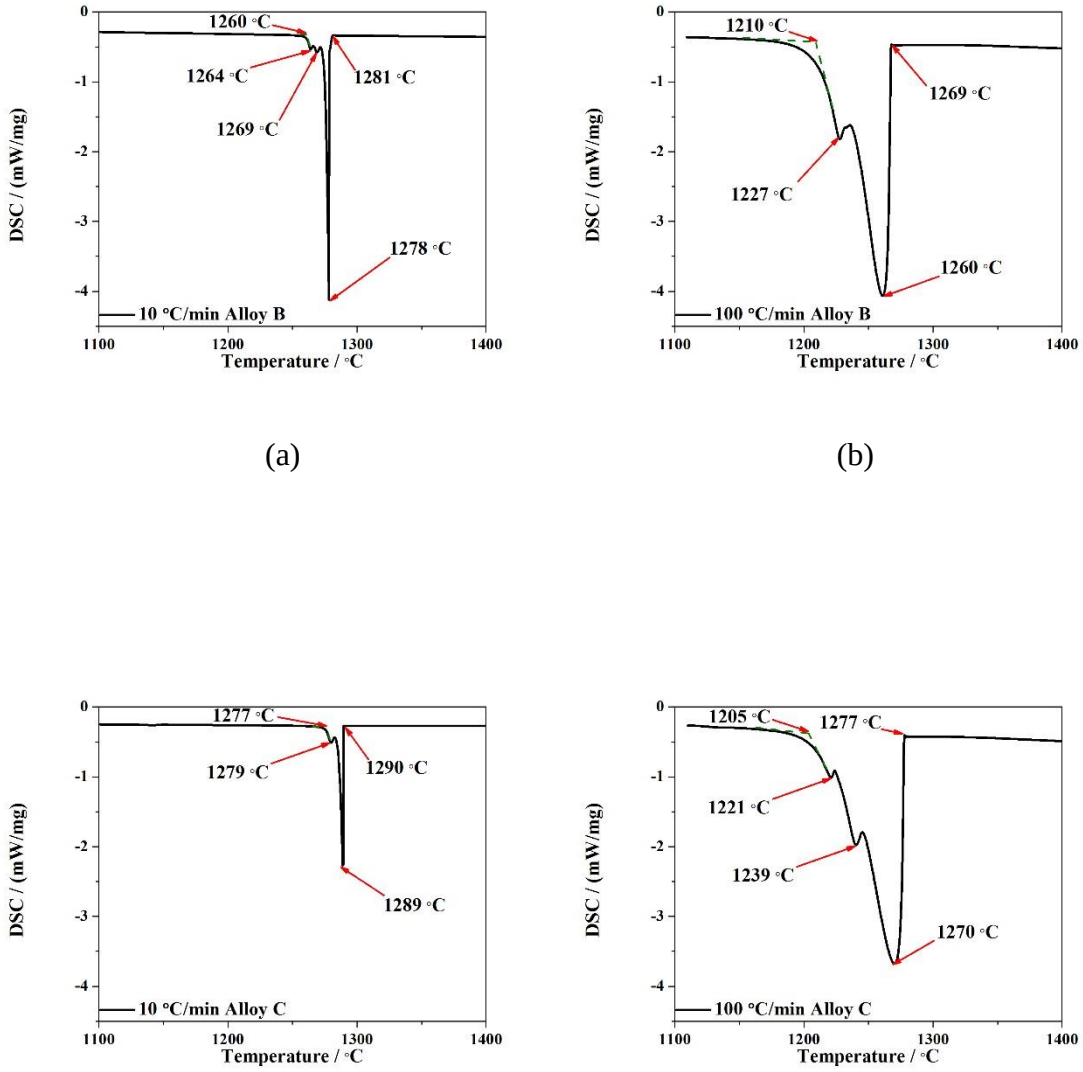

Figure 6.17 DSC curves during second cycle cooling from 1530 °C to 1100 °C of Alloy B with cooling rates of (a) 10 °C/min and (b) 100 °C/min; Alloy C with cooling rates of (c) 10 °C/min and (d) 100 °C/min

BSE images obtained from the slowly cooled Alloy B (10 ºC/min) and the quickly cooled Alloy B (100 ºC/min) are shown in Figure 6.18 (b) and (c) respectively, and compared with as-cast Alloy B. It is obvious that the dendrite cell size after 10 ºC/min is similar to that of as-cast Alloy B and is much larger than that for 100 ºC/min. BSE images obtained from the slowly cooled Alloy C (10 ºC/min) and the quickly cooled Alloy C (100 ºC/min) are shown in Figure 6.19 (b) and (c) respectively, and compared with as-cast Alloy C. The same relationship between cooling rates and dendrite cell size was found in Alloy C. The area fractions of Cr-carbide and Nb-carbide were measured and listed in Table 6.7. However, due to the limit of specimen size, only one measurement in each specimen was taken and may not present the accurate value of carbide area fraction.

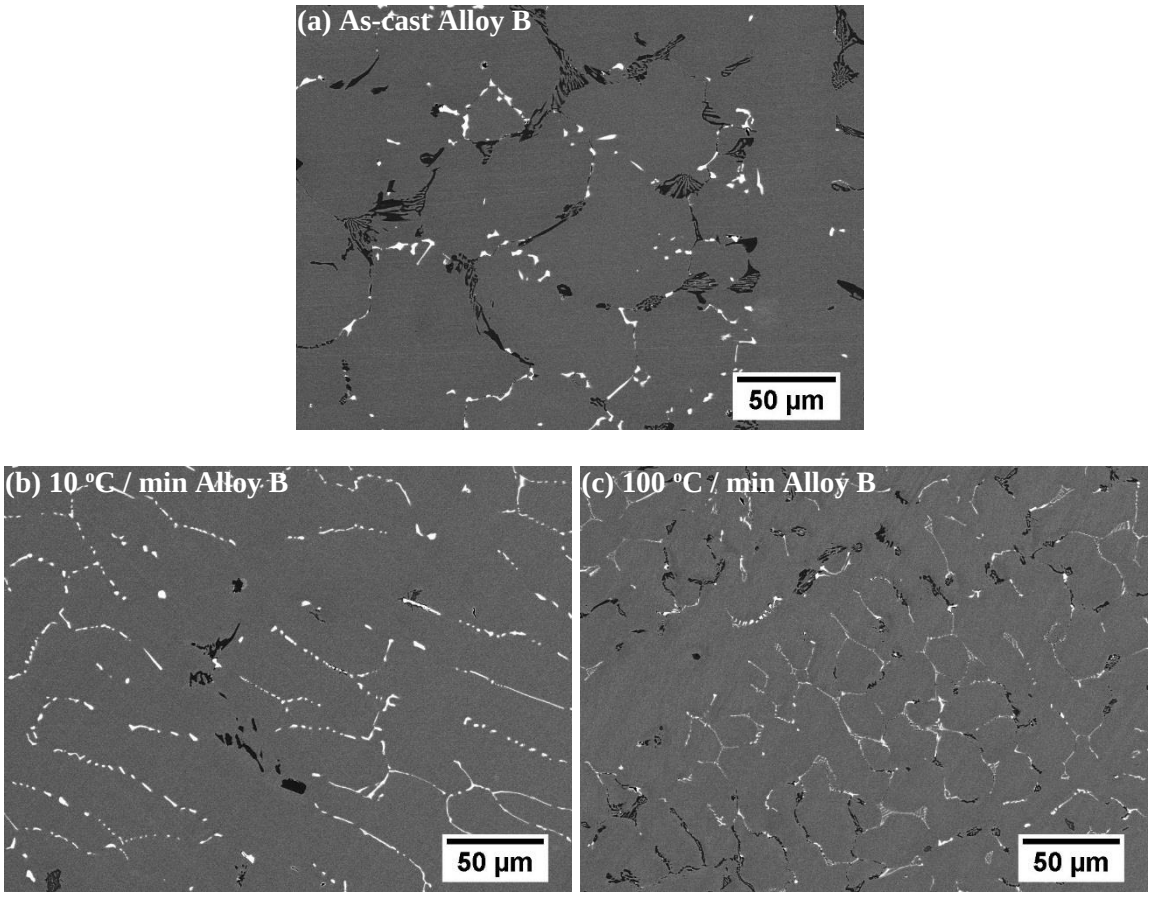

Figure 6.18 BSE images obtained from (a) as-cast Alloy B (b) Alloy B with a cooling rate of 10 ºC/min and (c) Alloy B with a cooling rate of 100 ºC/min

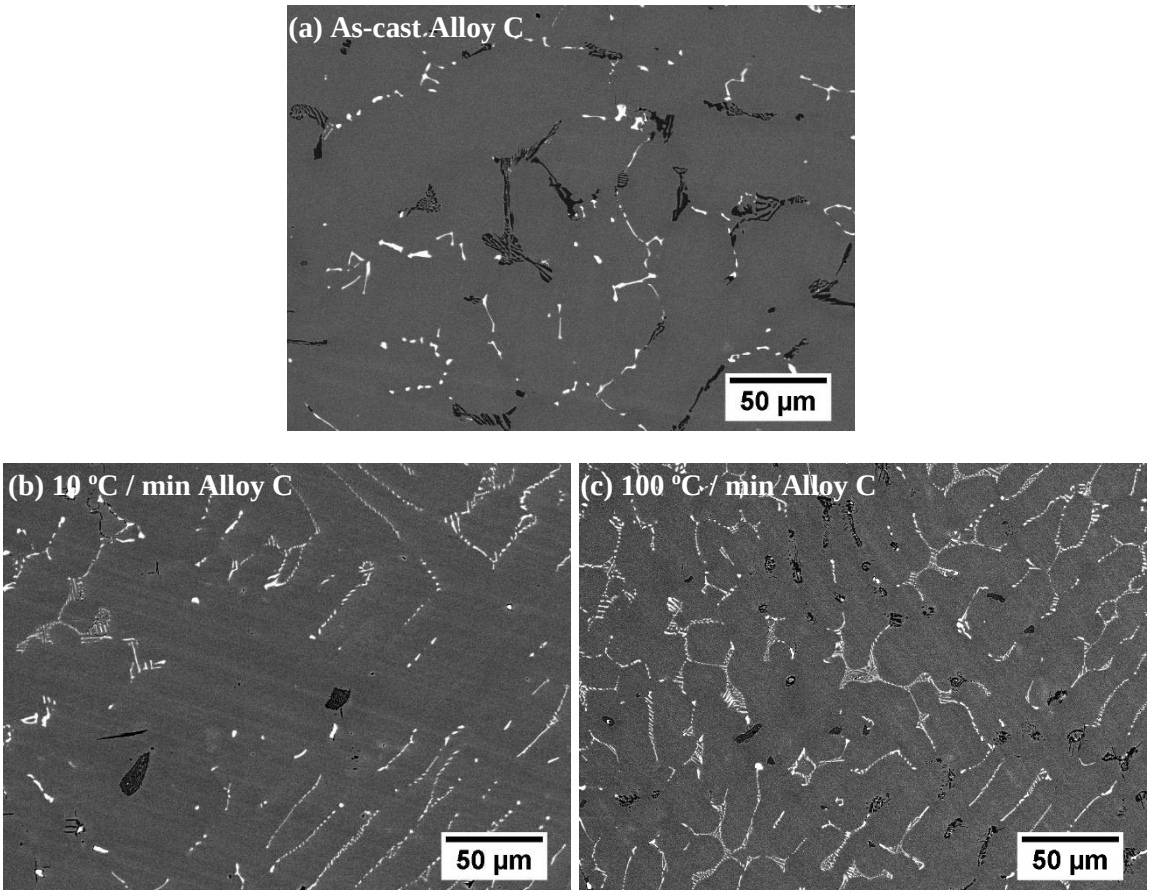

Figure 6.19 BSE images obtained from (a) as-cast Alloy C (b) Alloy C with a cooling rate of 10 ºC/min and (c) Alloy C with a cooling rate of 100 ºC/min

Table 6.8 Area fractions of carbides in as-cast, slowly cooled and quickly cooled Alloy B and Alloy C

Specimen		Area fraction%		
		As-cast	10 ºC/min	100 ºC/min
Alloy B	Cr-carbide	2.75±0.08	0.82	3.11
	Nb-carbide	1.34±0.11	2.66	1.82
Alloy C	Cr-carbide	2.12±0.18	0.60	1.40
	Nb-carbide	1.80±0.10	2.61	1.98

6.5 Summary of results

1. As-cast Alloy C contains less M_7C_3 (2.75 % vs 2.12 %) and more NbC (1.34 % vs 1.80 %) as compared with as-cast Alloy B. Meanwhile, as-cast Alloy C has smaller dendrite cell size and secondary dendritic arm spacing than as-cast Alloy B due to different solidification rates;

2. After creep, the area fractions of primary Cr-carbide and primary Nb-carbide are both larger in crept Alloy C than Alloy B indicating a faster coarsening behaviour in Alloy C. Meanwhile, the average precipitate size of secondary Cr-carbide is smaller in crept Alloy C (108 ± 37 nm) than that in crept Alloy B (136 ± 68 nm);

3. During heat treatment of Alloy C at 1000 ^oC for 1 to 150 hours, the area fraction of primary Cr-carbide fluctuates at first and then increases from 20 hours and the area fraction of primary Nb-carbide continuously increases from the beginning of heat treatment;

4. The average precipitate size in Alloy C is smaller than that of Alloy B up to 50 hours although the secondary Cr-carbides in Alloy C continue growing and become larger than those in Alloy B after 100 hours. The linear fit shows the coarsening rate *K* of secondary Cr-carbide in Alloy C is 5.6 $nm^{-3}s^{-1}$, larger than that in Alloy B (3.4 $nm^{-3}s^{-1}$);

5. In Alloy C HT-1, HT-2 and HT-5, different contrast was observed in the BSE images of primary Cr-carbide. EBSD mapping and TEM analysis of primary Cr-carbide in HT-5 Alloy C confirms that the outside shell is $M_{23}C_6$ carbide and that the core is M_7C_3 type carbide suggesting an *in situ* transformation from M_7C_3 to $M_{23}C_6$. Meanwhile, the orientation mapping illustrates that the $M_{23}C_6$ has a similar orientation to the austenite matrix;

6. From DSC tests with two cooling rates, 10 ^oC/min and 100 ^oC/min, the undercoolings in both alloys became much larger with increase of cooling rate. Meanwhile, a larger cooling rate leads to a smaller measured enthalpy of solidification.

6.6 Discussion

6.6.1 Effect of solidification rate on the microstructure of HP40

As mentioned in Section 3.1, the chemical compositions of Alloys B and C fall into the same broad HP40 alloy range; the main difference between Alloys B and C is the solidification rate. Although the actual solidification rate during production is impossible to measure definitely Alloy B has a lower solidification rate than Alloy C due to the different refractory compositions coatings on the casting moulds.

As shown in Table 6.2, as-cast Alloy B, which was produced with a lower solidification rate, has larger dendrite cell size (DCS) and secondary dendrite arm spacing (SDAS) as compared with the as-cast Alloy C. The similar inverse relationship, between solidification rate and DCS and SDAS, has been found empirically in casting steels and magnesium alloys and is described by the following equations:

$D = A \cdot R^n$ --- Equation 6.1

$S = B \cdot R^m$ --- Equation 6.2

where *R* is the solidification rate, *D* is dendrite cell size and *S* is the secondary dendrite arm spacing. *A, B, n* and *m* are constants specific to the material.

This relationship is explained by the nucleation theory presented by Flemings [70]. The energy and critical radius of a nucleus, at a certain undercooling, are given by

$\Delta G_v = \frac{\Delta H \cdot \Delta T}{V_s T_m}$ --- Equation 6.3

$r^* = \frac{2\gamma}{\Delta G_v}$ --- Equation 6.4

where T_m is the equilibrium melting point, V_s is the molar volume, γ is the surface energy, ΔH is the latent heat of solidification and ΔT is the undercooling.

Combining Equations 6.3 and 6.4, we have $r^* = \frac{2\gamma T_M V_s}{\Delta H \Delta T}$ --- Equation 6.5

Equation 6.5 reveals that as the undercooling ΔT increases, the critical radius of a stable nucleus will decrease, which makes more small nuclei survive and grow to be dendrite cells. As the undercooling ΔT is proportional to solidification rate, it can be deduced that with an increase of solidification rate, the dendrite cells will have a much smaller average size and the dendrite arm spacing will also be reduced. Therefore, a higher solidification rate leads to a smaller DCS and a smaller SDAS in the as-cast Alloy C compared with as-cast Alloy B.

For the area fractions of primary Cr-carbide and Nb-carbide (Table 6.1), as-cast Alloy C contains more primary Nb-carbide than as-cast Alloy B. The effect of solidification rates on phase fraction evolution can be explained as follows. Firstly, Mitchell et al. [167] found that by varying the cooling rate of a 15Cr-Ni superalloy from 3 to 50 ^{o}C/min the precipitation of γ' can be suppressed. As shown in Figure 6.20, a reduction of approximate 15 ^{o}C in γ' precipitation temperature was achieved when the cooling rate increased from 3 ^{o}C/min to 50 ^{o}C/min. This suppression of precipitation formation temperature is also observed by DSC on Alloys B and C with two different cooling rates. For example, as shown in Figure 6.17 (c) and (d), the formation of NbC in Alloy C at 10 ^{o}C/min is 1279 ^{o}C while that at 100 ^{o}C/min becomes 1239 ^{o}C. As discussed in Section 4.4.1, the solubility of NbC in the austenitic matrix will reduce with decrease in temperature, resulting in a larger number of precipitates. When the material is cooled at a higher solidification rate, the precipitation temperature of NbC is suppressed, leading to a lower solubility. For instance, when the NbC formation temperature decreases from 1279 ^{o}C to 1239 ^{o}C, the solubility of NbC will reduce from 0.034 wt% to 0.023wt%. This reduction in solubility of NbC will be reflected in a larger area fraction of NbC-carbide.

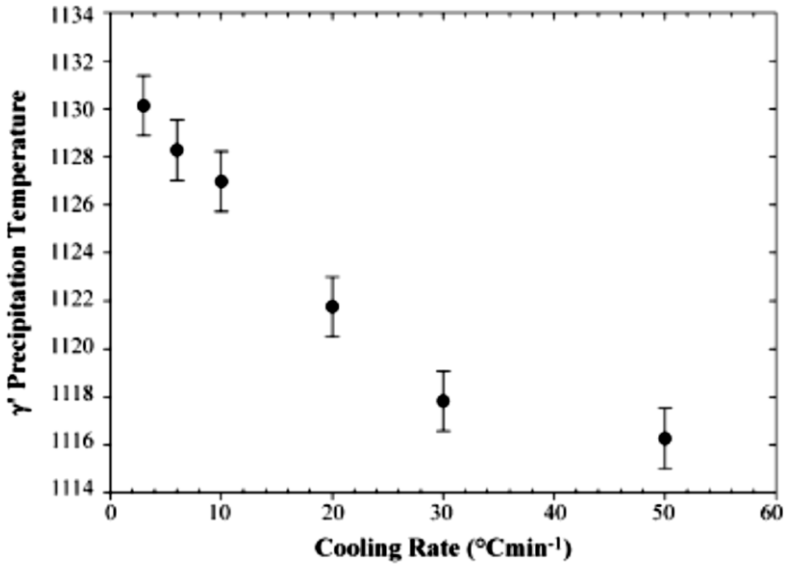

Figure 6.20 Effect of undercooling in a 15Cr-Ni superalloy for cooling rates between 3 and 50 °C/min indicating that here the reduction of precipitation temperature is approximately 15 °C [167]

Secondarily, besides the suppression of precipitation temperature, a larger solidification rate can also restrain the rejection of solute atoms from the solid back into the solid-liquid interface [168]. A low cooling rate, however, will leave enough time for solute back diffusion, leading to a decrease in the precipitation fraction.

Thirdly, an increasing solidification rate can accelerate segregation of solute atoms and thus increase the precipitation fraction during solidification. Boccalini and Goldenstein [169] found that the segregation of vanadium to the residual liquid from the reaction increased with a larger cooling rate. This increase in segregation promotes the formation of the M_2C carbide, which is rich in vanadium. However, Won and Thomas [170] pointed out that the effect of cooling rates on segregation and phase fraction is insignificant in low-alloy steels when the cooling rate is less than 100 °C/s.

Therefore, the as-cast Alloy C, which was cooled down more quickly than Alloy B, contains a larger area fraction of NbC compared with that in as-cast Alloy B. The area fraction of primary Cr-carbide alters in the opposite sense to the primary Nb-carbide. Based on the solidification sequence (Section 4.4.1), the primary Nb-carbide (NbC) will precipitate before the formation of primary Cr-carbide (M_7C_3). During the precipitation of NbC, the free carbon in the liquid will be attracted. Therefore, the more NbC precipitates, the less carbon will be left for further precipitation of M_7C_3. As the carbon content in Alloys B and C is the same (0.41 wt%), a larger amount of NbC in as-cast Alloy C leads to less M_7C_3 Cr-carbide than in as-cast Alloy B, which is in agreement with the area fraction measurements in the as-cast Alloys B and C (Table 6.1).

The effect of solidification rate is reflected not only in the as-cast microstructure but also on the evolution of precipitates during heat treatment, such as the precipitate size and coarsening rate of secondary Cr-carbide.

For precipitation in solids, the free energy change associated with the nucleation process will be different from precipitation from liquid and have the following two contributions. First, the creation of a volume of precipitates will cause a volume free energy reduction in ΔG_v. Second, the transformed volume will not fit perfectly into the space originally occupied by the matrix and this gives rise to a misfit strain energy ΔG_s. The critical radius for nucleation in a solid is shown in Equation 6.6 [171]:

$r^* = \frac{2\gamma}{\Delta G_v - \Delta G_s}$ --- Equation 6.6

From Equations 6.3 and 6.6, with an increase of undercooling ΔT, the critical radius of a stable nucleus will decrease since the misfit strain energy has no relationship with the undercooling. Therefore, Alloy C, which has a higher solidification rate and a larger undercooling will have smaller precipitates than Alloy B. This is confirmed by the experimental measurements in the two alloys of average precipitate size and precipitate size distribution.

At the beginning of heat treatment (1 to 10 hours), Alloy C has smaller secondary Cr-carbides (Figure 6.13), the precipitate size distribution is much narrower than that of Alloy B and the highest frequency in the Alloy C distributions is larger than those in Alloy B (Figure 6.15).

After a longer heat treatment, the secondary Cr-carbide will coarsen. Secondary Cr-carbide in Alloy C coarsened more quickly making the average precipitate size larger than that of Alloy B after 100 hours. During solidification, the higher cooling rate leads to a larger supersaturation [172] in Alloy C than in Alloy B. Based on Ostwald ripening theory, a larger supersaturation results in a faster coarsening rate, which is consistent with the coarsening rates measured by the linearly fitted 3.4 for Alloy B and 5.6 for Alloy C (Table 6.6).

6.6.2 Transformation from M_7C_3 to $M_{23}C_6$ in Alloy C

In Alloy C HT-1, HT-2 and HT-5, BSE images of primary Cr-carbide (Figure 6.6) and EBSD mapping (Figure 6.7) confirmed that the outside shell is $M_{23}C_6$ carbide and that the core is M_7C_3 type carbide.

Two facts suggest that the $M_{23}C_6$ nucleates at first over the entire interface between the matrix and the M_7C_3 and then grows into the M_7C_3.

Firstly, the orientation mapping (Figure 6.7 (c)) illustrates that the $M_{23}C_6$ is coherent with the austenite matrix. Kaneko et al. [26] found by *in situ* TEM observation that the $M_{23}C_6$ precipitates which nucleated on grain boundaries have a cube-cube relationship with one of the grains. This preference for one grain, which minimizes the activation energy for nucleation, was also confirmed by Hong et al. [28] in AISI 304 austenitic stainless steel. Meanwhile, subsequent carbide growth will proceed towards the interior of the other grain, which is not coherent with the carbide. In the case shown in Figure 6.7, the $M_{23}C_6$ was coherent with the austenite matrix and thus it should grow into the primary M_7C_3-carbide. Although a specific crystallographic relationship at the growth interface between $M_{23}C_6$ into M_7C_3 was observed in a high carbon Cr-W steel by Ingue and Masumoto [173], this relationship seems to be weak and has not been found in the current work.

Secondly, Nb-rich particles and MnS particles were found at the interface between the $M_{23}C_6$ and the matrix. Both the Nb-rich particles and the MnS particles existed before the transformation from M_7C_3 to $M_{23}C_6$, due to their high formation temperatures. If the $M_{23}C_6$ grew into the austenitic matrix, the pre-existing Nb-rich particle and the MnS would be expected to be at the interface between the M_7C_3 and $M_{23}C_6$. However, this assumption is opposite to the experimental observations. Therefore, the growth direction of $M_{23}C_6$ is from the matrix-M_7C_3 interface into the M_7C_3.

The process of transformation from $M_{23}C_6$ to M_7C_3 is shown schematically in Figure 6.21. At the beginning of this transformation, the $M_{23}C_6$ nucleates at the M_7C_3-matrix interface due to the relatively high energy of the interface. The nucleated $M_{23}C_6$ precipitates will have a cube-cube relationship with the austenitic matrix. With increasing $M_{23}C_6$ nucleation, the $M_{23}C_6$ particles will cluster together and form a shell around the original M_7C_3 precipitates. As the dissolution of M_7C_3, which leaves enough free solute atoms, occurs at the same time, the $M_{23}C_6$ will continually grow into the M_7C_3 until the transformation completes.

Furthermore, since the M_7C_3 contains much more carbon than the $M_{23}C_6$, the transformation of M_7C_3 to $M_{23}C_6$ will lead to a release of carbon atoms into the matrix. The released carbon will give a larger amount of secondary Cr-carbide close to the primary carbides, which is in agreement with the observation (Figure 6.22).

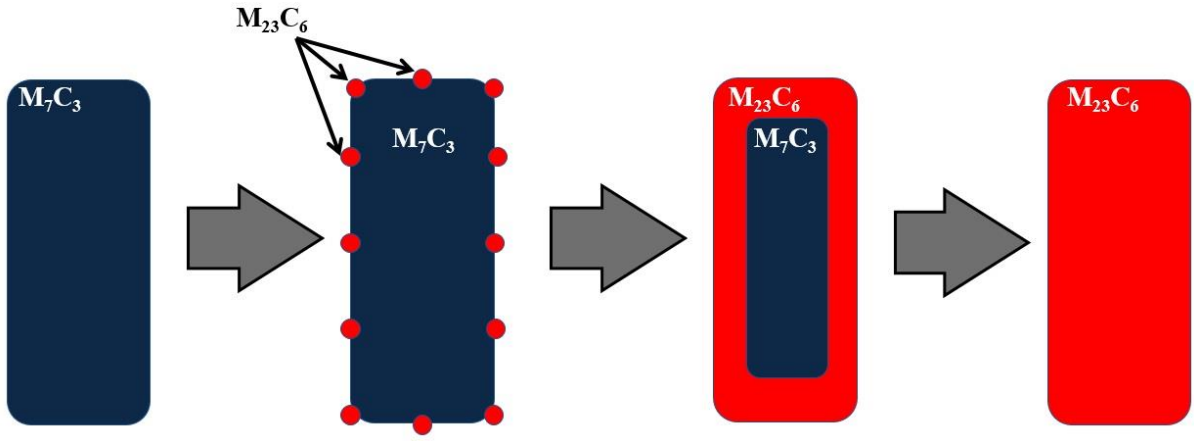

Figure 6.21 Schematic diagram illustrating the transformation from M_7C_3 to $M_{23}C_6$

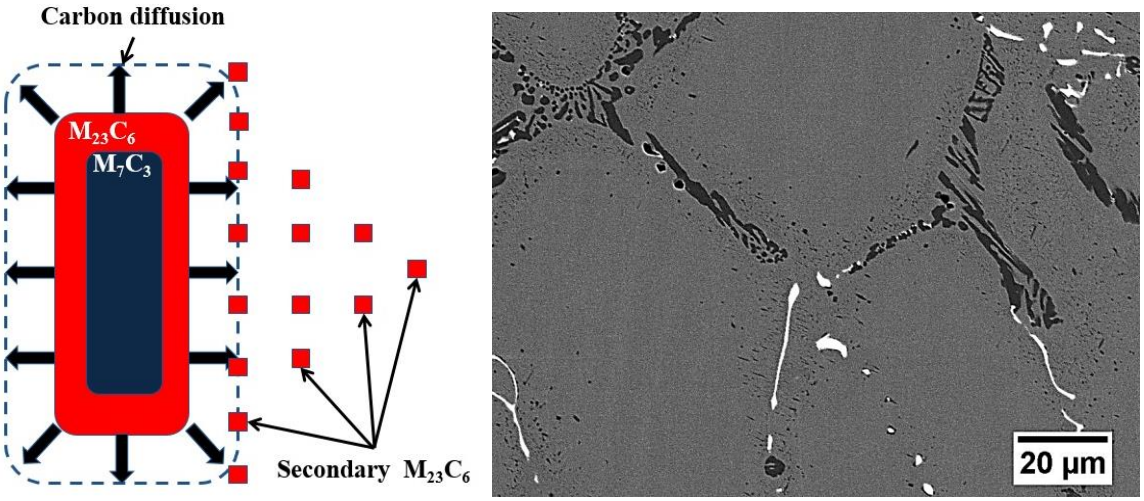

Figure 6.22 Release of carbon from the $M_7C_3 \rightarrow M_{23}C_6$ transformation causing the precipitation of secondary $M_{23}C_6$ carbide close to the primary carbides

As shown in Figure 6.9 (b) and Figure 6.11, besides the difference in carbon concentration between M_7C_3 and $M_{23}C_6$, the $M_{23}C_6$ also contains more Fe, Cr and Ni. Therefore, the growth of $M_{23}C_6$ carbides is controlled by the solute atom diffusion (mainly Cr diffusion). According to Zener's empirical relation [174], for n (n=1,2 or 3) dimensional isotropic diffusion, the size of precipitates can be expressed by Equation 6.7:

$r = \sqrt{2nDt}$ --- Equation 6.7

where r is the precipitate size, D is the diffusion rate and t is time.

If it is assumed that the growth is controlled by the diffusion of Cr, D in Equation 6.7 is the diffusion rate of Cr in $M_{23}C_6$, which is 2.72×10^{-17} m^2/s at 1000 ^oC [175].

To verify this calculated precipitate size, the equivalent size of $M_{23}C_6$ was measured by the method described in Section 5.5.3. The areas of the carbides were measured and then equivalent precipitate sizes deduced. The area of M_7C_3 and the total area were measured and their difference is the area of $M_{23}C_6$, as shown in Figure 6.23.

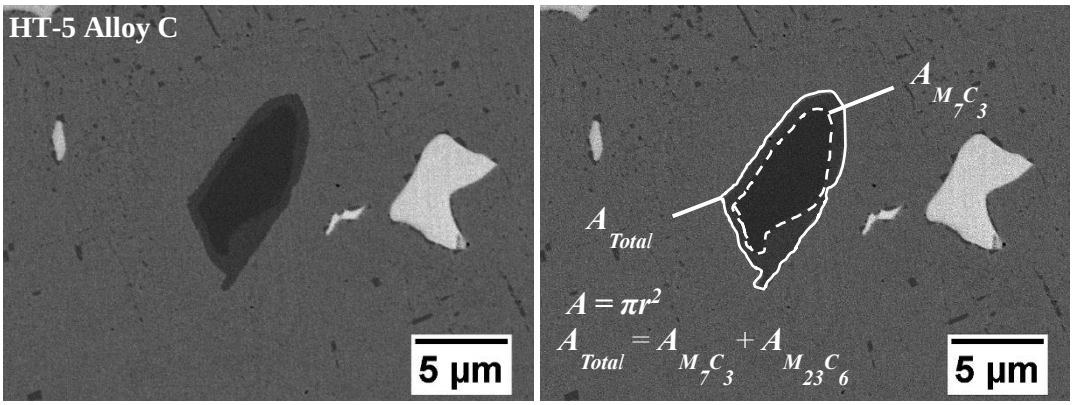

Figure 6.23 Example of measurement of carbide area in HT-5 Alloy C

Table 6.9 Measured areas and equivalent sizes of Cr-carbides in heat treated Alloy C

Specimen	Measured area / μm²			Equivalent size/ μm		
	Total	M_7C_3	$M_{23}C_6$	Total	M_7C_3	$M_{23}C_6$
HT-1	20.29 ± 13.21	11.83 ± 8.28	8.46 ± 7.02	2.40 ± 0.83	1.8 ± 0.72	0.60 ± 0.31
HT–3	20.59 ± 12.31	9.82 ± 7.13	10.76 ± 6.27	2.45 ± 0.76	1.65 ± 0.63	0.79 ± 0.28
HT-5	16.75 ± 9.09	4.99 ± 3.83	11.76 ± 6.94	2.23 ± 0.63	1.17 ± 0.48	1.06 ± 0.39
HT-7	17.15 ± 10.68	4.07 ± 3.52	13.08 ± 8.76	2.24 ± 0.68	1.05 ± 0.45	1.19 ± 0.49
HT-9	19.14 ± 11.61	3.73 ± 3.02	15.42 ± 9.20	2.36 ± 0.72	1.00 ± 0.43	1.36 ± 0.41

From Table 6.9, the measured sizes of $M_{23}C_6$ after 1 hour is 0.60 μm, and increases to 1.36 μm after 9 hours. Figure 6.24 illustrates the comparison of calculated $M_{23}C_6$ size based on Equation 6.7 (n=1,2 and 3) and $M_{23}C_6$ size from experimental measurement. It is obvious that when the diffusion is one dimensional diffusion (n=1), the calculation and experimental measurement are in good agreement expect the $M_{23}C_6$ size after 1 hour heat treatment. This indicates that the transformation from M_7C_3 to $M_{23}C_6$ is one dimensional diffusion process and the growth is mainly controlled by the diffusion of Cr.

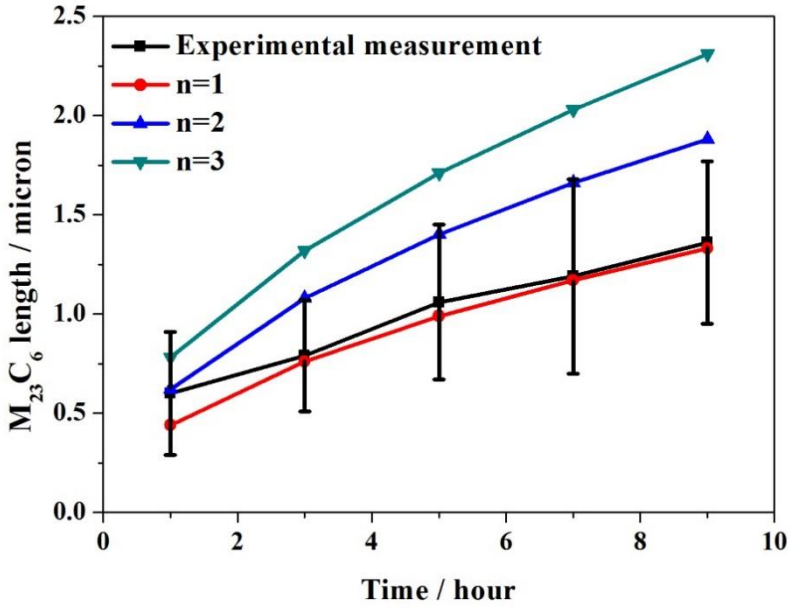

Figure 6.24 Calculated $M_{23}C_6$ size based on Equation 6.7 (n=1,2 and 3) and $M_{23}C_6$ size from experimental measurement

6.6.3 Creep behaviour of Alloy B and Alloy C

The creep behaviours of Alloys B and C have been compared in Section 2.4.5; Alloy C shows a better creep performance, i.e. a longer creep life (Figure 2.53) and a slightly smaller minimum creep rate (Figure 2.54). In intragranular precipitation strengthened alloys like HP40, the microstructural parameters of the precipitates and thus the back stress obtained from the dislocation climb process are the key factor for the creep properties. As discussed in Section 5.6.3, the back-stress σ_b (bypass by climb in this case) can be calculated based on Equations 2.3, 5.6 and 5.7.

The average precipitate interspacings of Alloy B and C have been measured and are listed in Table 6.3: 497 nm for crept Alloy B and 399 nm for crept Alloy C. The shear moduli and Burgers vectors of Alloys B and C, which are needed for calculations of the climb threshold stress using Equation 5.6, are listed in Table 6.10:

Table 6.10 Calculations of climb CRSS, back stress and effective stress of Alloy B and C

		Alloy B	Alloy C
Creep properties	Creep life / hour	124	154
	Minimum creep rate / s^{-1}	2.45×10^{-8}	2.40×10^{-8}
Microstructural parameters for crept specimens	Average precipitate size / nm	136 ± 68	108 ± 37
	Average precipitate interspacing / nm	497 ± 149	399 ± 64
Parameters for calculations	Shear modulus / GPa [165]	45.27	45.27
	Burgers vector / nm [166]	0.25	0.25
Calculation results based on Equation 2.3, 5.6 and 5.7	Climb threshold stress / MPa	7.29	9.08
	Back stress / MPa	7.29	9.08
	Effective applied stress / MPa	32.71	30.92

It is obvious that the climb threshold stress in Alloy C is much larger than that in Alloy B due to the relatively small precipitate interspacing. The larger climb threshold stress will contribute more to back stress in Alloy C. Based on Equations 2.3 and 2.4, with the same applied stress of 40 MPa during the creep tests, there is a smaller effective stress and thus a smaller creep rate in Alloy C. This smaller minimum creep rate helps lead to a longer creep life for Alloy C (154 h) than that for Alloy B (124 h).

Since the microstructures of heat treated Alloy B and C have been described in Section 5.4 and 6.3, the evolution of back stress with increasing time, which is from the interactions between dislocations and secondary Cr-carbides, can be calculated. As shown in Figure 6.25, the back stress of Alloy C is larger than that of Alloy B until 100 hours, leading to a smaller creep rate of Alloy C. However, the back stresses in both alloys decrease, indicating that the intragranular strengthening mechanism loses its effectiveness during long exposure due to precipitation coarsening, which is in agreement with the progressive increase of creep rate.

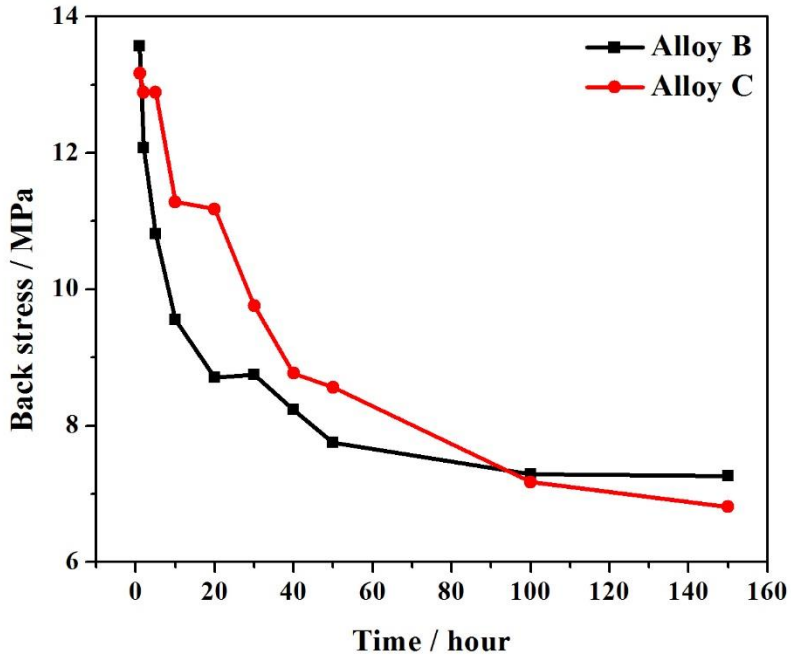

Figure 6.25 Calculated back stress of Alloy B and C as a function of heat treatment time

6.7 Conclusions

1. The higher solidification rate of Alloy C leads to a lager undercooling and thus a smaller critical radius of stable nucleus, which is confirmed by the smaller dendrite cell size (DCS) and secondary dendritic arm spacing (SDAS) in as-cast Alloy C than in as-cast Alloy B;

2. The suppression of formation temperature of NbC due to the faster solidification lead to a larger area fraction of primary Nb-carbide in as-cast Alloy C than in as-cast Alloy B. Meanwhile, as-cast Alloy C contains less primary Cr-carbide since there is less carbon available for the precipitation of M_7C_3 after the formation of NbC.;

3. The average precipitate size in Alloy C is smaller than that of Alloy B up to 50 hours although the secondary Cr-carbides in Alloy C continue growing and become larger than those in Alloy B after 100 hours. This higher coarsening rate of secondary $M_{23}C_6$ in heat treated Alloy C was due to the lager supersaturation after the faster solidification;

4. The *in situ* transformation of primary Cr-carbide from M_7C_3 to $M_{23}C_6$ was analysed by EBSD, TEM-EDS and SAD patterns indicating that the $M_{23}C_6$ nucleates at the interface between the matrix and the M_7C_3 and then grows into the primary M_7C_3, which is mainly controlled by the diffusion of Cr;

5. It is the larger back stress (via a dislocation-precipitate interaction) exerted by the smaller precipitates of secondary $M_{23}C_6$ that leads to a smaller creep rate and thus a longer creep life for Alloy C as compared with Alloy B.

Chapter 7 Microstructure-based climb-glide bypass creep model of HP40

In this study, the microstructures of Alloy A, B and C have been analysed so as to assess their relative creep performances. It would be useful to develop a creep model which has a more quantitative relationship to the microstructural features such as precipitate fraction, precipitate size and interspacing. The microstructure characterisations from this study can be applied to a microstructure-based climb-glide bypass creep model, which is illustrated in Appendix, to predict the creep behaviour of HP40. However, the simulated creep curves fit well with experimental creep curves under special conditions only. This leads to a reconsideration of the limits of current model and discussion of potential modified points.

7.1 Background

Creep curves of pure metals and of single-phase alloys consist, in general, of the three easily identifiable stages of primary, secondary and tertiary creep [176].

The secondary creep rate maintains a constant minimum value over most of the creep life with a steady state being achieved through a balance of recovery and work hardening.

Based on abundant experimental results, Norton [177] found that, up to a life of 10000 hours, there is a straight line relationship between stress and creep rate when the curves are plotted on a logarithmic scale. This relationship can be described as

$$\dot{\varepsilon} = A\sigma^n \quad \text{--- (1)}$$

where $\dot{\varepsilon}$ is creep rate, A is constant, σ is applied stress and n is called the stress exponent.

By including in A a term involving the activation energy of creep, equation (1) represents the creep rate as a function of stress and temperature:

$$\dot{\varepsilon} = A'\sigma^n \exp\left(-\frac{Q}{kT}\right) \text{ --- (2)}$$

where A' is constant, Q is the activation energy of creep (roughly equal to the self-diffusion activation energy), k is Boltzmann's constant and T is the temperature.

Equation (2) is known as the Power Law, and is the most commonly invoked constitutive law to describe creep behaviour. For precipitation-free materials, n generally varies from 1 to 10 [16]. Weertman [94] showed that n should be 4 for steady-state creep by dislocation climb.

Although the power law fits well for pure metals and single-phase alloys, it becomes inadequate for complex engineering alloys, such as nickel-based superalloys and precipitation-strengthened steels. The creep behaviour of such materials deviates from the power law in two main ways:

(i) The values of n and Q are higher than those observed in pure materials: n can be above 20 and Q three times the expected value;

(ii) An established steady state is rarely observed; the creep rate, after a decrease during the primary creep stage, progressively increases from a minimum value until fracture occurs.

To correct these two deviations, the concept of "back-stress" σ_b is invoked. The back-stress is the minimum stress to overcome the interactions between dislocations and precipitates, such as via Orowan looping, cutting and bypass by climb [109]. These interactions oppose the glide of the dislocations, leading to a decrease in the effective applied stress on the material.

$$\sigma_{eff} = \sigma - \sigma_b \text{ --- (3)}$$

where σ_{eff} is the effective stress

Incorporating equation (3) into (2), results in the modified power law equation

$$\dot{\varepsilon} = A''(\sigma - \sigma_b)^n \exp\left(-\frac{Q}{kT}\right) = A''\sigma_{eff}{}^n \exp\left(-\frac{Q}{kT}\right) \quad \text{--- (4)}$$

Threadgill and Wilshire [110] studied a two-phase copper-cobalt alloy and found that, for equation (2), n=5 and Q=140 kJ/mol at low stress and n=12 and Q=210 kJ/mol at high stress. However, Parker and Wilshire [111] applied equation (4) to the same alloy with an experimentally determined back stress σ_b, resulting in Q=110 kJ/mol and n=4 at all stresses; the self-diffusion activation energy for pure copper Q=115 kJ/mol.

The value of σ_b will depend on the characterisation of the precipitate distribution and on the nature of the dislocation precipitate interaction. It thus will not be constant but vary with temperature, stress and time. For example, by introducing the time-dependent coarsening of precipitates, Dyson and McLean [79] established a time-dependent creep model for IN597. This approach is now known as continuum damage mechanics (CDM). Similar approaches have been developed by Stevens and Flewitt [109, 123] for IN738, Williams and Cane [124] for 0.5Cr0.5Mo0.25V steel and Rosler and Arzt [120] for aluminium alloys and bubble-strengthened tungsten.

The above approaches (based on equation (4)) to modelling the creep behaviour of complex engineering alloys are generally empirical and lack physical justification of the stress exponent n and constant A. Furthermore, these models have no immediate quantitative relationship to microstructural parameters such as dislocation density, precipitate volume, precipitate size and precipitate interspacing. Basoalto et al. [125, 126] were the first to derive a creep equation for nickel-based superalloys with consideration of microstructural parameters. A refinement of this model had been presented by Dyson [127], which is a microstructure-based climb-glide bypass model linking

microstructural evolution to the creep rate. The model accounts for three previously identified changes in microstructure that occur during creep:

(i) Coarsening of the precipitates based on Ostwald ripening

(ii) A progressive increase in mobile dislocation density with accumulated creep strain

(iii) The development of grain boundary cavities

However, Coakley et al. [128] pointed out that Dyson's model is only suitable for a unimodal particle size distribution while some nickel-based superalloys have a bimodal particle size distribution.

Oruganti et al. [129, 178] presented a similar model for 9-10% Cr ferritic steels assuming that creep occurs by the thermally activated release of dislocations from pinning. Zhu et al. [130] made the spherical particles into cubic ones for CMSX-4 and introduced an effective diffusivity D_{eff} to account for the dependence of creep deformation on alloy chemistry.

In the present work, Dyson's microstructure-based climb-glide bypass model has been selected for the prediction of HP40's creep behaviour for the following reasons:

(i) The model is created via kinetic equations. Most of the parameters in this model have a physical justification and interpretation rather than being just empirical;

(ii) The model contains terms to predict the microstructure evolution and its influence on creep rate during the whole creep process;

(iii) The model has been applied to several nickel-based superalloys and precipitation-strengthened steels and it fitted well over a range of temperatures and pressures.

Furthermore, some refinements have been included in this model in this work.

7.2 Model description

7.2.1 Initial microstructural features (crept Alloy A)

Figure 7.1 is a schematic illustration of the dislocation and particle microstructure being modelled:

The material, loaded under a uniaxial tension σ, is simplified with a unimodal set of distributed precipitates with a volume fraction f_p.

The precipitates are assumed to be cubic with a particle size d_p and an interspacing λ_p.

For a constant volume fraction f_p:

$$f_p = d_p^{\,3} / \left(d_p + \lambda_p\right)^3 \text{--- (5)}$$

So that

$$\lambda_p = d_p (1/ f_p^{\,1/3} - 1) \text{ --- (6)}$$

The initial microstructural parameters (d_p, λ_p , and f_p) need to be measured.

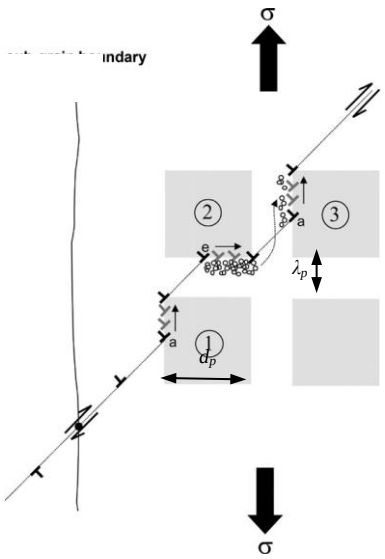

Figure 7.1 Geometry of climb/glide events in a precipitation-strengthened material [130]

From Figure 7.2 (a), the minimum strain rate of Alloy A, at the transition from primary creep to secondary creep, occurs at a strain of 0.4 %. In Figure 7.2 (b), it took 12 hours to get to a strain of 0.4 %. Therefore, the initial microstructural parameters should be obtained from the specimen crept at 1000 ^{o}C-40 MPa for 12 hours, which was crept Alloy A in all specimens. The measurement area (Figure 7.3) is selected to be close to grain boundaries with a width of 2 μm for the following reasons:

(i) From Figure 7.3 (a), most of intragranular precipitates are in the area of 0~2μm from grain boundaries indicating that this area has highest particle density;

(ii) The particle size in the area of 0~2μm from grain boundaries is around 100 nm, which is suitable for dislocation-precipitate interactions. However, the size of precipitates beyond this area can be to several microns (particle 1 and 2 in Figure 7.3 (b)) making them difficult to act as effective obstacles for dislocation movement;

(iii) Grain boundaries can be potential sites for dislocation generation during creep leading to a great possibility for dislocation-precipitate interactions in the area close to grain boundaries.

The initial microstructural parameters are shown in Table 7.1. Figure 7.4 confirms that the crept Alloy A contains a unimodal particle distribution, which is in agreement with the assumptions of the model.

Table 7.1 Initial microstructural parameters for crept Alloy A

Microstructure features		
Particle size d_p / nm	Volume fraction f_p / %	Average interspacing λ_p / nm
159	21.24	92

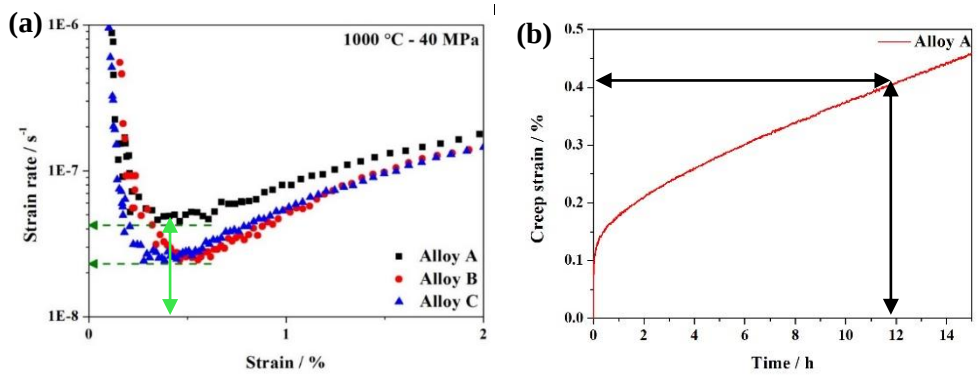

Figure 7.2 Alloy A (a) Strain rate as a function of strain and (b) strain at a function of time

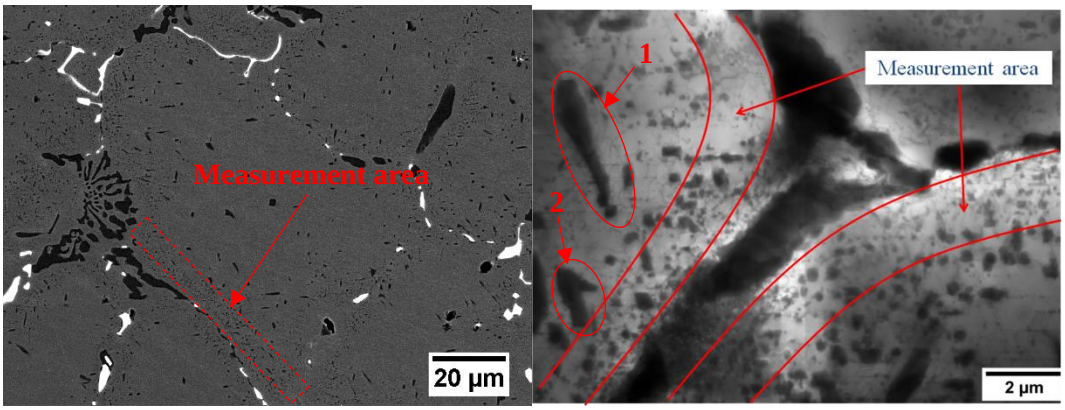

Figure 7.3 (a) BSE image and (b) TEM BF image illustrating the measurement area in crept Alloy A

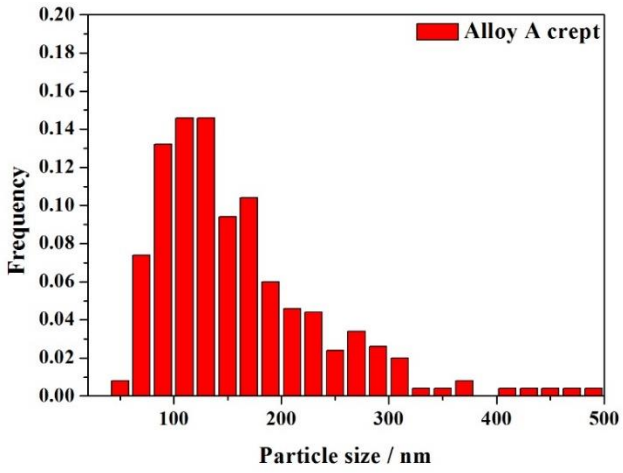

Figure 7.4 Particle size distribution for crept Alloy A

7.2.2 Assessment of creep deformation mechanisms

In order to interpret the creep results, one must first assess the deformation mechanisms: Orowan looping, cutting or by-pass by climb.

(i) Critical shear stress for Orowan looping [179] (Figure 7.5):

$$\tau_{c(looping)} = \frac{Gb}{\lambda_p} \text{ --- (7)}$$

where G is the shear modulus and b is the Burgers vector

(ii) Critical shear stress for cutting [180]:

$$\tau_{c(cutting)} = \frac{\gamma_{APB}}{2b}\left[\left(\frac{8\gamma_{APB} f_p d_p}{\pi G b^2}\right)^{1/2} - f_p\right] \text{ --- (8)}$$

where γ_{APB} is the anti-phase boundary energy

(iii) Critical shear stress for climb [164]:

$$\tau_{c(climb)} = \frac{0.32Gb}{\lambda_p} \text{ --- (9)}$$

For Alloy A at 1000 ^{o}C the shear modulus is 47.39 GPa, the Burgers vector is 3.3×10^{-10} m and the anti-phase boundary energy is 0.2 J/m^2

The critical stresses for the three deformation mechanisms are shown in Table 7.2

Table 7.2 Calculation of critical stresses for deformation mechanisms with G=47.39 GPa, b=3.3×10^{-10} m, γ_{APB} = 0.2 J/m^2, d_p=159 nm, f_p=21.24%, λ_p=92 nm and Taylor factor M=3.1 (σ=M•τ)

Critical stresses						
Applied stress	Orowan looping		Cutting		Climb	
σ / MPa	$\tau_{c(looping)}$/MPa	$\sigma_{c(looping)}$/MPa	$\tau_{c(cutting)}$/MPa	$\sigma_{c(cutting)}$/MPa	$\tau_{c(climb)}$/MPa	$\sigma_{c(climb)}$/MPa
40	169.99	526.97	894.80	2773.88	54.40	168.64

Although the accuracy of the equations for critical shear stress are approximate, it is obvious that the critical shear stress for climb is much lower than that for Orowan looping or cutting, confirming that the climb is the dominant deformation mechanism at 1000 °C and 40 MPa.

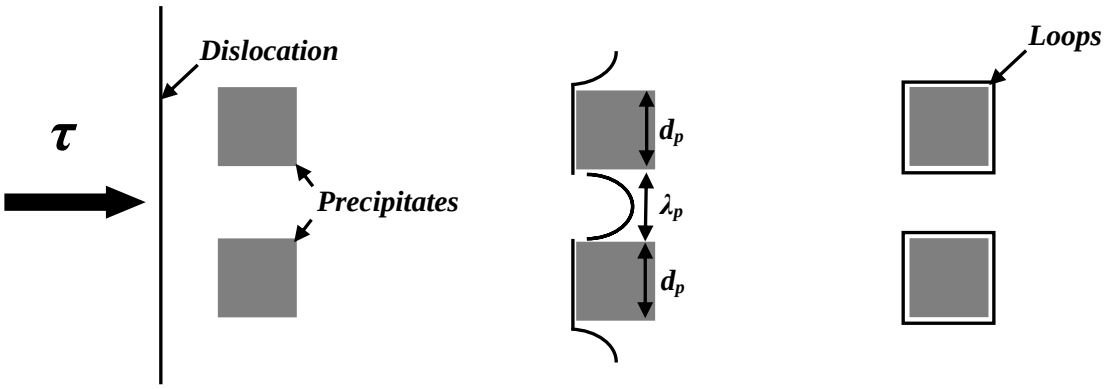

Figure 7.5 Schematic of Orowan looping

7.2.3 Microstructure

The dislocations are assumed to be active. In the absence of diffusion, the dislocations will start to glide until the nearest particle is reached. At a test temperature greater than half the melting temperature (0.5 T_m is 973 K while the creep test temperature is 1273 K), the dislocations can climb along the particle/matrix interface. Consider the dislocations interacting with particle 1 in Figure 7.1. The slip plane/particle geometry dictates the direction of climb and the need for an associated coupled glide. The local climb force is such that the dislocations climb by vacancy absorption --- symbol 'a' on particle 1. The dislocation then climbs along the matrix/particle interface until it is in a position to glide further within the matrix. After being stopped at particle 2, climb occurs again, this time by vacancy emission --- symbol 'e' on particle 2. Under uniaxial stress, these absorptions/emissions would be reversed. On average, the number of 'a' and 'e' types of climb will be equal.

7.2.4 Estimation of shear strain rate

According to Orowan's equation, the microscopic creep shear strain rate $\dot{\gamma}$ is related to the mobile gliding dislocation density ρ_g:

$$\dot{\gamma} = b\rho_g v_g \quad \text{--- (10)}$$

where b is the Burgers vector and v_g is the glide velocity.

For precipitation-strengthened alloys deforming via climb-bypass, only the matrix will be sheared; the particles deform elastically only. Therefore, the equation can be modified by limiting the deformation to the matrix.

$$\dot{\gamma} = (1 - f_g) b\rho_g v_g \quad \text{--- (11)}$$

At elevated temperature, f_g, b and v_g can be considered as constant. Attention must therefore be paid to the gliding dislocation density ρ_g.

The total mobile dislocation density ρ_m is divided between that gliding within the matrix ρ_g and that climbing along the matrix/particle interface ρ_c. Thus

$$\rho_m = \rho_g + \rho_c \text{ --- (12)}$$

As ρ_m is constant in equation (12), the probability of climbing dislocations' escape ("C" in Figure 7.6) from matrix/particle interface into the matrix ($\rho_c \downarrow$) will increase the number of gliding dislocations ($\rho_g \uparrow$). Meanwhile, the gliding dislocations can be trapped by particles ("A" in Figure 7.6) leading to a decrease of the number of gliding dislocations.

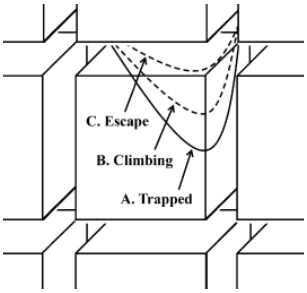

Figure 7.6 Dislocation movement during creep

Thus, the next step is to determine the net rate of change of gliding dislocation density $\dot{\rho}_g$.

$$\dot{\rho}_g = \dot{\rho}_{g,i} - \dot{\rho}_{g,d} \text{ --- (13)}$$

where $\dot{\rho}_{g,i}$ and $\dot{\rho}_{g,d}$ are the rates of increase and decrease of gliding dislocation density, respectively.

The climbing dislocation density in contact with the particles is $\rho_c f_p$. A fraction $b/(d_p/2)$ will be in a position to escape into the matrix. Let climbing dislocations escape at a frequency Γ_e. Then

$$\dot{\rho}_{g,i} = \rho_c f_p \frac{2b}{d_p} \Gamma_e \text{ --- (14)}$$

The rate at which gliding dislocations are trapped depends on the time required for a gliding dislocation to move from one particle to the nearest particle. Thus

$$\dot{\rho}_{g,d} = \rho_g \frac{v_g}{\lambda_p} \quad \text{--- (15)}$$

$$\dot{\rho}_g = \dot{\rho}_{g,i} - \dot{\rho}_{g,d} = \rho_c f_p \frac{2b}{d_p} \Gamma_e - \rho_g \frac{v_g}{\lambda_p} \quad \text{--- (16)}$$

Taking equation (12) into equation (16)

$$\rho_g = \rho_m \frac{f_p \frac{2b}{d_p} \lambda_p \Gamma_e}{v_g + f_p \frac{2b}{d_p} \lambda_p \Gamma_e} \left\{ 1 - \exp\left[- \frac{v_g + f_p \frac{2b}{d_p} \lambda_p \Gamma_e}{\lambda_p} t \right] \right\} \quad \text{--- (17)}$$

Since creep is a long-time process, it can be assumed that $\left\{ 1 - \exp\left[- \frac{v_g + f_p \frac{2b}{d_p} \lambda_p \Gamma_e}{\lambda_p} t \right] \right\} \approx 1$. Thus

$$\rho_g = \rho_m \frac{f_p \frac{2b}{d_p} \lambda_p \Gamma_e}{v_g + f_p \frac{2b}{d_p} \lambda_p \Gamma_e} \quad \text{--- (18)}$$

Assuming that $v_g >> f_p \frac{2b}{d_p} \lambda_p \Gamma_e$, i.e. for precipitation-strengthened alloy, the glide rate within the matrix is fast and the shear strain rate is controlled by the rate at which climbing dislocations escape from particles, then

$$\rho_g = \rho_m \frac{f_p \frac{2b}{d_p} \lambda_p \Gamma_e}{v_g} \quad \text{--- (19)}$$

Recalling equations (6) and (11), the shear creep rate is

$$\dot{\gamma} = 2\rho_m b^2 f_p (1 - f_p)(1/ f_p^{1/3} - 1)\Gamma_e \quad \text{--- (20)}$$

The climb escape frequency now needs to be estimated.

7.2.5 Climb frequency Γ_e

Since climb occurs by migration of jogs along the dislocations, the frequency Γ_e is expected to be given by a vacancy emission process. Climb occurs by migration of jogs on the dislocation line through emission or absorption of vacancies. Thus

$$\Gamma_{e,e} = c_j n v \exp(-\frac{\Delta E - \Delta W}{kT}) \quad \text{--- (21)}$$

where the second subscript 'e' refers to vacancy emission, c_j is the jog density, n is the density of locations where vacancies can emit or absorb, v is the Debye frequency, ΔE is the activation energy and ΔW is the work done by movement of the dislocations.

$$\Delta W = \tau b \bullet b \lambda_p \quad \text{--- (22)}$$

Since the mass transport during this process will be effected by vacancy flow, the rate of climb can be described as:

$$D_v = n v b^2 \exp(-\frac{\Delta E}{kT}) \quad \text{--- (23)}$$

Combining equations (15), (16) and (17),

$$\Gamma_{e,e} = \frac{c_j D_v}{b^2} \exp(\frac{\tau b^2 \lambda_p}{kT}) \quad \text{--- (24)}$$

Similarly, for vacancy absorption

$$\Gamma_{e,a} = \frac{c_j D_v}{b^2} \exp(-\frac{\tau b^2 \lambda_p}{kT}) \quad \text{--- (25)}$$

Therefore the net escape frequency is given by

$$\Gamma_e = \Gamma_{e,e} - \Gamma_{e,a} = \frac{c_j D_v}{b^2} \exp(\frac{\tau b^2 \lambda_p}{kT}) - \frac{c_j D_v}{b^2} \exp(-\frac{\tau b^2 \lambda_p}{kT}) = \frac{c_j D_v}{b^2} \sinh(\frac{\tau b^2 \lambda_p}{kT}) \quad \text{--- (26)}$$

Substituting equation (26) into equation (20), the shear strain rate is

$$\dot{\gamma} = 2\rho_m f_p(1-f_p)(1/f_p^{1/3}-1)c_j D_v \sinh(\frac{\tau b^2 \lambda_p}{kT}) \quad \text{--- (27)}$$

The shear strain can then be transferred to tensile strain rate (creep rate)

7.2.6 Estimation of tensile strain rate

For a polycrystal material under uniaxial tension, the Taylor factor must be included. The tensile strain rate then is

$$\dot{\varepsilon} = 2M^{-1}\rho_m f_p(1-f_p)(1/f_p^{1/3}-1)c_j D_v \sinh(\frac{\sigma b^2 \lambda_p}{MkT}) \quad \text{--- (28)}$$

where M is the Taylor factor (M = 3.1 for fcc crystal)

For material held at a certain temperature, such as 1000 ^{o}C, the precipitate volume fraction and diffusion rate can be considered constant. Thus equation (28) can be simplified to

$$\dot{\varepsilon} = A \bullet \rho_m \sinh(\frac{\sigma}{\sigma_p}) \quad \text{--- (29)}$$

where $A = 2M^{-1} f_p(1-f_p)(1/f_p^{1/3}-1)c_j D_v$

$$\sigma_p = MkT / b^2 \lambda_p$$

Equation (29) is only for the case of a stable microstructure without consideration of change of microstructure features during service at elevated temperature.

7.2.7 Modified tensile strain rate based on microstructure evolution

The microstructure of precipitation-strengthened material is not stable at elevated temperature. The model can be modified to account for the following microstructure evolution during service.

(i) As inelastic strain accumulates, dislocation source will be activated leading to a progressive increase in dislocation density. This lead to an increase in ρ_m by a factor $(1+I_d)$

where $I_d = \frac{\rho}{\rho_m} - 1$ --- (30)

Based on a empirical equation for the evolution rate of dislocations,

$\dot{I}_d = C\dot{\varepsilon}$ --- (31)

(ii) The particles will coarsen during service. As particle size increase, there will be an increase of interspacing λ_p. This leads to a decrease in σ_p (Equation 29) by a factor $(1-I_p)$. Assuming Ostwald ripening to occur with a kinetic rate constant K'_p, the factor I_p can be given by

$\frac{d_o}{d} = 1 - I_p$ --- (32)

For Ostwald ripening law

$d^3 - d_o{}^3 = K_p \exp(-Q_p / RT)t$ --- (33)

$\frac{d_o{}^3}{d^3} = \frac{d_o{}^3}{K_p \exp(-Q_p / RT)t + d_o{}^3}$ --- (34)

$\left(1 - I_p\right)^{-3} = 1 + \frac{K_p}{d_o{}^3} \exp(-Q_p / RT)t$ --- (35)

Differentiating with respect to time

$$3\left(1-I_p\right)^{-4}\dot{I}_p=\frac{K_p}{d_o^{\,3}}\exp(-Q_p/RT)\ \text{--- (36)}$$

Rearranging, one has

$$\dot{I}_p=\frac{K_p}{3d_o^{\,3}}\exp(-Q_p/RT)\left(1-I_p\right)^4=\frac{K_p'}{3}(1-I_p)^4\ \text{--- (37)}$$

$$K_p'=\frac{K_p}{d_o^{\,3}}\exp(-Q_p/RT)\ \text{--- (38)}$$

(iii) In precipitation-strengthened alloy, the applied stress should be replaced by σ_{eff}

$$\sigma_{eff}=\sigma-\sigma_b\ \text{--- (39)}$$

Where σ is applied stress and σ_b is back stress.

Based on the description by Ion

$$\dot{\sigma}_b=\frac{f_pE}{1-f_p}(1-\frac{\sigma_b}{\sigma_b^*})\dot{\varepsilon}\ \text{--- (40)}$$

where E is the Young's modulus and σ_b^* is the upper bound value fro back stress.

$$\sigma_b^*=\frac{2f_p}{1+2f_p}\sigma\ \text{--- (41)}$$

7.2.8 The final model description

$$\dot{\varepsilon} = A \bullet \rho_m (1 + I_d) \sinh\left(\frac{\sigma_{eff}}{\sigma_p (1 - I_p)}\right)$$

$$A = 2M^{-1} f_p (1 - f_p)(1/ f_p^{1/3} - 1) c_j D_v$$

$$\sigma_p = MkT / b^2 \lambda_p$$

$$\dot{I}_d = C \dot{\varepsilon}$$

$$\dot{I}_p = \frac{K_p}{3} (1 - I_p)^4$$

$$\sigma_{eff} = \sigma - \sigma_b$$

$$\dot{\sigma}_b = \frac{f_p E}{1 - f_p} \left(1 - \frac{\sigma_b}{\sigma_b^*}\right) \dot{\varepsilon}$$

$$\sigma_b^* = \frac{2 f_p}{1 + 2 f_p} \sigma$$

7.3 Application of the model

7.3.1 Application of the model to Alloy A

The first step to apply the current model on Alloy A is to estimate the various physical and microstructural constants, which are listed in Table 7.3.

Table 7.3 Estimates of physical constants and microstrutural parameters for Alloy A

Applied stress σ	Temperature T	Taylor factor M	Young's modulus E	Burgers vector b	Dislocation density ρ_m
40 MPa	1273 k	3.1	117.7 GPa	2.5×10^{-10} m	10^{10} m^{-2}
Jog density c_j	Diffusivity rate D_v	Coarsening rate	Particle size d_p	Interspacing λ_p	Volume fraction f_p
1	1.58×10^{-15} m^2/s	3.4×10^{-27} m^3/s	159 nm	92 nm	21.24 %

Some of the constants and parameters, such as coarsening rate and particle size, are from experimental measurements. Others, like dislocation density and jog density, are uncertain and pre-set.

Figure 7.7 shows the comparison of simulated (red line) and experimental (black line) creep curves for Alloy A at 1000 ^oC and 40 MPa. The simulated creep curve shows a much shorter creep life, which creep strain reaches 20 % at 3 hours. As current model is sensitive to microstructural features, to explain such a difference between simulated and experimental creep curves, consideration needs to be paid on pre-set microstructrual parameters, such as the volume fraction of precipitates.

From Figure 7.8, it is important to note that the volume fractions for each measurement can vary from 10 % to 45 %. Therefore, the average value of volume fraction 21.24% is not suitable to represent each measurement area. To find out the influence of volume fraction on current model, further predictions are made in function of volume fraction (Figure 7.9).

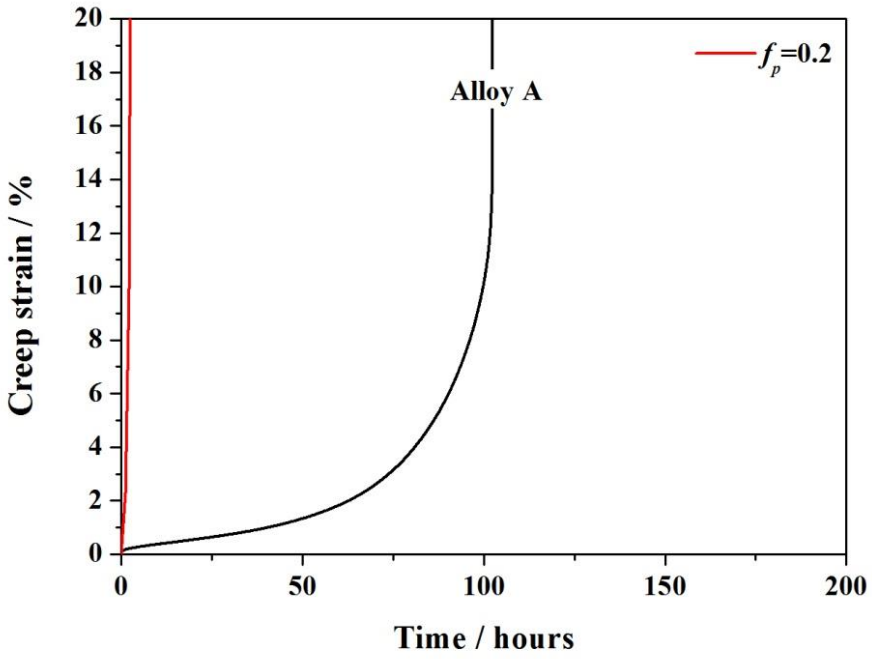

Figure 7.7 Comparison of simulated and experimental creep curves for Alloy A

f_p=0.1

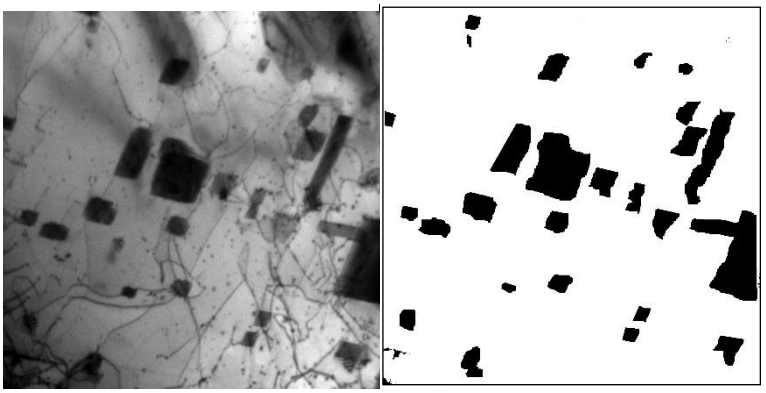

f_p=0.2

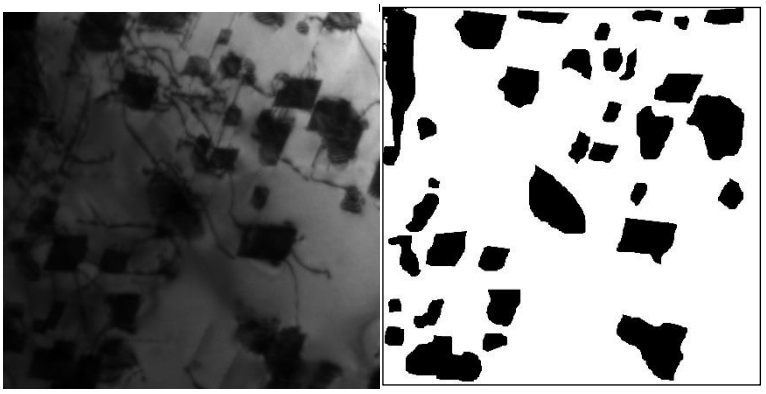

f_p=0.3

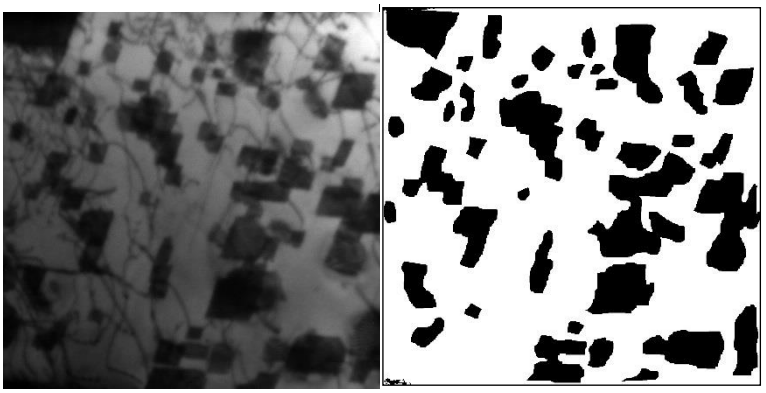

f_p=0.45

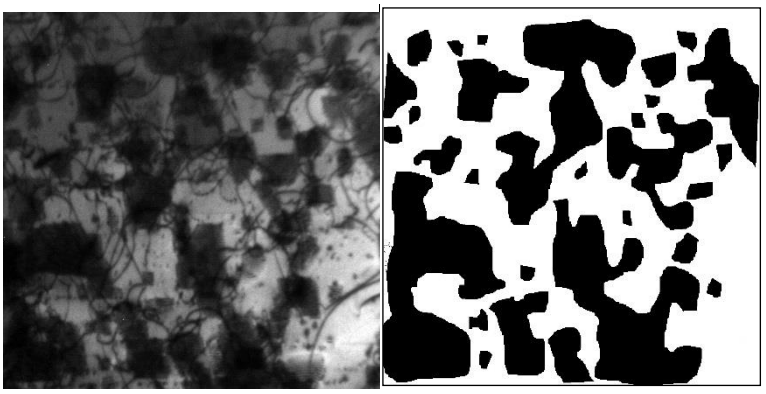

Figure 7.8 Volume fractions for different measurement areas

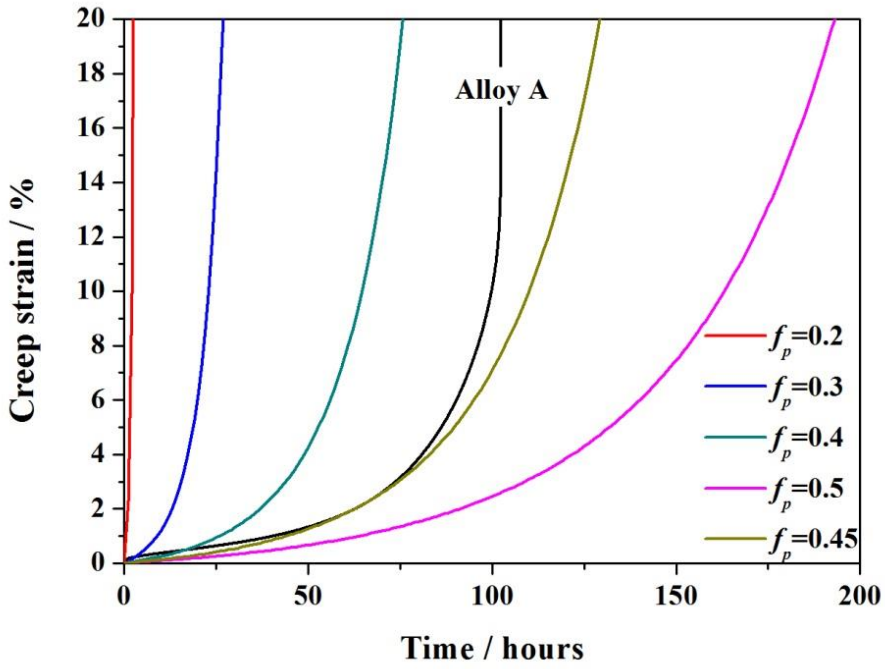

Figure 7.9 Simulated creep curves in function of volume fraction

In Figure 7.9, simulated creep curves show similar shapes, but only the simulated creep curve with volume fraction of 0.45 fits well compared with experimental creep curve. This leads to a reconsideration of the accuracy of volume fraction measurement and discussion of the limits of current model.

Another problem for current simulation result is that, if we assume the volume fraction is 0.45, the simulated result shows a slower strain rate after about 75 hours, which is the tertiary creep stage. This is probably due to lack of involvement of cavity growth, which is a general damage mechanism in tertiary creep and leads to an increase of strain rate.

7.3.2 Application of the model to Alloy B and Alloy C

The same model was applied to Alloy B and Alloy C. All the physical constants for Alloy B and Alloy C were the same as for Alloy A. The microstructural parameters used for the three alloys were all obtained from crept specimens and are listed in Table 7.4. As discussed above, only the simulated creep curve for a precipitate volume fraction of 0.45 fits well compared with experiment; the volume fractions of precipitates for Alloy B and Alloy C are controlled to be 0.45. Therefore, the only difference among the three alloys for model application is the microstructural parameter, i.e., precipitate size of secondary Cr-carbide.

Figure 7.10 shows comparisons of simulated (red line) and experimental (black line) creep curves for the three alloys at 1000 ^{o}C and 40 MPa. Simulated creep curves for the three alloys have similar shapes and only fit well with experimental creep curves before the tertiary stages. Furthermore, with a decrease of precipitate size, the creep life in the simulated creep curves increases (Figure 7.10 (d)), in agreement with the experimental results (Figure 2.57), which can be explained as the larger back stress obtained from a smaller precipitate size.

Table 7.4 Microstructural parameters for simulation

Specimens	Microstructural parameters	
	Precipitate size / nm	Volume fraction / %
Crept Alloy A	159	45
Crept Alloy B	136	
Crept Alloy C	108	

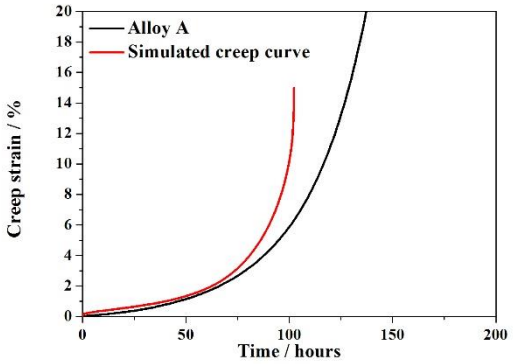

(a)

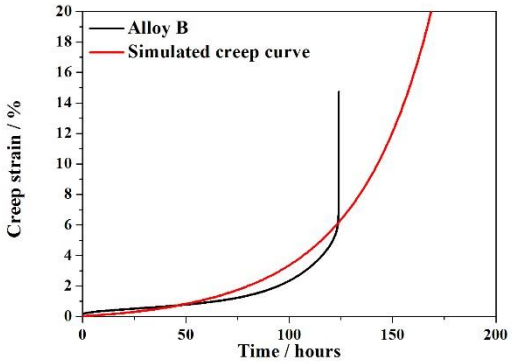

(b)

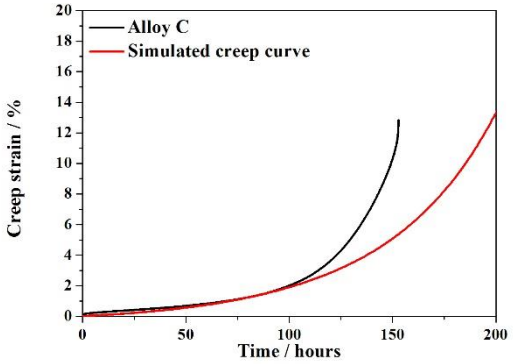

(c)

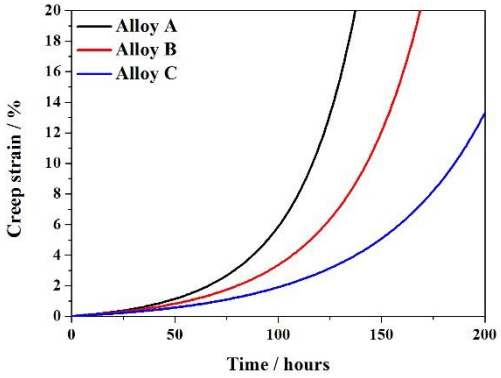

(d)

Figure 7.10 Simulated and experimental creep curves for (a) Alloy A, (b) Alloy B and (c) Alloy C; (d) comparison of simulated creep curves for the three alloys

7.4 Limitations and potential modified points

(i) Microstructural definition:

The microstructural definition in original model is for nickel-based superalloys, which contain a uniform distribution of precipitates and a constant volume fraction. However, in HP40 stainless steel, the distribution of secondary Cr-carbide varies within grains leading to a non-uniform distribution. As mentioned above, the volume fraction of secondary Cr-carbide can vary from 0.1 to 0.45. The role of primary carbides which are of also intragranular type is not taken into consideration in this model. A finer definition of microstructure is needed to be done.

(ii) Precipitation evolution:

The current model considers the evolution of precipitation as Ostwald ripening with a constant coarsening rate. The Ostwald ripening (or LSW theory) has its limits and can only be applied in specific cases. As discussed in Chapter 5.4, the evolution of secondary Cr-carbide contains not only coarsening but also growth of precipitates during service. The nucleation and growth of precipitates shall a faster rate than the rate of coarsening and need to be involved to refine current model.

(iii) Grain boundary cavity during tertiary creep stage:

During the tertiary creep stage, the nucleation and growth of cavity on grain boundary will lead to a rapid increase of creep strain rate. The current model does not include the damage caused by cavity during tertiary creep stage. Furthermore, the role of nucleation and growth of cavity should be involved in the simulation.

7.5 Conclusions

1. A microstructure-based climb-glide bypass creep model, which has a quantitative relationship to the microstructural features, was described. Microstructure parameters determined in this study, such as precipitate size and interspacing, were applied in this model to predict the creep behaviour of HP40;

2. Comparison of simulated and experimental creep curves for Alloy A (at 1000 ^{o}C and 40 MPa) illustrates that the simulated creep curve shows a much shorter creep life; creep strain reaches 20 % at 3 hours. As the current model is sensitive to microstructural features, to explain such a difference between simulated and experimental creep curves, consideration needs to be paid to the pre-set microstructural parameters, such as the volume fraction of the precipitates;

3. Simulated creep curves with different volume fractions of precipitates show similar shapes, but only the simulated creep curve with a volume fraction of 0.45 fits well to the experimental creep curve. For the tertiary creep stage, the simulated result shows a much slower strain rate than the experimental one, which is due to not taking grain boundary cavitation into consideration;

4. With a decrease of precipitate size from Alloy A to Alloy C, the creep life in the simulated creep curves increases, in agreement with the experimental results, which can be explained via the larger back stress obtained from a smaller precipitate size;

5. Since the simulated creep curves fit well with experimental creep curves under special conditions only, the current model has its limitations and needs modifications including microstructural definition, precipitation evolution and grain boundary cavitation during the tertiary creep stage.

Chapter 8 Summary of conclusions and suggestions for future work

8.1 Conclusions

Microstructural characterisdation of HP40 (Alloy A)

1. During casting of HP40, austenite is the first to solidify from the liquid and forms primary dendrite cells followed by the precipitation of NbC and eutectic reaction $L \rightarrow \gamma + M_7C_3$. This solidification sequence leads to the as-cast microstructure of Alloy A, which contains austenitic matrix and a primary precipitation network (primary Cr-carbides (M_7C_3) and primary Nb-carbides (NbC));

2. In crept Alloy A, the primary Cr-carbides transformed from metastable M_7C_3 to stable $M_{23}C_6$ to reduce the system free energy. G-phase, which is likely transformed from NbC, was observed in crept Alloy A at the interface between the primary Cr-carbide and the matrix due to the instability of the NbC. Area fractions of primary Cr-carbides and primary Nb-carbides both increased after creep due to the growth of precipitates;

3. After creep, secondary precipitation was observed within the matrix due to the supersaturation of the matrix solid solution, which are identified as secondary Cr-carbides ($M_{23}C_6$) and fine particles (NbN). The microstructural parameters of secondary Cr-carbides ($M_{23}C_6$) were measured, i.e. the precipitate size distribution of secondary Cr-carbides ($M_{23}C_6$) shows a unimodal distribution with a Gaussian mean of 126 nm and a full width at half maximum of 109 nm;

4. In HT-12 Alloy A (without stress), the area fractions of various carbides and the average precipitate size of secondary Cr-carbides are both smaller than those of crept Alloy A (with stress), indicating that the stress can enhance the coarsening of precipitate by accelerating the diffusion coefficient (distortion of the crystal symmetry and reduction of diffusion activation) and providing easier diffusion paths (increase of dislocation density);

Effect of chemical composition on microstructure of HP40 (Alloy B c.f. Alloy A)

5. The additions of W and Nb in Alloy B suppressed the formation of carbides by reducing free carbon in the matrix, leading to a smaller area fraction of primary Cr-carbide (2.75 %) and primary Nb-carbide (1.34 %) in as-cast Alloy B compared with as-cast Alloy A (3.89 % for primary Cr-carbide and 1.40 % for primary Nb-carbide);

6. The combined effects of Ti and W led to a slower coarsening behaviour of secondary Cr-carbides in Alloy B than in Alloy A, which is in agreement with experimental observation, i.e., a smaller area fraction and a smaller average precipitate size in crept Alloy B than in crept Alloy A;

7. The area fractions of primary and secondary carbides, precipitate size and interspacing of secondary $M_{23}C_6$ in heat treated Alloy B were also characterised. During heat treatment of Alloy B at 1000 ^{o}C from 1 to 150 hours, the area fractions of primary Nb-carbide and secondary Cr-carbide and the average size of secondary $M_{23}C_6$ increases continuously from the beginning of heat treatment due to the growth and coarsening of precipitates;

8. The combination of M_7C_3 dissolution, $M_7C_3 \rightarrow M_{23}C_6$ transformation and $M_{23}C_6$ growth leads to a fluctuation in area fraction of primary Cr-carbide up to 20 hours in heat treated Alloy B. After 20 hours, the area fraction of primary Cr-carbide increase continuously with a faster rate than that of primary Nb-carbide due to the insufficient solute content and slow diffusion rate of niobium in the matrix.;

Effect of solidification rate on microstructure of HP40 (Alloy C c.f. Alloy B)

9. The higher solidification rate of Alloy C leads to a lager undercooling and thus a smaller critical radius of stable nucleus, which is confirmed by the smaller dendrite cell size (DCS) and secondary dendritic arm spacing (SDAS) in as-cast Alloy C than in as-cast Alloy B;

10. The suppression of formation temperature of NbC due to the faster solidification lead to a larger area fraction of primary Nb-carbide in as-cast Alloy C than in as-cast Alloy B. Meanwhile, as-cast Alloy C contains less primary Cr-carbide since there is less carbon available for the precipitation of M_7C_3 after the formation of NbC.;

11. The average precipitate size in Alloy C is smaller than that of Alloy B up to 50 hours although the secondary Cr-carbides in Alloy C continue growing and become larger than those in Alloy B after 100 hours. This higher coarsening rate of secondary $M_{23}C_6$ in heat treated Alloy C was due to the lager supersaturation after the faster solidification;

12. The *in situ* transformation of primary Cr-carbide from M_7C_3 to $M_{23}C_6$ was analysed by EBSD, TEM-EDS and SAD patterns indicating that the $M_{23}C_6$ nucleates at the interface between the matrix and the M_7C_3 and then grows into the primary M_7C_3, which is mainly controlled by the diffusion of Cr;

13. It is the larger back stress (exerted by dislocation-precipitate interaction) exerted by the smaller precipitates of secondary $M_{23}C_6$ that leads to a smaller creep rate and thus a longer creep life for Alloy B and Alloy C compared with Alloy A, which is in agreement with observations obtained from creep tests at 1000 ^oC and 40 MPa.

Microstructure-based climb-glide bypass creep model of HP40

14. A microstructure-based climb-glide bypass creep model, which has a quantitative relationship to the microstructural features, was described. Microstructure parameters determined in this study, such as precipitate size and interspacing, were applied in this model to predict the creep behaviour of HP40;

15. Comparison of simulated and experimental creep curves for Alloy A (at 1000 ^{o}C and 40 MPa) illustrates that the simulated creep curve shows a much shorter creep life; creep strain reaches 20 % at 3 hours. As the current model is sensitive to microstructural features, to explain such a difference between simulated and experimental creep curves, consideration needs to be paid to the pre-set microstructural parameters, such as the volume fraction of the precipitates;

16. Simulated creep curves with different volume fractions of precipitates show similar shapes, but only the simulated creep curve with a volume fraction of 0.45 fits well to the experimental creep curve. For the tertiary creep stage, the simulated result shows a much slower strain rate than the experimental one, which is due to not taking grain boundary cavitation into consideration;

17. With a decrease of precipitate size, the creep life in the simulated creep curves increases, in agreement with the experimental results, which can be explained via the larger back stress obtained from a smaller precipitate size;

18. Since the simulated creep curves fit well with experimental creep curves under special conditions only, the current model has its limitations and needs modifications including microstructural definition, precipitation evolution and grain boundary cavitation during the tertiary creep stage.

8.2 Suggestions for future work

1. Since Alloy C has the best creep resistance of the alloys in this project, it is necessary to characterise further the microstructure of Alloy C at different temperatures and stresses, in order to study more systematically the microstructural evolution of HP40 under steam reforming service conditions;

2. Modifications need to be made for current microstructure-based climb-glide bypass creep model, including microstructural definition, precipitation evolution and grain boundary cavity during tertiary creep stage, to accurately predict the creep behaviour of HP40 and suggest directions of further modifications to HP40;

3. With further requirements from the steam reforming process, the effort to improve HP40 creep properties has been progressing for 70 years and will no doubt keep moving forward. It is required to develop a next generation HP40 alloy, ‘Alloy D’, with optimised creep performance. In order to achieve a better creep resistance, Alloy D should have a larger content of molybdenum or tungsten to delay the coarsening of secondary Cr-carbide and a higher solidification rate to refine the as-cast microstructure.

Appendix Code via Fortran

```
!!!!!!!!!!!!!!!!!!!!!!!!!!!!!!!!!!!!
!  Define various parameters !
!!!!!!!!!!!!!!!!!!!!!!!!!!!!!!!!!!!!
  Real*8 e                ! strain
  Real*8 e_dot            ! strain rate (epsilon_dot) in Eq. (2a)
  Real*8 e_dot_0          ! strain rate coefficient (epsilon_dot_0) in Eq. (2a)
  Real*8 D_d              ! damage variable in Eq. (2a)
  Real*8 sigma            ! applied stress (sigma) in Eq. (2a)
  Real*8 H                ! normalised back stress (H=sigma_b/sigma) in Eq. (2a)
  Real*8 sigma_0          ! isotropic strength parameter (sigma_0) in Eq. (2a)
  Real*8 D_p              ! damage state variable in Eq. (2a)

  Real*8 H_dot            ! H rate (H_dot) in Eq. (2b)
  Real*8 h_p              ! coefficient related with E and phi_p (h) in Eq. (2b)
  Real*8 H_star           ! coefficient related with phi_p (H*) in Eq. (2b)

  Real*8 D_d_dot          ! rate of D_d in Eq. (2c)
  Real*8 C                ! constant in Eq. (2c)

  Real*8 D_p_dot          ! rate of D_p in Eq. (2d)
  Real*8 K_p              ! kinetic rate constant K_p in Eq. (2d)

  Real*8 rho_i            ! dislocation density (rho_i) in Eq. for e_dot_0
  Real*8 phi_p            ! gamma_prime volume fraction (phi_p) in Eq. for e_dot_0
  Real*8 M_bar            ! mean Taylor factor (M_bar) in Eq. for e_dot_0
  Real*8 pai              ! constant pai = 3.14
  Real*8 c_j              ! jog density (c_j) in Eq. for e_dot_0
  Real*8 D_v              ! volume diffusivity (D_v) in Eq. for e_dot_0
  Real*8 e_dot_0_p        ! strain rate coefficient (epsilon_dot_0_prime) in Eq. for e_dot_0
```

```
  Real*8 Q_dj                ! activation energy (Q_d,j) in Eq. for e_dot_0
  Real*8 R                   ! gas constant
  Real*8 Temp                ! temperature
  Real*8 K_CF                ! constraint factor (K_CF) in Eq. for e_dot_0, (K_CF=1 for phi_p<0.3) in
Eq. for sigma_0
  Real*8 k_boltz             ! boltzmann constant
  Real*8 b_vec               ! burger's vector in Eq. for sigma_0
  Real*8 lambda_p            ! inter-partical (surface to surface) spacing (lambda_p) in Eq. for sigma_0
  Real*8 E_Ymod              ! Young's modulus (E) in Eq. for h_p

  Real*8 time                ! time
  Real*8 delta_t             ! time step

    integer i,j,k, iteration
!     Real*8 double_contracted
!!!!!!!!!!!!!!!!!!!!!!!!!!!!!!
! Values of parameters   !
!!!!!!!!!!!!!!!!!!!!!!!!!!!!!!
phi_p=0.45          ! from experimental results

E_Ymod=135.3E9              ! Young's modulus from JMat Pro simulation

K_CF=1.71                ! phi_p=0.217<0.3

sigma=40E6          ! applied stress sigma=40MPa from creep test condition

sigma_0=20.63E6        ! sigma_0=20.63MPa

Q_dj=300E3           ! Q_dj=300kJ/mol activation energy

R=8.314              ! gas constant
```

```
Temp=1273              ! creep temperature

C=67                   ! constant

K_p=3.7E-5             ! kinetic rate constant

e=0                    ! boundary condition

H=0                ! boundary condition

D_d=0              ! boundary condition

D_p=0              ! boundary conditionn

!H_star=2*phi_p/(1+2*phi_p)    ! Eq. for H_star
H_star=0.474

!h_p=E_Ymod*phi_p                    ! Eq. for h_p
h_p=60.89E9

!e_dot_0=e_dot_0_p*exp(-Q_dj/R/Temp)      ! Eq. for e_dot_0
e_dot_0=1.97E-8

e_dot=e_dot_0*(1+D_d)*sinh(sigma*(1-H)/sigma_0/(1-D_p))      ! Eq. (2a)

H_dot=h_p/sigma*(1-H/H_star)*e_dot      ! Eq. (2b)

D_d_dot=C*e_dot            ! Eq. (2c)

D_p_dot=K_p/3*(1-D_p)**4      ! Eq. (2d)
```

```
time=0

delta_t=1

    write(*,*)'time:', time
    write(*,*)'nomalised back stress (H):', H
    write(*,*)'strain (e):', e
    write(*,*)'D_d:', D_d
    write(*,*)'D_p:', D_p
    write(*,*)'e_dot_p:',e_dot_0_p
    write(*,*)'back stress rate (H_dot):', H_dot
    write(*,*)'strain rate (e_dot):', e_dot
      write(*,*)'D_d_dot:',D_d_dot
      write(*,*)'D_p_dot:',D_p_dot
    write(*,*)'-----------------------------------','-----------'

  open (unit=10, file='strain-2.txt')          ! output file strain-2.txt
  write (10, *)    '    time              strain                        b_stress'
   write (10, *)  time, e, H

!      do while (time<(3600*500))
       do while (time<3600*500)

       time=time+delta_t

        H=H+H_dot*delta_t       ! new H value from previous time step

        e=e+e_dot*delta_t                ! new e value from previous time step

        D_d=D_d+D_d_dot*delta_t         ! new D_d value from previous time step
```

```
      D_p=D_p+D_p_dot*delta_t          ! new D_p value from previous time step
      e_dot=e_dot_0*(1+D_d)*sinh(sigma*(1-H)/sigma_0/(1-D_p))     ! new e_dot value in Eq. (2a)
       H_dot=h_p/sigma*(1-H/H_star)*e_dot    ! new H_dot value in Eq. (2b)
      D_d_dot=C*e_dot              ! new D_d_dot value in Eq. (2c)
      D_p_dot=K_p/3*(1-D_p)**4      ! new D_p_dot value in Eq. (2d)

     if (abs(time/3600-nint(time/3600))<0.00001) then     ! output data very 1 hour
      write (10,*)   time/3600, e, H
     endif
 !open (unit=11, file='strain-2.txt')
  !    write (11,*)  'time', 'strain'
  !open (unit=11, file='creep_strain.txt')
    !  write (11, *)  time, e

!    write(*,*)'time:', time
!    write(*,*)'nomalised back stress (H):', H
!    write(*,*)'strain (e):', e
!    write(*,*)'D_d:',D_d
!    write(*,*)'D_p:',D_p
!    write(*,*)'back stress rate (H_dot):', H_dot
!    write(*,*)'strain rate (e_dot):', e_dot
!      write(*,*)'D_d_dot:',D_d_dot
!      write(*,*)'D_p_dot:',D_p_dot
!    write(*,*)'-----------------------------------','-----------'
     enddo

   write(*,*)'Check','the results now!
!!!!!!!!!!!!!!!!!!!!!!
! End of the program  !
!!!!!!!!!!!!!!!!!!!!!!
```

Reference

1. B. Johnston, M.C. Mayo, and A. Khare, *Hydrogen: the energy source for the 21st century.* Technovation, 2005. **25**(6): p. 569-585.
2. R. Ramachandran and R.K. Menon, *An overview of industrial uses of hydrogen.* International Journal of Hydrogen Energy, 1998. **23**(7): p. 593-598.
3. M. Ball and M. Wietschel, *The future of hydrogen - opportunities and challenges.* International Journal of Hydrogen Energy, 2009. **34**(2): p. 615-627.
4. C.M. Kalamaras and A.M. Efstathiou, *Hydrogen production technologies: current state and future developments*, in *Power options for the eastern mediterrancean region*. 2013, Hindawi Publishing Corporation: Limassol, Cyprus. p. 9.
5. H.F. Abbas and W.M.A.W. Daud, *Hydrogen production by thermocatalytic decomposition of methane using a fixed bed activated carbon in a pilot scale unit: Apparent kinetic, deactivation and diffusional limitation studies.* International Journal of Hydrogen Energy, 2010. **35**(22): p. 12268-12276.
6. S. Ayabe, H. Omoto, T. Utaka, R. Kikuchi, K. Sasaki, Y. Teraoka, and K. Eguchi, *Catalytic autothermal reforming of methane and propane over supported metal catalysts.* Applied Catalysis A-General, 2003. **241**(1-2): p. 261-269.
7. M.A. Rakib, J.R. Grace, C.J. Lim, S.H. Elnashaie, and B. Ghiasi, *Steam reforming of propane in a fluidized bed membrane reactor for hydrogen production.* International Journal of Hydrogen Energy, 2010. **35**(12): p. 6276-6290.
8. L. Pino, V. Recupero, S. Beninati, A.K. Shukla, M.S. Hegde, and P. Bera, *Catalytic partial-oxidation of methane on a ceria-supported platinum catalyst for application in fuel cell electric vehicles.* Applied Catalysis A-General, 2002. **225**(1-2): p. 63-75.
9. H.F. Abbas and W.W. Daud, *Hydrogen production by methane decomposition: A review.* International Journal of Hydrogen Energy, 2010. **35**(3): p. 1160-1190.
10. T.L. LeValley, A.R. Richard, and M.H. Fan, *The progress in water gas shift and steam reforming hydrogen production technologies - A review.* International Journal of Hydrogen Energy, 2014. **39**(30): p. 16983-17000.
11. T. Silveira and I. May, *Reformer furnaces: Materials, damage mechanisms and assessment.* Arabian Journal for Science and Engineering Section B: Engineering, 2006. **31**(2C): p. 99-119.
12. A. Liquide, *Air Liquide starts up a large hydrogen production unit in Germany*. Paris, France: Air Liquide, 2015. **2016**.
13. K. Aasberg-Petersen, I. Dybkjaer, C.V. Ovesen, N.C. Schjodt, J. Sehested, and S.G. Thomsen, *Natural gas to synthesis gas - Catalysts and catalytic processes.* Journal of Natural Gas Science and Engineering, 2011. **3**(2): p. 423-459.
14. A.P. Simpson and A.E. Lutz, *Exergy analysis of hydrogen production via steam methane reforming.* International Journal of Hydrogen Energy, 2007. **32**(18): p. 4811-4820.
15. J.D. Holladay, J. Hu, D.L. King, and Y. Wang, *An overview of hydrogen production technologies.* Catalysis Today, 2009. **139**(4): p. 244-260.
16. F. Abe, T.U. Kern, and R. Viswanathan, *Creep-Resistant Steels*. 2008: Elsevier Science.
17. I.M. Nowak, *Development of heat resistant alloys for optimal creep performance*. 2015, University of Birmingham: Eng.D. thesis.
18. C. Edeleanu, *Materials Technology in Steam Reforming Processes: Proceedings*. 1966: Symposium Publications Division, Pergamon Press.
19. A.S. Khanna, *5 - High Temperature Oxidation*, in *Handbook of Environmental Degradation of Materials (Second Edition)*, M. Kutz, Editor. 2012, William Andrew Publishing: Oxford. p. 127-194.
20. *Design Guidelines for the Selection and Use of Stainless Steel*. 1993: Specialty Steel Industry of the United States.
21. J.R. Davis and A.S. Committee, *Stainless Steels*. 1994: ASM International.

22. R.W. Honeycombe, H.H. Bhadeshia, and H. Bhadeshia, *Steels: Microstructure and Properties*. 1995: E. Arnold.
23. R. Kirchheiner and P. Woelpert, *Niobium in centrifugally cast tubes for petrochemical applications.* Niobium: Science & Technology, 2001: p. 1041-1054.
24. W.T. Hou and R.W.K. Honeycombe, *Structure of Centrifugally Cast Austenitic Stainless-Steels .2. Effects of Nb, Ti, and Zr*. Materials Science and Technology, 1985. **1**(5): p. 390-397.
25. C. Agrafiotis, H. von Storch, M. Roeb, and C. Sattler, *Solar thermal reforming of methane feedstocks for hydrogen and syngas production-A review*. Renewable & Sustainable Energy Reviews, 2014. **29**: p. 656-682.
26. K. Kaneko, T. Fukunaga, K. Yamada, N. Nakada, M. Kikuchi, Z. Saghi, J.S. Barnard, and P.A. Midgley, *Formation of $M_{23}C_6$-type precipitates and chromium-depleted zones in austenite stainless steel.* Scripta Materialia, 2011. **65**(6): p. 509-512.
27. J.P. Adamson and J.W. Martin, *Nucleation of $M_{23}C_6$ Carbide Particles in Grain Boundaries of an Austenitic Stainless Steel.* Acta Metallurgica, 1971. **19**(10): p. 1015-1018.
28. H.U. Hong, B.S. Rho, and S.W. Nam, *Correlation of the $M_{23}C_6$ precipitation morphology with grain boundary characteristics in austenitic stainless steel.* Materials Science and Engineering A-Structural Materials Properties Microstructure and Processing, 2001. **318**(1-2): p. 285-292.
29. R.A. Carolan and R.G. Faulkner, *Grain-Boundary Precipitation of $M_{23}C_6$ in an Austenitic Steel.* Acta Metallurgica, 1988. **36**(2): p. 257-266.
30. R. Stickler and A. Vinckier, *Morphology of Grain Boundary Carbides in a 304 Stainless Steel.* Acta Metallurgica, 1961. **9**(9): p. 898-899.
31. F.R. Beckitt and B.R. Clark, *Shape and Mechanism of Formation of $M_{23}C_6$ Carbide in Austenite.* Acta Metallurgica, 1967. **15**(1): p. 113-129.
32. N. Terao and B. Sasmal, *Precipitation of $M_{23}C_6$ Type Carbide on Twin Boundaries in Austenitic Stainless-Steels.* Metallography, 1980. **13**(2): p. 117-133.
33. W.H. Jiang, X.D. Yao, H.R. Guan, and Z.Q. Hu, *Relationship between degeneration of M_7C_3 and precipitation of $M_{23}C_6$ in a cobalt base superalloy.* Materials Science and Technology, 1999. **15**(5): p. 596-598.
34. M. Vardavoulias, G. Papadimitriou, and D. Pantelis, *Effect of M_7C_3-$M_{23}C_6$ Transformation on Fracture-Behavior of Cast Ferritic Stainless-Steels.* Materials Science and Technology, 1993. **9**(8): p. 711-717.
35. A. Wiengmoon, T. Chairuangsri, and J.T.H. Pearce, *A microstructural study of destabilised 30wt%Cr-2.3wt%C high chromium cast iron.* ISIJ International, 2004. **44**(2): p. 396-403.
36. B. Cho, S. Chung, K. Kim, T. Kang, C. Park, and B. Kim, *Photoemission study of the stainless steel surface interacting with oxygen.* Applied Surface Science, 2001. **173**(1-2): p. 22-29.
37. R. Voicu, E. Andrieu, D. Poquillon, J. Furtado, and J. Lacaze, *Microstructure evolution of HP40-Nb alloys during aging under air at 1000 °C.* Materials Characterization, 2009. **60**(9): p. 1020-1027.
38. H.L. Yakel, *Atom Distributions in Tau Carbide Phases - Fe and Cr Distributions in $(Cr_{23-x}Fe_x)C_6$ with x=0, 0.74, 1.70, 4.13 and 7.36.* Acta Crystallographica Section B-Structural Science, 1987. **43**: p. 230-238.
39. M.A. Rouault, P. Herpin, and M.R. Fruchart, *Crystallographic Study of Carbides Cr_7C_3 and Mn_7C_3.* Annales De Chimie France, 1970. **5**(6): p. 461-470.
40. W.B. Pearson, P. Villars, and L.D. Calvert, *Pearson's handbook of crystallographic data for intermetallic phases*. 1985: American Society for Metals.
41. V. Vodarek, *Morphology and Orientation Relationship of Z-Phase in Austenite.* Scripta Metallurgica Et Materialia, 1991. **25**(3): p. 549-552.
42. F. Shi, L.J. Wang, W.F. Cui, and C.M. Liu, *Precipitation Kinetics of Cr_2N in High Nitrogen Austenitic Stainless Steel.* Journal of Iron and Steel Research, International, 2008. **15**(6): p. 72-77.
43. H.J. Beattie and F.L. Versnyder, *New Complex Phase in a High-Temperature Alloy.* Nature, 1956. **178**(4526): p. 208-209.

44. G.V. Raynor and V.G. Rivlin, *Phase Equilibria in Iron Ternary Alloys*. 1988, London: The Institute of Metals.
45. M.F. McGuire, *Stainless Steels for Design Engineers*. 2008: ASM International.
46. M. Onink, C.M. Brakman, F.D. Tichelaar, E.J. Mittemeijer, S. Vanderzwaag, J.H. Root, and N.B. Konyer, *The Lattice-Parameters of Austenite and Ferrite in Fe-C Alloys as Functions of Carbon Concentration and Temperature.* Scripta Metallurgica Et Materialia, 1993. **29**(8): p. 1011-1016.
47. P. Marshall, *Austenitic Stainless Steels: Microstructure and mechanical properties*. 1984: Springer Netherlands.
48. D.F. West and N. Saunders, *Ternary Phase Diagrams in Materials Science*. 2002: Maney for the Institute of Materials.
49. J.L. Lai, *A Study of Precipitation in AISI Type 316 Stainless-Steel.* Materials Science and Engineering, 1983. **58**(2): p. 195-209.
50. T. Matsuo, T. Shinoda, and R. Tanaka, *Effect of Nitrogen, Boron and Phosphorous on High Temperature Strength of 18Cr-10Ni and 18Cr-10Ni-Mo Austenitic Steels Bearing Small Amounts of Titanium and Niobium.* Tetsu-to-Hagane, 1973. **59**(7): p. 907-918.
51. A. Golpayegani, H.O. Andren, H. Danielsen, and J. Hald, *A study on Z-phase nucleation in martensitic chromium steels.* Materials Science and Engineering A-Structural Materials Properties Microstructure and Processing, 2008. **489**(1-2): p. 310-318.
52. V. Vodarek, *Creep behaviour and microstructural evolution in AISI 316LN+Nb steels at 650 ^{o}C.* Materials Science and Engineering A-Structural Materials Properties Microstructure and Processing, 2011. **528**(12): p. 4232-4238.
53. H.K. Danielsen and J. Hald, *On the nucleation and dissolution process of Z-phase Cr(V,Nb)N in martensitic 12%Cr steels.* Materials Science and Engineering A-Structural Materials Properties Microstructure and Processing, 2009. **505**(1-2): p. 169-177.
54. J. Erneman, M. Schwind, P. Liu, J.O. Nilsson, H.O. Andren, and J. Agren, *Precipitation reactions caused by nitrogen uptake during service at high temperatures of a niobium stabilised austenitic steel.* Acta Materialia, 2004. **52**(14): p. 4337-4350.
55. V. Raghavan, *Effect of Manganese on the Stability of Austenite in Fe-Cr-Ni Alloys.* Metallurgical and Materials Transactions A-Physical Metallurgy and Materials Science, 1995. **26**(2): p. 237-242.
56. F.C. Nunes, L.H. de Almeida, J. Dille, J.L. Delplancke, and I. Le May, *Microstructural changes caused by yttrium addition to NbTi-modified centrifugally cast HP-type stainless steels.* Materials Characterization, 2007. **58**(2): p. 132-142.
57. D.J. Powell, R. Pilkington, and D.A. Miller, *The Precipitation Characteristics of 20% Cr 25% Ni-Nb Stabilized Stainless-Steel.* Acta Metallurgica, 1988. **36**(3): p. 713-724.
58. F. Abe, *Precipitate design for creep strengthening of 9% Cr tempered martensitic steel for ultra-supercritical power plants.* Science and Technology of Advanced Materials, 2008. **9**(1): p. 1-15.
59. M. Taneike, K. Sawada, and F. Abe, *Effect of carbon concentration on precipitation behavior of $M_{23}C_6$ carbides and MX carbonitrides in martensitic 9Cr steel during heat treatment.* Metallurgical and Materials Transactions A-Physical Metallurgy and Materials Science, 2004. **35A**(4): p. 1255-1262.
60. G.D. Soares, L.H. Dealmeida, T.L. Dasilveira, and I. Lemay, *Niobium Additions in HP Heat-Resistant Cast Stainless-Steels.* Materials Characterization, 1992. **29**(4): p. 387-396.
61. R.P. Ibanez, G.D. Soares, L.H. Dealmeida, and I. Lemay, *Effects of Si Content on the Microstructure of Modified-HP Austenitic Steels.* Materials Characterization, 1993. **30**(4): p. 243-249.
62. J.B. Yan, Y.M. Gao, F. Yang, C.Y. Yao, Z.Z. Ye, D.W. Yi, and S.Q. Ma, *Effect of tungsten on the microstructure evolution and mechanical properties of yttrium modified HP40Nb alloy.* Materials Science and Engineering A-Structural Materials Properties Microstructure and Processing, 2011. **529**: p. 361-369.

63. G.D. Barbabela, L.H. Dealmeida, T.L. Dasilveira, and I. Lemay, *Role of Nb in Modifying the Microstructure of Heat-Resistant Cast HP Steel.* Materials Characterization, 1991. **26**(3): p. 193-197.
64. L.H. de Almeida, A.F. Ribeiro, and I. Le May, *Microstructural characterization of modified 25Cr-35Ni centrifugally cast steel furnace tubes.* Materials Characterization, 2002. **49**(3): p. 219-229.
65. J.B. Yan, Y.M. Gao, L. Liang, Z.Z. Ye, Y.F. Li, W. Chen, and J.J. Zhang, *Effect of yttrium on the cyclic oxidation behaviour of HP40 heat-resistant steel at 1373 K.* Corrosion Science, 2011. **53**(1): p. 329-337.
66. V. Kuzucu, M. Aksoy, and M.H. Korkut, *The effect of strong carbide-forming elements such as Mo, Ti, V and Nb on the microstructure of ferritic stainless steel.* Journal of Materials Processing Technology, 1998. **82**(1-3): p. 165-171.
67. K.G. Swift and J.D. Booker, *Chapter 3 - Casting Processes*, in *Manufacturing Process Selection Handbook*, K.G.S.D. Booker, Editor. 2013, Butterworth-Heinemann: Oxford. p. 61-91.
68. X.Q. Wu, H.M. Jing, Y.G. Zheng, Z.M. Yao, W. Ke, and Z.Q. Hu, *The eutectic carbides and creep rupture strength of 25Cr20Ni heat-resistant steel tubes centrifugally cast with different solidification conditions.* Materials Science and Engineering A-Structural Materials Properties Microstructure and Processing, 2000. **293**(1-2): p. 252-260.
69. N.H. Pryds and X. Huang, *The effect of cooling rate on the microstructures formed during solidification of ferritic steel.* Metallurgical and Materials Transactions A-Physical Metallurgy and Materials Science, 2000. **31**(12): p. 3155-3166.
70. M.C. Flemings, *Solidification Processing*. 1974: McGraw-Hill.
71. M. Bleckmann, J. Gleinig, J. Hufenbach, H. Wendrock, L. Giebeler, J. Zeisig, U. Diekmann, J. Eckert, and U. Kuhn, *Effect of cooling rate on the microstructure and properties of FeCrVC.* Journal of Alloys and Compounds, 2015. **634**: p. 200-207.
72. J.C. Zhao and P. Yan, *The effect of cooling rate of solidification on microstructure and alloy element segregation of as cast Alloy 718*, in *TMS (The Minerals. Metals & Materials Society)*. 2001. p. 8.
73. Y.K. Luan, N.N. Song, Y.L. Bai, X.H. Kang, and D.Z. Li, *Effect of solidification rate on the morphology and distribution of eutectic carbides in centrifugal casting high-speed steel rolls.* Journal of Materials Processing Technology, 2010. **210**(3): p. 536-541.
74. M. Zuo, X.F. Liu, Q.Q. Sun, and K. Jiang, *Effect of rapid solidification on the microstructure and refining performance of an Al-Si-P master alloy.* Journal of Materials Processing Technology, 2009. **209**(15-16): p. 5504-5508.
75. F.N. Nabarro and F. de Villiers, *Physics Of Creep And Creep-Resistant Alloys*. 1995: Taylor & Francis.
76. A.P. Mouritz, *5 - Mechanical and durability testing of aerospace materials*, in *Introduction to Aerospace Materials*. 2012, Woodhead Publishing. p. 91-127.
77. R.W. Evans, B. Wilshire, and I.o. Metals, *Creep of Metals and Alloys*. 1985: Institute of Metals.
78. D. Mclean, *Physics of High Temperature Creep in Metals.* Reports on Progress in Physics, 1966. **29**: p. 1-33.
79. B.F. Dyson and M. Mclean, *Particle-Coarsening, σ_o and Tertiary Creep.* Acta Metallurgica, 1983. **31**(1): p. 17-27.
80. F.H. Norton, *The Creep of Steel at High Temperatures*. 1929: McGraw-Hill Book Company, Incorporated.
81. J.O. Nilsson, P.R. Howell, and G.L. Dunlop, *Interfacial Microstructure and Low Stress, High-Temperature Creep of an Austenitic Stainless-Steel.* Acta Metallurgica, 1979. **27**(2): p. 179-186.
82. G.E. Dieter, *Mechanical metallurgy*. 1976: McGraw-Hill.
83. F. Garofalo, *Fundamentals of creep and creep-rupture in metals*. 1965, New York, NY: Macmillan.

84. R.W. Evans and B. Wilshire, *Introduction to creep*. 1993: Institute of Materials.
85. M.E. Kassner, *Chapter 8 - Creep Behavior of Particle-Strengthened Alloys*, in *Fundamentals of Creep in Metals and Alloys (Third Edition)*, M.E. Kassner, Editor. 2015, Butterworth-Heinemann: Boston. p. 167-188.
86. D.G. Morris and D.R. Harries, *Wedge Crack Nucleation in Type-316 Stainless-Steel.* Journal of Materials Science, 1977. **12**(8): p. 1587-1597.
87. M. Tabuchi, T. Adachi, A.T. Yokoburi, A. Fuji, J.C. Ha, and T. Yokobori, *Evaluation of creep crack growth properties using circular notched specimens.* International Journal of Pressure Vessels and Piping, 2003. **80**(7-8): p. 417-425.
88. K. Kimura, H. Kushima, and K. Sawada, *Long-term creep deformation property of modified 9Cr-1Mo steel.* Materials Science and Engineering a-Structural Materials Properties Microstructure and Processing, 2009. **510-11**: p. 58-63.
89. H.E. Evans, *Mechanisms of Creep Fracture*. 1984: Elsevier Applied Science.
90. C. Herring, *Diffusional Viscosity of a Polycrystalline Solid.* Journal of Applied Physics, 1950. **21**(5): p. 437-445.
91. R.L. Coble, *A Model for Boundary Diffusion Controlled Creep in Polycrystalline Materials.* Journal of Applied Physics, 1963. **34**(6): p. 1679-1682.
92. C.R. Barrett and W.D. Nix, *A Model for Steady State Creep Based on Motion of Jogged Screw Dislocations.* Acta Metallurgica, 1965. **13**(12): p. 1247-1258.
93. P.W. Davies and B. Wilshire, *Internal Stress Measurement and Mechanism of High Temperature Creep.* Scripta Metallurgica, 1971. **5**(6): p. 475-478.
94. J. Weertman, *Theory of Steady-State Creep Based on Dislocation Climb.* Journal of Applied Physics, 1955. **26**(10): p. 1213-1217.
95. M.F. Ashby, *FIRST REPORT ON DEFORMATION-MECHANISM MAPS.* Acta Metallurgica, 1972. **20**(7): p. 887-897.
96. H.J. Frost and M.F. Ashby, *Deformation-mechanism maps: the plasticity and creep of metals and ceramics*. 1982: Pergamon Press.
97. Y. Takahashi and T. Yamane, *Application of Deformation Mechanism Maps to the Study of High-Temperature Creep of a Precipitate-Free 25wt%-Cr-20wt%-Ni Austenitic Stainless-Steel.* Journal of Materials Science, 1981. **16**(11): p. 3171-3182.
98. Y. Kondo, T. Matsuo, T. Shinoda, and R. Tanaka, *Effect of Grain Size on the High Temperature Creep Properties of 17Cr-14Ni Steel.* Tetsu-to-Hagane, 1979. **65**(7): p. 896-905.
99. K. Kimura, N. Ohi, K. Shimazu, T. Matsuo, R. Tanaka, and M. Kikuchi, *Effect of Prior Austenite Grain-Size on High-Temperature Creep-Properties of Cr-Mo-V Rotor Steel.* Scripta Metallurgica, 1987. **21**(1): p. 19-22.
100. Y. Kondo, T. Matsuo, T. Shinoda, and R. Tanaka, *Effect of Grain Size on High Temperature Creep Properties of Hastelloy X.* Tetsu-to-Hagane, 1981. **67**(10): p. 1805-1814.
101. S.L. Mannan and P. Rodriguez, *Effect of Grain-Size on Creep Rate in Type-316 Stainless-Steel at 873 K and 973 K.* Metal Science, 1983. **17**(2): p. 63-69.
102. G. Nelmes and B. Wilshire, *Some Factors Affecting Creep Resistance of Single-Phase Copper-Alloys.* Scripta Metallurgica, 1976. **10**(8): p. 697-700.
103. Y. Kondo, T. Matsuo, T. Shinoda, and R. Tanaka, *Effects of Cr, Mo, W, Nb, Ta, Ti, Zr and Hf on High Temperature Creep Properties of Carbon Free 25 Cr-35 Ni Steel.* Tetsu-to-Hagane, 1981. **67**(7): p. 987-995.
104. M. Takeyama, K. Kawasaki, T. Matsuo, and R. Tanaka, *Effect of Grain Boundary Precipitates on High Temperature Creep Properties of Ni-20Cr-Nb-W Alloys.* Tetsu-to-Hagane, 1986. **72**(10): p. 1605-1612.
105. M.D. Mathew, G. Sasikala, K.B.S. Rao, and S.L. Mannan, *Influence of Carbon and Nitrogen on the Creep-Properties of Type 316 Stainless-Steel at 873 K.* Materials Science and Engineering A-Structural Materials Properties Microstructure and Processing, 1991. **148**(2): p. 253-260.

106. R. Tanaka, T. Shinoda, and Y. Tobe, *The Effect of Mo, N, and C on High Temperature Properties of 25%Cr-28%Ni Heat Resisting Steels.* Tetsu-to-Hagane, 1970. **56**(8): p. 1014-1033.
107. J.S. Zhang, P.E. Li, W.X. Chen, and J.Z. Jin, *Grain-Boundary Precipitation Strengthening in High-Temperature Creep of Fe-15Cr-25Ni Alloys.* Scripta Metallurgica, 1989. **23**(4): p. 547-551.
108. T. Matsuo, K. Nakajima, Y. Terada, and M. Kikuchi, *High-Temperature Creep Resistance of Austenitic Heat-Resisting Steels.* Materials Science and Engineering A-Structural Materials Properties Microstructure and Processing, 1991. **146**(1-2): p. 261-272.
109. R.A. Stevens and P.E.J. Flewitt, *The Dependence of Creep Rate on Microstructure in a γ'-Strengthened Super-Alloy.* Acta Metallurgica, 1981. **29**(5): p. 867-882.
110. P.L. Threadgill and B. Wilshire, *The Effect of Particle Size and Spacing on Creep of Two-Phase Copper–Cobalt Alloys.* Metal Science, 1974. **8**(1): p. 117-124.
111. J.D. Parker and B. Wilshire, *The Effect of a Dispersion of Cobalt Particles on High-Temperature Creep of Copper.* Metal Science, 1975. **9**(1): p. 248-252.
112. E. Arzt and M.F. Ashby, *Threshold Stresses in Materials Containing Dispersed Particles.* Scripta Metallurgica, 1982. **16**(11): p. 1285-1290.
113. R. Lagnebor, *Bypassing of Dislocations Past Particles by a Climb Mechanism.* Scripta Metallurgica, 1973. **7**(6): p. 605-613.
114. H.E. Evans and G. Knowles, *Threshold Stress for Creep in Dispersion-Strengthened Alloys.* Metal Science, 1980. **14**(7): p. 262-266.
115. M. Mclean, *On the Threshold Stress for Dislocation Creep in Particle Strengthened Alloys.* Acta Metallurgica, 1985. **33**(4): p. 545-556.
116. V.C. Nardone, D.E. Matejczyk, and J.K. Tien, *The Threshold Stress and Departure Side Pinning of Dislocations by Dispersoids.* Acta Metallurgica, 1984. **32**(9): p. 1509-1517.
117. J.H. Schroder and E. Arzt, *Weak Beam Studies of Dislocation Dispersoid Interaction in an ODS Superalloy.* Scripta Metallurgica, 1985. **19**(9): p. 1129-1134.
118. E. Arzt and D.S. Wilkinson, *Threshold Stresses for Dislocation Climb over Hard Particles - the Effect of an Attractive Interaction.* Acta Metallurgica, 1986. **34**(10): p. 1893-1898.
119. E. Arzt and J. Rosler, *The Kinetics of Dislocation Climb over Hard Particles .2. Effects of an Attractive Particle Dislocation Interaction.* Acta Metallurgica, 1988. **36**(4): p. 1053-1060.
120. J. Rosler and E. Arzt, *A New Model-Based Creep Equation for Dispersion Strengthened Materials.* Acta Metallurgica Et Materialia, 1990. **38**(4): p. 671-683.
121. M.Y. Wey, T. Sakuma, and T. Nishizawa, *Growth of Alloy Carbide Particles in Austenite.* Transactions of the Japan Institute of Metals, 1981. **22**(10): p. 733-742.
122. N.Q. Zhu, L. Lu, Y.L. He, L. Li, and X.G. Lu, *Coarsening of $M_{23}C_6$ Precipitates in an Fe-Cr-C Ternary Alloy.* Journal of Iron and Steel Research International, 2012. **19**(9): p. 62-67.
123. R.A. Stevens and P.E.J. Flewitt, *Effects of γ'-Precipitate Coarsening during Isothermal Aging and Creep of the Nickel-Base Superalloy-IN738.* Materials Science and Engineering, 1979. **37**(3): p. 237-247.
124. K.R. Williams and B.J. Cane, *Creep-Behavior of 0.5Cr0.5Mo0.25V Steel at Engineering Stresses.* Materials Science and Engineering, 1979. **38**(3): p. 199-210.
125. H. Basoalto, S.K. Sondhi, B.F. Dyson, and M. McLean, *A generic microstructure-explicit model of creep in nickel-base superalloys.* Superalloys 2004, 2004: p. 897-906.
126. H.C. Basoalto, J.W. Brooks, and I. Di Martino, *Multiscale microstructure modelling for nickel based superalloys.* Materials Science and Technology, 2009. **25**(2): p. 221-227.
127. B.F. Dyson, *Microstructure based creep constitutive model for precipitation strengthened alloys: theory and application.* Materials Science and Technology, 2009. **25**(2): p. 213-220.
128. J. Coakley, D. Dye, and H. Basoalto, *Creep and creep modelling of a multimodal nickel-base superalloy.* Acta Materialia, 2011. **59**(3): p. 854-863.
129. R. Oruganti, M. Karadge, and S. Swaminathan, *Damage mechanics-based creep model for 9-10% Cr ferritic steels.* Acta Materialia, 2011. **59**(5): p. 2145-2155.

130. Z. Zhu, H. Basoalto, N. Warnken, and R.C. Reed, *A model for the creep deformation behaviour of nickel-based single crystal superalloys.* Acta Materialia, 2012. **60**(12): p. 4888-4900.
131. M. Whittaker, B. Wilshire, and J. Brear, *Creep fracture of the centrifugally-cast superaustenitic steels, HK40 and HP40.* Materials Science and Engineering A-Structural Materials Properties Microstructure and Processing, 2013. **580**: p. 391-396.
132. N. Saunders, Z. Guo, X. Li, A.P. Miodownik, and J.P. Schille, *Using JMatPro to model materials properties and behavior.* Jom-Journal of the Minerals Metals & Materials Society, 2003. **55**(12): p. 60-65.
133. U.R. Kattner, *The thermodynamic modeling of multicomponent phase equilibria.* Jom-Journal of the Minerals Metals & Materials Society, 1997. **49**(12): p. 14-19.
134. A. Aghajani, C. Somsen, and G. Eggeler, *On the effect of long-term creep on the microstructure of a 12% chromium tempered martensite ferritic steel.* Acta Materialia, 2009. **57**(17): p. 5093-5106.
135. O. Prat, J. Garcia, D. Rojas, C. Carrasco, and A.R. Kaysser-Pyzalla, *Investigations on coarsening of MX and $M_{23}C_6$ precipitates in 12% Cr creep resistant steels assisted by computational thermodynamics.* Materials Science and Engineering A-Structural Materials Properties Microstructure and Processing, 2010. **527**(21-22): p. 5976-5983.
136. Y. Qin, G. Gotz, W. Blum, and Z.G. Zhu, *Determination of size distribution of precipitates in the cast martensitic steel G-X12CrMoWVNbN 10-1-1 by direct and indirect method.* Journal of Alloys and Compounds, 2003. **352**(1-2): p. 260-264.
137. D.B. Williams and C.B. Carter, *Transmission Electron Microscopy: A Textbook for Materials Science. Diffraction. II*. 1996: Springer.
138. A.F. Padilha and P.R. Rios, *Decomposition of austenite in austenitic stainless steels.* ISIJ International, 2002. **42**(4): p. 325-337.
139. M. Deighton, *Solubility of $M_{23}C_6$ in Type-316 Stainless Steel.* Journal of the Iron and Steel Institute, 1970. **208**(Nov): p. 1012-1014.
140. J.R. Gregolin and N.G. Alcantara, *Solidification and Phase-Equilibria in the Fe-C-Cr-NbC System.* Metallurgical Transactions A-Physical Metallurgy and Materials Science, 1991. **22**(10): p. 2181-2186.
141. R. Kesri and M. Durandcharre, *Phase-Equilibria, Solidification and Solid-State Transformations of White Cast Irons Containing Niobium.* Journal of Materials Science, 1987. **22**(8): p. 2959-2964.
142. D.V. Shtansky, K. Nakai, and Y. Ohmori, *Decomposition of martensite by discontinuous-like precipitation reaction in an Fe-17Cr-0.5C alloy.* Acta Materialia, 2000. **48**(4): p. 969-983.
143. S.R. Shatynski, *Thermochemistry of Transition-Metal Carbides.* Oxidation of Metals, 1979. **13**(2): p. 105-118.
144. R. Benz, J.F. Elliott, and J. Chipman, *Thermodynamics of Carbides in System Fe-Cr-C.* Metallurgical Transactions, 1974. **5**(10): p. 2235-2240.
145. M. Hattestrand and H.O. Andren, *Influence of strain on precipitation reactions during creep of an advanced 9% chromium steel.* Acta Materialia, 2001. **49**(12): p. 2123-2128.
146. I.M. Lifshitz and V.V. Slyozov, *The Kinetics of Precipitation from Supersaturated Solid Solutions.* Journal of Physics and Chemistry of Solids, 1961. **19**(1-2): p. 35-50.
147. J.F. Chen, L.C. Zou, Y.L. Chen, and Q. Li, *Effect of stress on precipitation behaviour of 7xxx alloy during age forming process.* Materials Science and Technology, 2016. **32**(1): p. 87-97.
148. D.L. Olmsted, R. Phillips, and W.A. Curtin, *Modelling diffusion in crystals under high internal stress gradients.* Modelling and Simulation in Materials Science and Engineering, 2004. **12**(5): p. 781-797.
149. G. Eggeler, *The Effect of Long-Term Creep on Particle Coarsening in Tempered Martensite Ferritic Steels.* Acta Metallurgica, 1989. **37**(12): p. 3225-3234.
150. S. Spigarelli, E. Cerri, P. Bianchi, and E. Evangelista, *Interpretation of creep behaviour of a 9Cr-Mo-Nb-V-N (T91) steel using threshold stress concept.* Materials Science and Technology, 1999. **15**(12): p. 1433-1440.

151. Y. Kawabe, R. Nakagawa, and T. Mukoyama, *Effect of Nitrogen and Molybdenum on High Temperature Strength of 18Cr-12Ni-0.2C Austenitic Steel.* Transactions of the Iron and Steel Institute of Japan, 1968. **8**(6): p. 353.
152. Q. Lu, W. Xu, and S. van der Zwaag, *Computational design of precipitation strengthened austenitic heat-resistant steels.* Philosophical Magazine, 2013. **93**(25): p. 3391-3412.
153. Q. Chen, J. Jeppsson, and J. Agren, *Analytical treatment of diffusion during precipitate growth in multicomponent systems.* Acta Materialia, 2008. **56**(8): p. 1890-1896.
154. G. Neumann and C. Tuijn, *Self-diffusion and Impurity Diffusion in Pure Metals: Handbook of Experimental Data*. 2009: Pergamon.
155. S.J. Rothman, L.J. Nowicki, and G.E. Murch, *Self-Diffusion in Austenitic Fe-Cr-Ni Alloys.* Journal of Physics F-Metal Physics, 1980. **10**(3): p. 383-398.
156. H. Thier, A. Baumel, and E. Schmidtm, *Effect of Nitrogen on Precipitation Behaviour of Steel X-5 Crnimo-17-13.* Archiv Fur Das Eisenhuttenwesen, 1969. **40**(4): p. 333-339.
157. W.H. Jiang, X.D. Yao, H.R. Guan, and Z.Q. Hu, *Carbide behaviour during high temperature low cycle fatigue in a cobalt-base superalloy.* Journal of Materials Science, 1999. **34**(12): p. 2859-2864.
158. J. Sobotova, P. Jurci, J. Cejp, P. Salabova, and O. Prikner, *Structure and Properties of Sub-Zero Processed Vanadis 6 P/M Ledeburitic Tool Steel.* Metal 2011: 20th Anniversary International Conference on Metallurgy and Materials, 2011: p. 456-461.
159. A.A. Gadhikar, C.P. Sharma, D.B. Goel, and A. Sharma, *Effect of Heat Treatment on Carbides in 23-8-N Steel.* Metal Science and Heat Treatment, 2011. **53**(5-6): p. 293-298.
160. J. Agren, *Computer-Simulations of Diffusion-Controlled Precipitation and Dissolution of Carbide Particles in Steel.* Materials Science and Engineering, 1982. **55**(1): p. 135-141.
161. M. Qian, *In-situ observations of the dissolution of carbides in an Fe-Cr-C alloy.* Scripta Materialia, 1999. **41**(12): p. 1301-1303.
162. F. Masoumi, M. Jahazi, D. Shahriari, and J. Cormier, *Coarsening and dissolution of γ' precipitates during solution treatment of AD730 (TM) Ni-based superalloy: Mechanisms and kinetics models.* Journal of Alloys and Compounds, 2016. **658**: p. 981-995.
163. J. Moon, C. Lee, S. Uhm, and J. Lee, *Coarsening kinetics of TiN particle in a low alloyed steel in weld HAZ: Considering critical particle size.* Acta Materialia, 2006. **54**(4): p. 1053-1061.
164. R.W. Shewfelt and L.M. Brown, *High-Temperature Strength of Dispersion-Hardened Single-Crystals .2. Theory.* Philosophical Magazine, 1977. **35**(4): p. 945-962.
165. A. Ghatak and P.S. Robi, *High-temperature Deformation Behavior of HP40Nb Micro-alloyed Reformer Steel.* Metallography, Microstructure, and Analysis, 2015. **4**(6): p. 508-517.
166. S. Chatterjee, H.S. Wang, J.R. Yang, and H.H. Bhadeshia, *Mechanical stabilisation of austenite.* Materials Science and Technology, 2006. **22**(6): p. 641-644.
167. R.J. Mitchell, M. Preuss, S. Tin, and M.C. Hardy, *The influence of cooling rate from temperatures above the γ' solvus on morphology, mismatch and hardness in advanced polycrystalline nickel-base superalloys.* Materials Science and Engineering A-Structural Materials Properties Microstructure and Processing, 2008. **473**(1-2): p. 158-165.
168. M. Masoumi and M. Pekguleryuz, *Effect of Cooling Rate on the Microstructure of AZ31 Magnesium Alloy*. Transactions of the American Foundry Society, Vol 117, 2009. **117**: p. 617-626.
169. M. Boccalini and H. Goldenstein, *Solidification of high speed steels.* International Materials Reviews, 2001. **46**(2): p. 92-115.
170. Y.M. Won and B.G. Thomas, *Simple model of microsegregation during solidification of steels.* Metallurgical and Materials Transactions A-Physical Metallurgy and Materials Science, 2001. **32**(7): p. 1755-1767.
171. D.A. Porter, K.E. Easterling, and M. Sherif, *Phase Transformations in Metals and Alloys, Third Edition (Revised Reprint)*. 2009: CRC Press.
172. R. Chen, Y.F. Shi, Q.Y. Xu, and B.C. Liu, *Effect of cooling rate on solidification parameters and microstructure of Al-7Si-0.3Mg-0.15Fe alloy*. Transactions of Nonferrous Metals Society of China, 2014. **24**(6): p. 1645-1652.

173. A. Inoue and T. Masumoto, *Carbide Reactions M_3C-M_7C_3-$M_{23}C_6$-M_6C during Tempering of Rapidly Solidified High-Carbon Cr-W and Cr-Mo Steels.* Metallurgical Transactions a-Physical Metallurgy and Materials Science, 1980. **11**(5): p. 739-747.
174. H. Sahlaoui, H. Sidhom, and J. Philibert, *Prediction of chromium depleted-zone evolution during aging of Ni-Cr-Fe alloys.* Acta Materialia, 2002. **50**(6): p. 1383-1392.
175. W. Mayr, W. Lengauer, P. Ettmayer, D. Rafaja, J. Bauer, and M. Bohn, *Phase equilibria and multiphase reaction diffusion in the Cr-C and Cr-N systems.* Journal of Phase Equilibria, 1999. **20**(1): p. 35-44.
176. R.E. B.Wilshire, *Creep of metals and alloys*. 1985, London: The Institute of Metals.
177. F.H.Norton, *The creep of steel at high temperature*. 1929, New York: McGRAW-HILL BOOK COMPANY.
178. R. Oruganti, *A new approach to dislocation creep.* Acta Materialia, 2012. **60**(4): p. 1695-1702.
179. E. Nembcah, *Particle strengthening of metals and alloys*. 1997, New York: John Wiley & Sons, Inc.
180. L.B.R. Ham, *Strengthening methods in crystals*. 1971, London: Applied Science Pulbishers.